UNIVERSITY OF COPENHAGEN
FACULTY OF SCIENCE
NIELS BOHR INSTITUTE

# QUANTUM MEASUREMENT AND CONTROL OF A MECHANICAL RESONATOR

PHD THESIS

MASSIMILIANO ROSSI

This thesis has been submitted to the
PhD school of Science at the University of Copenhagen

2020

| | |
|---|---|
| Supervisor: | Prof. Dr. Albert Schliesser |
| External referees: | Prof. Dr. Klemens Hammerer |
| | Prof. Dr. Tobias J. Kippenberg |
| Local referee: | Prof. Dr. Jesper Nygård |
| | |
| Thesis submission: | July 31, 2020 |
| Thesis defense: | September 29, 2020 |

## ABSTRACT

Displacement measurements are found everywhere, both in scientific applications and in the everyday life. Classical physics and experience suggest that one can perform these measurements with unlimited precision upon technological improvements, without perturbing the measured system. Quantum physics, instead, changes this picture, predicting that the more precise a displacement measurement is done, the larger the disturbance, or quantum backaction, affecting the momentum of the measured system.

As of today, the most precise displacement measurements are done by reflecting a laser field off a mechanical resonator and interferometrically measuring the phase of that field. This interaction, stemming from radiation pressure forces, is at the heart of the field of optomechanics. In such a displacement measurement, the imprecision and the quantum backaction arise from the quantum fluctuations of the optical phase and amplitude quadratures, respectively. In addition, mechanical systems unavoidably couple to a thermal environment, which introduces more disturbance and hinders the observation of quantum effects of the measurement. Nevertheless, an efficient quantum measurement can be realized whenever the information about the displacement is gathered at a rate close to the one at which the mechanical resonator is perturbed, due to both thermal forces and the quantum backaction. When available, the result of this measurement can be used to purify the state-of-knowledge held by an observer about the mechanics, that is, the conditional state. Based on this knowledge, the observer can exert a measurement-based quantum control to convert this conditional state into an unconditional one.

In this thesis, we report experiments achieving quantum displacement measurements of a soft-clamped membrane resonator, inserted in the middle of an optical cavity. The cornerstones of the experiments are the extremely low dissipation rate of the mechanical energy and the high total detection efficiency, which together result in a measurement efficiency of up to 56%. This corresponds to a system operating at the Heisenberg measurement-disturbance limit to within 33%. Furthermore, we employ the quantum trajectory formalism and a retrodiction measurement to experimentally verify the conditional state, which is a coherent one with purity of 78%. Based on the measurement outcomes, we design a feedback loop to exert a viscous force on the resonator. This feedback cools the mechanical mode down to its ground state, with a residual occupation of 0.29 phonons, thus realizing a long-standing goal in the field.

Quantum measurements form an important tool for several applications, from ultra-precise sensing to the generation of entangled states. We exploit these quantum-limited measurements to perform displacement sensing below the standard quantum limit and to generate and verify the entanglement between two lasers, stemming from the simultaneous measurement of a common mechanical motion. The results shown in this thesis make this optomechanical platform attractive for further applications, such as the quantum transduction of information via an electro-opto-mechanical system and the generation of non-classical mechanical states by measurements.

# SAMMENFATNING

Forskydningsmålinger findes overalt, både i videnskabelige anvendelser og i hverdagen. Klassisk fysik og hverdagserfaring tyder på at man kan lave disse målinger med ubegrænset præcision, givet teknologiske forbedringer, uden at forstyrre det målte system. Kvantefysik ændrer dette billede og forudsiger tværtimod at jo mere præcist en forskydningsmåling udføres, desto større en forstyrrelse, eller kvantetilbagevirkning, virker på impulsen af det målte system.

Til dags dato udføres de mest præcise forskydningsmålinger ved at reflektere et laser felt på en mekanisk resonator og interferometrisk måle fasen af det pågældende felt. Denne vekselvirkning, der stammer fra strålingstrykskræfter, ligger til grund for feltet optomekanik. I sådan en forskydningsmåling stammer unøjagtigheden og kvantetilbagevirkningen fra kvantefluktuationer af de optiske fase- og amplitudekvadraturer, respektivt. I tillæg kobler mekaniske systemer uundgåeligt med et termisk miljø, hvilket introducerer yderligere forstyrrelse og forhindrer observation af kvantemekaniske effekter af målingen. Alligevel kan en effektiv kvantemekanisk måling realiseres såfremt information om forskydningen indsamles med en hastighed tæt på den hvormed den mekaniske resonator forstyrres, af både termiske kræfter og den kvantemekaniske tilbagevirkning. Hvis det er tilgængeligt, kan resultatet af denne måling udnyttes til at rense en observatørs videnstilstand om mekanikken, det vil sige den betingede tilstand. På baggrund af denne viden kan observatøren udøve målingsbaseret kvantekontrol for at omdanne den betingede tilstand til en ubetinget en.

I denne afhandling rapporterer vi eksperimenter der opnår kvantemekaniske forskydningsmålinger af en blødt-hæftet membranresonator, indsat i midten af en optisk kavitet. Hjørnestenene af eksperimenterne er den ekstremt lave mekaniske energidissipationsrate samt den høje samlede detektionseffektivitet, hvilket resulterer i en måleeffektivitet på op til 56%. Dette svarer til et system der opererer indenfor 33% af Heisenberggrænsen for måling og forstyrrelse. Vi udnytter yderligere kvantebaneformalismen og en retrodiktionsmåling til eksperimentelt at verificere den betingede tilstand, der er en kohærent en, med en renhed på 78%. På baggrund af måleudfaldene designer vi en tilbagevirkningskreds til at udøve en viskøs kraft på resonatoren. Denne tilbagevirkning nedkøler den mekaniske svingning til dens grundtilstand, med en resterende befolkning på 0.29 fononer, og realiserer således et mangeårigt mål i feltet.

Kvantemålinger udgør et vigtigt værktøj for flere anvendelser, fra ultrapræcise sensorer til generering af sammenfiltrede tilstande. Vi udnytter disse kvantestøjsbegrænsede målinger til at udføre forskyd-

ningsoptegnelser under standardkvantegrænsen og til at generere og verificere sammenfiltringen af to lasere der stammer fra deres simultane måling af en fælles mekanisk tilstand. Resultatet der vises i denne afhandling gør den optomekaniske platform attraktiv for yderligere anvendelser, såsom kvantetransduktion af information ved hjælp af et elektro-opto-mekanisk system og gennem målinger generering af uklassiske mekaniske tilstande.

# PUBLICATIONS

## PEER-REVIEWED JOURNAL ARTICLES

[Ros+18] Rossi, M., Mason, D., Chen, J., Tsaturyan, Y., and Schliesser, A. "Measurement-Based Quantum Control of Mechanical Motion" *Nature* 563, 7729 (2018), pp. 53–58

When I joined the group, a primitive optical setup was already built by J. Chen and Y. Tsaturyan. I improved that existing setup and implemented an efficient balanced homodyne detector, a cavity-based experiment and the electronic locking schemes. Together with D. Mason, I developed the quantum noise thermometry calibration, as well as most of the other calibration methods. I also implemented the digital filters for multi-mode mechanical feedback cooling, with help from D. Mason. I conducted the majority of the data taking run and analyzed part of them. I wrote the manuscript together with D. Mason.

[Ros+19] Rossi, M., Mason, D., Chen, J., and Schliesser, A. "Observing and Verifying the Quantum Trajectory of a Mechanical Resonator." *Phys. Rev. Lett.* 123, 16 (2019), p. 163601

I implemented the time-domain measurement protocol and conducted the data taking. I developed part of the theory. Together with D. Mason, I analyzed most of the data and wrote the manuscript.

[Mas+19] Mason, D., Chen, J., Rossi, M., Tsaturyan, Y., and Schliesser, A. "Continuous Force and Displacement Measurement below the Standard Quantum Limit." *Nat. Phys.* 15, 8 (2019), pp. 745–749

I derived the theoretical model and analyzed all data, with help from D. Mason. I wrote the supplementary information and contributed to the main manuscript.

[Che+20] Chen, J., Rossi, M., Mason, D., and Schliesser, A. "Entanglement of Propagating Optical Modes via a Mechanical Interface." *Nat. Commun.* 11, 1 (2020), p. 943

I implemented the digital electronics to lock the homodyne detectors to an arbitrary quadrature. I devised the measurement protocols for

the verification of the entanglement and the tomography of the state, and I experimentally implemented them in an automatized way. I derived the whole theoretical framework, including the bright/dark mode interpretation. I analyzed most of data, with help from D. Mason. I contributed to the writing of the article.

PREPRINT

[Ros+20] Rossi, M., Mancino, L., Landi, G. T., Paternostro, M., Schliesser, A., and Belenchia, A. "Experimental Asses ment of Entropy Production in a Continuously Measured Mechanical Resonator." *arXiv:2005.03429*, accepted in Phys. Rev. Lett. (2020)

I conducted the experiment and analyzed the data, with the theoretical support from A. Belenchia. I wrote the manuscript, together with all the authors.

[Pag+20] Page, M. A., Goryachev, M., Miao, H., Chen, Y., Ma, Y., Mason, D., Rossi, M., Blair, C. D., Ju, L., Blair, D. G., Schliesser, A., Tobar, M. E., and Zhao, C. "Gravitational Wave Detectors with Broadband High Frequency Sensitivity." *arXiv:2007.08766* (2020)

I performed preliminary experiments on the membrane thermalisaztion properties at mK temperature, together with D. Mason. I contributed to write the relevant sections in the article.

# CONTENTS

# LIST OF FIGURES

## LIST OF TABLES



## ACRONYMS

AOM acousto-optic modulator

APD avalanche photodiode

BAE backaction-evading

BHD balanced homodyne detector

BS beam-splitter

CCD charge-coupled device

CCR canonical commutation relation

CW continuous-wave

DAQ data acquisition system

EOM electro-optic modulator

EPR Einstein-Podolsky-Rosen

FFT fast Fourier transform

FSR free spectral range

FWHM full-width half-maximum

HWP half-waveplate

LIA lock-in amplifier

LMI linear matrix inequality

LO local oscillator

LQG linear-quadratic-Gaussian

MIM membrane-in-the-middle

MXC mixing chamber

NIR near-infrared

OMIT optomechanically induced transparency

PBS polarizing beam-splitter

PDH Pound-Drever-Hall

POVM positive-operator-valued measure

PSD power spectral density

QLE quantum Langevin equations

QND quantum non-demolition

RHS right hand side

RWA rotating wave approximation

SME stochastic master equation

SQL standard quantum limit

TiS Ti:shappire

m.a.d. mean absolute deviation

s.d. standard deviation

## CONVENTIONS

Hereby we report the conventions used throughout the thesis for the spectral analysis. Analogous relations hold for classical processes, $a(t)$ and $b(t)$, where the Hermitian adjoint, $^\dagger$, is replaced by the complex conjugate, $^*$.

$$\mathcal{F}\left[\hat{a}(t)\right](\Omega) \coloneqq \hat{a}(\Omega) = \int_{-\infty}^{\infty} dt e^{\imath\Omega t}\hat{a}(t) \qquad \text{Fourier transform}$$

$$\mathcal{F}^{-1}\left[\hat{a}(\Omega)\right](t) = \int_{-\infty}^{\infty} \frac{d\Omega}{2\pi} e^{-\imath\Omega t}\hat{a}(\Omega) \qquad \text{Inverse Fourier transform}$$

$$\hat{a}(\Omega)^\dagger = \hat{a}^\dagger(-\Omega) = \mathcal{F}\left[\hat{a}(t)^\dagger\right](-\Omega)$$

$$R_{\hat{a}\hat{b}}(\tau) = \left\langle \hat{a}(t+\tau)^\dagger \hat{b}(t) \right\rangle \qquad \text{Two-time correlation function}$$

$$S_{\hat{a}\hat{b}}(\Omega) = \mathcal{F}\left[R_{\hat{a}\hat{b}}(\tau)\right](\Omega) \qquad \text{Power spectral density}$$

$$R_{\hat{a}\hat{b}}(\tau)^* = R_{\hat{b}\hat{a}}(-\tau)$$

$$S_{\hat{a}\hat{b}}(\Omega)^* = S_{\hat{b}\hat{a}}(\Omega)$$

$$\overline{S}_{\hat{a}\hat{b}}(\Omega) \coloneqq \frac{S_{\hat{a}\hat{b}}(\Omega) + S_{\hat{b}\hat{a}}(-\Omega)}{2} \qquad \text{Symmetrization}$$

Classical and quantum noise processes differ in the relation between negative and positive frequency components of the spectrum. Classically, one always has

$$S_{ab}(-\Omega) = S_{b^*a^*}(\Omega)$$

The quantum counterpart is instead not valid, as the operators $\hat{a}(t+\tau)$ and $\hat{b}(\tau)$, in general, do not commute.

# INTRODUCTION

The beginning of the last century was marked by the dawn of quantum physics. The new theory rapidly received wide acceptance from the scientific community as it allowed to explain, with large degree of precision, the new experimental results in atomic physics, in evident contrast with the laws of classical physics. At the same time, quantum theory brought up the necessity to revisit some of the most deep-rooted concepts in human knowledge, formed from everyday life experience. Among them, a special role was played by the concept of measurement, a key part of any science for it allows to connect the world around us to its abstraction we produce, i. e. a theory. Already in the 20s Bohr and Heisenberg promptly realized that a measurement has a profound impact on a quantum system, causing a "reduction of the wave packet" [Hei50]. Furthermore, this effect could not be explained by the dynamical quantum equations, making the relation between the physical world, quantum at its heart, and the measuring apparatus, a classical machine, hard to grasp.

To better understand the radical change let's recall that, according to the law of classical physics and experience, any measurement can be performed at arbitrary precision without incurring in perturbation of the measured system. In fact, experimenters can always refine and improve the measuring apparatus at their disposal at will, without any fundamental constraints. In contrast, quantum theory prohibits that. Peculiarly, it establishes that any measurement results in a dynamical disturbance of the measured system. As a consequence, this always limits the amount of knowledge about the system that one can extract, giving rise to a trade-off between information and disturbance, characteristic of quantum phenomena. To illustrate this fact, Heisenberg conceived a thought experiment already at the end of the 20's, now known as the *Heisenberg microscope* [Hei50]. The experiment aims to measure the position of a quantum particle, let's say an electron, along the x direction. To do that, one can use a microscope to focus a beam of electromagnetic rays, of wavelength $\lambda$, on the electron. The microscope does that with a given angular aperture, $\epsilon$, which results in an optical resolving power of $\Delta x = \lambda / \sin(\epsilon)$. Ideally, this is also the minimum precision with which we know the electron posi-

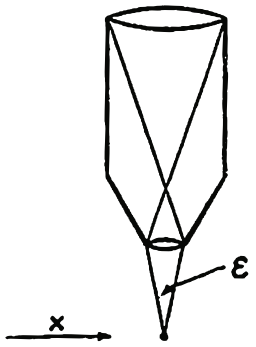


FIG. 5

The Heisenberg microscope. Reproduced from [Hei50].

tion. This precision can be made arbitrary small by choosing smaller and smaller wavelength. However, one should realize that, in order for the measurement to happen, at least a single impinging photon should be scattered from the electron back through the microscope and finally to the photographic plate. This scattering process results in a Compton recoil of the electron, to which the photon imparts a momentum. The recoil direction is, however, not exactly known, as the scattered photon can be anywhere within the cone formed by the rays. As such, along the $x$ direction the electron must have an unknown momentum of $\Delta p_x \approx \hbar \sin(\epsilon)/\lambda$, which increases as we decrease the wavelength. It is this momentum uncertainty that forms the quantum disturbance, as a consequence of the acquired knowledge about the position. It follows that $\Delta x \Delta p_x \approx \hbar$, which is the first example of Heisenberg measurement-disturbance relation, a quantum measurement feature.

This simple thought experiment is at the base of the theory of quantum measurements, which was rigorously formalized in the 30's mainly by Dirac and von Neumann [NW18]. To verify the predicted disturbance one needs to repeat non-destructive measurements on the same quantum system. Experiments at that time, however, were not so technologically advanced, as they allowed only to perform a destructive measurement on a single system or an ensemble of them. As a consequence, their results were well explained by Born's rule and the theory of quantum measurements ceased to be of interest for many physicists, who relegated it mainly to epistemological discussions. It was only after forty years, in the 80s, that the recent technological developments, with the invention of the maser and laser, enabled the experimental observation of the predicted quantum measurement disturbance. This led, in 1986, to the first observation of quantum jumps in a single ion, the energy of which was continuously measured [Ber+86; NSD86]. Since then, quantum measurement experiments have been performed on disparate systems of increasing size, permitting to enlarge the validity domain of quantum mechanics to a more and more macroscopic world. At the same time, quantum measurements have received increasing attention in the context of emerging quantum technologies, as they allow to gain a full control on the quantum state of a system.

Concurrently with the technological developments in the second half of the twentieth century, a new experimental branch of physics emerged. It was devoted to study and understand the implications of the mechanical effects of the radiation pressure force, as exerted by electromagnetic fields. Experimental observations of such a force existed since the beginning of the century, but it was only in the 70s that researchers started to recognize the prominent role of this force in many experiments. In that regard, the pioneering works of Ashkin on optical trapping of dielectric particles via radiation pressure

forces paved the way for electromagnetic manipulation and control of mechanical systems [Ash70; Ash78].

During the same years, Bragisnky and collaborators predicted and experimentally verified the dynamical effects of the radiation pressure force on a mechanical pendulum, used as a movable boundary in a microwave cavity [BM67; BMT70]. These effects amount to an additional rigidity and damping, due to the retarded nature of the radiation pressure force in cavities. The researchers also figured out that such a composite system can be used to perform sensitive displacement measurements of the center-of-mass of a mechanical system, a promising platform for testing quantum measurements of macroscopic systems. In this regard, Bragisnky also recognized the importance of the quantum nature of the electromagnetic field in such a measurement [Bra68]. In fact, he pointed out that the quantum fluctuations of the radiation pressure force lead to a disturbance on the mechanical system as a more and more precise measurement is performed, according to the Heisenberg measurement-disturbance relation. Since then, a large amount of theoretical and experimental work has been produced on optomechanical systems [AKM14]. Several different platforms have been devised and used to achieve important milestones in generating quantum resources, as the preparation of optical [Saf+13; Pur+13] and mechanical [Wol+15] squeezed states, ground state cooling [O'C+10; Cha+11; Teu+11] and stabilization of higher order Fock states [Chu+18], bipartite entangled states between electromagnetic [Bar+19; Che+20], mechanical [Lee+11; Rie+18; Ock+18] and hybrid modes [Pal+13]. The interest in optomechanics, and particularly in mechanical resonators, has rapidly grown over the past years, due to their promising outlooks. On one side, they are well-suited for high-sensitivity detection of a multitude of quantities, such as displacement, force, acceleration, mass and magnetic fields. On the other, the optomechanical interaction is capable of an unprecedented level of control of the mechanical quantum state, a necessary tool for further uses in quantum information processing applications. This is also appealing for addressing fundamental questions, as pushing the quantum-to-classical border to larger and larger systems and generating a gravity field by a massive quantum system.

One promising way to achieve such a quantum control is by exploiting the outcomes of a quantum measurement to shape and exert a force on the mechanical system itself. Performing this quantum measurement requires the mechanical system to behave, essentially, like an Heisenberg microscope. That is, all the information in the measurement should be recorded and the quantum backaction disturbance should overcome any other technical source of noise. Measurement-based quantum control has been recently achieved for electromagnetic degrees of freedom, both in a microwave cavity [Say+11] and in a superconducting qubit [Vij+12]. As of today, however, it has remained

elusive for mechanical degrees of freedom. In this context, an elementary form of quantum control is the stabilization of the ground state by feedback cooling [MVT98]. The last two decades have seen an increasing effort to achieve this milestone, with experiments involving disparate systems as trapped atoms [Kub+09] and ions [Bus+06], levitated particles [LKR11; Teb+20], cantilevers [KB06; Pog+07], nanomechanical resonators [Lee+10; GVK12; Wil+15], vibrational modes of a mirror [CHP99] and test masses of a gravitational-wave detector [Vin+08; Abb+09]. All these experiments were lacking of a clean quantum measurement, mainly due to detection inefficiencies, which led to additional imprecision in the recorded outcomes, and/or excess thermal noise, overcoming the quantum backaction. In contrast, we design an optomechanical experiment in which both issues are solved. This enables a deep operation in the quantum measurement regime. Based on that, we are able to exert quantum control on a membrane mechanical resonator and to stabilize its ground state via feedback cooling. It is precisely these experiments which form the central subject of this thesis.

### STRUCTURE OF THE THESIS

The present work is just the tip of a long succession of efforts and results, as pointed out by the historical background. As Bernard De Chartres said, "we are like dwarfs on the shoulders of giants", especially in the scientific community where forward steps always come from the legacy of the past. This thesis comprises two parts. The first one is a collection of already known materials from the abovementioned giants, which form the building blocks of our works. The second part, instead, contains novel experimental results, many of which have been already published, and specific theoretical discussions, if not presented in the first part. In details:

In Chapter 1 we provide a short summary of some useful results from quantum optics. In particular, we provide a theoretical description of open quantum systems, such as optical cavities, and of measuring devices, such as photodiodes. These two descriptions are merged in a stochastic dynamical theory. Also, we provide a general framework for quantum measurements and control on the class of linear-quadratic-Gaussian systems. In Chapter 2 we discuss the mechanical system, which is an elastic vibrating membrane, and provide some insights in its dissipation properties. Finally, we derive an effective quantum description for the motion of the membrane center-of-mass. In Chapter 3 we introduce the optomechanical coupling and the specifics of the system we employ. Then, we detail some basic consequences of the interaction, focusing on displacement measurements. In Chapter 4 we introduce the experimental setup and tools used throughout the

thesis, such as the lasers, the optomechanical cavity and the detectors. Also, it provides a detailed account of the calibration methods used.

The second part starts with Chapter 5, which reports the experimental achievement of a displacement quantum measurement. The implications of that are further studied in the second half of the chapter, which is devoted to describe how the recorded outcomes allow, via the quantum trajectory, to obtain a pure coherent mechanical state-of-knowledge. In Chapter 6 we experimentally exert quantum control on the resonator to transform this coherent state-of-knowledge into an unconditional state. In particular, we show the first experimental realization of feedback cooling to the ground state. In Chapter 7 we study some of the thermodynamic implications of a continuous measurement. In particular, we show how the act of measuring drastically changes the entropic balance by introducing a new entropy production term. Then, in Chapter 8, we move to report some preliminary results of experiments designed to explore different routes in quantum measurements. In the first part we describe how to perform a backaction-evading measurement by means of a stroboscopic probing. In the second part, instead, we focus on the entanglement generation between the optical field and the mechanical system, predicted by the quantum measurement theory. Finally, in Chapter 9, we report a couple of experiments which show useful applications of quantum measurements. In the first half, we show how the quantum correlations present in the measurement enable ultra-sensitive measurements below the standard quantum limit. In the second half, instead, we experimentally verify that two probe systems, measuring simultaneously the same mechanical motion, become entangled.

I acknowledge Nenad Kralj and Junxin Chen for helpful comments on this thesis. Also, I am grateful to David Mason for graphical inspiration, in particular for the wonderful palette he put together.

# Part I

# THEORETICAL AND EXPERIMENTAL METHODS

# 1

# QUANTUM OPTICS: A PRIMER

In this chapter we review some basic concepts of optical physics, which are of crucial importance for the experiments later described. We start with an introduction on optical cavities, then we move on a quantum description of the electromagnetic field and provide some basic results of quantum optics. In particular, we discuss how to treat open quantum systems, how to perform and correctly describe the photodetection, and finally how to embody this measurement in a dynamical description. At the end of the chapter, we apply these concepts to the important class of linear-quadratic-Gaussian systems.

## 1.1 OPTICAL CAVITIES

Any electric field, $E$, at location $x = (\mathbf{r}, t)$, can be decomposed into a positive and negative frequency components, i. e. $E(x) = E^{(+)}(x) + E^{(-)}(x)$ [WM08]. The term $E^{(+)}(x)$ contains all the components which oscillate at positive frequencies, $\Omega > 0$, according to $e^{-\imath\Omega t}$. Conversely, the other term, $E^{(-)}(x)$, contains components oscillating with negative frequencies, such that $E^{(-)} = \left(E^{(+)}\right)^*$. A general solution of Maxwell's equations for the electric field involves a superposition of orthonormal modes. In a finite volume, this superposition takes the form of a sum as

$$E(x) = \imath \sum_k \sqrt{\frac{\hbar\Omega_k}{2\epsilon_0}} \left(a_k(t)u_k(\mathbf{r})e^{-\imath\Omega_k t} + a_k^*(t)u_k(\mathbf{r})^* e^{\imath\Omega_k t}\right), \quad (1.1)$$

where $\hbar$ is the reduced Planck's constant, $\epsilon_0$ the vacuum permittivity, $\Omega_k$ the frequency of the mode labelled by the index $k$, $u_k$ are orthonormal mode functions determined by the appropriate boundary conditions and $a_k$ is known as *field mode amplitude*.

*Electric field in an optical cavity*

An important case is the electric field in the space delimited by two reflective mirrors in front of each other [Fow89]. Such an optical system, of central importance, is known as an *optical cavity* (Figure 1.1a). The presence of the mirrors impose as boundary conditions that the electric field should vanish at their location. For the simple case of a one dimensional system in vacuum, the resulting electric field, from Equation 1.1, is stationary with eigenmodes

$$E_n(z) = \sin(k_n z)\left(a_n e^{-\imath\Omega_n t} + a_n^* e^{\imath\Omega_n t}\right), \quad (1.2)$$

where $z$ is the direction along the optical axis, the wave vector satisfies $k_n = n\pi/L$, with $n$ a positive integer, and the frequency is $\Omega_n = ck_n$ from the dispersion relation. The frequency separation between

two adjacent modes is called the *free spectral range (FSR)*, i. e. $\Omega_{FSR} = \Omega_{n+1} - \Omega_n = 2\pi c/(2L)$, where L is the cavity length (Figure 1.1b). The FSR corresponds to the inverse cavity round-trip time for the bouncing electric field. A realistic description should take into consideration the tridimensional nature of the optical cavity. For mirrors with large area such that diffraction at the edges can be safely neglected, the electric field acquires a transverse structure, which is well described by Gaussian optics [Yar89]. Such transverse modes are represented by Hermite-Gauss polynomials.

So far we have assumed that the mirrors are perfectly reflecting. In real situations however, part of the impinging field is not reflected by the mirror, due to the presence of scattering and absorption processes and a non-zero transmissivity. Modern fabrication technologies, based on super-polished substrates and atomic layer deposition, enable the production of high quality mirrors, with losses and a transmissivity as low as a few ppm. Despite the extremely small value, the finite transmissivity plays an important role in the dynamics of cavity field, which will escape out of the cavity or, conversely, be populated from an external field. In particular, both the losses and the transmissivity determine the energy decay rate of the cavity field, $\kappa$. The inverse, $1/\kappa = \tau_{cav}$, represents the average time that the cavity field takes to escape. The average number of round-trips completed by the cavity field before decaying is called *finesse*, and corresponds to $\mathcal{F} = \tau_{cav}/(1/\Omega_{FSR}) = \pi c/(\kappa L)$.

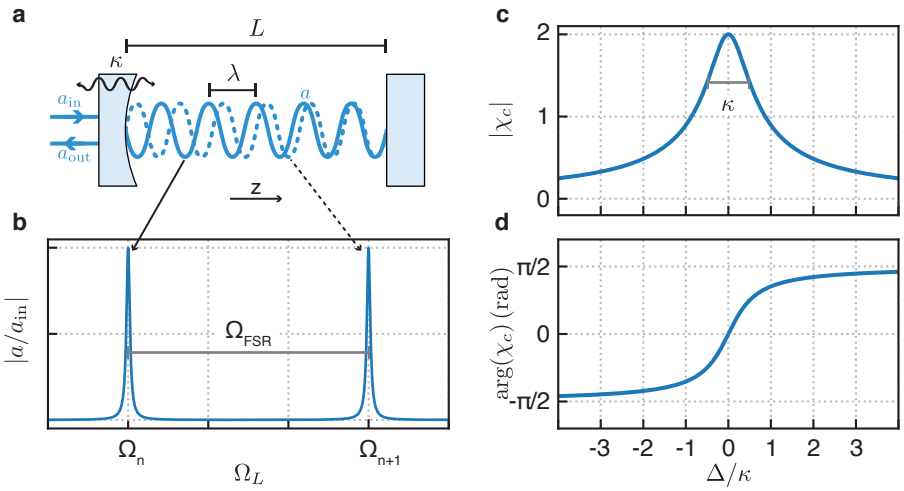


Figure 1.1: Optical cavity. a, Schematic of a linear optical cavity, with a partially transmissive mirror. Subsequent longitudinal optical modes differ by the numbers of antinodes. b, Wide cavity response. Subsequent longitudinal modes are spectrally separated by a FSR. c, Magnitude and d, phase of the cavity susceptibility, as a function of the driving laser detuning, around the resonance of a longitudinal mode. The full-width half-maximum (FWHM) of the magnitude is the decay rate of the intracavity electromagnetic energy.

For large finesse, the spectral width of the cavity modes becomes much narrower than their separation, that is, the FSR (Figure 1.1b). Then, one can, assume the modes $a_n$ to be independent from each other. In the following we always consider a single mode and omit the subscript. The equation of motion for the mode amplitude, $a$, assuming one perfectly reflective mirror, is

*Equation of motion for a cavity mode*

$$\dot{a}(t) = \left(-\frac{\kappa}{2} - \imath\Omega_c\right) a(t) + \sqrt{\kappa} a_{in}(t), \tag{1.3}$$

where $\Omega_c$ is the resonance frequency of the chosen mode and $a_{in}(t)$ is the external field coupled into to the cavity mode, $a$, through the partial transmissive mirror. The field $a_{in}(t)$ is usually referred to as the *input field*, and can have both a coherent part, e. g. any electric field derived from a laser that we use to drive the cavity, and a stochastic part, e. g. the excess noise in the intensity and frequency from the laser source. In many situations, the coherent part of the input field contains a monochromatic field at frequency $\Omega_L$, which is in the range of hundreds of THz. Therefore, it is common practice to describe the physics in a reference frame rotating at $\Omega_L$, compared to Equation 1.3. This transformation is performed by the substitutions $a(t) \to a(t)e^{-\imath\Omega_L t}$ and $a_{in}(t) \to a_{in}(t)e^{-\imath\Omega_L t}$, where $a(t)$ and $a_{in}(t)$ become slowly varying amplitudes. The new equation of motion becomes

$$\dot{a}(t) = \left(-\frac{\kappa}{2} + \imath\Delta\right) a(t) + \sqrt{\kappa} a_{in}(t), \tag{1.4}$$

where $\Delta = \Omega_L - \Omega_c$ is the laser-cavity detuning.

By taking the Fourier transform of Equation 1.4, one obtains the solution $a(\Omega) = \chi_c(\Omega) a_{in}(\Omega)$, which describes the response of the cavity field to an external perturbation. The response function, known as *cavity susceptibility*, is

$$\chi_c(\Omega) \coloneqq \frac{\sqrt{\kappa}}{\kappa/2 - \imath(\Delta + \Omega)}. \tag{1.5}$$

Its magnitude and phase are shown in Figure 1.1c and d, respectively. The energy decay rate, $\kappa$, can be interpreted also as the FWHM of the susceptibility.

An optical cavity can offer multiple decay channels to its field. Some examples are a cavity with both mirrors partially transmissive, or a cavity with an absorber in the middle. One can describe each decay channel by assigning to it the proper decay rate, $\kappa_l$. Thus, the total decay rate is $\kappa = \sum_l \kappa_l$. Any decay channel is also a port for external fields to enter the cavity. In this more general case, Equation 1.4 should take it into account by introducing additional input terms, $\sqrt{\kappa_l} a_{in,l}(t)$. The amount of field decaying through a given port is represented by the cavity overcoupling, $\eta_{c,j} \coloneqq \kappa_l/\kappa$.

Experimentally, one has no access to the cavity field and any measurement is performed on the *output field*, $a_{out}$. From the input-output theory, one can calculate the output field from the $l$-th port as

$$a_{out,l} + a_{in,l} = \sqrt{\kappa_l}\, a. \tag{1.6}$$

## 1.2 QUANTIZATION OF THE ELECTROMAGNETIC FIELD

A quantum mechanical description of the electromagnetic field requires to replace the c-number field amplitudes with non-Hermitian quantum operators, i. e. $a_k \to \hat{a}_k$ and $a_k^* \to \hat{a}_k^\dagger$. The amplitude operators, $\hat{a}_k$, also satisfies the commutation relations [WM08]

$$[\hat{a}_j, \hat{a}_k^\dagger] = \delta_{jk}, \tag{1.7}$$

where $\delta_{jk}$ is the Kronecker delta. They describe a bosonic field, the energy excitations of which are called *photons*.

The unitary dynamics is fully governed by the Hamiltonian operator. We derive it from the classical electromagnetic field energy

$$E_{em} = \frac{1}{2}\int \left(\epsilon_0 E^2 + \mu_o B^2\right) dV, \tag{1.8}$$

where $\mu_o$ is the vacuum permeability and $B$ the magnetic field, which can be calculated from the Maxwell's equations. Using Equation 1.1 with the quantum operators $\hat{a}_k$ we find the Hamiltonian operator

$$\hat{H} = \sum_K \hbar\Omega_k \left(\hat{a}_k^\dagger \hat{a}_k + \frac{1}{2}\right), \tag{1.9}$$

which describes each mode of the electric field as an independent harmonic oscillator. The last term in Equation 1.9 is associated with the energy due to fluctuations of the electric field even when no photons are present, a configuration called the *vacuum state*.

*Field amplitudes as ladder operator*

The operators $\hat{a}_k$ are of central importance in quantum optics. When applied to a field state, they describe the operation of removing, or annihilating, one photon in the mode $k$ from that field. Conversely, the adjoint operator $\hat{a}_k^\dagger$ describes the creation of a photon in the mode $k$. As such, the operators $\hat{a}_k, \hat{a}_k^\dagger$ are known as *annihilation* and *creation operators*, or equivalently *ladder operators*. The non-Hermitian property of these operators reflects their dissipative action. In fact, the Hermitian operator $\hat{n}_k = \hat{a}_k^\dagger \hat{a}_k$, which appears in Equation 1.9, represents the number of photons in the mode $k$ and is called the *number operator*. Then, the field energy Equation 1.9 can be interpreted as the total number of photons in all modes. The ladder operators, acting of the field, change this total photon number, thus the field energy, leading to a dissipative process.

Another important dissipative process is represented by the energy decay from an optical cavity. In order to properly describe the full non-unitary dynamics of dissipative systems, the Hamiltonian operator is

not enough and one needs to resort to the theory of open quantum systems.

## 1.3 OPEN QUANTUM SYSTEMS

We start by considering a large closed quantum system, which is sometimes referred to as *universe*. Being closed, its dynamics is fully determined by the Hamiltonian operator. The universe is further divided in two subsets: a *system*, which contains the degrees of freedom of our interest, and an *environment*, usually formed by a large number of degrees of freedom interacting with the system [Car93; WM08].

In quantum optics, the system usually comprises a single, or few, mode of an optical cavity. Instead, the environment is represented by the external electromagnetic field which is coupled to the system modes via partially transmissive mirrors. This suggests that the environment can be described as a set of independent quantum oscillators, with annihilation operators $\hat{b}_k$. The simplest interaction form is a bi-linear one between the environment operators, $\hat{b}_k$, and an arbitrary system operator, $\hat{o}$. For instance, the interaction term between an optical cavity mode, $\hat{a}$, and the external field is $\hat{b}_k^\dagger \hat{a} + \hat{a}^\dagger \hat{b}_k$, which describes the process by which a photon from the environment is annihilated to create a photon in the cavity mode, and vice versa.

Dissipation is introduced when the environment is traced out from the dynamics. This partial trace reflects the fact that the number of degrees of freedom in the environment is so large that it is impossible, for an observer, to completely describe them. Then, energy exchanges from the system to the environment effectively appear as dissipative processes. Assuming that the environment is in thermal equilibrium at temperature $T$ and memoryless, i. e. the system-environment interaction is instantaneous, the system state, described by a density operator $\hat{\rho}$, evolves according to a Lindblad master equation

*Master equation*

$$\dot{\hat{\rho}} = \frac{1}{\imath\hbar}\left[\hat{H}, \hat{\rho}\right] + \kappa\left(\overline{n}(\Omega_c) + 1\right)\mathcal{D}[\hat{o}]\rho + \kappa\overline{n}(\Omega_c)\mathcal{D}[\hat{o}^\dagger]\hat{\rho}, \tag{1.10}$$

where $\hat{H}$ is the system's Hamiltonian, $\kappa$ the coupling rate to the environment, $\mathcal{D}[\hat{o}]\rho = 2\hat{o}^\dagger\hat{\rho}\hat{o} - \hat{o}^\dagger\hat{o}\hat{\rho} - \rho\hat{o}^\dagger\hat{o}$ the dissipation superoperator and $\overline{n}(\Omega_c) = \left(e^{\hbar\Omega_c/(k_B T)} - 1\right)^{-1}$ is the average number of quanta in the environment at the frequency $\Omega_c$. For an optical cavity coupled to the external field, $\kappa$ is the energy decay rate through a transmissive mirror and the system operator coupled to the environment is the mode amplitude, i. e. $\hat{o} \equiv \hat{a}$. At optical frequencies, $\Omega_c \sim \mathcal{O}(100\ \text{THz})$, and at room temperature, $T \sim 300$ K, the average thermal occupation of the external field is $\overline{n}(\Omega_c) \approx 0$: the environment is in the vacuum state.

In general, the environment state can be engineered to be different from a thermal one. A common situation is when one of its mode is in

a coherent state, as realized by a laser source. In this case, Equation 1.10 can still be used to describe the coherent driving of the system.

*Quantum Langevin equations*

An alternative, but equivalent, formulation in the Heisenberg picture is provided by the quantum Langevin equations (QLE) [GZ04], which are equations of motion for the system operators, rather than the state. For a cavity mode amplitude, $\hat{a}$, in a frame rotating at the laser frequency, $\Omega_L$, one has

$$\dot{\hat{a}}(t) = \left(-\frac{\kappa}{2} + \imath\Delta\right)\hat{a}(t) + \sqrt{\kappa}\hat{a}_{in}, \tag{1.11}$$

which resembles the classical evolution of Equation 1.3. The input field, $\hat{a}_{in}(t)$, is a superposition of modes from the environment, which are coupled to the cavity at time *earlier* then $t$. This field obeys the commutation relation

$$[\hat{a}_{in}(t), \hat{a}^\dagger_{in}(t')] = \delta(t - t'), \tag{1.12}$$

where $\delta(t - t')$ is the Dirac delta. A main difference from the classical case is that the input field always carries fluctuations, or noise, in the form of vacuum fluctuations.

For time *later* than $t$, the modes in the environment carry information about the cavity amplitude, $\hat{a}$. These modes form an *output field* operator, $\hat{a}_{out}$, which satisfies the same commutation relation of Equation 1.12 and relates to the input and cavity fields via the *input-output relation*

$$\hat{a}_{out}(t) + \hat{a}_{in}(t) = \sqrt{\kappa}\hat{a}(t), \tag{1.13}$$

analogous to the classical Equation 1.6. The output field is of crucial importance because it is the only one which carries information about the cavity field and is accessible to the observers. In many cases in fact, it is interesting to know the two-time correlation function of the cavity field. For the input field in the vacuum state, the only non-zero correlation is

*Correlations of input and output fields*

$$\left\langle \hat{a}_{in}(t), \hat{a}^\dagger_{in}(t') \right\rangle = \delta(t - t'), \tag{1.14}$$

where we have introduced the correlator operation $\langle \cdot, \cdot \rangle = \langle \cdot\cdot \rangle - \langle \cdot \rangle \langle \cdot \rangle$. Using Equation 1.14, one can show that the output field satisfies

$$\left\langle \hat{a}_{out}(t), \hat{a}^\dagger_{out}(t') \right\rangle = \kappa \left\langle \hat{a}(t), \hat{a}^\dagger(t') \right\rangle, \tag{1.15a}$$

$$\left\langle \hat{a}_{out}(t), \hat{a}_{out}(t') \right\rangle = \kappa \mathcal{T} \left\langle \hat{a}(t), \hat{a}(t') \right\rangle, \tag{1.15b}$$

where $\mathcal{T}\cdot$ is the time-ordering operator [WM08]. In this sense, the measurable correlations of the output field directly reflect the ones of the cavity mode. In order to understand how the correlations in Equation 1.15 are measured, we should understand how the photodetection is done.

## 1.4 PHOTODETECTION

Optical fields are oscillating very fast, with frequencies in the range of hundreds of THz. As of today, there exists no technology which is capable of detecting the instantaneous value of this high-frequency electromagnetic field. Instead, optical detectors are based on energy measurements and on the photoelectric effect [RB04]. The first quantum theory of optical detection, or *photodetection*, was pioneered by Glauber [Gla63]. He recognized that a detector based on the photoelectric effect works by absorbing photons in the impinging field, $\hat{E}(x)$. Based on this, he derived the probability of absorbing a photon or, equivalently, of a detector click at $x$ to be

$$p_1(x) = \langle \hat{E}^{(-)}(x)\hat{E}^{(+)}(x)\rangle, \tag{1.16}$$

where the average $\langle \dots \rangle$ is performed over the quantum state of the field, $\hat{\rho}$, and the positive and negative field components are defined from Equation 1.1. In general, when $n$ detectors are present, the probability of clicks at $x_1, x_2, \dots, x_n$ is

$$p_n(x_1, \dots, x_n) = \langle \hat{E}^{(-)}(x_1) \dots \hat{E}^{(-)}(x_n)\hat{E}^{(+)}(x_n) \dots \hat{E}^{(+)}(x_1))\rangle. \tag{1.17}$$

Crucially, the order of appearance of the field operators in Equation 1.17 matters. Firstly, they should be *normally ordered*, i. e. all annihilation (creation) operators on the left (right). Secondly, they should also be *time ordered*, i. e. the time argument increases from right (left) to left (right) for the annihilation (creation) operators. These orderings originate from the choice of the optical detector used, based on photon absorption. In fact, normal ordering implies that photons are absorbed instead of emitted. Instead, time ordering assures that the absorption of photons is done subsequently, that is, in a causal way. The implication of these orderings is that the modes of the field in vacuum states do not contribute to the average value in Equation 1.17. Physically, this results from the fact that a detector cannot absorb a photon from the vacuum. This is a direct consequence of the detection mechanism employed: had we chosen a detector based on photon emission, this would have been different.

*Normal-time ordering in photodetection*

Absorbed photons become correlated with electrons emitted in the detector, thus called *photoelectrons*. To be recorded by an observer, photoelectrons are usually amplified. This involves the interaction with a large number of additional degrees of freedom, which destroys the quantum coherence property of these electrons. This forms a boundary, or cut, between the quantum and classical description of the system [Zur03a; WM10]. Then, photoelectrons form a classical, stochastic counting process, $dN(t)$. For large counts as in the situations we deal with, it is more useful to describe the photodetection via the rate of the counting process, referred to as the *photocurrent* $i(t) = dN(t)/dt$. This photocurrent is what we experimentally measure and it is a

classical stochastic process. However, its statistical properties can be connected to the quantum state of the optical field generating it, via the photoelectron-counting formula [KK64]

$$P(n;t,t+\Delta t)=\left\langle :\frac{\left(\eta_d\int_t^{t+\Delta t}\hat{\imath}(s)ds\right)^n}{n!}\exp\left(-\eta_d\int_t^{t+\Delta t}\hat{\imath}(s)ds\right):\right\rangle, \tag{1.18}$$

where :: indicates normal-time ordering of the embraced expression, $\eta_d$ the total detection efficiency and

$$\hat{\imath}(t)=\frac{2\epsilon_0}{\hbar\Omega}\int d\mathbf{r}\,\hat{E}^{(-)}(x)\hat{E}^{(+)}(x) \tag{1.19}$$

is the *photocurrent operator*. This is a formal object, useful for calculations, which should not be confused with the classical measured photocurrent, $i(t)$.

*Operation representation theorem*

Nevertheless, the operator representation theorem of Yuen and Shapiro [YS80] proved that the characteristic function of this formal operator, $\hat{\imath}$, equals the characteristic function of the measured photocurrent, provided that the field considered in Equation 1.19 is $\hat{E}^{(+)}(x)=\sqrt{\eta_d}\hat{a}(x)+\sqrt{1-\eta_d}\hat{a}_\nu(x)$, where $\hat{a}$ is the amplitude of the impinging field and $\hat{a}_\nu$ the amplitude of an additional fictitious field in the vacuum state, uncorrelated with $\hat{a}$. That is, the inefficiency is modelled as if there was a beam-splitter with transmissivity $\sqrt{\eta_d}$ in front of the detector, with a fictitious vacuum field, $\hat{a}_\nu$, entering through the unused port. With this prescription, all the statistical moments of the measured photocurrent can be calculated from the moments of the quantum observable $\hat{\imath}$, which is sometimes recognized as the observable measured by a photodetector.

However in this view, the normal-time order originally present in Glauber's theory is lost. As a consequence, vacuum fields as the ones stemming from inefficiencies give a non-zero contribution and should be taken into account in the calculations. To give correct predictions, one should carefully reintroduce the normal-time order at a later stage of the calculations. In particular, we will be interested in calculating the power spectral density (PSD) of the measured photocurrent, $S_{ii}$. This spectrum can be obtained from the PSD of the operator $\hat{\imath}$ with the additional prescription of *symmetrization*, i. e.

*Symmetrization of power spectral density*

$$\overline{S}_{\hat{a}\hat{b}}(\Omega)=\frac{S_{\hat{a}\hat{b}}(\Omega)+S_{\hat{b}\hat{a}}(-\Omega)}{2}. \tag{1.20}$$

Then, we have $S_{ii}=\overline{S}_{\hat{\imath}\hat{\imath}}$ which we often indicates as $\overline{S}_{ii}$ for the sake of conciseness. The symmetrization restores the symmetry between positive and negative frequencies, as required for a classical real signal.

We also mention that an alternative theory of photodetection with normal-time order is possible, as shown by Carmichael [Car87]. The

predictions obtained from these two theories are equivalent, however they provide two rather different perspective on the measurement interpretations.

We describe now two important photodetection schemes: direct and homodyne detections.

### 1.4.1 *Direct detection*

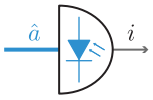

*Sketch of direct detection*

The simplest scheme one can imagine consists of a field impinging on a photodetector. We assume the field to be single-mode, i. e. it has all modes in the vacuum state but one. The field annihilation operator can be decomposed in a sum of a mean field, $\overline{a} = \langle \hat{a}(t) \rangle$ chosen to be real, and a displaced operator, $\delta\hat{a}(t)$, i. e. $\hat{a}(t) = \overline{a} + \delta\hat{a}(t)$. The operator $\delta\hat{a}(t)$ represents small fluctuations around the mean amplitude. The first two statistical moments of the photocurrent can then be linearized around $\overline{a}$ as

$$\left\langle \hat{i}(t) \right\rangle \approx \overline{a}^2 + \overline{a} \left\langle \delta\hat{a}(t) + \delta\hat{a}^\dagger(t) \right\rangle = \overline{a}^2 + \sqrt{2}\overline{a} \left\langle \hat{X}(t) \right\rangle, \tag{1.21a}$$

$$\left\langle \hat{i}(t)^2 \right\rangle - \left\langle \hat{i}(t) \right\rangle^2 \approx 2\overline{a}^2 \left( \left\langle \hat{X}(t)^2 \right\rangle - \left\langle \hat{X}(t) \right\rangle^2 \right), \tag{1.21b}$$

where we have introduce the amplitude quadrature operator, $\hat{X}$. In fact, the amplitude operator, $\hat{a}$, can be decomposed into a sum of Hermitian operators as $\hat{a} = \left(\hat{X} + \imath\hat{Y}\right)/\sqrt{2}$, where $\hat{X}$ ($\hat{Y}$) is the *amplitude* (*phase*) *quadrature operators*, satisfying the canonical commutation relation (CCR)

$$\left[\hat{X}, \hat{Y}\right] = \imath. \tag{1.22}$$

The photocurrent PSD is

$$S_{ii}(\Omega) = \overline{S}_{\hat{i}\hat{i}}(\Omega) \approx \overline{a}^4 \delta(\Omega) + 2\overline{a}^2 \overline{S}_{\hat{X}\hat{X}}(\Omega). \tag{1.23}$$

Equation 1.23 suggests that the fluctuations in the direct detection photocurrent stem from the fluctuations of the amplitude quadrature of the detected field.

### 1.4.2 *Homodyne detection*

Direct detection only provides a measurement of the amplitude quadrature of the field. A more general phase-sensitive detection scheme is offered by the *homodyne detection*, which can measure an arbitrary quadrature component [YS80]. This detection scheme comprises two fields: a signal, $\hat{a}_s$, and a local oscillator (LO), $\hat{a}_l$, which provides a phase reference. They are overlapped onto a 50:50 beam-splitter, the output fields of which, $\hat{a}_\pm$, are a linear combination of the input fields and can be written as

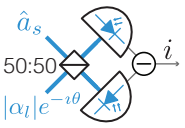

*Sketch of a homodyne detector*

$$\hat{a}_\pm(t) = \frac{\hat{a}_s(t) \pm \hat{a}_l(t)}{\sqrt{2}}. \tag{1.24}$$

Two photodetectors directly detect these fields. The corresponding photocurrent operators are

$$\hat{i}_{\pm}(t) = \frac{\hat{a}_s^\dagger(t)\hat{a}_s(t) + \hat{a}_l^\dagger(t)\hat{a}_l(t) \pm \hat{a}_s^\dagger(t)\hat{a}_l(t) \pm \hat{a}_l^\dagger(t)\hat{a}_s(t)}{2}. \quad (1.25)$$

We decompose the signal field into a mean and a fluctuating part, i. e. $\hat{a}_s(t) = \overline{a}_s + \delta\hat{a}_s(t)$ and we assume that $\overline{a}_s$ is real. The LO field is in a strong coherent state such that its mean amplitude, $\langle \hat{a}_l(t) \rangle_l = |\overline{a}_l| e^{-\imath\theta_l}$, is larger than the signal mean amplitude, i. e. $|\overline{a}_l| \gg 1, |\overline{a}_l| \gg \overline{a}_s$. Within these assumptions, one can consider the LO as a classical coherent field and Equation 1.25 simplifies

$$\hat{i}_{\pm}(t) \approx \frac{|\overline{a}_l|^2}{2} \pm \frac{|\overline{a}_l|}{\sqrt{2}} \hat{X}_s^{\theta_l}(t), \quad (1.26)$$

where we have introduced the generalized quadrature component

$$\hat{X}^\theta := \frac{e^{-\imath\theta}\hat{a} + e^{\imath\theta}\hat{a}^\dagger}{\sqrt{2}}, \quad (1.27)$$

where $\theta$ is the quadrature angle and $\hat{X} := \hat{X}^0$ ($\hat{Y} := \hat{X}^{\pi/2}$) the amplitude (phase) quadrature.

In the balanced configuration, the two photocurrents are subtracted from each other and the resulting measured photocurrent is

$$\hat{i}(t) = \hat{i}_+(t) - \hat{i}_-(t) = \sqrt{2}|\overline{a}_l| \hat{X}_s^{\theta_l}(t), \quad (1.28)$$

proportional to the generalized quadrature component individuated by the phase $\theta_l$ of the LO. In general, balancing is not needed for measuring an arbitrary quadrature, as done already in Equation 1.26. In practice however, it is advantageous since it removes the large DC term in the photocurrents of Equation 1.26, as well as any common excess noise present in the LO amplitude quadrature.

*Homodyne detection with losses and inefficiencies*

A more realistic description should include (i) inefficiencies, $\eta_l$, due to optical losses experienced by the signal field, (ii) finite quantum efficiency, $\eta_{qe}$, of the photodiodes, that is, the probability that an impinging photon emits a photoelectron, and (iii) any mode mismatch between the LO and the signal fields. The former two can be modelled by introducing fictitious beam-splitters with transmission $\sqrt{\eta_l}$ and $\sqrt{\eta_{qe}}$ in the signal path and in front of the photodetectors. The unused ports mix some uncorrelated vacuum fields with the signal field [YS80]. The mode mismatch is modelled by assuming that the LO state is a separable, two-mode coherent state, i. e. $|\nu\overline{a}_l\rangle_s |\sqrt{1-\nu^2}\overline{a}_l\rangle_\perp$, such that the total power sums up to $|\overline{a}_l|^2$. The first mode, denoted by $s$, corresponds to the signal mode and thus interferes with it, whereas the other mode, denoted by $\perp$, is orthogonal. The parameter $\nu$ is usually called the *interference visibility* or, simply, *visibility*. Combining all these requirement together, one can obtain a final expression for

the photocurrent, $\hat{\imath}(t)$, which is quite cumbersome. We are interested in its statistical moments, and in particular in its PSD which is

$$\overline{S}_{ii}(\Omega) = \eta_{qe}|\overline{a}_l|^2 \left(1 - \eta_d + 2\eta_d \overline{S}_{X^{\hat{\theta}_l} X^{\hat{\theta}_l}}(\Omega)\right), \tag{1.29}$$

where we have defined the total detection efficiency as $\eta_d \coloneqq \eta_l \eta_{qe} v^2$.

As an example, let's consider the case in which the signal field is in the vacuum state. Experimentally, this can be achieved by blocking all the fields to the balanced homodyne detector (BHD) but the LO. By substituting $\overline{S}_{X^{\hat{\theta}_l} X^{\hat{\theta}_l}}(\Omega) = 1/2$ in Equation 1.29 we get the flat spectrum

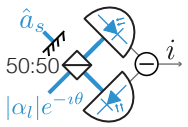

*Measuring the shot noise PSD*

$$S^{sn}_{ii}(\Omega) = \eta_{qe}|\overline{a}_l|^2, \tag{1.30}$$

due to the white shot noise present in homodyne detection. Within the operator representation theorem [YS80], used for the calculations, this noise originates from the vacuum fluctuations in the signal field and in any other vacuum fields coupled due to inefficiencies. In contrast, within the alternative normal-time ordered theory [Car87] this shot noise spectrum arises from self-correlations of the single photocurrent detection events, mainly coming from the strong LO field. Apart from interpretation debates, Equation 1.30 provides a fast and reliable method for calibrating the measured homodyne spectra in units of shot noise.

## 1.5 FILTERED MODES

Let's now analyze in more details the modal structure of a continuous propagating field, $\hat{E}$. In fact, this field contains infinite modes which are usually grouped into positive and negative frequency components, as done in Equation 1.1. In the limit of a continuous mode density, the term for the positive components is expressed as an integral over plane waves,

$$\hat{E}^{(+)}(z,t) = \imath \int_0^\infty \frac{d\Omega}{2\pi} \sqrt{\frac{\hbar\Omega}{2\epsilon_0 c\sigma}} e^{\imath(kz-\Omega t)} \hat{a}(\Omega) = \imath \sqrt{\frac{\hbar\Omega_L}{2\epsilon_0 c\sigma}} e^{\imath k_L z} \hat{a}(t). \tag{1.31}$$

The quantum mechanical operator $\hat{a}(t)$ is the field amplitude operator and usually employed, as seen, to describe the quantum optical properties of the field. From Equation 1.31 is clear that this field amplitude contains a multitude of modes. One can extract a single mode by filtering this amplitude with an arbitrary complex mode function, $f(t)$, according to [ZDGV15]

$$\hat{a}_f = \int_{-\infty}^{+\infty} dt f(t) \hat{a}(t), \tag{1.32}$$

with the additional constraint that $f(t)$ is normalizable, i. e.

$$\int_{-\infty}^{+\infty} dt|f(t)|^2 = 1. \tag{1.33}$$

This is necessary to assure that the mode operator, $\hat{a}_f$, satisfies the commutation relation in Equation 1.7. Then, it can be decomposed into quadrature operators as $\hat{a}_f = (\hat{X}_f + \imath\hat{Y}_f)/\sqrt{2}$, which satisfy the CCR.

Special and important modes are the *Fourier modes*, defined by the Fourier basis, i. e.

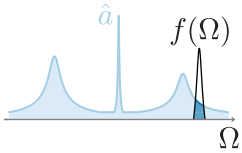


*Single filtered spectral mode*

$$\hat{a}_\Omega = \int_{-\infty}^{+\infty} ds e^{\imath\Omega s}\hat{a}(s). \tag{1.34}$$

The mode $\hat{a}_\Omega$ is the spectral frequency component $\Omega$ of the Fourier transform of the field $\hat{a}(t)$, i. e. $\hat{a}_\Omega \equiv \hat{a}(\Omega)$. We indicate now the frequency as a subscript rather than a variable to stress that it should be thought as a parameter defining a specific mode. Physically, the mode function required to filter out this mode corresponds to an infinitely long averaging of the propagating field. Mathematically, this makes the mode function non-normalizable according to Equation 1.33. In this case, the commutation relation take the singular form $[\hat{a}_\Omega, \hat{a}^\dagger_{\Omega'}] = \delta(\Omega - \Omega')$, where $\hat{a}^\dagger_\Omega \equiv \hat{a}(\Omega)^\dagger$ with the convention $\hat{a}(\Omega)^\dagger = \hat{a}^\dagger(-\Omega)$.

*Windowed Fourier modes*

Despite being unphysical, such Fourier modes are useful for calculations. Whenever a proper normalization is required, one can introduce the *windowed Fourier modes* as

$$\hat{a}_{\Omega,T} = \frac{1}{\sqrt{T}}\int_{-T/2}^{+T/2} dt e^{\imath\Omega t}\hat{a}(t), \tag{1.35}$$

which are normalizable and, as such, satisfies the standard commutation relation $[\hat{a}_{\Omega,T}, \hat{a}^\dagger_{\Omega',T}] = \delta_{\Omega,\Omega'}$.

### 1.5.1 *Interpretation of the homodyne detection*

Usually, filtering out single modes from a propagating field can be done either optically, e. g. via optical filtering, or electronically, e. g. in the detection process. We now reconsider the case of homodyne detection, and give an interpretation of the measurement in terms of filtered modes.

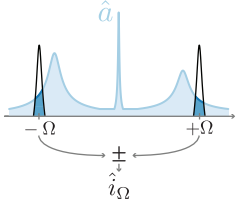


*Filtered mode measured by a homodyne detector*

In the ideal case of perfect detection with continuous LO, the normalized measured photocurrent at the quadrature angle $\theta_l$ is $\hat{i}(t) = \sqrt{2}\hat{X}^{\theta_l}(t)$, according to Equation 1.28. From this photocurrent, we can filter out the Fourier components at frequency $\Omega$, according to Equation 1.34, as

$$\hat{i}_\Omega = e^{-\imath\theta_l}\hat{a}_\Omega + e^{\imath\theta_l}\hat{a}^\dagger_{-\Omega}. \tag{1.36}$$

Such a filtered mode, $\hat{\imath}_\Omega$, actually contains a pair of symmetric Fourier modes of the signal field, $\hat{a}_{\pm\Omega}$, at frequencies $\pm\Omega$. In this sense, homodyne detection is a two-mode detection scheme with a phase relation between these two modes fixed by the phase of the LO. We refer to such a superposition of symmetric Fourier modes as a *quadrature mode*. We notice that this filtering can be performed in post-processing on the recorded photocurrent trace.

*Window function for normalizable modes*

For normalizable modes, one can filter the homodyne photocurrent either according to windowed Fourier modes or by introducing any window function in the Fourier modes definition Equation 1.34. When this is done, the quadrature mode will have two symmetric packets of Fourier modes at frequencies $\pm(\Omega \pm \delta\Omega)$, where the bandwidth $\delta\Omega$ is determined by the window function in the Fourier transform. For the sake of conciseness, we always refer to quadrature modes as $\hat{\imath}_\Omega$, disregarding if a window function is applied or not.

We can express Equation 1.36 in terms of the quadrature operators of the modes $\hat{a}_{\pm\Omega}$ [Bar+13; Lvo15]. By doing that, we have

$$\hat{\imath}_\Omega = \hat{X}^\theta_+ + \imath\hat{Y}^\theta_-, \tag{1.37}$$

where

$$\hat{X}^\theta_\pm = \cos(\theta)\frac{\hat{X}_\Omega \pm \hat{X}_{-\Omega}}{\sqrt{2}} + \sin(\theta)\frac{\hat{Y}_\Omega \pm \hat{Y}_{-\Omega}}{\sqrt{2}}, \tag{1.38a}$$

$$\hat{Y}^\theta_\pm = -\sin(\theta)\frac{\hat{X}_\Omega \pm \hat{X}_{-\Omega}}{\sqrt{2}} + \cos(\theta)\frac{\hat{Y}_\Omega \pm \hat{Y}_{-\Omega}}{\sqrt{2}} \tag{1.38b}$$

and $[\hat{X}^\theta_\pm, \hat{Y}^\phi_\mp] = 0$. The quadratures $\hat{X}^\theta_\pm$, $\hat{Y}^\theta_\pm$ are usually referred to as the *generalized Einstein-Podolsky-Rosen (EPR) quadratures* of the two modes $\hat{a}_\Omega$ and $\hat{a}_{-\Omega}$. Equation 1.37 clearly shows that homodyne detection measurements not only are two-mode measurements, but also directly probe a combination of commuting EPR quadratures of these two modes. In particular, the correlation

*Homodyne detection as a two-mode measurement*

$$\left\langle \hat{\imath}^\dagger_\Omega \hat{\imath}_\Omega \right\rangle = \left\langle \left(\hat{X}^\theta_+\right)^2 \right\rangle + \left\langle \left(\hat{Y}^\theta_-\right)^2 \right\rangle \tag{1.39}$$

has the form of an EPR variance, used as an entanglement witness [Dua+00; Gio+03]. A value of $\left\langle \hat{\imath}^\dagger_\Omega \hat{\imath}_\Omega \right\rangle < 1$ indicates that the bipartite state formed by the two modes $\hat{a}_{\pm\Omega}$ is entangled.

Finally, we notice that in the case of Fourier modes the correlation in Equation 1.39 corresponds to the frequency component $\Omega$ of the normalized homodyne photocurrent PSD in Equation 1.29, i. e. $\left\langle \hat{\imath}^\dagger_\Omega \hat{\imath}_\Omega \right\rangle \equiv \overline{S}_{ii}(\Omega)$. Usually, an optical field giving rise to a homodyne spectrum with frequency components less than the vacuum level,i. e. $\overline{S}_{ii}(\Omega) < 1$, is recognized as a squeezed field. According to the previous discussion, the underlying squeezed state, for $\Omega \neq 0$, is a two-mode squeezed state.

## 1.6 STOCHASTIC MASTER EQUATION

So far, we have been dealing with the outcomes of a measurement without worrying about its effect on the dynamics of the quantum system. As known, in fact, measurements in quantum mechanics have a profound impact on the measured system. For example, an ideal von Neumann projective measurement, once performed, abruptly changes the state of the system. More realistic measurement schemes are described by a generalized class of measurements, known as positive-operator-valued measure (POVM), which the projective measurement is part of. These generalized measurements also lead to an effect in the system [WM10; Jac14]. Whenever the measurement outcomes are recorded and available, one can observe the selective evolution of the state of the system. The dynamical equation describing this evolution is known as the stochastic master equation (SME) [Di688; JS06]. The selective state, $\hat{\rho}_c$, is also known as a *conditional state*.

Here, we focus on a specific class of quantum measurements known as *monitoring*, namely time-continuous Gaussian measurement of a system's observable. With Gaussian measurement, we intend that the random measurement outcomes follow a Gaussian distribution. For instance, the homodyne detection is an example of monitoring. The SME for a quantum system, subjected to monitoring of the observbales $\hat{o}_k$, is

$$d\hat{\rho}_c = \frac{1}{i\hbar}\left[\hat{H}, \hat{\rho}_c\right] dt + \sum_k \mathcal{D}[\hat{o}_k]\hat{\rho}_c\, dt + \sum_k \sqrt{\eta_k}\mathcal{H}[\hat{o}_k]\hat{\rho}_c\, dW_k, \quad (1.40)$$

where the superoperator $\mathcal{H}[\hat{o}_k]\hat{\rho}_c = \hat{o}_k\hat{\rho}_c + \hat{\rho}_c\hat{o}_k^\dagger - \left\langle \hat{o}_k + \hat{o}_k^\dagger \right\rangle_c \hat{\rho}_c$ describes the conditioning upon the outcomes from the $k$-th measurement channel, with efficiency $\eta_k$, $\langle\cdot\rangle_c$ is the expectation value over the conditional state and $W_k$ is a Wiener process, with $dW_k$ the associated Wiener increment satisfying

$$\mathbb{E}\left[dW_k\right] = 0, \quad (1.41a)$$

$$dW_k\, dW_j = \delta_{kj}\, dt. \quad (1.41b)$$

In addition, the measurement outcomes $i_k$ is

$$di_k(t) = \frac{\left\langle \hat{o}_k + \hat{o}_k^\dagger \right\rangle_c}{2} dt + \frac{dW_k}{2\sqrt{\eta_k}}. \quad (1.42)$$

Then, the conditional state $\hat{\rho}_c$ is driven by the measurement outcomes through the process $dW_k$.

The non-selective evolution for the system state can be obtained from averaging Equation 1.40 over all possible realizations of the noise

processes $dW_k$. When doing that using Equation 1.41, the measurement superoperators cancel and one is left with

$$d\hat{\rho} = \frac{1}{\imath\hbar}\left[\hat{H}, \hat{\rho}\right] dt + \sum_k \mathcal{D}[\hat{o}_k]\hat{\rho}\, dt, \tag{1.43}$$

where $\hat{\rho} := \mathbb{E}[\hat{\rho}_c]$. When not recorded, the effect of a measurement is fully captured by the additional terms $\mathcal{D}[\hat{o}_k]\hat{\rho}$, which represent the *quantum backaction* of the measurements on the system. These terms introduce a decay of the coherence elements of the density operator, a process called *decoherence*.

We also notice a resemblance between Equation 1.43 and the master equation for an open system, Equation 1.10. In fact, we can now interpret an open system as a system monitored by the environment. Because the environment is inaccessible to an observer, the measurement outcomes are not available and the non-selective evolution is retrieved. This effective loss of information in the environment leads to decoherence and energy dissipation.

## 1.7 LINEAR-QUADRATIC-GAUSSIAN QUANTUM SYSTEMS

Based on what we discussed so far, we now introduce an important class of quantum systems, that is, the linear-quadratic-Gaussian (LQG) quantum systems, and how they can be optimally controlled [WM10]. Their importance relies on the fact that they always have an analogue classical system. As such, many of the results hereby reported are a direct consequence of the classical counterparts, with system's variables replaced by operators. The fundamental difference for quantum systems lies on some additional constraints imposed in the source of noise present in the dynamics, as we will see. Such constraints result from the different phase-space structure in quantum mechanics, and in particular from the commutation relations for canonical conjugate observables.

### 1.7.1 *Unconditional dynamics*

The linearity assumption implies that the non-selective, or unconditional, dynamics is governed by a linear equation, whose general matrix form is

$$d\hat{\mathbf{x}} = A\hat{\mathbf{x}}dt + B\mathbf{u}(t)dt + E d\mathbf{n}_p(t), \tag{1.44}$$

where $\hat{\mathbf{x}} = (\hat{x}_1, \hat{p}_1, \hat{x}_2, \hat{p}_2, \cdots, \hat{x}_n, \hat{p}_n)^T$ is the vector of canonical conjugate observables, $A$ is a drift matrix, encoding both unitary and dissipative dynamics, $B$ is the control matrix and $\mathbf{u}(t)$ the control or feedback signal, $E d\mathbf{n}_p(t)$ is a Wiener process vector with $\mathfrak{R}\left[E d\mathbf{n}_p(t) d\mathbf{n}_p(t)^T E^T\right] = D dt$, with $D$ a diffusion matrix.

The drift matrix can be obtained from the underlying master equation

$$\dot{\hat{\rho}} = \frac{1}{\imath\hbar}\left[\hat{H}, \hat{\rho}\right] + \mathcal{D}[\hat{\mathbf{c}}/\sqrt{\hbar}]\hat{\rho}, \tag{1.45}$$

where $\hat{\mathbf{c}} = \widetilde{C}\hat{\mathbf{x}}$. For a linear system, the general form of the Hamiltonian is

$$\hat{H} = \frac{1}{2}\hat{\mathbf{x}}^{\mathsf{T}} G \hat{\mathbf{x}} - \hat{\mathbf{x}}^{\mathsf{T}} \Sigma B \mathbf{u}(t), \tag{1.46}$$

with $G$ real and symmetric and $\Sigma$ the symplectic matrix

$$\Sigma = \bigoplus_{1}^{n} \begin{pmatrix} 0 & 1 \\ -1 & 0 \end{pmatrix}. \tag{1.47}$$

Introducing the matrix

$$\overline{C}^{\mathsf{T}} = \left(\mathrm{Re}[\widetilde{C}^{\mathsf{T}}], \mathrm{Im}[\widetilde{C}^{\mathsf{T}}]\right), \tag{1.48}$$

we have that

$$A = \Sigma\left(G + \overline{C}^{\mathsf{T}} S \overline{C}\right), \tag{1.49a}$$

$$D = \hbar \Sigma \overline{C}^{\mathsf{T}} \overline{C} \Sigma^{\mathsf{T}}, \tag{1.49b}$$

where

$$S = \begin{pmatrix} 0 & \mathbb{1} \\ -\mathbb{1} & 0 \end{pmatrix}. \tag{1.50}$$

The assumption of Gaussian noise implies that the state is fully determined only by the first two moments, $\langle\hat{\mathbf{x}}\rangle$ and $V$, which evolve according to

$$\left\langle \dot{\hat{\mathbf{x}}} \right\rangle = A\left\langle \hat{\mathbf{x}} \right\rangle + B\mathbf{u}(t), \tag{1.51a}$$

$$\dot{V} = AV + VA^{\mathsf{T}} + D. \tag{1.51b}$$

The fundamental difference between a classical and a quantum system lies in the drift and diffusion matrices, $A$ and $D$. For quantum systems, these matrices are not independent because they both depend on $\overline{C}$. In fact, they satisfy the linear matrix inequality (LMI)

*Fluctuation-dissipation relation*

$$D - \imath\hbar\frac{A\Sigma - \Sigma^{\mathsf{T}}A^{\mathsf{T}}}{2} \geqslant 0, \tag{1.52}$$

which is sometimes called the *fluctuation-dissipation relation*. It is weaker than the homonymous relation in equilibrium thermodynamics, as no assumption about thermal equilibrium is made here.

### 1.7.2 *Conditional dynamics*

We also let the system being monitored via a linear measurement, as discussed in Section 1.6. The measurement outcome, similarly to Equation 1.42, can be written as

$$\hat{\mathbf{y}}dt = C\hat{\mathbf{x}}dt + d\mathbf{n}_m(t), \tag{1.53}$$

where $\hat{\mathbf{y}}$ is the outcome operator vector, $d\mathbf{n}_m$ is a Wiener process known as the *measurement noise* and the matrix C represents a specific monitoring scheme. This matrix can be obtained from the underlying diffusive SME

$$d\hat{\rho}_c = \frac{1}{\imath\hbar}\left[\hat{H}dt, \hat{\rho}_c\right] + dt\mathcal{D}[\hat{\mathbf{c}}/\sqrt{\hbar}]\hat{\rho}_c + \mathcal{H}[\frac{d\mathbf{z}^\dagger(t)}{\sqrt{\hbar}}\frac{\hat{\mathbf{c}}}{\sqrt{\hbar}}]\hat{\rho}_c, \tag{1.54}$$

where $\mathbb{E}[d\mathbf{z}] = 0$, $d\mathbf{z}d\mathbf{z}^\dagger = \hbar N dt$ and $d\mathbf{z}d\mathbf{z}^T = \hbar\Lambda dt$, with $\Lambda$ a complex symmetric matrix. The matrix $N = \mathrm{diag}(\eta_1, \ldots, \eta_L)$ includes the detection inefficiency for each detection channel. We combine these two matrices in an *unravelling matrix*

$$U = \frac{1}{2}\begin{pmatrix} N + \mathrm{Re}(\Lambda) & \mathrm{Im}[\Lambda] \\ \mathrm{Im}[\Lambda] & N - \mathrm{Re}(\Lambda) \end{pmatrix}. \tag{1.55}$$

The measurement scheme matrix C is obtained as

$$C = 2T^T\overline{C}/\hbar, \tag{1.56}$$

where $TT^T = \hbar U$ and $\overline{C}$ is defined in Equation 1.48. The measurement noise, $d\mathbf{n}_m(t)$, has the following correlations

$$d\mathbf{n}_m d\mathbf{n}_m^T = \mathbb{1}dt, \tag{1.57a}$$

$$\Re\left[E d\mathbf{n}_p(t) d\mathbf{n}_m^T\right] = \Gamma^T dt, \tag{1.57b}$$

where $\Gamma = -T^T S\overline{C}\Sigma^T$.

For a linear Gaussian system, the conditional state is again fully determined by the first two moments, $\langle\hat{\mathbf{x}}\rangle_c$ and $V_c$, which evolve according to

$$d\langle\hat{\mathbf{x}}\rangle_c = A\langle\hat{\mathbf{x}}\rangle_c dt + B\mathbf{u}(t)dt + \left(V_c C^T + \Gamma^T\right) d\hat{\mathbf{w}}, \tag{1.58a}$$

$$\dot{V}_c = AV_c + V_c A^T + D - \left(V_c C^T + \Gamma^T\right)(CV_c + \Gamma), \tag{1.58b}$$

where we have introduced the *innovation* $d\hat{\mathbf{w}} = d\mathbf{n}_m + C(\hat{\mathbf{x}} - \langle\hat{\mathbf{x}}\rangle_c)$, which quantifies the deviation between the first moment of the conditional state and the measurement outcome. Again, the fundamental difference between classical and quantum systems is the presence of additional constrains on the fluctuations, due to the measurement. Defining $\widetilde{E}\widetilde{E}^T := D - \Gamma^T\Gamma$, we find that a quantum system satisfies the LMI

$$\widetilde{E}\widetilde{E}^T - \frac{\hbar^2}{4}\Sigma C^T C\Sigma^T \geqslant 0. \tag{1.59}$$

*Measurement-disturbance relation*

This is called the *fluctuation-observcation relation* or, sometimes, the *Heisenberg measurement-disturbance relation*, as it originates from the Heisenberg uncertainty relation. It connects the system fluctuations, $\widetilde{E}\widetilde{E}^T$, to the measurement strength, $C^T C$, and imposes more fluctuations as the measurement strength increases.

### 1.7.3 *Optimal control*

This system can be controlled by exerting the external forces $\mathbf{u}$. Any optimal control strategy aims to minimize a cost function, $j$, which takes the general form

$$j = \int_{t_0}^{t_1} \mathbb{E}\left[h(\hat{\mathbf{x}}, \mathbf{u}, t)\right] dt, \tag{1.60}$$

which is additive over time. This allows to make use of the separation principle, which states that the optimal control strategy should be based *only* on the conditional state. For LQG systems, the cost function is at most quadratic in the system's observable, i. e.

$$h(\hat{\mathbf{x}}, \mathbf{u}, t) = \hat{\mathbf{x}}^T P \hat{\mathbf{x}} + \mathbf{u}^T Q \mathbf{u}. \tag{1.61}$$

Then, the stronger *certainty equivalence* holds. That is, the optimal control force $\mathbf{u}(t)$ is linear on the conditional state first moments $\langle \hat{\mathbf{x}} \rangle_c$, i. e.

$$\mathbf{u}(t) = -K(t) \langle \hat{\mathbf{x}}(t) \rangle_c , \tag{1.62}$$

where $K(t) = Q^{-1} B^T X(T)$ and $X(t)$ is a symmetric, positive semi-definite matrix. At the steady-state, the matrix $\overline{X} \coloneqq X(\infty)$ is a solution of the Riccati equation

$$A^T \overline{X} + \overline{X} A + P - \overline{X} B Q^{-1} B^T \overline{X} = 0. \tag{1.63}$$

Two important figures of merit are the steady-state variance of the closed loop system, $\overline{V}_{cl}$, and the average integrand of the cost function, $\mathbb{E}[h]_{ss}$. The former one satisfies the following Lyapunov equation

$$N \overline{V}_{cl} + \overline{V}_{cl} N^T + F^T F - N \overline{V}_C - \overline{V}_C N^T = 0, \tag{1.64}$$

with $N^T \coloneqq A^T - \overline{X} B Q^{-1} B^T$, $F \coloneqq C \overline{V}_c + \Gamma$ and $\overline{V}_c$ is the steady-state solution of Equation 1.58b. The latter, instead, is expressed by

$$\mathbb{E}[h]_{ss} = \operatorname{tr}\left[\overline{X} B Q^{-1} B^T \overline{X} \overline{V}_c\right] + \operatorname{tr}\left[\overline{X} D\right]. \tag{1.65}$$

A summary of a generic LQG system is shown in Figure 1.2.

In practice, the controller is represented by a filter: it takes the measurement record $\mathbf{y}$ as input, processes it and outputs the control signal $\mathbf{u}$. To experimentally implement this filter, it is useful to compute the transfer function of the controller. Taking the Fourier transform

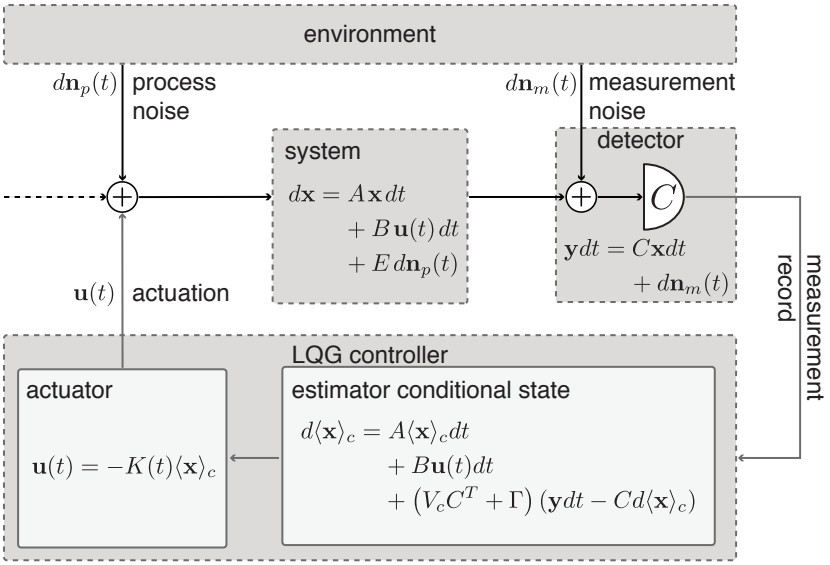


Figure 1.2: Linear-quadratic-Gaussian system. Block schematic of a linear Gaussian system undergoing continuous monitoring and subjected to the optimal control, constrained to a quadratic cost functions.

of Equation 1.58a with $d\hat{\mathbf{w}} = \hat{\mathbf{y}} - C\,\langle\hat{\mathbf{x}}\rangle_c$ and $\mathbf{u}(\Omega) = -\overline{K}\,\langle\hat{\mathbf{x}}\rangle_c\,(\Omega)$, we find

$$\langle\hat{\mathbf{x}}\rangle_c\,(\Omega) = \left[-\imath\Omega\mathbb{1} - A + B\overline{K} + (\overline{V}_c C^T + \Gamma^T)C\right]^{-1}\left(\overline{V}_c C^T + \Gamma^T\right)\mathbf{y}(\Omega). \tag{1.66}$$

The controller transfer function, from $\hat{\mathbf{y}}$ to $\hat{\mathbf{u}}$, is

$$H_{oc}(\Omega) = -\overline{K}\left[-\imath\Omega\mathbb{1} - A + B\overline{K} + (\overline{V}_c C^T + \Gamma^T)C\right]^{-1}\left(\overline{V}_c C^T + \Gamma^T\right). \tag{1.67}$$

# 2

# MECHANICAL VIBRATIONS OF MEMBRANES

In this chapter we provide a basic theory of mechanical vibrating structures, which constitute one of the building blocks for optomechanical experiments, together with optical cavities. We first review the equations of motion for a vibrating elastic plate, taking into account also an energy dissipation mechanism. Then, we focus on understanding the origin of this dissipation for pre-stressed structures and introduce a recent approach to reduce its contribution. Finally, we provide a method to reduce the dynamics of such a tridimensional structure to the one of a point-like oscillator, for which we derive the quantum mechanical description.

## 2.1 EQUATIONS OF MOTION FOR A VIBRATING MEMBRANE

In this thesis, we focus on mechanical systems in the form of membrane resonators. They are composed of a thin plate, firmly clamped at the edges to a supporting frame which is assumed at rest. The membrane has a continuous mass density, $\rho$, which deforms when subjected to forces. In particular, we assume that the membrane material is elastic to some extent, i. e. for small deformations, the internal forces are linear in the deformation and opposite to the direction of the deformation itself.

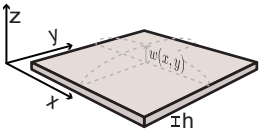

*Sketch of a vibrating plate*

In the following, we use the notation $u_i$ for a vector and $u_{ijk}$ for a tensor. Also, we use the convention that repeated indices are summed over. Let's assume a reference frame in which the membrane frame is at rest. The membrane motion can be represented by the *displacement vector* $u_i$, with $i = x, y, z$. The membrane deformation is quantified by the *strain tensor* $e_{ij}$, defined as [LLo8]

$$e_{ij} = 2^{-1}\left(\partial_j u_i + \partial_i u_j + \partial_i u_k \partial_j u_k\right), \tag{2.1}$$

where $\partial_i$ indicates the partial derivative with respect to coordinate $i$.

The internal forces arising in the membrane are quantified by the *stress tensor* $\sigma_{ij}$. In general, its response to a given strain field is arbitrary and depends on the chosen material. In many cases however, one can safely assume that this response is linear in the strain. Within this assumption, one can obtain the following stress-strain relation

$$\sigma_{ij} = h_{ijkl} e_{kl} = \frac{E}{1+\nu}\left(e_{ij} + \frac{\nu}{1-2\nu} e_{ll}\delta ik\right), \tag{2.2}$$

where $E$ and $\nu$ are, respectively, the Young's modulus and the Poisson ratio, parameters specific of a given material. Equation 2.2 is known as *Hooke's law* and forms the basis of the theory of elasticity.

From the strain and the stress tensors, one can calculate the free energy density as

$$f = 2^{-1}\sigma_{ij}e_{ij}. \tag{2.3}$$

*von Kármán strain approximations*

Minimizing Equation 2.3 via a variational calculus gives the equations of motion governing the displacement vector $u_i$. These general equations are cumbersome and hard to solve without any further approximations. For thin vibrating membranes, where the thickness dimension is usually much smaller than the other two, the approximations one can make are that (i) the surfaces normal to the membrane plane remain normal even after the deformation occurs; (ii) the in-plane displacement components are negligible, compared to the out-of-plane ones and (iii) any change in thickness, during the vibration, is negligible. Within these assumptions [Cia80; Cia90], the displacement vector is parameterized only by the out-of-plane component $w(x,y) \coloneqq u_z$ and the strain tensor can be approximated by the *von Kármán strain* tensor

$$e_{\alpha\beta} = e_0\delta_{\alpha\beta} - z\partial_{\alpha\beta}w + 2^{-1}\partial_\alpha w\partial_\beta w, \tag{2.4}$$

where the Greek subscripts indicate the in-plane coordinates, i. e. $\alpha = x,y$. The first constant term, $e_0\delta_{\alpha\beta}$, represents an in-plane pre-strain. The second term, linear in the displacement $w$, describes the structure bending as it moves out of plane. The last term, quadratic in the displacement $w$, represents a non-linearity of the structure. It originates from the geometrical elongation of the structure as it moves out of plane, and is referred to as the *geometrical non-linearity*. Inserting Equation 2.4 in Equation 2.2, we obtain

$$\begin{aligned}\sigma_{\alpha\beta} =& \frac{E}{1-\nu^2}\left[(1-\nu)e_{\alpha\beta} + \nu e_{\gamma\gamma}\delta_{\alpha\beta}\right] \\ =& \sigma_0\delta_{\alpha\beta} - z\frac{E}{1-\nu^2}\left((1-\nu)\partial_{\alpha\beta}w + \nu\partial_{\gamma\gamma}w\delta_{\alpha\beta}\right) \\ &+ \frac{E}{2(1-\nu^2)}\left((1-\nu)\partial_\alpha w\partial_\beta w + \nu\partial_\gamma w\partial_\gamma w\delta_{\alpha\beta}\right),\end{aligned} \tag{2.5}$$

where $\sigma_0 \coloneqq e_0 E/(1-\nu)$ is the constant, in-plane stress resulting from the pre-strain $e_0$.

The in-plane free energy density, $f_{ip}$, obtained from integrating Equation 2.3 along the thickness coordinate, $z$, comprises three contributions, $f_{ip} = f_t + f_b + f_e$, where

$$f_t = \frac{\sigma_0}{2}h\partial_\gamma w\partial_\gamma w \tag{2.6}$$

is the energy stored in the initial pre-stress,

$$f_b = \frac{D}{2}\left[\partial_{\gamma\gamma}w\partial_{\lambda\lambda}w + (1-\nu)\left(\partial_{\alpha\beta}w\partial_{\alpha\beta}w - \partial_{\gamma\gamma}w\partial_{\lambda\lambda}w\right)\right] \tag{2.7}$$

where $D = Eh^3/\left(12(1-\nu^2)\right)$ is the *flexural rigidity*, is the energy stored in the material bending, which relates to the structure curvature as shown by the presence of second-order derivatives and

$$f_e = \frac{Eh}{8(1-\nu^2)}\partial_\alpha w \partial_\alpha w \partial_\beta w \partial_\beta w \tag{2.8}$$

is the energy stored in the material elongation.

The equations of motion, in terms of the stress resultants

$$N_{\alpha\beta} = \int_{-h/2}^{h/2} \sigma_{\alpha\beta}\, dz, \tag{2.9a}$$

$$M_{\alpha\beta} = \int_{-h/2}^{h/2} z\sigma_{\alpha\beta}\, dz, \tag{2.9b}$$

are

$$\partial_{\alpha\beta} M_{\alpha\beta} + \partial_\alpha \left(N_{\alpha\beta}\partial_\beta w\right) = \rho h \ddot{w}, \tag{2.10a}$$

$$\partial_\alpha N_{\alpha\beta} = 0, \tag{2.10b}$$

where $\dot{w} \coloneqq \partial_t w$. In many cases, one is interested only in small displacements around the equilibrium configuration, thus the non-linear contribution arising from the elongation can be safely neglected. In this case, the equation of motion for the displacement $w$ becomes linear

*Neglecting the geometrical non-linearity*

$$\left(h\sigma_0 \partial_{\alpha\alpha} - D\partial_{\alpha\alpha\beta\beta}\right) w = \rho h \ddot{w}, \tag{2.11}$$

This is a bi-harmonic equation for the displacement $w$, which undergoes a harmonic motion. In particular, a general solution of Equation 2.11 can be decomposed into a sum of orthonormal functions, $w_k(x, y, t)$, satisfying appropriate boundary conditions. The functions $w_k$ are called the *normal modes* of the structure. To find them, one can solve Equation 2.11 from numerical simulations employing techniques as finite element modelling.

## 2.2 INTRODUCTION OF THE DISSIPATIVE DYNAMICS

We now introduce the dissipation of the elastic energy stored in the material. In order to model it, we assume that there exists a time lag, $\tau$, in the stress-strain response [LRoo]. For $\tau$ much shorter than any relevant dynamical timescale, we can approximate Equation 2.2 as

$$\sigma_{ij}(t) = h_{ijkl} e_{kl}(t-\tau) \approx \underbrace{h_{ijkl} e_{kl}(t)}_{\sigma^c_{ij}(t)} \underbrace{-\tau\, h_{ijkl} \partial_t e_{kl}(t)}_{\sigma^d_{ij}(t)}, \tag{2.12}$$

where $\sigma^c_{ij}(t)$ is the conservative part of the stress, as calculated in Equation 2.5, and $\sigma^d_{ij}(t)$ is the dissipative contribution. Inserting the time derivative of Equation 2.4, we have

$$\sigma^d_{\alpha\beta}(t) = \frac{-\tau E}{1-\nu^2}\left\{-z\left[(1-\nu)\partial_{\alpha\beta}\dot{w} + \nu\partial_{\gamma\gamma}\dot{w}\delta_{\alpha\beta}\right]\right.$$
$$\left. +2^{-1}(1-\nu)\left(\partial_\alpha\dot{w}\partial_\beta w + \partial_\alpha w\partial_\beta\dot{w}\right) + \nu\partial_\gamma\dot{w}\partial_\gamma w\delta_{\alpha\beta}\right\}. \quad (2.13)$$

The instantaneous dissipated power density is $p = \sigma^d_{ij}\partial_t e_{ij}$. After integrating over the thickness dimension, the in-plane dissipated power density comprises two contributions, $p_{ip} = p_b + p_e$, where

$$p_b = \tau D\left[\underbrace{\partial_{\gamma\gamma}\dot{w}\partial_{\lambda\lambda}\dot{w}}_{\text{mean curvature}} + (1-\nu)\left(\underbrace{\partial_{\alpha\beta}\dot{w}\partial_{\alpha\beta}\dot{w} - \partial_{\gamma\gamma}\dot{w}\partial_{\lambda\lambda}\dot{w}}_{\text{Gaussian curvature}}\right)\right] \quad (2.14)$$

corresponds to the power dissipated in bending the structure, proportional to the mean and the Gaussian curvatures, and

$$p_e = \frac{-\tau E h}{1-\nu^2}\left[(1-\nu)\partial_\alpha\dot{w}\partial_\alpha\dot{w}\partial_\beta w\partial_\beta w + (1+\nu)\partial_\alpha\dot{w}\partial_\alpha w\partial_\beta\dot{w}\partial_\beta w\right] \quad (2.15)$$

is a small non-linear contribution arising from the dissipation in elongating the material. The dissipated energy density can be obtained from the integration of the dissipated power over one oscillation cycle, i. e. $\Delta f_{ip} = \oint p_{ip}\,dt$.

The linear bending dissipation can be included in the equation of motion Equation 2.11 for the displacement $w$ as

$$\rho h\ddot{w} + \left(D\partial_{\alpha\alpha\beta\beta} - h\sigma_0\partial_{\alpha\alpha}\right)w - \tau D\partial_{\alpha\alpha\beta\beta}\dot{w} = 0, \quad (2.16)$$

which takes the form of a damped harmonic oscillator. A correct formulation of the problem also requires to take into account the inevitable fluctuations that dissipation brings into the dynamics [LLP08]. For a system in thermal equilibrium, the fluctuation-dissipation theorem links the power spectral density of the fluctuating force to the dissipation rate of the system.

*Other dissipative mechanisms*

In general, there are more sources of dissipation present in addition to the one arising from the lag between the stress and the strain. Two of them, which are worth of mention, are the *gas damping* and the *radiation* or *clamping loss*, both originating from external causes [SVR16].

GAS DAMPING It is produced by random collisions with gas molecules surrounding the membrane, and decreases with the gas pressure. To mitigate its effect, one should operate the mechanical structure in a high-vacuum environment, where the pressure can reach values below $< 10^{-6}$ mbar.

RADIATION LOSS The mechanical structure is connected to a supporting frame, which itself can sustain vibrational modes. When the modes from the membrane and the frame are matched, the mechanical energy propagates into the frame. This is, in turn, in physical contact with some other holding structure, which can absorb the propagating mechanical energy, thus dissipating it. In order to mitigate this loss, one can embody the membrane in a larger *phononic crystal* [Mal13], such that the membrane normal modes of interest lie in the bandgap region, where energy propagation is not allowed. As such, these modes do not interact with frame modes, therefore are shielded from radiation losses.

In the following, we assume that these other dissipation mechanisms are taken care of and do not play a significant role.

### 2.2.1 *Dissipation dilution and soft clamping*

A useful concept to classify the influence of dissipation is the *quality factor*, Q, defined as the amount of stored energy per dissipated energy per cycle, i. e.

$$Q = \frac{f}{\Delta f} = \frac{f_t + f_b + f_e}{\Delta f_b + \Delta f_e} \approx \frac{f_t + f_b}{\Delta f_b}, \tag{2.17}$$

where the approximation holds for negligible contributions from the non-linear elongation terms.

An important situations is when the pre-stress, $\sigma_0$, is large such that the stored tensile energy $f_t$ dominates over the stored bending energy. When this is true, the quality factor becomes $Q = f_t/\Delta f_b$ and can be enhanced by increasing the pre-stress $\sigma_0$. The increase of the quality factor as a consequence of pre-stress in the structure is a phenomenon known as *dissipation dilution*, firstly recognized by the researchers in the gravitational wave detectors [HS98]. In this case, the quality factor is limited by the structural bending dissipation, $\Delta f_b$, the rate of which has been calculated in Equation 2.14. In order to better understand the origin of this limitation, it is instructive to look at the simple case of a doubly-clamped beam, that is, a string [SVR16]. The shape of the fundamental normal mode is shown in red in Figure 2.1a. This shape, at the maximum displacement location, resembles a sinusoidal shape, shown in gray, and deviates from it as the clamping regions, at the edges, are approached. In particular, the boundary conditions impose that the structure should clamp to the frame horizontally. The consequence is that, at the clamping region, the string significantly bends and the mean curvature, shown in Figure 2.1b, is greatly enhanced compared to a pure sine wave. Given that the Gaussian curvature averages to zero, the mean curvature dominates the bending losses of Equation 2.14. Then, improving the quality factor requires to drastically reduce this clamping loss mechanism due to

*Soft clamping*

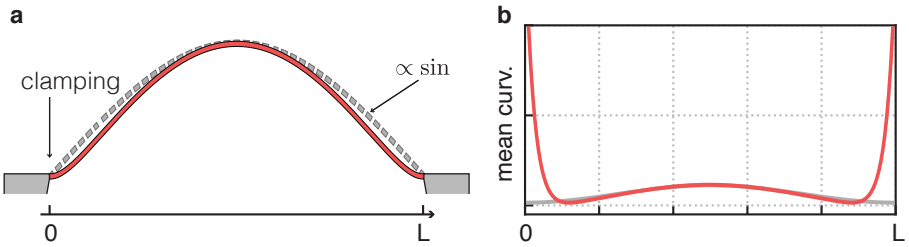


Figure 2.1: Vibrational modeshape and curvature of a string. a, The ideal modeshape, which neglects boundary conditions, is a sinusoidal shape, shown as a dashed gray beam. The boundary conditions impose a deviation from the ideal shape at the clamping region, resulting in a different modeshape as shown by the red beam. b, The mean curvature of a real beam (red) is greatly enhanced compared to the one of an ideal sinusoidal beam (gray), due to the clamping requirements. As a consequence, the bending loss at the clamping dominates.

the bending. This can be done by engineering the mode shape such that it evanescently decays towards the edges. This is the idea beyond the recently developed *soft clamping* approach [Tsa+17; Gha+18].

We exploit both the dissipation dilution and soft clamping in designing our membrane resonators. They are made of thin films of silicon nitride ($Si_3N_4$), deposited on a silicon (Si) wafer which forms the supporting frame. During the fabrication process, the $Si_3N_4$ acquires a large in-plane stress of $\sigma_0 \approx 1.3$ GPa. The membrane area is also patterned with a honeycomb lattice of holes. This forms a phononic crystal which opens up a bandgap. By modifying the lattice, we implant a defect at the center of the structure. This defect can sustain localized vibrational modes, which lie within the bandgap, thus are shielded by radiation losses. At the same time, the profile of such defect modes enables soft clamping, reducing by orders of magnitude their bending dissipation.

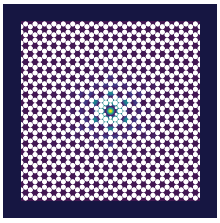

*Soft-clamped membrane resonator*

## 2.3 REDUCTION TO AN EFFECTIVE POINT-MASS MODEL

The equation of motion Equation 2.16 deals with a continuous distribution of mass. However, we are often interested only in the temporal evolution of a given normal mode. Then, we can simplify the treatment by ignoring the mode profile and reducing the equation of motion to the one of a point-like oscillator, with effective parameters. This is what the Galerkin's method does [SVR16]. We start by assuming a variable separation between the spatial and temporal parts of a normal mode, i. e. $w_k(z, y, t) = \widetilde{w}_k(x, y)q_k(t)$. The orthonormality condition of normal modes implies that $\int \widetilde{w}_k \widetilde{w}_j \, dx dy = \delta_{kj}$. The effective equation for the temporal mode, $q_k(t)$, is obtained by multiplying Equation 2.16

for $w_k$ and integrating over the surface to exploit the orthogonality. The resulting equation is

$$m\ddot{q}_k + m\Gamma_m\dot{q}_k + m\Omega_m^2 q_k = F(t), \tag{2.18}$$

where we have introduced a fluctuating force $F(t)$ driving the mode $k$. The effective mass, $m$, energy damping rate, $\Gamma_m$, and resonance frequency, $\Omega_m$, are related to the transverse mode profile via

*Effective parameters*

$$m = \int_S \rho h \widetilde{w}_k^2(x,y)\,dx\,dy, \tag{2.19a}$$

$$m\Gamma_m = \int_S \widetilde{w}_k(x,y)\left(-\tau D\partial_{\alpha\alpha\beta\beta}\right)\widetilde{w}_k(x,y)\,dx\,dy, \tag{2.19b}$$

$$m\Omega_m^2 = \int_S \widetilde{w}_k(x,y)\left(D\partial_{\alpha\alpha\beta\beta} - h\sigma_0\partial_{\alpha\alpha}\right)\widetilde{w}_k(x,y)\,dx\,dy, \tag{2.19c}$$

where the integration is performed over the area of the membrane, $S$. In this simplified model the quality factor becomes $Q = \Omega_m/\Gamma_m$.

Equation 2.18 describes a driven damped harmonic oscillator and can be exactly solved by taking the Fourier transform. From the solution, $q_k(\Omega) = \chi_m(\Omega)F(\Omega)$, we define the *mechanical susceptibility*

$$\chi_m(\Omega) = \frac{m^{-1}}{\Omega_m^2 - \Omega^2 - \imath\Gamma_m\Omega}, \tag{2.20}$$

which quantifies the response of the mechanical displacement to the exerted sinusoidal force, $F(\Omega)$, at frequency $\Omega$. The magnitude and phase are shown in Figure 2.2. For high quality factors, i. e. $Q \gg 1$, the mechanical susceptibility can be approximated by a Lorentzian function around resonance as

$$\chi_m(\Omega) \approx \frac{1}{2m\Omega_m}\frac{1}{\Omega_m - \Omega - \imath\Gamma_m/2}. \tag{2.21}$$

When the system is at thermal equilibrium at temperature $T$, the force $F(t)$ is a fluctuating thermal force which induces a Brownian motion. In this case, the fluctuation-dissipation theorem holds and links the PSD of the thermal force to the imaginary part of the susceptibility as

$$S_{FF}(\Omega) = \frac{2k_B T}{\Omega}\mathrm{Im}\left(\frac{1}{\chi_m(\Omega)^*}\right) = 2m\Gamma_m k_B T, \tag{2.22}$$

where $k_B$ is the Boltzmann constant.

## 2.4 QUANTIZATION OF MECHANICAL VIBRATIONS

The quantum description of a harmonic oscillator is obtained from replacing the classical position, $q_k$, with the position operator, $\hat{q}_k$.

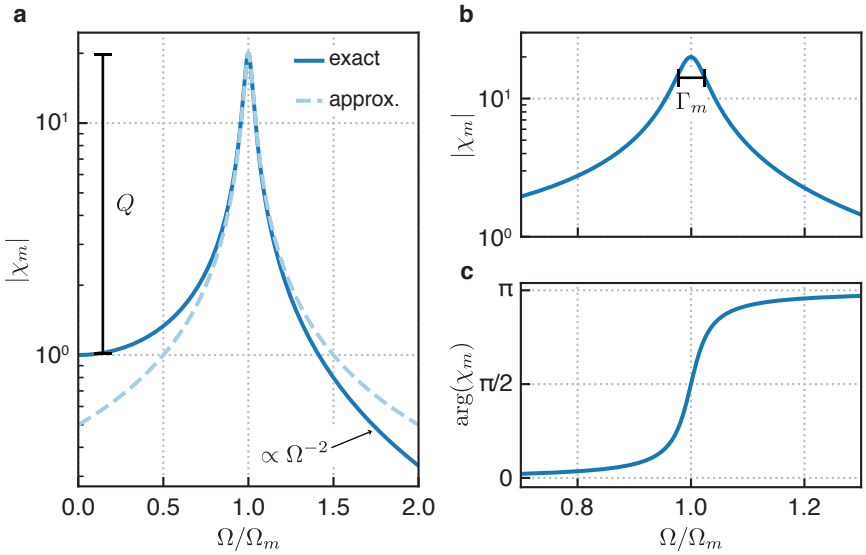


Figure 2.2: Mechanical susceptibility. a, Mechanical susceptibility (blue) and Lorentzian approximation (dashed light blue). The approximation is valid around the mechanical resonance and considerably deviates away from it. The height of the resonance, compared to the zero frequency response, is the quality factor Q. b, Magnitude and c, phase of the susceptibility, around the mechanical resonance frequency $\Omega_m$. The FWHM of the magnitude is the mechanical energy damping rate $\Gamma_m$.

Together with the momentum operator, $\hat{p}_k$, they form a pair of non-commuting canonical observables satisfying the CCR $[\hat{q}_k, \hat{p}_l] = i\hbar\delta_{kl}$. A first consequence is that, differently from the classical counterpart, the mechanical energy is discretized. The smallest packet of energy is called a *phonon* and its energy is $\hbar\Omega_m$. Also, there exists a lowest energy state, or *ground state*, which exactly contains half of a phonon. For convenience, we use the dimensionless position and momentum operators defined as $\hat{q} \to \hat{q}/(\sqrt{2}x_{zp})$ and $\hat{p} \to \hat{p}/(\sqrt{2}p_{zp})$. The quantity $x_{zp} = \sqrt{\hbar/(2m\Omega_m)}$ and $p_{zp} = \sqrt{\hbar m\Omega_m/2}$ are, respectively, the position and momentum fluctuations at the ground state, such that its energy is $E_0 = \hbar\Omega_m/2 = p_{zp}^2/(2m) + m\Omega_m^2 x_{zp}^2/2$. In these units, the mechanical susceptibility Equation 2.20 rescales according to $\chi_m \to \chi_m/(x_{zp}/p_{zp})$. For these dimensionless operators, the CCR becomes $[\hat{q}, \hat{p}] = i$.

When dissipations are present, the fluctuations from the environment drive the harmonic oscillator. For thermal equilibrium situations, the resulting motion is a quantum Brownian process. One needs to properly account for the environment and its interaction with the system to model the dissipative process, as seen in Section 1.3. However, the assumptions made there to derive the Lindblad master equation are not always well justified by mechanical systems, for which more

attention should be paid. As shown by Giovannetti and Vitali [GV01], the correct QLE for the quantum Brownian motion are

$$\dot{\hat{q}} = \Omega_m \hat{p}, \tag{2.23a}$$

$$\dot{\hat{p}} = -\Omega_m \hat{q} - \Gamma_m \hat{p} + \sqrt{2\Gamma_m}\hat{\xi}(t). \tag{2.23b}$$

*Quantum Brownian motion*

The operator $\hat{\xi}(t)$ represents the fluctuating force from the thermal environment in equilibrium at temperature T. Its correlation function is

$$\left\langle \hat{\xi}(t+\tau)\hat{\xi}(t) \right\rangle = \int_0^{\Omega_e} \frac{d\Omega}{2\pi} \frac{\Omega}{\Omega_m} \left[ e^{\imath\Omega\tau} \overline{n}_{th}(\Omega) + e^{-\imath\Omega\tau} \left( \overline{n}_{th}(\Omega) + 1 \right) \right], \tag{2.24}$$

where $\overline{n}_{th}(\Omega) = \left( e^{\hbar\Omega/(k_B T)} - 1 \right)^{-1}$ is the average number of phonons in the environment and $\Omega_e$ its bandwidth. The correlation function has a non-white structure, corresponding to a non-Markovian process. In the limit of broadband environment, $\Omega_e \to \infty$, one recovers the Markovian nature and the correlation function, in the Fourier domain, becomes

$$\left\langle \hat{\xi}(\Omega)\hat{\xi}(\Omega') \right\rangle \approx 2\pi\delta(\Omega + \Omega') \frac{\Omega}{\Omega_m} \left( \overline{n}(\Omega) + 1 \right). \tag{2.25}$$

In this limit, the PSD of the thermal force is [BM16]

$$S_{\hat{\xi}\hat{\xi}}(\Omega) = \frac{\Omega}{\Omega_m} \left( \overline{n}_{th}(\Omega) + 1 \right), \tag{2.26a}$$

$$S_{\hat{\xi}\hat{\xi}}(-\Omega) = \frac{\Omega}{\Omega_m} \overline{n}_{th}(\Omega). \tag{2.26b}$$

where we have used the identity $\overline{n}_{th}(-\Omega) = -1 - \overline{n}_{th}(\Omega)$. The asymmetry of the force spectrum between positive and negative frequencies is a quantum feature, and relates to the different rates at which the environment absorbs and emits phonons. The classical limit can be retrieved in the large temperature limit, $k_B T \gg \hbar\Omega$, for which the average number of phonon becomes $\overline{n}_{th}(\Omega) + 1 \approx \overline{n}_{th}(\Omega) \approx k_B T/(\hbar\Omega)$.

# 3

# CAVITY OPTOMECHANICS

We now review the basics of cavity optomechanics, a branch of physics which studies the interaction between optical and mechanical systems. We first describe the physical origin of this interaction, namely the radiation pressure force, for both the canonical, "rubber cavity" system and the membrane-in-the-middle cavity, of relevance for the experiments later reported. Then, we summarize the major effects arising on both the mechanics and optical field. In particular, we show how this interaction can be tailored to perform a quantum-limited displacement measurement.

## 3.1 RADIATION PRESSURE COUPLING

The canonical optomechanical system is composed of an oscillating mirror which, combined with another mirror at rest, forms an optical cavity. An external laser resonantly populates one of its mode, and a stationary electromagnetic field inside the cavity is built up [AKM14; BM16]. According to Maxwell's equations, the field carries a momentum proportional to its intensity. Upon reflection, this momentum is exchanged with the movable mirror via a radiation pressure force. This is the origin of the optomechanical interaction, which we will now intuitively explain. In fact, the consequence of the momentum exchange is that the mirror is accelerated, starting to oscillate, thus changing the cavity length. This leads to a shift of the cavity resonance frequency, as shown in Section 1.1. Then, the external laser, resonant with the cavity before the motion of the mirror, becomes now detuned and the intracavity intensity redistributes, finally affecting the radiation pressure force. This is the basic mechanism of the optomechanical interaction, which we will explore in details throughout the thesis.

*Canonical optomechanical interaction*

To be more quantitative, we start with a simple yet powerful one-dimensional model. We consider the non-interacting classical Hamiltonian of a single cavity mode, with amplitude $a(t)$, and a single mechanical mode for the oscillating mirror, with position $q(t)$ and momentum $p(t)$, which is

$$H = \hbar\Omega_c\, a(t)^* a(t) + \frac{1}{2} m\Omega_m^2 q(t)^2 + \frac{p(t)^2}{2m}, \tag{3.1}$$

where $\Omega_c$ is the cavity mode resonance frequency, $m$ the effective mass of the mechanical mode and $\Omega_m$ its resonance frequency. We recall that the resonance frequency for the $n$th longitudinal cavity mode is $\Omega_c^0 = nc/(2L)$, from Section 1.1. The displacement of the mirror, $q$,

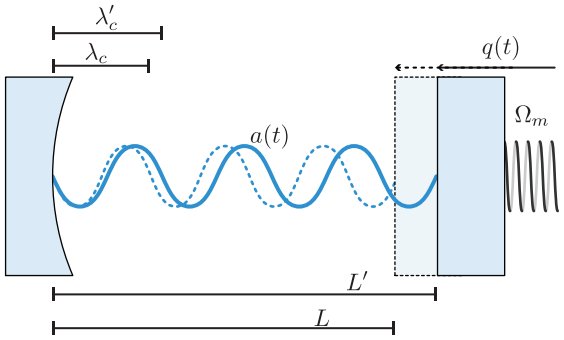


Figure 3.1: Canonical optomechanical cavity. A cavity mode is resonantly driven with an external field at wavelength$\lambda_c$. One mirror is oscillating at frequency $\Omega_m$. As the mirror moves, the cavity resonance frequency is shifted, because the new intracavity field is resonant for a different wavelength, $\lambda_c'$. This leads to a coupling between the optical cavity mode and the displacement of the movable mirror.

*Optomechanical parametric coupling*

leads to a change of the cavity length, thus of its resonance frequency. We can model it as

$$\Omega_c(q) = \frac{nc}{2(L+q)} \approx \Omega_c^0 - \frac{\Omega_c^0}{L} q, \tag{3.2}$$

where we have assumed that the displacement $q$ is small compared to the cavity length $L$. After substitution in Equation 3.1, we obtain the interaction Hamiltonian

$$H_{int} = -\hbar \frac{\Omega_c^0}{L} q(t) a^*(t) a(t) = q(t) F_{rp}(t), \tag{3.3}$$

where we have introduced the radiation pressure force $F_{rp}(t) = \hbar G a^*(t) a(t)$, with the *optomechanical coupling constant* $G \coloneqq -\Omega_c^0/L$.

A more careful analysis would require to solve the Maxwell's equations for the electromagnetic field inside the cavity, with the oscillating boundary condition at the mirror's location, as done by Law [Law95]. In addition, the mechanical motion can scatter the field into different cavity modes, leading to a multimode interaction. All the optical modes not driven by the external laser can, however, be adiabatically eliminated if the mechanical resonance frequency is much smaller than any frequency separation between the cavity modes. In the following we assume this condition to be always satisfied, thus the simple single-optical mode description will be used.

## 3.2 MEMBRANE-IN-THE-MIDDLE CAVITY

The canonical system just described is, however, of difficult practical implementation. The movable mirror should have high reflectivity in order to achieve a large finesse and enhance the optomechanical

interaction. At the same time, a large mechanical quality factor is required for quantum protocols, where the thermal contribution should be kept at minimum. It turns out that the fabrication of such a device, with simultaneously excellent optical and mechanical properties, is far from being trivial. An alternative route to achieve well performing optomechanical systems is to separate the mechanical element from the optical one, which can then be engineered separately to achieve the best performance. In the last decades, this approach led to a variety of different systems, ranging from optomechanical crystals [Eic+09] to levitated particles [Cha+10]. Among them, we employ the so called *membrane-in-the-middle (MIM) cavity* [Tho+08], in which a mechanical resonator in the form of a vibrating dielectric membrane (cf. Chapter 2) is placed in the middle of an optical cavity at rest, as sketched in Figure 3.2a.

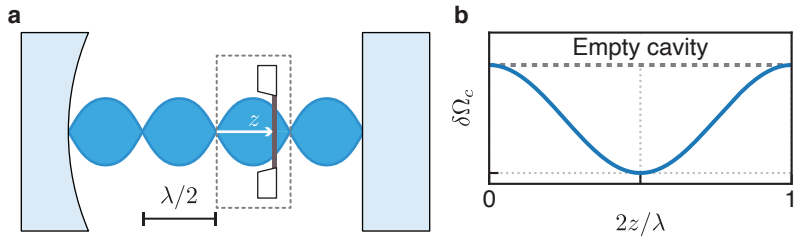


Figure 3.2: Membrane-in-the-middle optomechanical cavity. a, A thin dielectric vibrating membrane is inserted in an optical cavity, with fixed mirrors, perpendicular to its axis. The refractive index of the membrane material, different from the one of the surrounding environment, effectively increases the optical cavity length, depending on its position relative to the intracavity intensity. This modulates the cavity resonance frequency as the membrane moves. b, Sketch of the cavity resonance shift as a function of the membrane position $z$, relative to a node of the intracavity field. This shift has a periodicity of $\lambda/2$ and is always negative, as the membrane refractive index can only lead to an increase of the optical length.

*Optomechanical interaction in a MIM system*

The membrane's material has a different refractive index from the surrounding medium. This leads to an effectively longer optical path for the field in the cavity, thereby to a different cavity resonance frequency, compared to the empty case. If the membrane thickness is smaller than the optical wavelength, the effective optical path depends on the relative position, $z$, between the membrane and the intensity standing wave of the cavity field (Figure 3.2a). Intuitively, the smallest (largest) effect is achieved when the membrane is at a node (antinode) of the standing wave. As before, the cavity resonance frequency shifts depending on the membrane position, as shown in Figure 3.2b. As seen in Equation 3.2, this leads to an optomechanical coupling.

### 3.2.1 *Modulation of the main parameters*

The expression for the cavity frequency shift has been derived in a rigorous way [CL11; Bia+11]. Here, we simplify the treatment assuming that the fields are plane waves, as outlined by Jayich et al. [Jay+08]. This approximation holds if the membrane lies within the Rayleigh range of the cavity Gaussian mode. The reflection and transmission coefficient, respectively $r_i$ and $t_i$, characterize each optical element, which is modelled by a scattering matrix transforming the input fields, impinging from left and right, into output fields, reflected and transmitted. The optical cavity, of length L, is in general composed of two different mirrors, with $r_1, t_1$ and $r_2, t_2$. The membrane, of thickness $h \ll \lambda$ and refractive index $n$, is located at distance $z_m$ from the mirror 2, here assumed to be the one with the largest transmissivity. The membrane reflection and transmission coefficients, $r_m$ and $t_m$, can be calculated from the Fresnel equations.

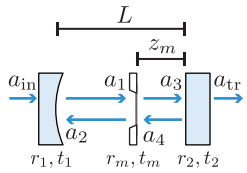


We also assume that an external laser field, $a_{in}$, at wavelength $\lambda$, is used to drive the cavity from mirror 1. In this case, one can calculate the fraction of the field transmitted through mirror 2, i. e. $a_{tr}/a_{in}$, by concatenating the right combination of scattering matrices of the optical elements and propagation in vacuum. We find that

$$\frac{a_{tr}}{a_{in}} = \frac{-\imath\, t1\, t2}{e^{-\imath k L} - r_m\left(e^{-\imath k(2z_m - L)} r_1 + e^{\imath k(2z_m - L)} r_2\right) + e^{\imath k L} r1 r2 (r_m^2 + t_m^2)}, \tag{3.4}$$

where $k = 2\pi/\lambda$ is the input field wavenumber. To find the resonance frequencies, we look for the zeros of the denominator in Equation 3.4, assuming that the mirrors are perfectly reflecting, $r_1 = r_2 = 1$, and that the membrane is lossless, $|r_m|^2 + |t_m|^2 = 1$. Then, the resonant wavenumber, $k_c$, satisfy

*Cavity resonance shift in a MIM system*

$$\cos(k_c L + \phi_r) + |r_m| \cos(2 k_c z_m - k_c L) = 0, \tag{3.5}$$

where $r_m = |r_m| e^{\imath \phi_r}$ [Jay+08; Dum+19]. The cavity resonance frequency shift, $\delta\Omega_c = c k_c - \Omega_c^0$, from the empty resonance, $\Omega_c^0$, can be found by numerically solving Equation 3.5. We do that for a fixed membrane position, $z_m$, and show the resulting frequency shifts in Figure 3.3a, for several subsequent longitudinal modes. The horizontal axis is formed by the resonant wavenumbers, $k_c$, in units of membrane position, $2z_m$, modulus $2\pi$, as suggested by the periodicity in Equation 3.5. That is, even keeping the membrane position fixed, one can get different cavity resonance shifts by addressing different longitudinal modes. From $\delta\Omega_c$, we can calculate the optomechanical coupling constant, G, for each resonance in $2kz_m$, by taking the first derivative with respect to the membrane position, as done in Figure 3.3b.

Differently from the canonical optomechanical system, the membrane affects the spatial distribution of the electric field in the cavity. In

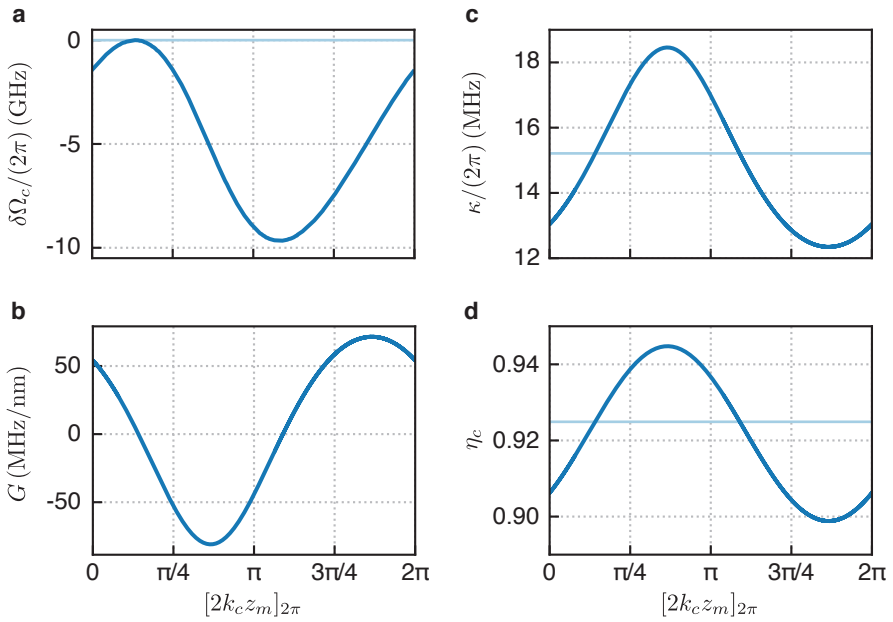


Figure 3.3: Optomechanical parameters modulation. a, Cavity resonance frequency shift (blue) relative to the empty cavity one (light blue). b, From the first-order derivative compared to the membrane position $z_m$ we obtain the optomechanical coupling constant. c, Total cavity linewidth and d, cavity overcoupling, both in blue, modulated by the presence of the membrane. The corresponding value in the case of an empty cavity is shown in light blue. We assume, for these simulations, $L = 1.61$ mm, $z_m = 0.5$ mm, $\lambda \sim 796$ nm, $t_1^2 = 77$ ppm, $t_2^2 = 950$ ppm, $|r_m|^2 = 2.6 \times 10^{-2}$ and $\phi_r = -0.4\pi$.

particular, the field differs in the two sub-cavities formed by each mirror and the membrane itself. This leads to an effective cavity linewidth, $\kappa$, and overcoupling, $\eta_c$, different from the empty case. Analytical expressions, derived by Dumont et al. [Dum+19], are used to show their dependence in Figure 3.3c and d, respectively.

### 3.2.2 *Equations of motion: Heisenberg picture*

We are now interested in the optomechanical quantum dynamics happening around some working point in the $2kz_m$ space, as shown in Figure 3.3. By choosing such a working point, either by moving the membrane at the proper location $z_m$ or by tuning the laser resonantly with the chosen cavity resonance $k_c$, one fixes the optomechanical coupling constant, G, the cavity linewidth, $\kappa$, and overcoupling, $\eta_c$. For a single optical mode, characterized by the amplitude $\hat{a}$ and $\hat{a}^\dagger$, and a single mechanical mode, with dimensionless position $\hat{q}$ and momentum $\hat{p}$, the interacting Hamiltonian can be derived from Equation 3.3 by substituting the system's variables with the proper

quantum operators and using the correct coupling constant G. We find that

$$\hat{H}_{int} = -\sqrt{2}\hbar g_0 \hat{q}\hat{a}^\dagger\hat{a}, \tag{3.6}$$

where we introduced the *vacuum optomechanical coupling rate* $g_0 := G\, x_{zp}\, \Lambda$, with $\Lambda$ a geometrical overlap factor between the transverse mode functions of the cavity Gaussian mode and the chosen membrane normal mode [AKM14; BM16]. The vacuum coupling rate, $g_0$, expresses the cavity frequency shift caused by a zero-point displacement. By taking into account coupling with the external optical bath and the thermal bath, the non-unitary dynamics can be described by means of QLE, as done in Section 1.3 and Section 2.4, which are

*Non-linear equations of motion*

$$\dot{\hat{a}} = -\frac{\kappa}{2}\hat{a} - \imath\Omega_c\,\hat{a} + \imath\sqrt{2}g_0\hat{q}\hat{a} + \sqrt{\kappa_1}\hat{a}_{in,1} + \sqrt{\kappa_2}\hat{a}_{in,2}, \tag{3.7a}$$

$$\dot{\hat{a}}^\dagger = -\frac{\kappa}{2}\hat{a}^\dagger + \imath\Omega_c\,\hat{a}^\dagger - \imath\sqrt{2}g_0\hat{q}\hat{a}^\dagger + \sqrt{\kappa_1}\hat{a}^\dagger_{in,1} + \sqrt{\kappa_2}\hat{a}^\dagger_{in,2}, \tag{3.7b}$$

$$\dot{\hat{q}} = \Omega_m\hat{p}, \tag{3.7c}$$

$$\dot{\hat{p}} = -\Omega_m\hat{q} - \Gamma_m\hat{p} + \sqrt{2}g_0\hat{a}^\dagger\hat{a} + \sqrt{2\Gamma_m}\hat{\xi}. \tag{3.7d}$$

The initial state is assumed to be separable, with the mechanics in a thermal state and the cavity in the ground state. The radiation pressure force, proportional to the photon number $\hat{a}^\dagger\hat{a}$, makes these equations non-linear, thus hard to solve analytically. In many cases however, the non-linearity has a small contribution to the dynamics, which can be described in a linearized regime.

#### 3.2.2.1 *Mean-field steady-state solution*

The optomechanical system is usually driven through one of the cavity ports by a strong coherent external field, from a laser. Here, we assume that it is injected through port 1. This coherent field is modelled by the mean complex amplitude of the input field $\hat{a}_{in,1}$, i. e.

$$\langle\hat{a}_{in,1}\rangle = \bar{a}_{in}e^{-\imath(\Omega_L t+\theta_{in})}, \tag{3.8}$$

where $\Omega_L$ is the laser frequency and $\theta_{in}$ an explicit phase term, which arises from the adopted convention of taking the cavity field as the phase reference. The absolute value of Equation 3.8 is related to the laser optical power, $P_{in}$, via $\bar{a}_{in} = \sqrt{P_{in}/(\hbar\Omega_L)}$. To make the driving term time-independent, we switch to a frame rotating at the laser frequency, $\Omega_L$. Then, the cavity field rotates at the detuning frequency, $\Delta = \Omega_L - \Omega_c$. Under this continuous driving, the optomechanical steady-state solution can be found by putting the time derivatives to zero in Equation 3.7 and taking the quantum expectation value over

the initial state. The solutions for the cavity amplitude, $\bar{a}$, and the mechanical displacement, $\bar{q}$, are

$$\bar{a} = \frac{\sqrt{\kappa_1}}{\sqrt{\left(\frac{\kappa}{2}\right)^2 + \left(\Delta + \sqrt{2}g_0\bar{q}\right)^2}}\bar{a}_{in}, \tag{3.9a}$$

$$\bar{q} = \frac{\sqrt{2}g_0}{\Omega_m}\bar{a}^2. \tag{3.9b}$$

*Steady-state solution*

Choosing the cavity field as a phase reference implies that $\bar{a}$ is real and that the input field phase should satisfy

$$\theta_{in} = \arctan\left(\frac{\Delta + \sqrt{2}g_0\bar{q}}{\kappa/2}\right). \tag{3.10}$$

One can find the steady-state solution by solving the coupled non-linear Equation 3.9. They form a pair of known equations, which can lead to the appearance of phenomena like the *static bistability*. The optical power, built up in the cavity, exerts a static, net radiation pressure force on the membrane, which consequently displaces to a new rest position, $\bar{q}$. However according to Equation 3.5, this leads to a new cavity resonance frequency, thus a different detuning, $\tilde{\Delta} = \Delta + \sqrt{2}g_0\bar{q}$, and a different intracavity intensity, $\bar{n}_{cav} = \bar{a}^2$. The effective potential experienced by the membrane deforms and shows multiple stable solutions under certain circumstances. In the following we always choose to operate in a regime where bistability does not occur.

Also, we finally notice that the new displaced rest position $\bar{q}$ changes the optomechanical parameters, as described in Section 3.2.1. However, this shift remains always much smaller than the optical wavelength, thus has no significant effect in the $2k_c z_m$ space. For instance, under the typical conditions of the experiments described in this thesis, the steady-state displacement is $\bar{q} \sim \mathcal{O}(10^3)$, which corresponds to few pm.

#### 3.2.2.2 *Linearized dynamics of the fluctuations*

Away from the bistable regime, we can displace the cavity and mechanical operators by their average value, i. e. $\hat{a} \to \bar{a} + \hat{a}$ and $\hat{q} \to \bar{q} + \hat{q}$. The operators $\hat{a}, \hat{q}$ are now interpreted as fluctuations around their mean values. If the frequency shift, $g_0$, caused by a mechanical resonator in the ground state is smaller than the cavity linewidth, i. e. $g_0 \ll \kappa$, these fluctuations can be considered small compared to the mean values. Then, higher order terms in the fluctuation operators appearing in Equation 3.7 can be neglected. The linearized equations of motion are

*Linearized equations of motion*

$$\dot{\hat{X}} = -\frac{\kappa}{2}\hat{X} - \tilde{\Delta}\hat{Y} + \sqrt{\kappa_1}\hat{X}_{in,1}^{\theta_{in}} + \sqrt{\kappa_2}\hat{X}_{in,2}, \tag{3.11a}$$

$$\dot{\hat{Y}} = -\frac{\kappa}{2}\hat{Y} + \tilde{\Delta}\hat{X} + 2g\hat{q} + \sqrt{\kappa_1}\hat{Y}_{in,1}^{\theta_{in}} + \sqrt{\kappa_2}\hat{Y}_{in,2}, \tag{3.11b}$$

$$\dot{\hat{q}} = \Omega_m \hat{p}, \tag{3.11c}$$

$$\dot{\hat{p}} = -\Omega_m \hat{q} - \Gamma_m \hat{p} + 2g\hat{X} + \sqrt{2\Gamma_m}\hat{\xi}, \tag{3.11d}$$

where $\hat{X}$ and $\hat{Y}$ are the cavity field quadrature operators, such that $\hat{a} = (\hat{X} + \imath\hat{Y})/\sqrt{2}$, $\tilde{\Delta} = \Delta + \sqrt{2}g_0\overline{q}$ is the effective detuning and $g \coloneqq g_0\overline{a}$ is the *field-enhanced optomechanical coupling rate*. In the following, we will refer to the effective detuning simply as $\Delta$, for the sake of notation conciseness. The linearization procedure corresponds to adopting the linearized, bi-linear Hamiltonian

$$\hat{H}_{int,\,lin} = -2\hbar g\hat{q}\,\hat{X}, \tag{3.12}$$

a well known linear interaction between coupled harmonic oscillators, in our case the optical cavity field and the vibrating membrane.

The linear Equation 3.11 can be recast in a simple matrix form as $\dot{\hat{\mathbf{x}}} = A\hat{\mathbf{x}} + \hat{\mathbf{n}}$, with the system's observables vector $\hat{\mathbf{x}} = (\hat{X}, \hat{Y}, \hat{q}, \hat{p})^T$ and the noise vector $\hat{\mathbf{n}} = (\sqrt{\kappa 1}\hat{X}_{in,1}^{\theta_{in}} + \sqrt{\kappa 2}\hat{X}_{in,2}, \sqrt{\kappa 1}\hat{Y}_{in,1}^{\theta_{in}} + \sqrt{\kappa 2}\hat{Y}_{in,2}, 0, \sqrt{2\Gamma_m}\hat{\xi})^T$. The matrix $A$ is called the drift matrix, according to the nomenclature derived in Section 1.7, and describes the unitary and dissipative dynamics. In particular, the optomechanical system is stable, and thus reaches a stationary steady-state when all the real parts of the drift matrix eigenvalues are negative. Based on this, stability criterion can be found. Importantly, it turns out that the dynamics remains stable if a non-positive detuning, $\Delta$, is chosen, as far as static bistablity is avoided.

*Stability condition*

For stable systems, Equation 3.11 can be solved ignoring any transient by taking their Fourier transform. In a matrix notation, the solution corresponds to $\hat{\mathbf{x}}(\Omega) = (-A - \imath\Omega\mathbb{1})^{-1}\,\hat{\mathbf{n}}(\Omega)$. This can be further used to calculate the PSD of the system's observable and the output fields, obtained via the input-output relation Equation 1.13.

Finally, we notice that the linear dynamics and the white input noise assures that the optomechanical state remains Gaussian throughout the evolution. Then, it can be fully characterized only by the first two statistical moments of the system's observables.

### 3.2.3 *Equations of motion: Schrödinger picture*

The optomechanical dynamics can also be described in the Schrödinger picture. Here, dissipations can be described by means of a master equation. However, we have seen in Section 2.4 that the quantum Brownian process leads to non-Markovian dynamics, which cannot be described by a Lindblad master equation. This problem can be circumvented for a mechanical resonator with high quality factor, $Q \gg 1$, and high temperature, $k_B T \gg \hbar\Omega_m$. Within these limits and the rotating wave

approximation (RWA), the mechanical dynamics becomes Markovian and a Lindblad master equation is recovered. When combined with the optical mode and the linearized optomechanical interaction, one finds

$$\dot{\hat{\rho}} = \frac{1}{\imath\hbar}\left[\hat{H}, \hat{\rho}\right] + \kappa\mathcal{D}[\hat{a}]\hat{\rho} + \Gamma_m\left(\overline{n}_{th} + 1\right)\mathcal{D}[\hat{b}]\hat{\rho} + \Gamma_m\overline{n}_{th}\mathcal{D}[\hat{b}^\dagger]\hat{\rho}, \quad (3.13)$$

where $\hat{\rho}$ is the optomechanical state, $\hat{b} = (\hat{q} + \imath\hat{p})/\sqrt{2}$ is the mechanical amplitude and $\hat{H}$ includes both the systems and the interacting Hamiltonians. The initial separable state is $\hat{\rho}(0) = |0\rangle\langle 0|_c \bigotimes \hat{\rho}_m^{th}$, where $\hat{\rho}_m^{th}$ is the mechanical thermal state, with average phonon number $\overline{n}_{th}$.

An interesting limit is when the cavity mode evolves much faster than the mechanics and the interaction, i. e. $\kappa \gg \Omega_m, g$. In this case the cavity can be adiabatically eliminated [Hof17], reducing the problem effectively to a description of the mechanical mode only. In a frame rotating at the mechanical resonance frequency, $\Omega_m$, the effective mechanical master equation is

*Cavity adiabatic elimination*

$$\dot{\hat{\rho}}_m = -\imath\left[\delta\Omega_m\hat{b}^\dagger\hat{b}, \hat{\rho}_m\right] + \Gamma_-\mathcal{D}[\hat{b}]\hat{\rho}_m + \Gamma_+\mathcal{D}[\hat{b}^\dagger]\hat{\rho}_m, \quad (3.14)$$

where $\hat{\rho}_m$ is the mechanical state density matrix. The radiation pressure force induces a shift of the mechanical resonance frequency, known as *optical spring effect* and equals to

$$\delta\Omega_m = \frac{\Delta + \Omega_m}{\kappa}A_+ + \frac{\Delta - \Omega_m}{\kappa}A_-. \quad (3.15)$$

where $A_\pm = g^2|\chi_c(\pm\Omega_m)|^2$ are the optomechanical Stokes/anti-Stokes scattering rates and $\chi_c$ the cavity susceptibility as defined in Equation 1.5.

From a comparison of the dissipation terms in Equation 3.14 and in Equation 3.13, we define the effective mechanical energy decay rate and the average phonon occupation as

$$\Gamma_{eff} = \Gamma_- - \Gamma_+ = \Gamma_m + \Gamma_{opt}, \quad (3.16a)$$

$$\overline{n}_{eff} = \frac{\Gamma_+}{\Gamma_- - \Gamma_+} = \frac{\Gamma_m\overline{n}_{th} + \Gamma_{opt}\overline{n}_{opt}}{\Gamma_m + \Gamma_{opt}}, \quad (3.16b)$$

with the rates

$$\Gamma_\pm = A_\pm + \Gamma_m\left(\overline{n}_{th} + \frac{1}{2} \mp \frac{1}{2}\right). \quad (3.17)$$

In Equation 3.16 we have introduced the additional decay rate, $\Gamma_{opt} = A_- - A_+$, known as the *optical damping rate*, and $\overline{n}_{opt} = A_+/(A_- - A_+)$, which is the *effective optical bath occupation*.

## 3.3 CONSEQUENCES FOR THE MECHANICAL SYSTEM

The optomechanical effects on the mechanical system can be alternatively derived from the solution of Equation 3.11, obtained in the Fourier domain. The mechanical displacement is fully characterized by its average value, $\overline{q}$, and by the PSD of the fluctuations $\hat{q}$, whose symmetrized version is

$$\overline{S}_{\hat{q}\,\hat{q}}(\Omega) = |\chi_{\mathrm{eff}}(\Omega)|^2\, \overline{S}^{\mathrm{tot}}_{\mathrm{FF}}(\Omega), \tag{3.18}$$

where we have introduced the total force noise PSD,

$$\overline{S}^{\mathrm{tot}}_{\mathrm{FF}}(\Omega) = \overline{S}_{\mathrm{qba}}(\Omega) + \overline{S}_{\mathrm{th}}(\Omega), \tag{3.19}$$

and the effective mechanical susceptibility, $\chi_{\mathrm{eff}}(\Omega)$.

The first optomechanical effect we notice is indeed a modification of the bare susceptibility, $\chi_m$, as defined in Equation 2.20–here used in terms of dimensionless units, see Section 2.4. The new effective susceptibility is

$$\chi_{\mathrm{eff}}(\Omega)^{-1} = \chi_m(\Omega)^{-1} - \imath\frac{2g^2}{\sqrt{\kappa}}\left[\chi_c(\Omega) - \chi_c(-\Omega)^*\right], \tag{3.20}$$

*Dynamical backaction*

due to the radiation pressure force. On one side, this force modifies the conservative potential landscape in which the mechanical resonator moves, by changing its stiffness. This leads to a shift, $\delta\Omega_m$, of the mechanical resonance frequency, known as optical spring effect. For a high-Q resonators, the second term on the right hand side (RHS) of Equation 3.20 can be considered constant over the mechanical resonance, i. e. $\Omega = \Omega_m$, and the shift is expressed by Equation 3.15.

On the other side, the radiation pressure force does not instantaneously act, but is retarded due to the presence of the optical cavity. For a detuning different from zero, the optical phase quadrature, proportional to the mechanical displacement, is partially rotated into the amplitude quadrature, which is responsible for the radiation pressure force (cf. Equation 3.11). Then, a component of this force is proportional to the displacement of resonator at *previous* time, yielding a viscous force, thus additional damping. For a high-Q resonator, this optical damping rate can be approximated by $\Gamma_{\mathrm{opt}}$, derived in Equation 3.16.

The dynamical backaction can be controlled by the power and the detuning of the laser. For *red detunings*, i. e. $\Delta < 0$, the optical damping is positive and increases the overall dissipation rate; conversely for *blue detunings*, i. e. $\Delta > 0$, the radiation pressure force compensates for the mechanical dissipation, leading to an overall reduction of the damping rate. Eventually, this damping rate can become zero, leading to no energy decay and thus unbounded motion. This represents the typical scenario of dynamical instabilities, which would preclude continuous operation of the system, thus the achievement of a steady-state.

The other optomechanical effect on the mechanical motion is the introduction of an additional fluctuating force, as shown in Equation 3.18 and Equation 3.19. This adds to the usual Brownian force noise, the symmetrized PSD of which is, from Equation 2.26,

$$\bar{S}_{th}(\Omega) = 2\Gamma_m \bar{S}_{\hat{\xi}\hat{\xi}}(\Omega) \approx 2\Gamma_m \left(\bar{n}_{th}(\Omega_m) + 1/2\right), \tag{3.21}$$

where the approximation holds for a high-Q mechanical resonator, for which the susceptibility is higly peaked around $\Omega_m$ and the force noise can be considered constant there around.

*Quantum backaction fluctuations*

The additional force noise arises from fluctuations in the radiation pressure force. If the input optical field contains no excess noise, then such fluctuations are generated by the vacuum fluctuations, which drive the optical cavity mode. The variance of such vacuum fluctuations is expressed by the two-time correlation function in Equation 1.14. Then, the additional force noise PSD on the mechanical resonator is

$$\bar{S}_{qba}(\Omega) = g^2 \left(|\chi_c(\Omega)|^2 + |\chi_c(-\Omega)|^2\right), \tag{3.22}$$

usually referred to as the *quantum backaction noise*. As we will see, the optical field is continuously performing a displacement measurement on the mechanical resonator. Then, quantum physics imposes that this measurement should introduce a disturbance on the system, via a backaction mechanism, as expressed by the Heisenberg measurement-disturbance relations in Equation 1.59. In the optomechanical context, this backaction mechanism is accomplished by the fluctuating radiation pressure force.

*Effective mechanical energy*

In absence of optomechanical interaction, the mechanical system is in thermal equilibrium with a bath at temperature T. The average mechanical energy can be calculated from the equipartition theorem, which states that any conjugate observable shares the same energy content, corresponding to $k_B T/2$. For a mechanical resonator, the average energy is then $\bar{E} = k_B T = \hbar\Omega_m(\bar{n}_{th} + 1/2)$, where the temperature can be equivalently expressed in terms of average phonon number, $\bar{n}_{th}$.

When we turn on the optomechanical interaction, the quantum backaction noise displaces the mechanical system away from thermal equilibrium and increases its energy. As a consequence, the equipartition theorem does not hold anymore and the mechanical energy should be computed as a quantum expectation value over the mechanical state, i.e. $\bar{E} = \langle \hat{H} \rangle$ [Gen+08a]. This energy can be equivalently expressed in terms of an effective average phonon occupation as $\bar{n}_{eff} = \bar{E}/(\hbar\Omega_m) - 1/2$. The effective phonon occupation is usually interpreted as the average phonon occupation of a single, effective thermal bath in contact with the mechanical system and it is used to define an effective temperature.

For a mechanical resonator, undergoing optomechanical interaction, we have

$$\bar{n}_{\text{eff}} = \frac{\langle \hat{q}^2 \rangle + \langle \hat{p}^2 \rangle - 1}{2} = \int_0^\infty \frac{d\Omega}{2\pi} \left(1 + \frac{\Omega^2}{\Omega_m^2}\right) \bar{S}_{\hat{q}\hat{q}}(\Omega) - \frac{1}{2}, \quad (3.23)$$

where we have use the fact that $\hat{p}(\Omega) = -i\Omega\hat{q}(\Omega)$, from the Fourier transform of Equation 9.5c. For a high-Q resonator, one can assume that $\langle \hat{q}^2 \rangle \approx \langle \hat{p}^2 \rangle$, leading to the simpler expression

$$\bar{n}_{\text{eff}} \approx \frac{2\langle \hat{q}^2 \rangle - 1}{2} = \int_0^\infty \frac{d\Omega}{\pi} \bar{S}_{\hat{q}\hat{q}}(\Omega) - \frac{1}{2}. \quad (3.24)$$

Inserting Equation 3.18 in Equation 3.24 we obtain the effective phonon occupation

$$\bar{n}_{\text{eff}} = \frac{\Gamma_{\text{opt}}\bar{n}_{\text{opt}} + \Gamma_m \bar{n}_{\text{th}}}{\Gamma_m + \Gamma_{\text{opt}}}, \quad (3.25)$$

which is the average between the thermal bath occupation, $\bar{n}_{\text{th}}$, and effective optical bath occupation, $\bar{n}_{\text{opt}}$, weighted with the respective coupling rates, $\Gamma_m$ and $\Gamma_{\text{opt}}$. This is in agreement with Equation 3.14, where

$$\bar{n}_{\text{opt}} = \frac{|\chi_c(-\Omega_m)|^2}{|\chi_c(\Omega_m)|^2 - |\chi_c(-\Omega_m)|^2}. \quad (3.26)$$

*Decoherence rates and quantum cooperativity*

The thermal and optical baths destroy the coherence present in the mechanical state, by introducing uncorrelated bath phonons into the dynamics. The typical rate at which a single phonon from the bath is absorbed by a mechanical resonator in the ground state is called the *decoherence rate*. We define the *thermal decoherence rate* as $\gamma = \Gamma_m(\bar{n}_{\text{th}} + 1/2)$ and the optical, or *quantum backaction decoherence rate*, as $\Gamma_{\text{qba}} = \Gamma_{\text{opt}}(\bar{n}_{\text{opt}} + 1/2)$. Their ratio, known as *quantum cooperativity*, forms a useful figure of merit for the appearance of quantum effects. It is defined as

$$\mathcal{C}_q := \frac{\Gamma_{\text{qba}}}{\gamma} = \frac{\bar{S}_{\text{qba}}(\Omega_m)/2}{\bar{S}_{\text{th}}(\Omega_m)/2}, \quad (3.27)$$

where, in the last equality, we connect the decoherence rates back to their spectral definitions. Based on this figure of merit, one can outline two qualitatively different regimes:

$\mathcal{C}_q \ll 1$: The thermal decoherence dominates over the quantum backaction, which can thus be neglected. The effective mechanical occupation, according to Equation 3.25, is $\bar{n}_{\text{eff}} \approx \bar{n}_{\text{th}}\Gamma_m/(\Gamma_m + \Gamma_{\text{opt}})$. For $\Gamma_{\text{opt}} > 0$, which happens whenever $\Delta < 0$, the final occupation is reduced below the thermal one, therefor the effective temperature is lowered, leading to an *optical cooling effect*, known also as *sideband cooling*. This cooling can be enhanced by increasing the optomechanical coupling $g$. Eventually, the quantum backaction decoherence rate becomes significant and the system enters a different regime.

$\mathcal{C}_q \gg 1$: The quantum backaction decoherence now dominates over the thermal one. The effective mechanical occupation becomes $\bar{n}_{eff} \approx \bar{n}_{opt}\Gamma_{opt}/(\Gamma_m + \Gamma_{opt})$. For many situations one has $\Gamma_{opt} \gg \Gamma_m$ and the bare mechanical damping rate can be neglected. Then, the mechanical resonator fully thermalizes to the effective optical bath and $\bar{n}_{eff} \approx \bar{n}_{opt}$. This effective occupation, calculated in Equation 3.26, is determined by few parameters, as $\kappa$, $\Delta$ and $\Omega_m$, and is independent of the optomechanical coupling, $g$. This occupation represents the ultimate limit of sideband cooling, known as *quantum backaction limit*, or *sideband cooling limit* [Wil+07; Mar+07; Pet+16].

## 3.4 DISPLACEMENT MEASUREMENTS

So far, we have focused on the optomechanical effects arising in the mechanical resonator. However, this system is ultimately inaccessible to the experimenter, which can only perform measurements on the output optical fields outside the cavity. We now turn our attention to such fields and to the signatures of mechanical motion they carry. From Equation 3.11, we notice that the phase quadrature of the cavity field, $\hat{Y}$, is displaced by an amount proportional to the mechanical displacement, $\hat{q}$. This phase quadrature couples to the external output field, on which a measurement can be performed. This will effectively realize a mechanical displacement measurement [BK92], as we will see.

### 3.4.1 *Standard phase detection*

Let's first consider the case of a measurement on the output phase quadrature from a resonantly driven optomechanical cavity, $\Delta = 0$. In particular, we assume that the measurement is performed on the transmitted field, i. e. the output field from port 2. Experimentally, this can be achieved by directing the transmitted field to a BHD. The transmitted phase quadrature, obtained from the Fourier transform of Equation 3.11 and the input-output relation Equation 1.13, is

*Transmitted phase quadrature*

$$\hat{Y}_{out} = \underbrace{2g\sqrt{\eta_c}\chi_{c,0}(\Omega)\hat{q}}_{\text{mechanical displacement}} + \underbrace{\sqrt{(1-\eta_c)\eta_c\kappa}\chi_{c,0}(\Omega)\hat{Y}^{\theta_{in}}_{in,1} + \left(\eta_c\sqrt{\kappa}\chi_{c,0}(\Omega) - 1\right)\hat{Y}_{in,2}}_{\text{imprecision noise}}, \quad (3.28)$$

proportional to the mechanical displacement, $\hat{q}$, with $\eta_c = \kappa_2/\kappa$ the cavity overcoupling and $\chi_{c,0}(\Omega)$ the cavity susceptibility at $\Delta = 0$.

The latter two terms in Equation 3.28 are the fluctuating phase quadratures of the input fields. They hinder the inference of the displacement $\hat{q}$ from the measured phase, limiting the measurement

precision. As such, they are called the *measurement imprecision noise*. For an ideal laser source with no excess noise, these input phase noises, $\hat{Y}_{in,i}$, represent vacuum fluctuations, with correlation function given by Equation 1.14.

The imprecision noise is strictly related to the quantum backaction noise. Both arise from vacuum fluctuations present in orthogonal quadratures of the input optical fields. The fluctuations in these quadratures, according to quantum mechanics, satisfy the Heisenberg uncertainty relation. This implies an analogous relation between the imprecision and quantum backaction noise, as we will see soon. Intuitively, when the imprecision noise becomes comparable to, or less than the typical size of the mechanical ground state wavefunction, one expects the appearance of a significant disturbance on its momentum, in order to satisfy the Heisenberg relation uncertainty. It is the quantum backaction noise, in the form of a fluctuating force, which plays the role of this disturbance.

The PSD of Equation 3.28 can be calculated from the spectrum of the BHD photocurrent. Including detection inefficiencies and normalizing it to the shot noise, as discussed in Section 1.4.2, the measured spectrum becomes

$$\bar{S}_{ii}(\Omega) = 1 + \bar{S}_{imp}(\Omega)^{-1}|\chi_m(\Omega)|^2\left(\bar{S}_{th}(\Omega) + \bar{S}_{qba}(\Omega)\right), \tag{3.29}$$

where

$$\bar{S}_{imp}(\Omega) = \frac{1}{32\eta g^2/\kappa}\left(1+\left(\frac{2\Omega}{\kappa}\right)^2\right) = \frac{1}{8\Gamma_{meas}}\left(1+\left(\frac{2\Omega}{\kappa}\right)^2\right), \tag{3.30a}$$

$$\bar{S}_{qba}(\Omega) = \frac{8g^2}{\kappa}\left(1+\left(\frac{2\Omega}{\kappa}\right)^2\right)^{-1} = 2\Gamma_{qba}\left(1+\left(\frac{2\Omega}{\kappa}\right)^2\right)^{-1}, \tag{3.30b}$$

and $\eta := \eta_l\eta_{qe}v^2\eta_c$ is the total efficiency, which contains both the total detection efficiency (optical losses, photodetectors quantum efficiency and visibility) and the cavity overcoupling $\eta_c$ and we have defined the *measurement rate* $\Gamma_{meas} := \eta\Gamma_{qba}$ [Cle+10].

This measured PSD can be calibrated into displacement units in order to infer the mechanical displacement spectrum. This corresponds to calibrate out the transduction factor $\bar{S}_{imp}^{-1}(\Omega)$ from Equation 3.29, yielding

$$\bar{S}^{inf}_{\hat{q}\hat{q}}(\Omega) = \bar{S}_{imp}(\Omega) + |\chi_m(\Omega)|^2\left(\bar{S}_{th}(\Omega) + \bar{S}_{qba}(\Omega)\right). \tag{3.31}$$

The interpretation of $\bar{S}_{imp}$, arising from the imprecision noise terms, becomes now clear: spectrally, it represents the background floor of the spectrum of the inferred mechanical displacement, $\bar{S}^{inf}_{\hat{q}\hat{q}}(\Omega)$. This

imprecision, compared to the mechanical displacement signal, can be reduced by increasing the quantum backaction decoherence rate $\Gamma_{qba}$, sometimes referred to as the *measurement strength* in the context of displacement measurements.

*Heisenberg measurement-disturbance relation*

As pointed out earlier, the imprecision noise is not independent from the quantum backaction noise. From Equation 3.30 we observe that the product of their spectral value is lower bounded by

$$\bar{S}_{imp}(\Omega)\,\bar{S}_{qba}(\Omega) = \frac{1}{4\eta} \geqslant \frac{1}{4}, \tag{3.32}$$

which suggests that an increase in the measurement precision is always accompanied by a non-zero amount of disturbance, in the form of quantum backaction noise. Equation 3.32 is part of a class of inequalities, known as *Heisenberg measurement-disturbance relations* [BK92; WM10; AKM14; BM16] in the context of quantum measurement theory and it represents the optomechanical form of the more general LMI Equation 1.59. This is a genuine quantum bound, as measurements with unlimited precision without disturbance are perfectly allowed by classical physics.

In the context of quantum measurements, the important figure of merit is represented by the *measurement efficiency* [Cle+10], that is, the ratio between the information acquired from the measurement and the total disturbance on the system under measurement. In terms of measurement and decoherence rates, it can be defined as

*Measurement efficiency*

$$\eta_{meas} = \frac{\Gamma_{meas}}{\Gamma_{qba} + \gamma + \gamma_{add}}, \tag{3.33}$$

where $\gamma_{add}$ is any additional mechanical decoherence, e. g. the one coming from excess classical noise of from an unmonitored populated cavity mode. In the case of no additional decoherence, $\gamma_{add} = 0$, inserting the definitions of the measurement and quantum backaction rates in Equation 3.34 we find

$$\eta_{meas} = \frac{\eta}{1 + \mathcal{C}_q^{-1}}. \tag{3.34}$$

The Heisenberg measurement-disturbance relation, Equation 3.32, is equivalently expressed as

$$\eta_{meas} \leqslant 1, \tag{3.35}$$

as expected for an efficiency. The measurement efficiency is important as $\eta_{meas} \approx 1$ is the hallmark of measurement-based quantum effects. This is a stronger condition than what we have derived for quantum effects in the mechanical resonator, for which $\mathcal{C}_q \gg 1$ is required. Here, one also needs a large total efficiency, $\eta \approx 1$.

#### 3.4.1.1 *Limit of standard measurements*

The Heisenberg relation, Equation 3.32, also defines an important limit for sensors based on continuous displacement measurements, as in Equation 3.31. Let's suppose that an unknown force, $f$, couples to the mechanical resonator. A standard displacement measurement assumes a resonant laser and a phase quadrature detection. After calibration, the spectrum of the inferred displacement is

$$\overline{S}^{\text{inf}}_{\hat{q}\,\hat{q}}(\Omega) = \overline{S}_{\text{imp}}(\Omega) + |\chi_m(\Omega)|^2 \left(\overline{S}_{\text{th}}(\Omega) + \overline{S}_{\text{qba}}(\Omega) + \overline{S}_{ff}(\Omega)\right), \quad (3.36)$$

where the unknown force, $f$, is supposed to be uncorrelated from all the other sources of noise. If the motion caused by $f$ is the signal we want to measure, then we refer to $|\chi_m|^2\overline{S}_{ff}$ as the spectral *signal*, whereas the remaining terms form a spectral *noise*. Rather, if the unknown force is what we want to measure, we can calibrate out the mechanical susceptibility from Equation 3.36 to obtain the inferred force PSD, i. e. $\overline{S}^{\text{inf}}_{FF} \coloneqq |\chi_m|^{-2}\overline{S}^{\text{inf}}_{\hat{q}\,\hat{q}}$. Then, the same nomenclature and division used in the displacement measurement case for signal and noise holds. In the following we always refer to the case of displacement measurements.

*Spectral noise*

The spectral noise can be broken down in three contributions

$$\overline{S}^{n}_{\hat{q}\,\hat{q}}(\Omega) = \underbrace{\overline{S}_{\text{imp}}(\Omega) + |\chi_m(\Omega)|^2\overline{S}_{\text{qba}}(\Omega)}_{\text{added noise}} + \underbrace{|\chi_m(\Omega)|^2\overline{S}_{\text{th}}(\Omega)}_{\text{intrinsic noise}}, \quad (3.37)$$

where the *added noise* refers to the sum of the imprecision and quantum backaction noise, added by the measuring system, i. e. the coherent optical cavity field, and the *intrinsic noise* refers, instead, to the thermal and zero-point motion, intrinsic in the mechanical resonator and independent from the measuring system. To achieve the ultimate displacement sensitivity, it is important to understand all the sources of noise and minimize their contribution as much as possible. We now provide a description of each term in Equation 3.37, focusing in particular on their dependence on the bath temperature, $T$, the measurement strength, $\Gamma_{\text{qba}}$, and the total efficiency, $\eta$.

INTRINSIC NOISE The intrinsic noise contains fluctuations from both the thermal motion, which depends on the bath temperature $T$, and the zero-point motion, always present even at $T = 0$ K. In a calibrated spectral measurement, Equation 3.36, this noise has a Lorentzian lineshape and does not depend on $\Gamma_{\text{qba}}$ or $\eta$.

IMPRECISION NOISE This is expressed in Equation 3.30a. It can be approximated as a white noise for frequencies within the cavity linewidth. It is inversely proportional to the measurement strength, $\Gamma_{\text{qba}}$, and to the efficiency, $\eta$. In fact, any detector inefficiency corresponds to additional uncorrelated vacuum noise reaching the detector, leading to larger imprecision.

QUANTUM BACKACTION NOISE The mechanical displacement has additional fluctuations induced by the quantum backaction noise, as expressed in Equation 3.30b. This force spectrum can be approximately considered white for frequencies within the cavity linewidth. In this limit, the induced displacement has a Lorentzian lineshape and is proportional to the measurement strength, $\Gamma_{qba}$.

One parameter we can now tune to minimize the added noise is the measurement strength, $\Gamma_{qba}$. Experimentally, this is achieved by changing the driving optical power, proportional to the optomechanical coupling $g^2$. In Figure 3.4 we show all the noise contributions as a function of $\Gamma_{qba}$, at the fixed frequency $\Omega = \Omega_m$. It is clear that there exists a trade-off in the added noise between the imprecision and quantum backaction contributions. The minimum added noise, at the optimal measurement strength $\Gamma_{qba}^{opt} = \Gamma_m/4$ for the ideal total efficiency $\eta = 1$, is known as the *standard quantum limit (SQL)* [Bra68; BK92]. At the mechanical resonance, it corresponds to $\bar{S}^{SQL}_{\hat{q}\hat{q}}(\Omega_m) = 1/\Gamma_m$. It equals the resonant displacement spectrum of a resonator in the ground state, i. e. $\bar{S}^{zp}_{\hat{q}\hat{q}}(\Omega_m) \coloneqq |\chi_m(\Omega_m)|^2\Gamma_m = 1/\Gamma_m$: in this sense, the SQL is equivalent to half of a phonon, which is the energetic content of the ground state. Any inefficiency will precludes achieving this limit.

*Resonant standard quantum limit*

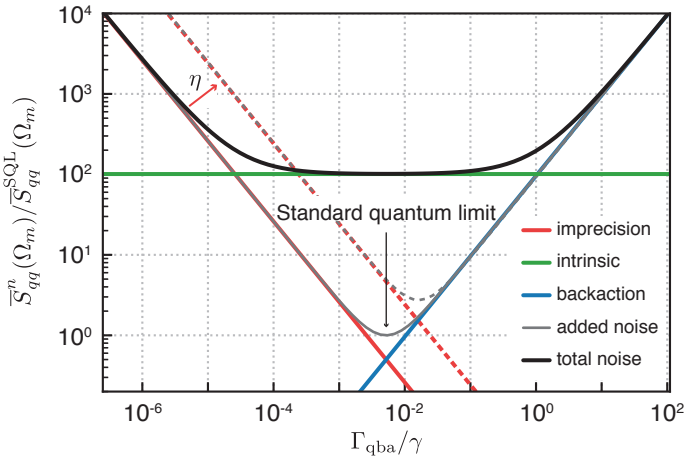


Figure 3.4: Resonant standard quantum limit. The total spectral noise (black), normalized to the SQL, at the mechanical resonance frequency, as a function of the measurement strength $\Gamma_{qba}$, in unit of the thermal decoherence rate $\gamma$. The spectral noise comprises the intrinsic noise (green), as well as the imprecision (red) and quantum backaction (blue) noise. The sum of the latter two is the added noise (gray). Its minimum value, achieved at $\Gamma_{qba}^{opt} = \Gamma_m/4$, is the SQL. Any detection inefficiency leads to a higher imprecision noise (dashed red), thus to a higher minimum added noise. The parameters used are $\kappa/(2\pi) = 10$ MHz, $\Omega_m/(2\pi) = 1$ MHz, $\Gamma_m/(2\pi) = 100$ Hz, $\bar{n}_{th} = 50$.

The SQL represents a very important limit and a benchmark for force and displacement sensors. In the recent decades, several experiments pushed the sensitivity closer and closer to the SQL [LaH+04; Teu+11; Sch+14; Mar+16]. However, it turned out that reaching it is quite challenging, in particular at the mechanical resonance frequency, where the thermal noise is dominant by many orders of magnitude. Then, achieving the SQL also requires to suppress this thermal noise, either via cryogenic techniques or laser cooling.

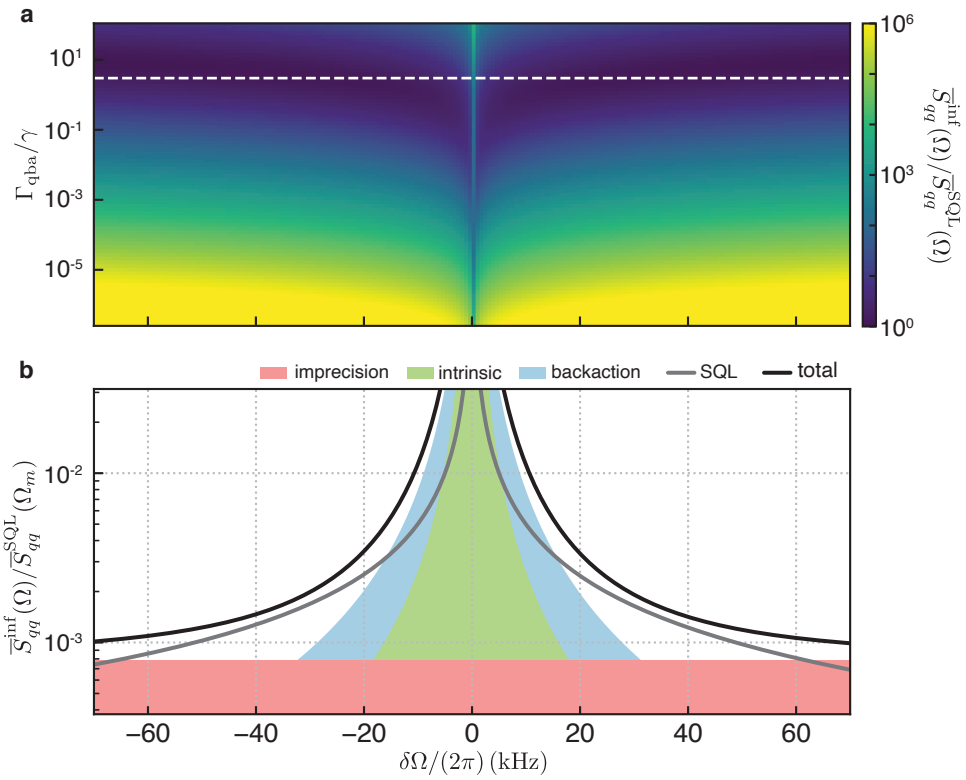


Figure 3.5: Off-resonant standard quantum limit. a, Spectra of the Inferred mechanical displacement, normalized to the corresponding SQL at each frequency, as a function of frequency, $\Omega$, and measurement strength, $\Gamma_{\mathrm{qba}}$, in unit of the thermal decoherence rate $\gamma$. Darker blue corresponds to spectral noise closer to the SQL. b, Spectrum corresponding to the dashed white line in a, at $\Gamma_{\mathrm{qba}} = 3\gamma$, i. e. a quantum cooperativity of $\mathcal{C}_{\mathrm{q}} = 3$. The total spectrum (black) consists of the imprecision (red), intrinsic (green) and quantum backaction noises (blue). Conversely to a, this spectrum is normalized to the resonant SQL. The spectral SQL is shown for reference in gray. Away from the resonance, at $\delta\Omega/(2\pi) \approx 30$ kHz, the quantum backaction and the imprecision noises balance each other and dominate the intrinsic noise, thereby approaching the SQL. The parameters are the same as in Figure 3.4. The parameters used are $\kappa/(2\pi) = 10$ MHz, $\Omega_{\mathrm{m}}/(2\pi) = 1$ MHz, $\Gamma_{\mathrm{m}}/(2\pi) = 100$ Hz, $\overline{n}_{\mathrm{th}} = 50$.

*Spectral standard quantum limit*

The situation is rather different if we consider noise contributions at frequencies off the mechanical resonance. An SQL can be derived

at each frequency, yielding a *spectral* SQL, $\overline{S}^{\mathrm{SQL}}_{\hat{q}\hat{q}}(\Omega) = |\chi_m(\Omega)|$. It rolls off slower than the intrinsic noise. Then, at some frequency range away from the mechanical resonance, the thermal noise contribution becomes negligible and the total spectral noise is only given by the added noise. Balancing the imprecision and quantum backaction noise at these frequencies allows to reach the SQL, as shown in Figure 3.5. Again, the condition for reaching the off-resonant SQL can be cast in terms of a large measurement efficiency, $\eta_{\mathrm{meas}} \approx 1$.

### 3.4.2 *Arbitrary quadrature detection*

So far, we have considered the case of a resonant laser. We now relax this assumption, and calculate the PSD for the general non-resonant case. The non-zero detuning dynamically couples the amplitude and phase quadratures of the cavity field. As a consequence, the information about the mechanical displacement is now distributed over both quadratures. The most general expression for the cross-spectrum of any two quadratures of the transmitted field at angles $\theta$ and $\phi$, normalized to the shot noise, is

$$\overline{S}_{\hat{X}^\theta\hat{X}^\phi}(\Omega) = \cos(\theta-\phi) + \overline{S}^{-1}_{\mathrm{imp}}(\Omega)\overline{S}_{\hat{q}\hat{q}}(\Omega) + 2\overline{S}^{-1}_{\mathrm{imp}}(\Omega)\Re\left[\chi_{\mathrm{eff}}(\Omega)^*\overline{S}_{\mathrm{corr}}(\Omega)\right], \quad (3.38)$$

where the transduction function

$$\overline{S}^{-1}_{\mathrm{imp}}(\Omega) = 2g^2\eta\Re\left[e^{-\imath(\theta-\phi)}\left(|\chi_c(\Omega)|^2 + |\chi_c(-\Omega)|^2\right) - 2e^{-\imath(\theta+\phi)}\chi_c(\Omega)\chi_c(-\Omega)\right] \quad (3.39)$$

generalizes the expression in Equation 3.30a, by taking into account the filtering effect from the cavity susceptibility. Analogously, we can define a generalized *measurement rate* as $\Gamma_{\mathrm{meas}} \coloneqq \overline{S}_{\mathrm{imp}}(\Omega_m)/4$.

The main difference compared to the resonant case is the appearance of a complex correlation term, which is

$$\overline{S}_{\mathrm{corr}}(\Omega) = \frac{\Im\left[e^{-\imath(\theta+\phi)}\chi_c(\Omega)\chi_c(-\Omega)\right] + \imath\Re\left[e^{-\imath(\theta-\phi)}\left(|\chi_c(\Omega)|^2 - |\chi_c(-\Omega)|^2\right)\right]}{\Re\left[-e^{-\imath(\theta-\phi)}\left(|\chi_c(\Omega)|^2 + |\chi_c(-\Omega)|^2\right) + 2e^{-\imath(\theta+\phi)}\chi_c(\Omega)\chi_c(-\Omega)\right]} \quad (3.40)$$

These are correlations between the fluctuations of the imprecision noise and the ones of the displacement induced by the quantum backaction. They are absent in the PSD for a standard phase measurement, Equation 3.29, because, there, the imprecision and quantum backaction noises originate from orthogonal quadratures, respectively the phase and amplitude quadratures.

To infer the mechanical displacement from Equation 3.38, one can calibrate the transduction out in order to obtain

$$\bar{S}^{\text{inf}}_{\hat{q}\,\hat{q}}(\Omega) = \bar{S}_{\text{imp}}(\Omega)\cos(\theta-\phi) + \bar{S}_{\hat{q}\,\hat{q}}(\Omega) + 2\Re\left[\chi_{\text{eff}}(\Omega)^*\bar{S}_{\text{corr}}(\Omega)\right]. \tag{3.41}$$

In this case the measurement added noise satisfies the relation [Cle13]

$$\bar{S}_{\text{imp}}(\Omega)\,\bar{S}_{\text{qba}}(\Omega) \geqslant \frac{1+4|\bar{S}_{\text{corr}}(\Omega)|^2+|1+4\bar{S}_{\text{corr}}(\Omega)^2|}{8}, \tag{3.42}$$

which is a generalization of the Heisenberg measurement-disturbance relation, Equation 3.32, and provides a quantum bound for the correlation strength, which is stronger than the classical bound

$$\bar{S}_{\text{imp}}(\Omega)\,\bar{S}_{\text{qba}}(\Omega) \geqslant |\bar{S}_{\text{corr}}(\Omega)|^2. \tag{3.43}$$

That is, imprecision and backaction noise cannot be zero in the quantum case, even more they cannot be perfectly correlated, as expressed by Equation 3.42.

We finally notice that Equation 3.38 represents the PSD of the arbitrary output quadrature at angle $\theta$, when $\theta = \phi$.

## 3.5 PONDEROMOTIVE CORRELATIONS

Let's now focus on the correlations created in the output field, Equation 3.40. They are created by the mechanical motion and, as such, are known as *ponderomotive correlations* [MT94; Fab+94]. In certain regimes, such correlations become quantum and find use in many applications, ranging from quantum-enhanced sensing to generation of entangled states.

To clarify the meaning of quantum correlations and when they arise, let's consider the PSD from Equation 3.38 with $\theta = \phi$ in the case of a broad, $\kappa \gg \Omega_m$, and resonant, $\Delta = 0$, cavity. Within this regime, the measured optical spectrum is

$$\bar{S}_{\hat{X}^\theta\hat{X}^\theta}(\Omega) = \underbrace{1}_{\text{shot noise}} + \underbrace{16\Gamma_{\text{meas}}\sin^2(\theta)|\chi_m(\Omega)|^2\left(\Gamma_{\text{qba}}+\gamma\right)}_{\text{effective mechanical displacement}} + \underbrace{4\Gamma_{\text{meas}}\Re\left[\chi_m(\Omega)\right]\sin(2\theta)}_{\text{ponderomotive correlations}}. \tag{3.44}$$

An example of such a spectrum is shown in Figure 3.6, as well as its dependence on the detected quadrature angle. The correlation term, Equation 3.40, becomes real and the generalized Heisenberg relation, Equation 3.42, takes the simple form

$$\bar{S}_{\text{imp}}(\Omega)\,\bar{S}_{\text{qba}}(\Omega) \geqslant \frac{1}{4} + \bar{S}_{\text{corr}}(\Omega)^2, \tag{3.45}$$

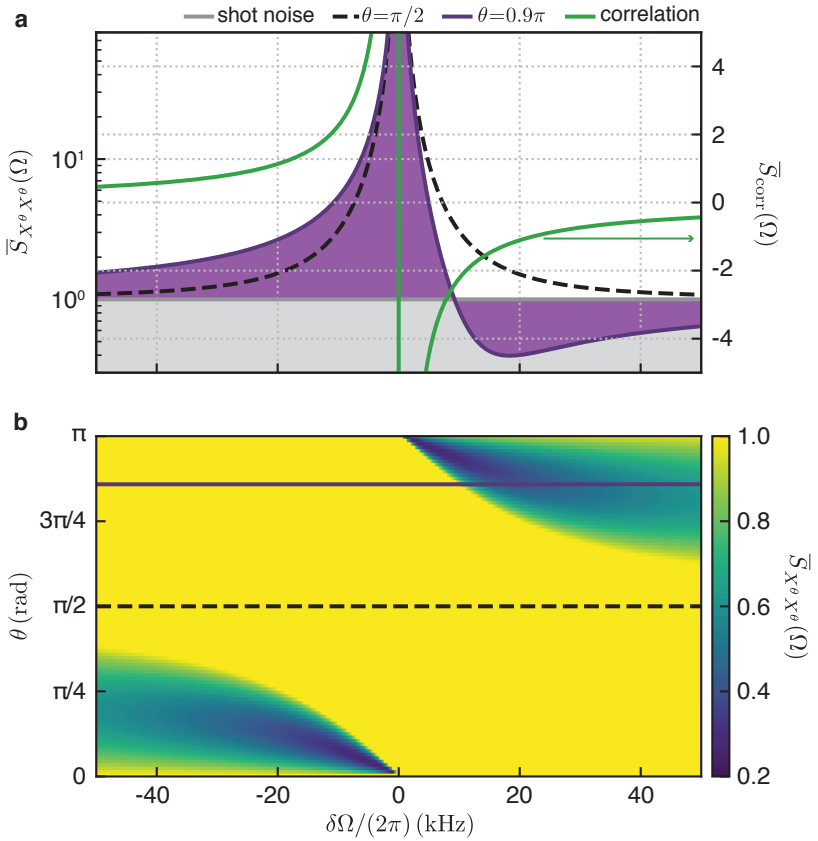


Figure 3.6: Spectrum of ponderomotive squeezing. a, Spectra of the detected output field quadratures, at the phase value $\theta = \pi/2$ (dashed black) and at $\theta = 0.9\pi$ (purple), as well as the shot noise (gray). The correlations appear in the non-phase quadrature as an asymmetric contribution (green). Such ponderomotive correlations lead to noise reduction below the shot noise, i. e. squeezing, at frequencies where they assume a negative value. b, Spectra as a function of the frequency, $\Omega$, and the detected quadrature angle, $\theta$. The amount of squeezing increases from yellow to blue. The dashed (solid) black (purple) line corresponds to the quadrature spectrum at $\theta = \pi/2$ ($0.9\pi$), shown in a.

which poses a bound on the maximum achievable correlation.

As expected, the ponderomotive correlations vanish at the phase quadrature $\theta = \pi/2$. Also, they disappear at the mechanical resonance $\Omega_m$, where the induced displacement has a phase shift of $\pi/2$ compared to the driving force. If the imprecision noise is correlated with the quantum backaction noise, the mechanical motion induced by the latter will be uncorrelated with the imprecision noise. Correlations are observed at frequencies away from the mechanical resonance. Their frequency lineshape is asymmetric and contributes to reduce the spectral noise, whenever it assumes negative values. From Figure 3.6b, it is easy to see that the minimum spectral value is obtained in the limits

$\theta \to 0^+$ and $\Omega \to \Omega_m^-$, or, equivalently, $\theta \to \pi^-$ and $\Omega \to \Omega_m^+$. In these limits, one finds the lower bound

$$\overline{S}_{\hat{X}^\theta \hat{X}^\theta}(\Omega) \geqslant 1 - \eta_{meas}. \tag{3.46}$$

This suggests that, for large measurement efficiency, the fluctuations of the measured optical quadrature can be reduced below the vacuum noise level of 1. The optical state giving raise to this quantum noise reduction is often called a *squeezed state*. In the optomechanical case this noise reduction phenomenon, caused by mechanically induced correlations, is referred to as *ponderomotive squeezing* and was recently experimentally observed [Bro+12; Saf+13].

*Quantum correlations in ponderomotive squeezing*

We can also interpret the spectrum measured by the homodyne detector as a two-mode measurement, as detailed in Section 1.5.1. Then, ponderomotive squeezing can be understood as the verification of the entanglement of a bipartite states, composed of two spectral components mode at $\pm\Omega$, where $\Omega$ is the frequency component in Equation 3.44 showing squeezing. This entangled state is in the form of a two-mode squeezed state and its two-mode intensity correlation function violates a classical Cauchy-Schwarz inequality [WM08]. In this sense, the ponderomotive correlations can become quantum ones.

The entangled spectral components are co-propagating modes of the same field. To find use in entanglement-based applications, one should spatially separate them, e. g. via a frequency discriminator like an optical cavity. A different approach would be, instead, to generate these correlations between modes of two different fields, separated from the beginning. This is indeed possible, and forms the basic idea of the experiment reported in Section 9.2.

# 4

# EXPERIMENTAL TOOLS AND METHODS

In this chapter we transition to reviewing the main experimental tools employed. In the first part we describe the setup, which includes both the optical and electronic components, as well as the mechanical hardware supporting the experiments and the cryogenic environment. In the second part we move to describe the experimental methods we use to measure the main optical and mechanical parameters. In particular, we provide a detailed explanation on how we characterize the optomechanical coupling, of crucial importance for the quantitative calibration of the raw measurements, which are just electric signals from a detector, into displacement units.

## 4.1 EXPERIMENTAL SETUP

In Figure 4.1 we show the conceptual blocks composing our main experimental optical setup. This figure and the description provided here form the general basis for the experiments reported in later chapters, where instead we include just a sketch of the setup. For more details, the reader should refer to this section. The setup comprises three main conceptual blocks: (i) the beam preparation, with the laser sources and the modulations, (ii) the optomechanical cavity, kept cold inside a cryostat, and (iii) the optical detection stage, in turn composed of a monitoring and a measurement part.

### 4.1.1 *Beam preparation*

The main light sources are two commercial continuous-wave (CW) Solstis Ti:shappire (TiS) lasers, from MSquared[1]. They are both pumped by a common CW diode laser at 532 nm, a Sprout-G from Lighthouse Photonics[2], with power up to 10 W. Such pump power determines both the TiS output power and, more importantly, its excess intensity noise characteristics, due to the laser medium relaxation oscillations. For quantum optomechanical experiments it is important to employ a quantum-noise-limited optical field in the frequency range around the mechanical resonance frequency, $\sim 1$ MHz for the experiments hereby reported. Thus, we tune the pump power to achieve the minimum excess noise at these frequencies, guaranteeing at the same time a stable lasing operation. More details on the laser excess noise can be found in Appendix B.

1 m2lasers.com
2 lighthousephotonics.com

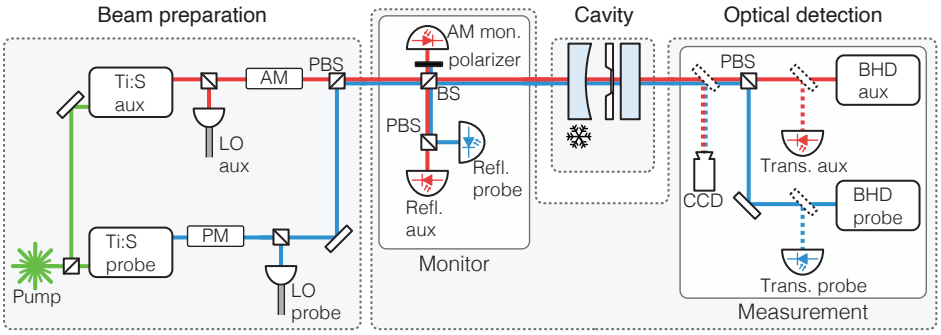


Figure 4.1: Principal elements of the optical experimental setup. From the left, a master diode laser, at 532 nm, is employed to pump two Ti:S lasers. They are subsequently processed by external amplitude and phase modulators to provide useful signals for locks and calibrations. Part of each laser is split and coupled into an optical fiber to provide an LO beam for homodyne detectors. The rest is combined by a polarizing beam-splitter (PBS) and sent to the next stage. Here, a 50 : 50 beam-splitter (BS) is used to monitor both the power through the amplitude modulator and the reflected powers from the optomechanical cavity. The transmitted beams can be measured by means of either a BHD or direct detection, by flipping the mirrors indicated by dashed black contours. Finally, the transmitted beam from the cavity can also be redirected to a charge-coupled device (CCD) to monitor its transverse profile.

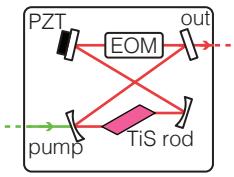


*Inside of a TiS laser*

The active medium of a TiS laser is a sapphire crystal rod, doped with titanium ions and placed inside a bow-tie ring cavity. A combination of an optical diode, a birefringent filter, an etalon and a piezo-translating cavity mirror allows continuous single-mode lasing, tunable over a broad range from ~ 700 nm to ~ 1000 nm. Together with stable optical mountings, this allows ultra-narrow-linewidth of $< 50$ kHz. In order to accurately monitor the laser wavelength, a small fraction of the output light is fiber-coupled into a wavelength-meter with pm precision. A mechanical fiber switch is used to swap the input fiber in the wavelength-meter.

The laser frequency can also be externally fine-tuned by means of a dual piezo, which translates one of the laser cavity mirrors. This provides both a slow (~ 50 Hz, 1.5 GHz/V) and fast (~ 100 kHz, 4 MHz/V) actuation, used to stabilize the frequency detuning between the lasers and the optomechanical cavity, as described later, in Section 4.1.3.1.

*Laser modulations*

We can modulate the laser field amplitude with an external fiber-based amplitude modulator, AM830 from Jenoptik[3]. The on-chip device is composed of a Mach-Zender interferometer with the phase difference electronically controlled via the electro-optic effect. The modulation response function thus has a sinusoidal shape. To obtain a linear response, one has to stabilize the working point in gray-fringe,

3 jenoptik.com

i. e. at phase shift of $\pi/2$. Despite the small size of the chip, passive stability is not sufficient and active stabilization is required [Bec05]. To do that, we split the field transmitted through the modulator and monitor its power via direct detection. The photocurrent forms the error signal for a PI servo. The output feedback signal is used to actuate the bias DC voltage of the modulator, to lock it at the chosen set-point.

We can also perform phase and frequency modulations on the laser. The former is done via a fiber-based modulator, a NIR-MPX800 from iXblue[4], based on the electro-optic effect. The main characteristic of such a device is the DC voltage, $V_\pi$, required to generate a $\pi$-phase shift. For our device, we measure it to be $V_\pi = 3.6$ V [Che20]. The frequency modulation is, instead, achieved by means of an electro-optic modulator (EOM) located directly inside the laser optical cavity.

### 4.1.2 *Optomechanical cavity*

The generated beams are distributed, via optical fibers, to both the homodyne detectors and the optomechanical cavity, which we discuss now. It comprises two high-reflective mirrors and a membrane resonator chip, assembled together in a sample holder kept in vacuum and at low temperature in a cryostat.

#### 4.1.2.1 *Optical cavity*

The optical cavity is formed by two asymmetric mirrors, one flat and the other spherical, with a radius of curvature of 25 mm, separated by a total length of $L \approx 1.6$ mm. The mirrors also differ in the coating specifications, as measured by Nielsen [Nie16] and shown in Figure 4.2a. Combined with our widely tunable lasers, this enables operation of the cavity in very different regimes, e. g. from very low finesse configurations to moderate finesse values and large overcoupling, which are interesting regimes for the experiments later reported.

*Mirror noise*

The mirrors' substrates are cylinders of fused silica, with diameter of 7.75 mm and thickness of 4 mm. They have structural normal modes which vibrate due to their coupling to a thermal bath. This thermal motion is kept relatively small due to the large mass of these normal modes. Nevertheless, this motion introduces fluctuations in the optical cavity length, which is transduced into frequency fluctuations of the transmitted optical field from the cavity. Such ponderomotive frequency noise, which we refer to as *mirror noise*, forms an additive, excess noise when measuring other mechanical motion, e. g. from a membrane in the cavity, and thus limits the achievable displacement sensitivity. It turns out that, for the low sensitivities required in quantum measurement experiments, such mirror noise can play

4 ixblue.com

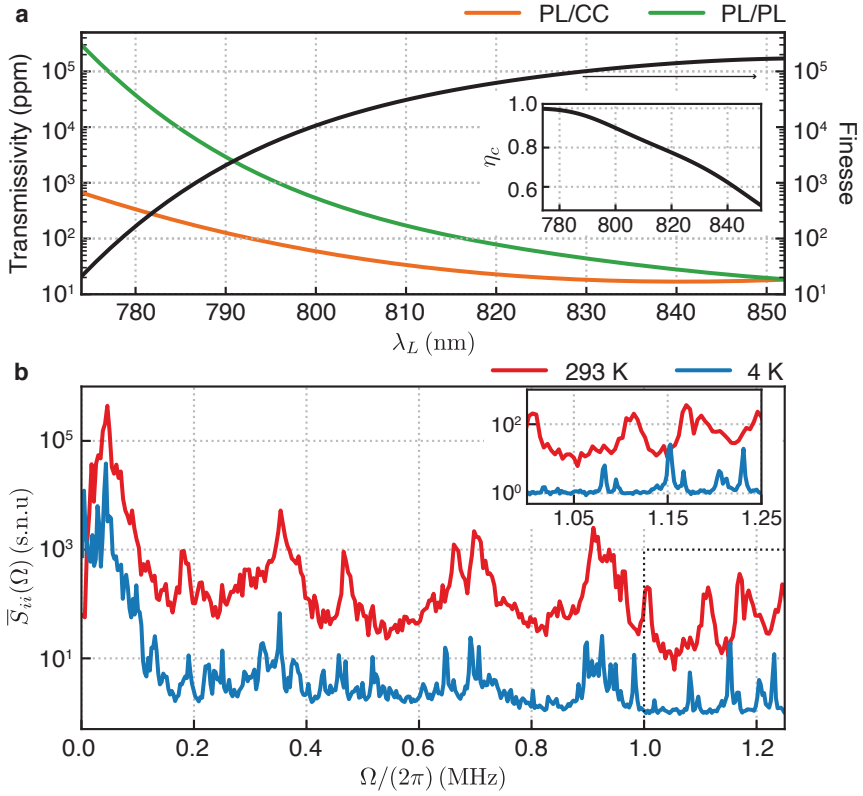


Figure 4.2: Optical and mechanical properties of the cavity mirrors. a, Transmissivity of the spherical (orange) and flat (green) mirrors, and corresponding finesse (black), as a function of the optical wavelength $\lambda$. The inset show the corresponding cavity overcoupling, $\eta_c$. b, Spectra of the amplitude quadrature of a transmitted field through the empty cavity, locked to the side of its resonance, at room (red) and cryogenic (blue) temperature. The observed peaks corresponds to Brownian motion of the vibrational modes of the mirrors' substrates. As they are cooled down the area diminishes and the resonance frequencies shift, as a results of the substrates thermal contraction. The inset shows an enlarged view of the boxed area, which is the spectral region of interest.

an important role and should be taken into account in designing the experiment.

We experimentally characterize the mirror noise by assembling an empty optical cavity and measuring the amplitude quadrature of a transmitted field, locked on the side of a cavity mode. A phenomenological fact is that such mirror noise largely depends on the material in direct contact with the mirrors' substrates. In order to mimic, as close as possible, the conditions in the optomechanical cavity, we assemble an analogous empty cavity in the same way, as described later in Section 4.1.2.3. The only difference, now, is that the membrane chip is replaced by a silicon chip of equal dimensions, with the membrane replaced by a square aperture. In Figure 4.2b we show the spectrum of the measured amplitude quadrature. The substrates' normal modes

appear as peaks at different frequencies, which have been recently verified also by numerical simulations [Mat19]. These measurements are useful as they guide us in choosing the mechanical resonance frequency when designing the membrane resonator. In particular, we choose to work in the region $1.0 \div 1.2$ MHz, where the spectrum becomes relatively quiet.

#### 4.1.2.2 *Membrane resonator*

The mechanical resonator is a soft-clamped membrane [Tsa+17], made of 3.6 mm x 3.6 mm x 20 nm highly-stressed $Si_3N_4$, suspended on top of a 15 mm x 15 mm x 0.5 mm silicon chip, as shown in Figure 4.3a.

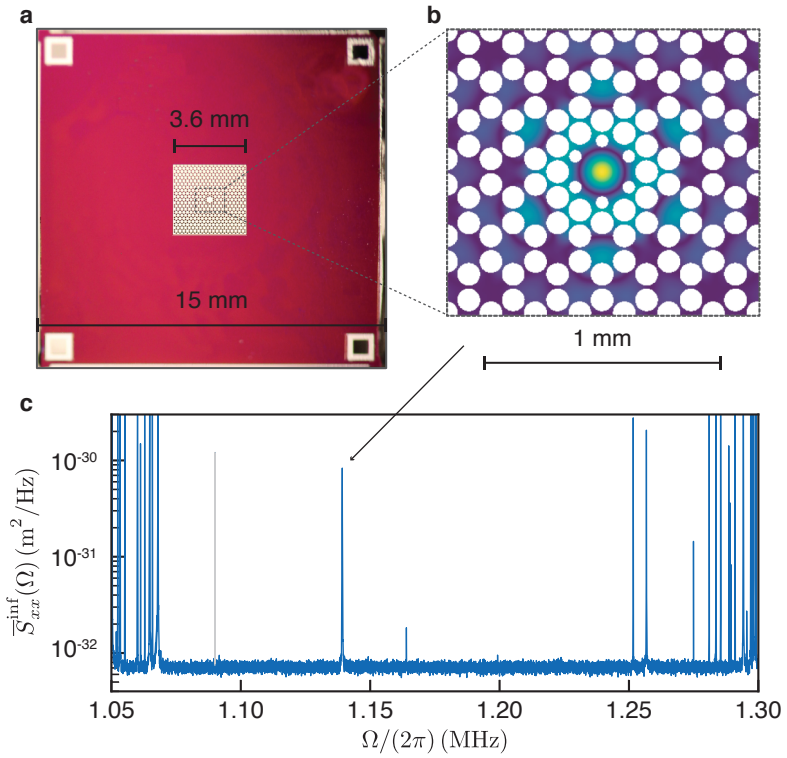


Figure 4.3: Soft-clamped membrane resonator. a, Real picture of a membrane chip. The large red area is the silicon frame, whereas the central white area is the $Si_3N_4$ membrane. The defect is the white spot at its center. Photo by David Mason. b, Simulation of the mode profile of the in-bandgap mode of interest, mostly localized at the defect and soft-clamped as it decays towards the edges. c, Measured mechanical displacement spectrum. The honeycomb structure provides a bandgap, visible from 1.07 MHz to 1.27 MHz. The few in-bandgap modes are localized to the central defect. The black arrow indicates the mode of interest, at 1.14 MHz. The gray peak, at 1.09 MHz, is a phase modulation tone for calibration purposes.

The honeycomb lattice provides a phononic bandgap for out-of-plane modes. The central defect has been engineered to support local-

ized vibrational modes which lie in the bandgap. This prevents their propagation towards the membrane edges, where the mechanical energy is dissipated, via radiation loss, into the supporting silicon frame, as discussed in Section 2.2. When combined with dissipation dilution and soft-clamping, extremely large quality factors of $Q \sim 10^9$ can be achieved for the in-bandgap defect modes at cryogenic temperature. We later focus on a single defect mode, whose mode profile is shown in Figure 4.3b. Unless otherwise stated, when we talk about the mechanical mode, we usually refer to this particular normal mode. The six small holes close to the defect edge allow to push the resonance frequency further towards the bandgap centre [Tsa19], as shown in Figure 4.3c, increasing the shielding from radiation loss.

Achieving a large, clean region in the spectrum around the mechanical mode in the bandgap is crucial for achieving control of that mode. When designing the membrane resonator, one needs to pay attention to other structural defects, which can introduce other modes even inside that bandgap. For example, the boundary between the membrane and the silicon frame requires the pads and tethers to be cut somewhere. These are, then, defects which can sustain vibrational modes, located at the edges. In order to tune their frequencies away from the bandgap and from the mechanical mode, one can shift the boundary line, thus reducing the amount of mass present in those edge defects.

#### 4.1.2.3 *Sample holder*

The membrane is then assembled in the middle of the optical cavity. The sample holder we employ is the result of several iterations and prototypes, efforts of several people over the years [Nie16; Tsa19; Che20]. Its design is based on two requirements: (i) high passive stability, obtained by a monolithic assembly with as few degrees of freedom as possible and (ii) large degree of orthogonality between the membrane surface and the cavity optical axis. The former requirement precludes the use of piezo actuators to tune the cavity length and the membrane position inside the optical cavity. This is necessary for tuning the optomechanical working point, as discussed in Section 3.2.1. Instead, we exploit the wide tuning range of our lasers to achieve such control. This corresponds, for a fixed membrane position $z_m$, to tuning the laser frequency to different longitudinal cavity modes, with wavenumber $k_c$. As already discussed, these different modes will effectively sample a different working point in $2k_c z_m$. In Figure 4.4a we show, in circles, the measured cavity frequency shifts for a sample of 9 subsequent cavity modes, and a fit based on Equation 3.5. From it we extract a FSR of $\Omega_{FSR}/(2\pi) = 93$ GHz, corresponding to a cavity length of $L = 1.6$ mm, and a membrane-mirror separation of $z_m = 0.5$ mm, consistent with the thickness of the silicon spacer used. Also, from the maximum frequency shift, we estimate a membrane thickness

*Control of optomechanical parameters*

of $h = 14$ nm, lower than the nominal value of 20 nm. We hypothesize that the discrepancy arises from a slow etching of the silicon nitride during the release of the structure, in the fabrication process [Tsa19]. We choose to work with the mode at 796.060 nm, located at the highest gradient point, where the optomechanical coupling constant G is maximum. Based on the fit line and on the knowledge of the mirror coatings we can also calculate the expected cavity overcoupling, for each mode, as shown in Figure 4.4b. For the chosen mode we expect $\eta_c \approx 0.95$.

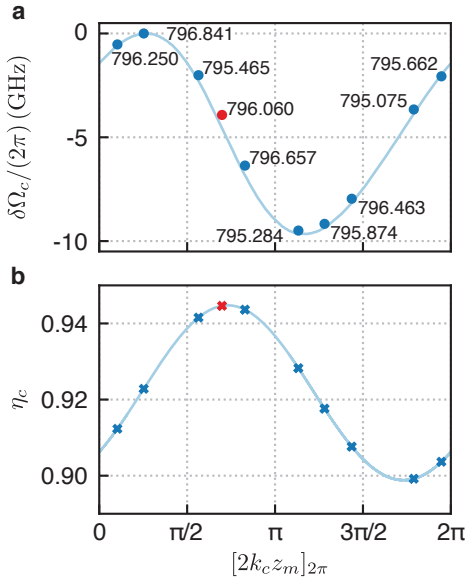


Figure 4.4: Measured cavity resonance frequency shifts and simulated overcoupling. a, The resonant wavelength of several cavity modes are measured (labels, in nm) and the corresponding frequency shifts (blue dot) are plotted in $2k_c z_m$. We fit them to a model (light blue). The mode indicated by the red dot features the largest optomechanical coupling constant. b, From the fit we infer the corresponding cavity overcoupling, $\eta_c$, for each cavity modes. The red cross is the cavity mode with largest optomechanical coupling constant.

Figure 4.5 shows a breakout schematic of the cryostat and sample holder. The latter is fully machined from elmedur copper to ensure good thermalization at cryogenic temperature of liquid helium, 4 K. The two mirrors are separated by a stack of three silicon chips, the middle of which contains the membrane resonator. A thin copper plate is used to clamp down both the flat mirror and the chips stack. One needs to take extra care when tightening the four screws which clamp this copper plate. In fact, overtightening this plate can break the silicon chips underneath, thereby destroying the membrane chip as well. We perform a series of assemblies in which we measure the torque we apply to the screws until the chips break, from which we find that the maximum torque we can apply without breaking them

is 3.1 $N \cdot cm$. We then always tighten the screws with this value, by using a torque driver. The curved mirror is placed on top of the stack and horizontally translated in order to align the cavity optical axis with the membrane defect. Then, it is clamped down by means of a copper cap. Both mirrors lay on rubber o-rings, which allow to reduce the mechanical dissipation of the substrates' normal modes and, thus, reduce the mirror noise [Nie16]. The membrane chip is separated from

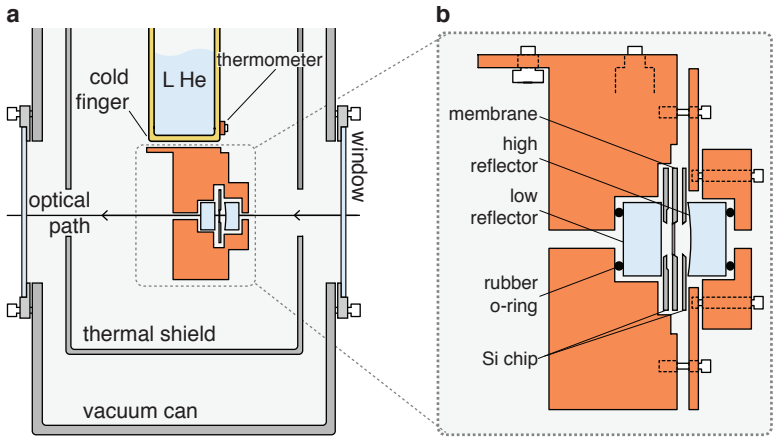


Figure 4.5: Breakout of the optomechanical cavity setup. a, Section view of the optomechanical cavity once attached to the cryostat cold finger. b, Detailed section view of the optomechanical cavity setup.

the flat mirror by a silicon spacer. The very small roughness of the mirror surface and of the silicon spacer ensures that, once everything is firmly clamped down, the membrane area is perpendicular to the cavity optical axis.

*Alignment of the optomechanical cavity*

During assembly, we only need to align the optical axis relative to the membrane. This is important in order to (i) avoid clipping the optical mode with the honeycomb lattice and (ii) obtain a large overlap, $\Lambda$, between the mechanical and optical modes transverse profile, required to have a large optomechanical coupling rate, $g_0$. Given that we always use the fundamental transverse optical mode, the TEM00, and the mechanical mode profile shown in Figure 4.3b, the optimal alignment is when the optical axis is centered with the membrane defect. To achieve that, we translate the spherical mirror horizontally, while sweeping the laser frequency and monitoring both the transmitted optical profile and imaging the membrane with the CCD (cf. [Che20] for more details).

#### 4.1.2.4 *Cryostat*

Once assembled, the sample holder is rigidly attached to the cold finger of a continuous flow cryostat ST-100 from Janis[5], as shown in Figure 4.5a. The cryostat comprises a metallic cylindrical vacuum

5 janis.com

*Cryostat operation*

can, evacuated with a turbo-molecular pump down to a pressure of $\sim 10^{-5}$ mbar. Inside, the cold finger is surrounded by another thin metallic can, which shields the cold sample from the hot, room temperature radiation coming from the outer can. After evacuation, cooling is initiated by flushing liquid helium from a storage dewar into the inner cold finger. The dewar is pressurized at $0.2 \div 0.5$ bar from the helium which is evaporated when the transfer line is inserted. Such pressure is sufficient to push the cryogenic liquid through the line down to the cold finger and guarantees continuous cryostat operation, until the dewar is emptied. A resistive thermometer is attached next to the cold finger and allows to monitor the inner temperature of the cryostat, which can reach at most 3.9 K. The cooling rate can be regulated by controlling the aperture of a needle valve, on the transfer line. Sometimes we observe that a cooldown happening "too fast", or "too slow" can result in degradation of the mechanical quality of the membrane, or even its rupture. Despite a lack of clear evidence, we hypothesize that this comes from either a fast stress redistribution, due to different materials' contraction, or a condensation of gas molecules on the membrane surface. In order to avoid that and to have a systematic cooldown method we choose to use a cooling rate, starting from room temperature, of 7 K/min, measured by the cold finger thermometer.

### 4.1.3 *Optical detection*

We measure the optical fields by means of photodetectors, as discussed in Section 1.4. We employ both direct and balanced homodyne detection. We employ these measurements to derive an error signal for stabilization purposes, to monitor the optical powers and to measure the membrane mechanical motion.

#### 4.1.3.1 *Direct detection*

As shown in Figure 4.1, we perform several direct detections. We have already seen an example when discussing the amplitude modulator and the error signal needed to stabilize its working point.

We directly detect the fields which are reflected from the optical cavity. The photocurrent is used to generate an error signal for a Pound-Drever-Hall (PDH) lock, which allows to stabilize the laser frequency at around the cavity resonance [Bla01]. This also requires a modulation of the laser frequency, which is imposed via the laser intracavity EOM. In Figure 4.6a we show a more detailed electronic schematic for the PDH locks we implemented in the experiments.

The transmitted beams can also be directly detected by two avalanche photodiodes (APDs). The DC photocurrent can be used as a measure of the optical power, to infer the cavity circulating power. In addition, the photocurrent forms the error signal for a *slope lock*, which can

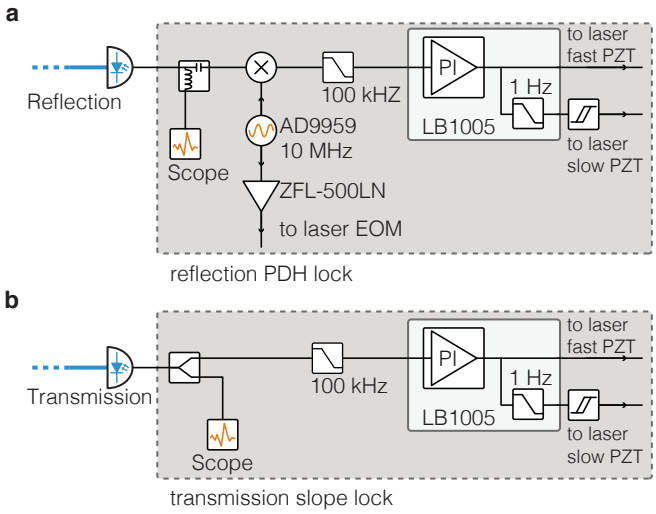


Figure 4.6: Electronic schematic of cavity locks. a, PDH lock, based on the directly detected reflected beam. b, Slope lock, based on the directly detected transmitted beam

stabilize the laser frequency on the side of a cavity resonance, where the intensity gradient is largest. In Figure 4.6b we show a schematic of the electronics used for the slope lock.

#### 4.1.3.2 *Balanced homodyne detector*

The main measurements of mechanical motion are performed via quantum-limited phase-sensitive detection, which takes the form of a polarization-multiplexed BHD. The LO and the signal fields, in linear orthogonal polarizations, are mixed on a PBS. A subsequent half-waveplate (HWP) rotates their polarization by 45 degrees, and they are then split by another PBS. The output fields are sent to two photodiodes, arranged in a subtraction configuration, as shown in Figure 4.7.

To achieve a large interference visibility we align and focus the LO, in order to mode-match the signal field, and employ photodiodes with large quantum efficiency, $\eta_{qe}$. At near-infrared (NIR) wavelengths, which we use, silicon photodiodes are best suited. They can, in fact, reach up to $\eta_{qe} = 98\%$, at a wavelength of $\lambda \sim 850$ nm. Standard commercial photodiodes, however, are packaged in an aluminium can with a protective glass window in front. This glass slab introduces optical absorption and reflection, degrading the efficiency down to 87%. To avoid that, we use custom S5971 photodiodes, from Hamamatsu[6], without the protective window. The electronic schematic of the balanced detector is shown in Figure 4.8. The photodiodes are reversed-biased with 12 V and arranged in a subtraction configuration. The resulting photocurrent is converted into a voltage signal via a transimpedance operational amplifier, with a gain of $-10$ kV/A. Then,

6 hamamatsu.com

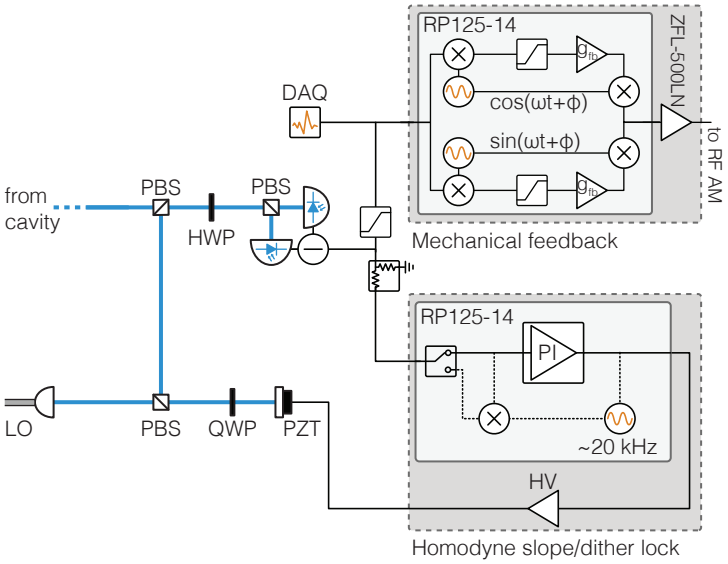


Figure 4.7: Optical and electronic schematic of a homodyne detector. The LO optical path is controlled by a piezo-actuated mirror. It is combined to the signal field from the cavity on a PBS, and sent to a balanced detector. The RF part of the photocurrent is split from the DC. The latter is fed into a digital controller and further processed to provide a feedback signal for stabilization of the signal-LO path difference. The RF part is digitized and acquired with a DAQ card for further data analysis. Simultaneously, it is sent to multiple digital controllers, which are used as tunable band-pass filters. This is part of a feedback loop aiming to cool down some mechanical modes of the membrane. The filtered signals are recombined together, amplified and sent to the amplitude modulator for actuation.

it is further amplified by an inverting operational amplifier, with a gain of $-2$. Finally, the output electrical signal is split in two parts, one of which is high-pass filtered to provide only the RF components. The other part, which contains also the DC, is used for monitoring and stabilization purposes.

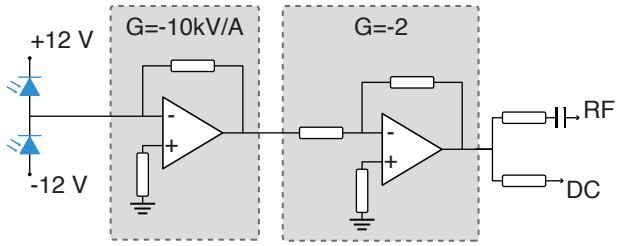


Figure 4.8: Electronic schematic of balanced detector.

The quadrature component measured by a BHD is chosen by controlling the path length difference, $\Delta L$, between the LO and the signal fields. Their path lengths fluctuate due to both slow drifts, as caused by temperature variations, and fast noises, as caused by environmental

vibrations. For optimal and accurate operation, one needs to actively stabilize the resulting phase difference $\theta_l := k\Delta L$, with $k$ the laser angular wavenumber. These fluctuations are imprinted in the DC part of the photocurrent, as $V_{DC} \propto \cos(\theta_l)$, which can be used as an error signal for a servo loop. The feedback actuates on a piezo, which translates a mirror on the LO path and controls the phase difference $\theta_l$, as shown in Figure 4.7.

*Stabilizing the homodyne detector*

Depending on the quadrature angle we want to measure, we use two different stabilization techniques. For measurements around the phase quadrature, $\theta_l \sim \pi/2$, we use directly the low frequency part of the BHD photocurrent, $V_{DC}$, as an error signal for a slope lock. Around the amplitude quadrature, $\theta_l \sim 0$, the photocurrent gradient is zero. Therefore, it cannot be used directly for stabilization, as it does not allow to discriminate between positive and negative drifts. In this case, we can derive a useful error signal from the photocurrent derivative. This is obtained by modulating the path difference $\Delta L$ with a known, coherent tone and demodulating the photocurrent at the same frequency. This forms the basic of the *dither lock* technique, which we implement for amplitude quadrature stabilization.

Both locks are digitally implemented via a RedPitaya system[7], which is equipped with fast ADCs and an FPGA. An open source Python project, PyRPL [Neu+17], provides the software for both the servo controller and the signal generators, to output the feedback signal and the dither tone. The analog output signal from RedPitaya is further amplified by a homemade high-voltage amplifier from $\pm 1$ V to $-30/+60$ V, then sent to the piezo.

*Data acquisition system*

The final part of the detection is formed by a digital acquisition system. The RF photocurrent component is digitized by a fast, high-resolution data acquisition system (DAQ) card, M2i.4931-exp from Spectrum[8]. Each channel has a 16 bit vertical resolution and a sampling rate of 15 MS/s. To avoid electronic aliasing effects, we use an analog 5 MHz low-pass filter in front of each channel.

For estimating the power spectra of the measured signal, we process the digitized time traces according to the Bartlett's method. It is based on averaging several periodograms obtained from non-overlapping portions of the digitized signal. In the periodograms' estimation we use a Hanning window function [PM07].

## 4.2 CALIBRATION METHODS

We now move to discuss the calibration procedures and preliminary measurements we perform to estimate the main parameters of the optomechanical experiments. On one side, these allow to independently derive theoretical predictions which can corroborate the experimental

7 redpitaya.com
8 spectrum-instrumentation.com

results. On the other side, they offer a way to calibrate the measured signals in the lab, which are electric voltages, into proper mechanical units.

### 4.2.1 *Optical cavity*

We start with an overview of measurement protocols and estimations of the main parameters of the optical cavity.

CAVITY LINEWIDTH, $\kappa$ We linearly sweep the laser frequency around the cavity resonance and detect the transmitted optical intensity via direct detection. The photocurrent is recorded on an oscilloscope, the horizontal axis of which is calibrated into frequency units by means of a known phase modulation tone. The recorded trace is fitted to a Lorentzian function to extract the cavity linewidth, $\kappa$. When there is a membrane inside the cavity, sweeping over the blue side, i. e. $\Delta > 0$, leads to mechanical dynamical instabilities (cf. Section 3.2.2.2). The consequent motion amplification causes fluctuations of the cavity resonance frequency, and thus also of the detuning, much larger than the cavity linewidth. Effectively, this broadens the cavity peak detected in the transmission intensity, making the fitting imprecise, if not impossible. To mitigate this problem, we turn on the auxiliary laser and tune it on the red side of a different longitudinal cavity mode, with $\kappa \gg \Omega_m$: this generates additional optical damping which counteracts the instability caused by the swept laser when blue-detuned. We finally note that addressing a different cavity mode with the auxiliary laser avoids having a low-frequency beating between the two lasers in the recorded photocurrent.

DETUNING, $\Delta$ We obtain the laser-cavity detuning from the transmitted optical powers. We first sweep the laser over the resonance and record the peak voltage, $V_p$, on the oscilloscope. Then, we lock the laser to the cavity and measure on the oscilloscope the transmitted power, i. e. the resulting voltage $V_t$. From these two voltage measurements we obtain the detuning, in units of the cavity linewidth, as

$$\frac{\Delta}{\kappa} = \frac{1}{2}\sqrt{\frac{V_p}{V_t} - 1}. \tag{4.1}$$

If the cavity linewidth is known, we can get the absolute value of the detuning.

OVERCOUPLING, $\eta_c$ We estimate it, for the empty cavity, from the measured coating curves of the mirrors, shown in Figure 4.2a. In presence of a membrane, the overcoupling is modulated according to the position in $2k_c z_m$, as discussed in Section 3.2.1.

We estimate the modified overcoupling from a model obtained from the mirror coatings and the fitted frequency shifts, as done in Figure 4.4.

### 4.2.2 *Optical detectors*

We now discuss how we calibrate the optical detection part, in particular how to measure the homodyne quadrature angle and the various contributions to the total detection efficiency, $\eta_d \coloneqq \eta_l \eta_{qe} v^2$.

QUADRATURE ANGLE, $\theta_l$ The DC part of the photocurrent carries information about which quadrature is measured. In general, the DC photocurrent is $V_{DC} = V_a \cos(\theta_l) + V_o$. The quadrature angle can be estimated from the knowledge of the actual value, $V_{DC}$, the maximum value of the interference fringe, $V_M = V_a + V_o$, and the minimum one, $V_m = -V_a + V_o$, as

$$\theta_l = \arccos\left(\frac{V_{DC} - V_o}{V_a}\right). \tag{4.2}$$

The offset $V_o$ accounts for imperfect power balancing. The maximum and minimum of the interference fringe can be measured by ramping the piezo for a distance $\Delta L > \lambda/2$.

OPTICAL LOSS EFFICIENCY, $\eta_l$ The optical losses are due to imperfect optical components along the beam path, as PBSs, HWPs and lenses. We measure the overall loss directly from the ratio of the optical powers measured in front of the photodiodes and just at the output of the cryostat, and find $\eta_l = 92\%$. This does not include losses from the cryostat optical window, which has a nominal transmissivity of 99.6%. The measured efficiency compares well with the expected one, from nominal values and independently measured losses. Their contribution is reported in Table 4.1.

PHOTODIODE QUANTUM EFFICIENCY, $\eta_{QE}$ We start by assembling the photodiode in a simple, passive transimpedance circuit, with a reverse bias voltage on the diode. The detector gain, $G_d$, is the value of the resistor used, which we previously measure with a voltmeter. We then measure the linear DC response of the photodiode by recording the photocurrent, $V_{DC}$, as a function of the impinging optical power, $P$. The linear relation is expressed as $V_{DC} = G_d \eta_{qe} e/(\hbar \Omega_L) P$, where $e$ is the electron charge and $\Omega_L$ the laser frequency. If all these quantities are accurately known, we can extract the quantum efficiency, $\eta_{qe}$, from the fitted slope. The detector gain is obtained from the measured resistance. The laser frequency is measured with a wavelength meter. Finally, the

| OPTICAL ELEMENT | VALUE | ORIGIN |
|---|---|---|
| Cavity overcoupling | 95% | Predictions |
| Cavity window | 99.6% | Specs |
| Lens | 99.6% | Specs |
| PBS, transmission | 99% | Measured |
| Lens | 99.6% | Specs |
| HWP | 99.2% | Specs |
| PBS, transmission | 99% | Measured |
| PBS, reflection | 99.5% | Specs |

Table 4.1: Contributions to the optical losses.

optical powers are detected with a commercial power meter, 843-R from Newport[9]. This instrument, although convenient for fast measurements, is not extremely accurate, and tends to go out of calibration over time, leading to significant systematic errors. To mitigate that, we calibrate its readings against a NIST-calibrated S5971 silicon photodiode, from Hamamatsu. Combining all these, we can infer the quantum efficiency of different photodiodes. Typical measured values, at $\lambda = 800$ nm, are $\eta_{qe} = 87\%$, for photodiodes with the protective windows and $\eta_{qe} = 93\%$ when the window is removed.

INTERFERENCE VISIBILITY, $\nu$ To measure the homodyne visibility, we first adjust the intensity of the LO and signal fields to the same value. Then we monitor on the oscilloscope the BHD photocurrent with one photodiode blocked, as we sweep the piezo which controls $\theta_l$. The observed signal shows an interference fringe, well described by $V_{DC} = V_a \cos(\theta_l) + V_o$. From the maximum and minimum values of the recorded photocurrent, $V_M$ and $V_m$ respectively, we obtain the visibility as

$$\nu = \frac{V_M - V_m}{V_M + V_m}. \tag{4.3}$$

For our BHD we can get visibilities of up to $\nu = 98\%$.

Later on, we report a different method for characterizing the total efficiency $\eta := \eta_d \eta_c$. It is based on measuring several optomechanical homodyne spectra, at different quadrature angles, and calibrating them into displacement units. The background spectral noise, that is the imprecision noise, can be fitted to Equation 3.39. If the optomechanical coupling rate, $g$, the cavity linewidth, $\kappa$, and detuning, $\Delta$, are known, one can extract the total efficiency, $\eta$, from the fit. An example of such a measurement is shown in Section 9.1.2.1.

9 newport.com

### 4.2.3 *Mechanical modes*

We now describe how to measure the main parameters of the mechanical mode.

RESONANCE FREQUENCY, $\Omega_M$ The mechanical resonance frequency can be obtained spectroscopically, from the PSD of a phase quadrature measurement. The mechanical motion appears as a peak, centered around $\Omega_m$. From fitting it to a Lorentzian, we can extract the resonance frequency.

ENERGY DAMPING RATE, $\Gamma_M$ We measure it via the ringdown technique. First, the mechanical mode is coherently excited to large amplitude. Then, the driving force is switched off and the mechanical displacement is monitored during its free decay. As discussed in Section 2.1, for moderate excitation amplitude, the dynamics remains linear and is well described by the exponential decay $x(t) = x(0)e^{-t\Gamma_m/2} + n$, where $x(0)$ is the initial amplitude and we introduce $n$, a constant value which takes into account noise in the detection. We fit the measured displacement to this function and extract the energy damping rate, $\Gamma_m$.

Experimentally, we perform this ringdown measurement on the membrane once it has been assembled in the optical cavity and put in the cryostat. We monitor the decaying displacement by direct detection of the detuned laser transmitted through the cavity, which transduces the mechanical motion into the field amplitude quadrature. While doing that we should pay attention that the induced optical damping from the laser, as discussed in Section 3.3, is negligible. One way is to ensure exactly resonant operation, $\Delta = 0$. In practice, however, this turns out to be unfeasible, as it is at the verge of instability. To avoid optical damping, we tune the wavelength of the monitoring laser down to $\lambda \sim 740$ nm, at which the optical cavity has a very low finesse of $\sim \mathcal{O}(10)$, as shown by the mirror coatings in Figure 4.2. This results in very broad cavity modes, for which the optical damping rate is much smaller than the natural mechanical decay rate, which we want to measure. The driving force to the mechanical mode is exerted as a classical radiation pressure force, resulting from an amplitude modulation of the monitoring laser.

The resulting photocurrent is analyzed by a lock-in amplifier (LIA), which extracts the slow, decaying amplitude of the frequency components around $\Omega_m$. The measured decay is shown in Figure 4.9a. Additional damping mechanisms can arise from photothermal forces, due to optical absorption. To rule these out, we perform another ringdown measurement by pulsing the monitoring laser, with a bright-to-dark ratio of $1:30$. The two measurements are in agreement and give a damping rate

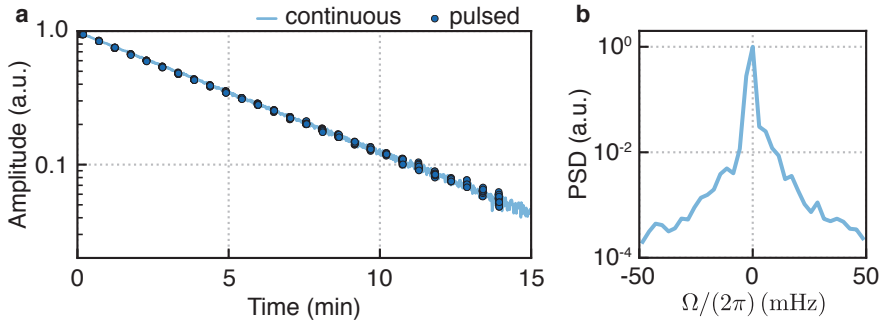


Figure 4.9: Mechanical ringdown. a, Mechanical amplitude decay for continuous (light blue) and pulsed (dot blue) monitoring laser, at frequencies around $\Omega_m$. b, Spectrum of the continuous ringdown photocurrent. The peak linewidth of 3 mHz is limited by the frequency resolution.

of $\Gamma_m/(2\pi) = 1.1$ mHz. This corroborates the fact that no additional backaction mechanisms, due to the monitoring optical field, are present [Ros+18]. In Figure 4.9b we calculate the PSD of the photocurrent measured via ringdown, from which we extract a linewidth of 3 mHz, limited by the frequency resolution of the spectrum. Finally, we notice that it is important that the monitoring field has a stable optical power over the duration of the measurement. Any drift of power would appear as a drift in the level of the photocurrent and can lead to systematic errors in the ringdown. Our laser source and the subsequent optics is optimized to reduce amplitude drift over the timescale of hours. For this ringdown measurement, we also employ a feedback loop on the amplitude modulator to stabilize its transmitted power.

THERMAL BATH OCCUPATION, $\overline{n}_{TH}$ The mechanical resonator is in a cryogenic environment. The cold finger, kept at 4 K, cools the membrane through several thermal links, such as copper parts, rubber o-rings, mirrors, silicon chips. At the same time, hot thermal radiation from the cryostat outer vessel provides a source of heating. Together, they determine a new equilibrium membrane temperature, different in general from the reading of the thermometer, positioned next to the cold finger. In addition, any force fluctuating at the mechanical mode frequency, which is coupled to the membrane, leads to an increase of the effective temperature of that given mode, sometimes referred to as *mode temperature*. The mode temperature can be defined from the total displacement fluctuations and variance, as discussed in Section 3.3. This method has two requirements: (i) the quantum backaction noise from the optical field is negligible, such that the mode temperature is not affected by it and (ii) the measured photocurrent should be converted into mechanical units, like phonon energy. The former can be satisfied by simply tuning the

optical power low enough, such that the quantum cooperativity is $\mathcal{C}_q \ll 1$. The latter, instead, requires the knowledge of the vacuum optomechanical coupling rate, $g_0$. We postpone the discussion on the thermal mode temperature measurement in the next section, where we introduce two methods for measuring this coupling rate.

### 4.2.4 *Vacuum optomechanical coupling rate*

The vacuum optomechanical coupling rate, $g_0$, is of fundamental importance to calibrate the measured photocurrent in mechanical energy and displacement units. It allows to make quantitative statements about the mechanical resonator. We provide here two methods to measure it, which rely on very different assumptions. Then, their reciprocal agreement would corroborate the results and strengthen their reliability.

#### 4.2.4.1 *Optomechanical coherent response via OMIT*

The first method we present is based on measuring the optomechanical response function to a coherent optical modulation of some sort. Part of this response, modified by dynamical backaction, is proportional to the optomechanical coupling $g$ which enables us extract it. Experimentally, we use a single laser, slope locked on the red side of the cavity resonance at detuning $\Delta$. Both the detuning and cavity linewidth are measured independently, as explained in Section 4.2.1. A LIA sends a coherent tone, at frequency $\Omega$, to a phase modulator in the input laser. We directly detect the transmitted field and analyze the resulting photocurrent with the LIA, which extracts the response at frequency $\Omega$ [Nie+17]. Sweeping the frequency $\Omega$ around the resonance of the mechanical mode allows to reconstruct the optomechanical coherent response function. For the case considered here, this response is

$$H_{omc}(\Omega) = \alpha\, \chi_{eff}(\Omega)\chi_m(\Omega)^{-1} \left( \chi_c(\Omega)\frac{\imath}{2}\frac{|\chi_c(0)|}{\chi_c(0)} - \chi_c(-\Omega)^*\frac{\imath}{2}\frac{|\chi_c(0)^*|}{\chi_c(0)^*} \right), \tag{4.4}$$

where $\alpha$ is an irrelevant normalization factor. The inverse mechanical susceptibility forms a notch window in the response known as optomechanically induced transparency (OMIT) [Wei+10]. In addition, the optomechanical response contains the cavity response to a phase modulation and the effective mechanical response to a driving force, which arises from the amplitude component of the rotated phase modulation once in the cavity.

In Figure 4.10 we show such a complex response, measured at different detuning. We fit the data to Equation 4.4 and extract the field-enhanced optomechanical coupling rate, $g$, from the effective mechanical susceptibility. We can further estimate the intracavity average

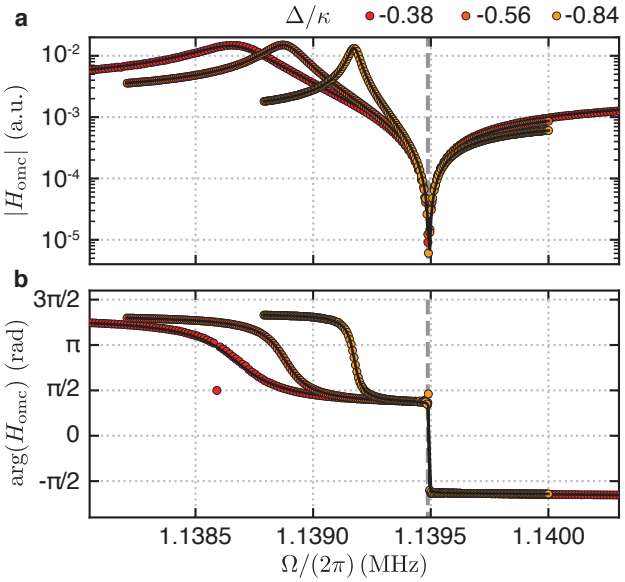


Figure 4.10: Optomechanical coherent response. a, Magnitude and b, phase response of the optomechanical cavity, at different detunings, $\Delta$ (coloured circles). A LIA provides a coherent tone, at frequency $\Omega$, which modulates the phase of the input field. At the same time, it extracts the frequency component $\Omega$ from the detected photocurrent. The complex response is reconstructed by sweeping $\Omega$. The vertical dashed gray line is at the resonance frequency, $\Omega_m$, of the natural mechanical response, which is responsible for the narrow, inverted Lorentzian peak. The black lines are fit.

photon number, $\overline{n}_{cav}$, from the measured transmitted power, $P_{tr}$, the direct detection efficiency, $\eta_d$, and the cavity overcoupling, $\eta_c$, as

$$\overline{n}_{cav} = \frac{P_{tr}}{\hbar \Omega_L \kappa \eta_c \eta_d}, \tag{4.5}$$

from which we get the vacuum coupling rate $g_0 = g/\sqrt{\overline{n}_{cav}}$. From the data shown in Figure 4.10, we extract $g/(2\pi) = (82, 70, 52)$ kHz and $\overline{n}_{cav} = (3.9, 2.9, 1.7) \times 10^5$, at the detuning $\Delta/\kappa = (-0.38, -0.56, -0.84)$. Combining all of them together, we finally estimate $g_0/(2\pi) = (129 \pm 2)$ Hz, where the error indicates the mean absolute deviation (m.a.d.).

This method relies on the precise knowledge of the intracavity average photon number, $\overline{n}_{cav}$, which in part stems from the knowledge of the cavity overcoupling, $\eta_c$, as shown by Equation 4.5. We have seen in Section 4.2.1 that this parameter is estimated from the transfer matrix model and the measured mirrors' transmissivities. In practice, however, there might be excess losses in the cavity, e. g. due to light scattering from a non-orthogonal membrane, which are not accounted for by the theory. Despite our effort to guarantee orthogonality during the optomechanical cavity assembly, this remains a major, unknown parameter.

#### 4.2.4.2 *Quantum noise thermometry*

A different method for measuring $g_0$, not based on the cavity overcoupling, relies on thermometry measurements. The mechanical displacement induces frequency fluctuations on the cavity resonance. These frequency fluctuations are imprinted in the phase quadrature of the driving field, which can be measured by means of a BHD. In particular, the measured photocurrent can be calibrated into frequency units by comparing it to a phase modulation tone, with known modulation depth. The total frequency variance, $\langle \delta\Omega_c^2 \rangle$, due to the mechanical motion, can be obtained by integrating the measured spectrum and is related to $g_0$ from

$$\langle \delta\Omega_c^2 \rangle = g_0^2 \, (2\overline{n}_{\mathrm{eff}} + 1) \, . \tag{4.6}$$

If the mode temperature, in units of phonon $\overline{n}_{\mathrm{eff}}$, is precisely known, one can estimate the vacuum coupling $g_0$. This method, differently from the one in Section 4.2.4.1, relies on (i) calibrating the measured photocurrent in frequency units and (ii) the precise knowledge of the effective mechanical mode temperature, and not of the cavity overcoupling.

*Frequency calibration via a phase-modulation*

The former is done by phase-modulating the laser with a known modulation depth, $\phi_{\mathrm{rms}}$, at frequency $\Omega_{\mathrm{cal}}$ [Gor+10]. Under certain conditions, the phase modulation of the input laser is transduced, through the optomechanical cavity and the detector, into a voltage in the photocurrent in the same way as the mechanical displacement does. The corresponding transduction function, $K(\Omega)$, can be experimentally obtained from a comparison between the variance $\sigma_{\mathrm{cal}}^2$, coming from integrating the PSD of the measured photocurrent around the calibration frequency $\Omega_{\mathrm{cal}}$, i. e. $\sigma_{\mathrm{cal}}^2 \coloneqq \int_{\Omega_{\mathrm{cal}}} d\nu \overline{S}_{ii}$, and the known modulation depth $\phi_{\mathrm{rms}}^2$, that is, $K(\Omega_{\mathrm{cal}}) = \sigma_{\mathrm{cal}}^2/\phi_{\mathrm{rms}}^2$. By changing the calibration frequency, we verify that this transduction function is constant over the frequency range around the mechanical mode, and we can assume that $K(\Omega_m) \approx K(\Omega_{\mathrm{cal}})$. Then, we use this transduction function to convert the variance $\sigma_m^2$, coming from integrating the photocurrent PSD around the mechanical mode, i. e. $\sigma_m^2 \coloneqq \int_{\Omega_m} d\nu \overline{S}_{ii}$, into frequency units according to $\sigma_\omega^2 \coloneqq \sigma_m^2 \Omega_m^2 / K(\Omega_m)$, where the term $\Omega_m^2$ is needed to convert the phase variance into a frequency one. The variance $\sigma_\omega^2$ is the variance of the frequency fluctuations around the mechanical mode, and corresponds to a measurement of the quantity $\langle \delta\Omega_c^2 \rangle$ in Equation 4.6.

*Temperature reference from quantum noise*

Regarding the latter requirement, that is, the precise knowledge of the mode temperature, we cannot use the cryostat temperature reading as a reliable value for the effective mode temperature, as previously explained in Section 4.2.3. We then use a strong auxiliary laser, with $\mathcal{C}_q \gg 1$, red-detuned with respect to a different cavity mode, to provide strong optical cooling, down to the sideband cooling

limit expressed by Equation 3.26. In this limit, the quantum backaction noise is the dominating source of displacement fluctuations and fully determines the effective temperature, making the thermal bath temperature negligible. Importantly, this effective temperature is a function of few, experimentally measurable parameters as the cavity linewidth, $\kappa$, detuning, $\Delta$, and mechanical resonance frequency, $\Omega_m$. In this sense, quantum noise is used as a reference temperature to calibrate the readings of our "optical thermometer" [Pur+17].

In practice, we employ two lasers, as sketched in Figure 4.11a. A weak probe laser with $\mathcal{C}_q \ll 1$, is resonantly locked, via PDH, to the cavity mode the coupling $g_0$ of which we want to measure, with $\lambda = 796.060$ nm, $\mathcal{C}_q \approx 0.08$ and $\kappa/(2\pi) = 15.9$ MHz. This laser is also phase-modulated at $\Omega_{cal}/(2\pi) = 1.09$ MHz, with $\phi_{rms} = 0.28$ mrad. A strong auxiliary laser, with $\mathcal{C}_q \gg 1$, is slope locked to the red side of a different cavity mode, at 795.075 nm, with $\kappa_a/(2\pi) = 12.9$ MHz and $\Delta_a/(2\pi) = -4.2$ MHz, in order to provide strong quantum backaction noise as a temperature reference. This cavity mode has been chosen since it features a large optomechanical coupling constant, as shown in Figure 4.4. We monitor the phase quadrature of the probe transmitted field via a BHD as we increase the auxiliary power, thereby also increasing its quantum cooperativity. The PSDs of the raw photocurrent are shown in Figure 4.11b. We fit the mechanical peak to a Lorentzian function and extract the effective linewidth, $\Gamma_{eff}$, the resonance frequency shift, $\delta\Omega_m$ and the area under the peak, $\sigma_m^2$. The former two linearly scale with the auxiliary laser power as

$$\delta\Omega_m = \Omega_{eff} - \Omega_m = g_a^2 \left[ \frac{\Delta_a + \Omega_m}{(\Delta_a + \Omega_m)^2 + (\kappa_a/2)^2} + \frac{\Delta_a - \Omega_m}{(\Delta_a - \Omega_m)^2 + (\kappa_a/2)^2} \right], \tag{4.7a}$$

$$\Gamma_{eff} = \Gamma_m + \Gamma_{opt} = \Gamma_m + g_a^2 \left[ \frac{\kappa_a}{(\Delta_a + \Omega_m)^2 + (\kappa_a/2)^2} - \frac{\kappa_a}{(\Delta_a - \Omega_m)^2 + (\kappa_a/2)^2} \right], \tag{4.7b}$$

where the auxiliary transmitted power, $P_{tr,a}$ is linked to the optomechanical coupling rate $g_a$ via $g_a^2 = g_{0,a}^2 P_{tr,a}/(\hbar\Omega_{L,a}\kappa_a\eta_{c,a})$. We fit both the extracted linewidths and the resonance shifts to Equation 4.7 by using orthogonal distance regression, which allows to include weights in the independent variable $P_{tr,a}$. From these fits, shown in Figure 4.11c and d, we extract $g_a/(2\pi) = 24$ kHz per 1 $\mu$W of transmitted power.

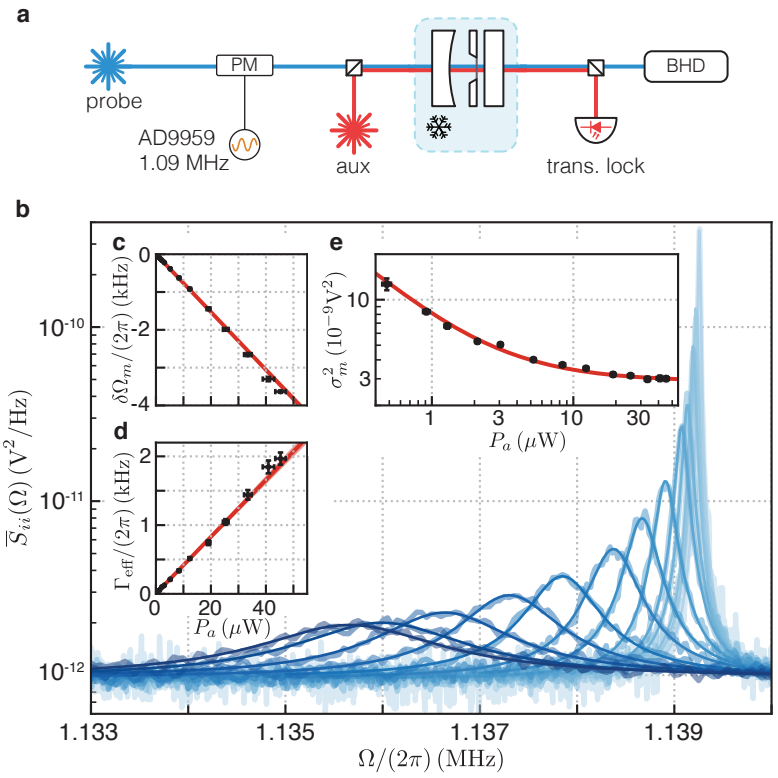


Figure 4.11: Quantum noise thermometry. a, Two-laser experiments for probing mechanical motion and providing a known temperature reference. b, Spectra of the phase quadrature of the transmitted probe field, for different auxiliary powers, increasing from light to dark blue. Smooth, solid lines are Lorentzian fits. c, Mechanical resonance shift, d, effective linewidth and e, area under the peak, extracted from the fits and shown as black dots. The horizontal and vertical error bars indicate, respectively, uncertainty in the power measurements and the confidence interval from the fit. The extracted parameters are further fitted to theoretical model and the results are shown in red. Adapted from [Ros+18].

The extracted area, $\sigma_m^2$, is related to the frequency fluctuations in Equation 4.6 via the transduction factor $K(\Omega_m)/\Omega_m^2$, as seen before. Inserting Equation 3.25 we find

$$\sigma_m^2 = \frac{K(\Omega_m)}{\Omega_m^2} g_0^2 \underbrace{\left(2\frac{\Gamma_m \overline{n}_{th} + \Gamma_{opt}(P_{tr,a})\overline{n}_{opt}}{\Gamma_m + \Gamma_{opt}(P_{tr,a})} + 1\right)}_{2\overline{n}_{eff}+1}, \tag{4.8}$$

where $g_0$ is the optomechanical coupling rate for the probe field and the dependence of the optical damping, $\Gamma_{opt}$, on the auxiliary power has been explicated. Equation 4.8 shows two regimes for the extracted area:

$\Gamma_{OPT}\overline{n}_{OPT} \gg \Gamma_M \overline{n}_{TH}$: achieved at large auxiliary powers, the extracted area $\sigma_m^2$ is proportional to the product $g_0^2\overline{n}_{opt}$, where $\overline{n}_{opt}$ can be easily calculated from known parameters. Then, from the

extracted area and the transduction function we can calculate the vacuum optomechanical coupling rate, $g_0$.

$\Gamma_{OPT}\bar{n}_{OPT} \ll \Gamma_M\bar{n}_{TH}$: conversely, for small auxiliary power, the area $\sigma_m^2$ becomes proportional to $g_0\bar{n}_{th}$, from which, employing the previously estimated $g_0$, we can extract the effective bath average occupation, $\bar{n}_{th}$, as anticipated in Section 4.2.3.

In practice, we fit all the areas to Equation 4.8, as shown in Figure 4.11e, from which we extract $g_0/(2\pi) = (127 \pm 2)$ Hz and $\bar{n}_{th} = (2.0 \pm 0.4) \times 10^5$, or equivalently $T = (11 \pm 2)$ K, where the errors indicate the fit confidence interval at 95%.

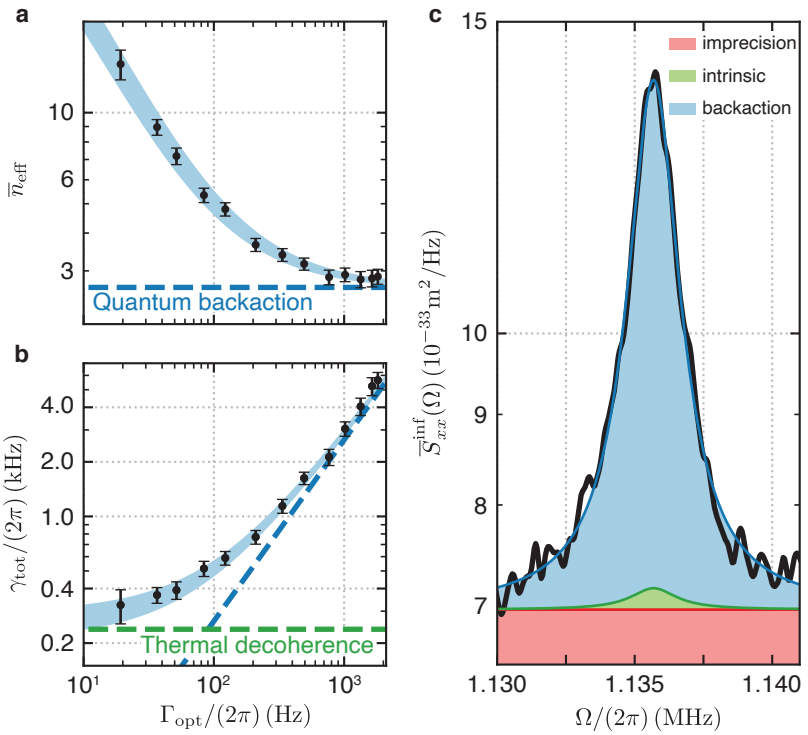


Figure 4.12: Calibrated quantum noise thermometry. a, Effective average phonon number and b, total decoherence rate as a function of the optical damping, $\Gamma_{opt}$, induced by the auxiliary laser, as black circles. They are fitted to theoretical models and the results are shown as shaded blue area, whose width reflects the confidence interval from the fit. Dashed lines indicate contributions from thermal decoherence (green) and quantum backaction (blue). Error bars are from the confidence interval of the fit used to extract the shown circles. c, Calibrated mechanical displacement spectrum (black), at the highest auxiliary power, with a Lorentzian fit (blue). The contributions from imprecision, quantum backaction and thermal noise are shown, respectively, in red, blue and green. Adapted from [Ros+18].

We can now use these results to calibrate the extracted area, $\sigma_m^2$, in units of phonons, as shown in Figure 4.12a. As expected for sideband

cooling, the effective mechanical phonon number saturates at the sideband cooling limit. In Figure 4.12b we plot the total mechanical decoherence rate, $\gamma_{tot} = \Gamma_{eff}\overline{n}_{eff}$. When the sideband cooling limit is approached, quantum backaction decoherence overcomes the thermal one. The linear dependence of the total decoherence with optical power, for large values, is characteristic of quantum vacuum noise, in contrast to the quadratic dependence arising for classical decoherence due to laser excess noise [PPR13]. Finally, we show in Figure 4.12c a measured spectrum for the largest auxiliary power. Here, the dominating source of fluctuations is quantum backaction while the unknown thermal noise contribution is reduced to only $(1 + \Gamma_{opt}\overline{n}_{opt}/\Gamma_m\overline{n}_{th})^{-1} \approx 4\%$.

The two methods presented for estimating the vacuum optomechanical coupling rate are based on very different assumptions and subjected to different systematic errors. In brief, the optomechanical coherent response is based on calibrating the intracavity photon number, while the quantum noise thermometry is based on knowing the mechanical phonon number. The former is affected by extra losses in the cavity. The latter is instead affected by additional classical decoherence. The agreement achieved in the two measurements then strengthens the assumptions made in modelling the optomechanical system.

### 4.2.5 *Effective mechanical occupation*

We later use the measured optomechanical coupling, $g_0$, to estimate the effective mechanical phonon number in different experiments, by exploiting Equation 4.8. For a measured area, $\sigma_m^2$, the inferred mechanical occupation, $n_{eff}^{inf}$, is $2n_{eff}^{inf} + 1 = \sigma_m^2\Omega_m^2/(K(\Omega_m)g_0^2)$, which explicitly depends on the transduction function $K(\Omega_m)$. Its determination, as we have seen, relies on the knowledge of the modulation depth, which in turn depends on the characteristic $V_\pi$ of the modulator. However, the coupling $g_0$, as measured via quantum noise thermometry, depends also on the modulator characteristic. In fact, one has that $g_0 = \overline{\sigma}_m^2\Omega_m^2\overline{K}(\Omega_m)^{-1}/(2\overline{n}_{cal} + 1)$, where $\overline{\sigma}_m^2$ and $\overline{K}(\Omega_m)$ are measured quantities from the quantum noise thermometry experiment at the sideband cooling limit and $\overline{n}_{cal}$ is the corresponding calculated reference occupation, very close to $\overline{n}_{opt}$. If this $g_0$ value is used in all the experiments and the phase modulation depth is kept always the same, such that $K(\Omega_m) = \overline{K}(\Omega_m)$, the calibrated effective phonon number becomes

$$2n_{eff}^{inf} + 1 = \frac{\sigma_m^2}{\overline{\sigma}_m^2}\,(2\overline{n}_{cal} + 1)\,, \tag{4.9}$$

that is, it comes from a comparison between the two measured areas and a known reference occupation. In particular, the modulator-dependent transduction function, subjected to systematic errors, can-

cels out in the final expression for the inferred phonon number [Mas+19].

# Part II

# EXPERIMENTAL RESULTS

# 5

# CONTINUOUS DISPLACEMENT MEASUREMENT OF A MECHANICAL RESONATOR

In the previous chapters we have seen, from the theory side, that optomechanical systems are particularly well-suited for performing quantum displacement measurements. Here, we report experiments aiming to achieve the quantum-limited measurement regime, a prerequisite for measurement-based quantum control.

In the first part we discuss some of the very first experiments, which had the merit of highlighting some limiting aspects of soft-clamped structures and how to overcome them. With these lessons learnt, we describe subsequent experiments, which clearly show that our platform enables measurements at the quantum limits.

In the second part we move to a different description of the quantum-limited displacement measurement, based on quantum trajectories. In particular, apart from offering a different interpretation framework, the quantum trajectory description provides a prescription which is used to experimentally obtain a mechanical conditional state from the measurement record. For a quantum measurement, such a state is predicted to be close to a pure coherent state. We verify this state by developing a new verification protocol based on a retrodiction measurement. In particular, this gives us access to the experimental observation of the conditional state throughout all the measurement-induced dynamics, from state reduction, happening at the beginning of the measurement, to decoherence, when the conditioning from the upcoming records is stopped.

## 5.1 PRELIMINARY ATTEMPTS

The first step towards quantum control of mechanical motion is to achieve displacement measurements in the quantum regime. In the first generation of the experiment, we attempt that by using a 5.4 mm x 5.4 mm x 35 nm soft-clamped membrane, with mechanical mode resonance frequency of $\Omega_m/(2\pi) = 753$ kHz and quality factor of $Q = 120 \times 10^6$, assembled in the optical cavity, at cryogenic temperature of $\sim 4$ K. We start by locking a single probe laser on the red side of a cavity mode, at $\lambda \approx 800$ nm with linewidth $\kappa/(2\pi) = 6.6$ MHz. The laser is phase-modulated with a known coherent tone. The non-zero detuning transduces the mechanical displacement into the amplitude quadrature, which is detected on the transmitted beam via direct detection. We collect several PSDs at different optical powers, for fixed detuning, as shown in Figure 5.1a. Surprisingly, extraneous in-bandgap

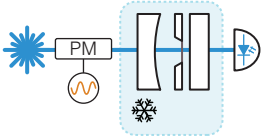

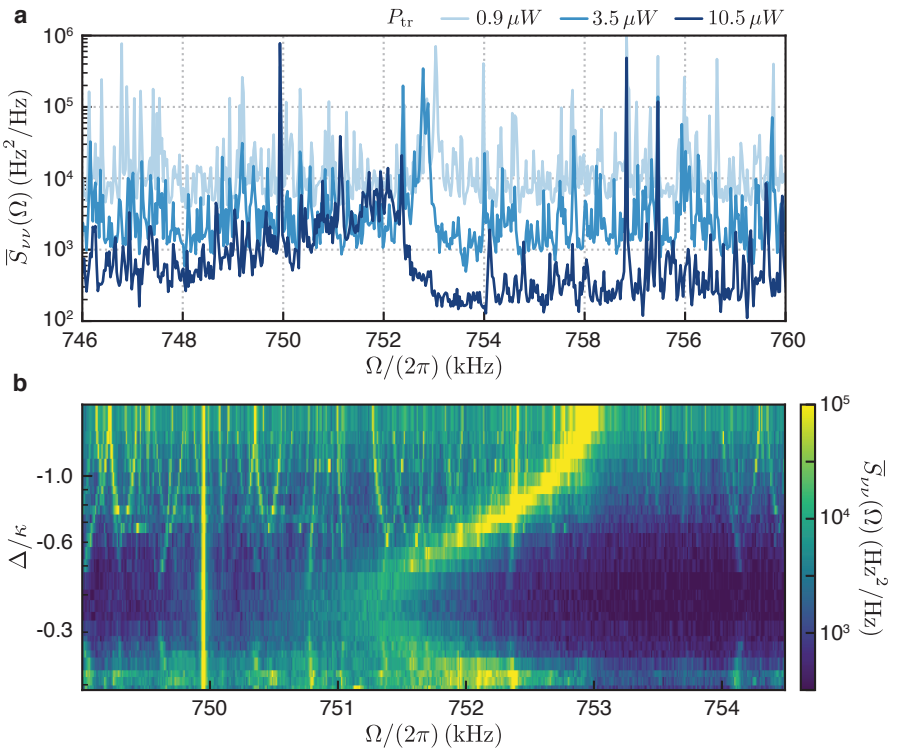


Figure 5.1: Appearance of extraneous in-bandgap modes. a, Spectra of the amplitude quadrature of a red-detuned laser, at $\Delta \approx -0.2\kappa$, as a function of its output optical power, $P_{tr}$. The defect mode, at $\approx$ 753 kHz, is surrounded by extraneous peaks. b, Spectra, at a fixed power of $P_{tr} = 10.5$ μW, as a function of the laser detuning. The defect mode shows a large optical spring effect. The extraneous peaks shift as well, both downward and upward.

peaks are present, in addition to the few localized defect modes. We exclude the possibility of them being electronic in origin and test their mechanical origin by collecting also PSDs for different detunings, with fixed power, as shown in Figure 5.1b. We make the following observations:

- The amplitude of many of these peaks is reduced as a function of detuning by orders of magnitude. This reduction is consistent with the optical cooling from a red-detuned laser, experienced by a mechanical mode. The defect mode at $\Omega_m$ serves as an example.
- In addition, the peaks' frequencies shift downward, as a function of detuning, as expected from the optical spring effect for modes with frequency $\Omega \ll \kappa$. Again, the typical dependence is shown for the defect mode at $\Omega_m$.
- However, some of these peaks shift upwards, oppositely to what is expected from optical spring. These peaks, then, are not di-

rectly mechanical peaks, but reflected copies of other mechanical peaks.

- There are also peaks which are not affected at all by the tuned laser, as the one visible at $\approx 750$ kHz.
- Finally, large frequency noise is induced by some mechanical modes at low frequencies, not shown in Figure 5.1, corresponding to normal modes of the whole membrane structure. For example, modes at $\approx 100$ kHz and $\approx 170$ kHz, at $\Delta = -0.2\kappa$ and for the lowest power, have a peak value of $\sim 10^{10}$ Hz$^2$/Hz, five orders of magnitude larger than the defect mode.

*In-bandgap extraneous peaks*

Based on these observations, we hypothesize that the extraneous in-bandgap peaks are the result of a frequency-mixing process due to a non-linear cavity transduction. In particular, the displacement of low-frequency modes induces large cavity detuning excursions which exceed the linear range of the cavity transduction. The consequence is that these large peaks acquire mechanical sidebands of "non-linear" nature, which mix with the "linear" sidebands around the laser carrier. The non-linear sidebands will show dynamical backaction as well, and negative sidebands will be reflected. More recently, an independent experiment performed by Fedorov et al. quantitatively verified such intermodulation noise mechanism [Fed+20]. Regarding the peaks not affected by dynamical backaction, e. g. the one at $\approx 750$ kHz, we verify that they come from modes localized at the edges of the membrane, where the boundary with the silicon frame forms additional defects. We move them away from the bandgap by reducing the mass of such defects.

The extraneous in-bandgap peaks form an additive, excess noise which limits the performance of our displacement measurements. In order to improve it, we need to reduce the fluctuations of the large modes at low frequencies. This is done with a combination of sideband cooling, from an auxiliary laser, and feedback cooling to selectively cool down these few disturbing modes. The latter technique exploits the measured low-frequency displacement to tailor and exert a viscous-like force on the resonator itself. This force increases the mode linewidth without introducing more fluctuations, leading to a net cooling effect. Experimentally, we derive the displacement signal by filtering the measured photocurrent around the mechanical resonance frequency. The viscous force is exerted via classical radiation pressure, by modulating the amplitude of an auxiliary laser with the filtered electronic signal. Reducing the amplitude of such modes brings the corresponding frequency excursions within the linear regime of the cavity transduction and eliminates these extraneous peaks.

The large displacement of these modes is not well understood yet. One hypothesis is that it is driven motion by excess laser noise, which is significant at those low frequencies of $\approx 100$ kHz. Reducing the

lateral size of the membrane increases the corresponding frequencies, where the laser noise is diminished. We decide, then, to do this for the next generation of experiments, for which we employ a membrane with size reduced by 50%, moving the defect modes to around 1 MHz, a good spot even in terms of mirrors' noise (cf. Figure 4.2).

## 5.2 STANDARD PHASE MEASUREMENTS

The setup of the second generation of experiments [Ros+18] is sketched in Figure 5.2. A probe laser is locked, via PDH, close to resonance of

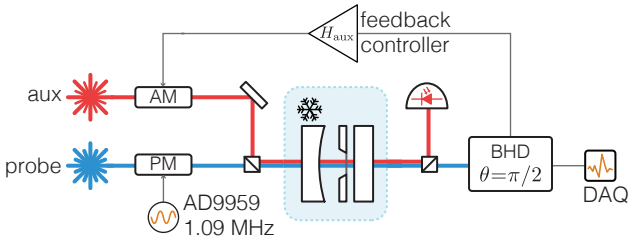


Figure 5.2: Experimental setup for displacement quantum measurements.

a cavity mode, at $\lambda = 796.060$ nm, $\kappa/(2\pi) = 15.9$ MHz and typical detuning $\Delta \approx -0.05\kappa$. The input phase is modulated by a known tone at $\Omega_{cal}/(2\pi) = 1.09$ MHz and used to calibrate the overall transduction function, as described in Section 4.2.4. We estimate a cavity overcoupling of $\eta_c = 0.95$, such that most of the intracavity fields is transmitted. We then measure the phase quadrature of this transmitted beam via a BHD and calculate the PSD of the photocurrent. We achieve a total detection efficiency of $\eta_d = 77\%$ for the BHD. At the same time, we also have an auxiliary laser, locked to the red side of a different longitudinal cavity mode, at $\lambda_a = 795.057$ nm with $\kappa_a/(2\pi) = 12.9$ MHz and $\Delta_a = -4.2$ MHz. We choose to keep its power low, such that $\mathcal{C}_q^a = 0.18$, in order to have a small contribution to the mechanical decoherence rate from its quantum backaction. This laser is used to stabilize and cool some of the low-frequency membrane modes which lead to additional in-bandgap noise, as seen in Section 5.1. The membrane, of size 3.6 mm x 3.6 mm x 20 nm, is assembled inside the optical cavity, and kept cold in the cryostat, at $\sim 4$ K. It has a mechanical resonance frequency of $\Omega_m/(2\pi) = 1.14$ MHz and a quality factor of $Q = 1.03 \times 10^9$. As typical of our experiments, we operate in the regime of a very broad cavity, i. e. $\kappa \gg \Omega_m$. The vacuum optomechanical coupling rate is measured in two different ways, as explained in Section 4.2.4, which yield values well in agreement. From the quantum noise thermometry, we obtain $g_0/(2\pi) = (127 \pm 2)$ Hz and $T = (11 \pm 2)$ K. More details about the experimental setup and the methods for measuring each parameter are found in Chapter 4.

We start by measuring the PSD of the probe homodyne photocurrent, measuring the phase quadrature, for different probe powers, as shown

in Figure 5.3a. The chosen power values is such that the probe quantum cooperativity, $\mathcal{C}_q$, ranges from the classical measurement regime, where $\mathcal{C}_q \ll 1$, to the quantum measurement one, where $\mathcal{C}_q \gg 1$. We also calibrate the measured photocurrent in units of displacement. This is done from the relation

*Calibration of the spectrum*

$$\overline{S}^{\text{inf}}_{qq}(\Omega) \equiv \frac{\overline{S}^{\text{inf}}_{xx}(\Omega)}{2x_{zp}^2} = \frac{\Omega_m^2}{K(\Omega_m)} \frac{1}{2g_0^2} \overline{S}_{ii}(\Omega), \tag{5.1}$$

where $K(\Omega_m)$ is the transduction function, measured with the known phase modulation tone (cf. Section 4.2.4.2). The dynamical backaction, from the residual detuning of the probe laser, shifts the mechanical resonance frequency as the power is increased. In order to compare all the spectra, we always refer the horizontal axis to the effective resonance frequency, $\Omega_{\text{eff}}$. For resonant phase measurements, the

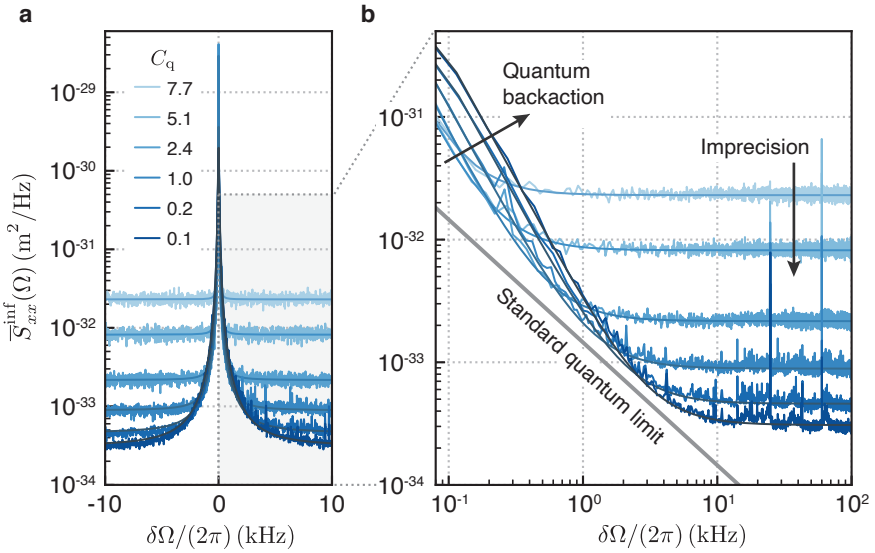


Figure 5.3: Displacement quantum measurements. a, Inferred displacement spectra around the effective mechanical frequency, $\Omega_{\text{eff}}$, for different quantum cooperativities, $C_q$. The Lorentzian fits are shown by smooth, thin solid lines. b, Logarithmic view of the off-resonant tails of the spectra shown in a. The spectral SQL is indicated by a solid gray line. Black arrows highlight the two main effects of increasing cooperativities, namely a reduction of the imprecision noise and an increase of the total force noise due to quantum backaction. Adapted from [Ros+18].

spectrum is governed by Equation 3.31. For a high-Q resonator, it consists of a Lorentzian peak, centered at $\Omega_m$ and driven by the total force noise spectrum, $\overline{S}^{\text{tot}}_{FF}$, on top of a constant imprecision noise, $\overline{S}_{\text{imp}}$. Increasing the quantum cooperativity has two main effects in the spectrum, as highlighted in Figure 5.3b: (i) reducing the imprecision noise, visible on the floor level and (ii) increasing the total force spectrum due to the increasing quantum backaction noise, visible as a raise of the Lorentzian tails, off resonance.

### 5.2.1 *Measurements at the Heisenberg limit*

*Imprecision and total noise effective occupation*

We fit, for each $\mathcal{C}_q$, the corresponding spectrum to a Lorentzian function with a constant background. From the fits we extract the area, $\overline{n}_{eff}$, the total linewidth, $\Gamma_{eff}$, and the background value, $\overline{S}_{imp}$. The total force noise equivalent occupation is obtained from $\overline{n}_{tot} = \overline{n}_{eff}\Gamma_{eff}/\Gamma_m$, where the last factor, $\Gamma_{eff}/\Gamma_m$, takes into account optical damping due to dynamical backaction. This represents the average phonon number that a single, effective bath should have to generate the same motion.

The imprecision noise, $\overline{S}_{imp}$, can also be expressed into an equivalent phonon number. This is accomplished by comparing it to the resonant displacement spectral value generated by a single-phonon-energy thermal bath, i. e. $\overline{S}^{1p}_{\hat{q}\hat{q}} := |\chi_m(\Omega_m)|^2 2\Gamma_m = 2\overline{S}^{zp}_{\hat{q}\hat{q}} = 2/\Gamma_m$ [Wil+15]. In SI units, this is given by $\overline{S}^{1p}_{\hat{x}\hat{x}} = 2x_{zp}^2\overline{S}^{1p}_{\hat{q}\hat{q}} = 4x_{zp}^2/\Gamma_m$. Then, the equivalent imprecision noise occupation is obtained as $\overline{n}_{imp} := \overline{S}_{imp}/\overline{S}^{1p}_{\hat{q}\hat{q}}$.

These occupations are theoretically modelled from Equation 3.30, assuming a resonant, broad cavity, i. e. $\Delta = 0$ and $\kappa \gg \Omega_m$, such that

$$\overline{n}_{imp} = \frac{\Gamma_m}{16\Gamma_{meas}} = \frac{1}{16\eta\,(\overline{n}_{th} + 1/2)\,\mathcal{C}_q}, \tag{5.2a}$$

$$\overline{n}_{tot} = \frac{2\gamma + 2\Gamma_{qba} + 2\Gamma^a_{qba}}{2\Gamma_m} = (\overline{n}_{th} + 1/2)\left(1 + \mathcal{C}_q + \mathcal{C}^a_q\right), \tag{5.2b}$$

where, in the total force noise occupation, we also take into account the weak quantum backaction noise from the auxiliary laser, with measurement strength $\Gamma^a_{qba}$ and quantum cooperativity $\mathcal{C}^a_q = \Gamma^a_{qba}/\gamma$.

We calculate these occupations, for each $\mathcal{C}_q$, from the Lorentzian fit parameters and fit them to Equation 5.2, as shown in Figure 5.4a and c. All measured imprecision (total force) noise occupation values agree with the theoretical expectation, from Equation 5.2a (Equation 5.2b), with independently measured parameters within a factor $1.03 \pm 0.06$ ($1.08 \pm 0.02$), where the uncertainty corresponds to $\pm 1$ standard deviation (s.d.).

In order to better assess the measurement regime of the experiment, we use these findings to compute the measurement efficiency, $\eta_{meas}$. We have in terms of the imprecision and total force occupation $\eta_{meas} = \left(16\overline{n}_{imp}\overline{n}_{tot}\right)^{-1}$ using Equation 3.33, and shown in Figure 5.4b. Our experiment, at $\mathcal{C}_q = 7.7$, features a measurement efficiency of $\eta_{meas} = 56\%$, close to the unity bound and operating, thus, in the quantum measurement regime. Indeed, this is sufficient for operating several quantum measurement and control protocols, as we will see.

*Heisenberg limit*

From the measurement efficiency we can also derive a bound on the Heisenberg measurement-disturbance relation for the probe field. We remind the reader that this inequality reads as $\overline{S}_{imp} \cdot \overline{S}_{qba} \geqslant 1/4$, as derived in Equation 3.32. The measurement efficiency can be recast as $\eta^{-1}_{meas} = 4\overline{S}_{imp}\overline{S}^{tot}_{FF} > 4\overline{S}_{imp}\overline{S}_{qba}$, since one always has $\overline{S}^{tot}_{FF} > \overline{S}_{qba}$. Thus, the Heisenberg measurement-disturbance relation can be upper

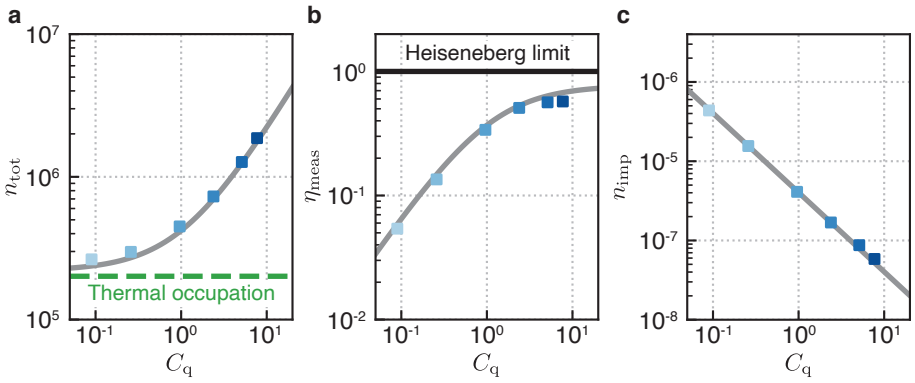


Figure 5.4: Imprecision and total force occupation and measurement efficiency. a, Total force noise, $\overline{n}_{\mathrm{tot}}$ and c, imprecision noise, $\overline{n}_{\mathrm{imp}}$, effective occupations (coloured squares), obtained from the Lorentzian fits of the spectra in Figure 5.3. The dashed green line indicates the thermal bath occupation. b, Measurement efficiency, $\eta_{\mathrm{meas}}$ (coloured squares) obtained from the values in a and c. The solid black line corresponds to the Heisenberg limit of $\eta_{\mathrm{meas}} = 1$. All data are fit to optomechanical models, shown in gray. Adapted from [Ros+18].

bounded by the measurement efficiency as $1/(4\eta_{\mathrm{meas}}) \geqslant \overline{S}_{\mathrm{imp}} \cdot \overline{S}_{\mathrm{qba}} \geqslant 1/4$. From our data, the largest measurement efficiency constraints the deviation from the ideal measurement at the Heisenberg limit to, at most, 33%. This result is, to our knowledge, the closest experimental value to the Heisenberg limit, making this experimental platform a mechanical realization of the Heisenberg microscope thought experiment [Hei27; Hei50].

Achieving such a large measurement efficiency is the result of two important aspects of our experimental platform: (i) a large probe quantum cooperativity and (ii) a large total detection efficiency for the BHD. The former aspect is achieved by drastically reducing the mechanical dissipation rate, $\Gamma_{\mathrm{m}}$. This reduces also the thermal decoherence rate well below the quantum backaction one. This requirement is common to other protocols, e. g. ground state preparation via sideband cooling. The latter aspect, instead, relates to the detection part and is a result of optimization of several optical components and alignment. It is crucial for any measurement-based protocol, in which the recorded measurement outcome plays a vital role in the preparation stage.

### 5.2.2 *Measurements at the SQL*

For a quantum measurement, at large measurement efficiency, the measured spectral noise approaches the SQL at some frequencies off resonance (cf. Section 3.4.1.1). In order to verify that we show, in Figure 5.3b, the spectral SQL, $\overline{S}^{\mathrm{SQL}}_{\hat{x}\hat{x}} = 2x_{\mathrm{zp}}^2|\chi_{\mathrm{eff}}(\Omega)|$, as discussed in Section 3.4.1.1. Here we use the effective susceptibility in order to cali-

brate out the effects of dynamical backaction. In particular, we notice that, upon a horizontal shift which brings the resonance frequency to zero, the effective susceptibility matches the natural one off resonance, at frequencies $|\delta\Omega| = |\Omega - \Omega_{\text{eff}}| \gg \Gamma_{\text{eff}}$. At the highest $\mathcal{C}_q$, from the Lorentzian fit in Figure 5.3, we find that the measured spectral noise is just 33% above the SQL, at $\delta\Omega/(2\pi) = 3.2$ kHz. This is, to our knowledge, the closest approach to the SQL achieved experimentally, improving what has been done in the past years in other experimental platforms, as ultracold atoms [Sch+14] or ultracold mechanical resonators [Kam+17].

*Effects of finite detuning*

The Lorentzian fits done so far assume a resonant probe field. In practice, this is not strictly the case as a finite, red detuning is always present, which we estimate to be $\Delta = -0.05\kappa$. Apart from small dynamical backaction effects, this also results in a correlation term in the measured phase quadrature spectrum, according to Equation 3.38. As seen, the correlations change sign around the mechanical resonance frequency, leading to a frequency asymmetric spectral lineshape. In particular, this can also improve the achievable sensitivity [Kam+17; Sud+17], at least in some frequency range.

In Figure 5.5a we show a closer view of the measured spectrum, at $\mathcal{C}_q = 7.7$, and the spectral SQL. The symmetric Lorentzian fit highlights a small asymmetry present in the data. To capture this feature, we also fit the data to a full model, in Equation 3.38, with $\theta = \phi = \pi/2$ and with the coupling rate, $g$, the total efficiency, $\eta$, and the detuning, $\Delta$, as free parameters. From the fitted values of the former two, we estimate a total force noise and imprecision occupations which agree with independent predictions, to within a factor of 1.08 and 1.07, respectively. The fitted detuning is $\Delta_{\text{fit}} = -0.04\kappa$, consistent with our initial estimation. The new, full fit can reproduce the measured asymmetric shape. To better visualize the distance to the SQL, we show in Figure 5.5b the same data and fit lines, normalized to the corresponding SQL at each frequency; that is, the spectral SQL now appears as a constant value at 1. From the full fit line, we estimate that the measured spectral noise approaches the SQL within 23%, for frequencies below the resonance, and within 46%, for frequencies above it. This represents an improvement compared to the simple Lorentzian fit, which averages together the two sides of the asymmetric spectrum.

### 5.2.3 *Consequences of quantum measurements for the mechanical state*

So far, we have focused on analyzing the different contributions to the measured spectrum. Regarding the mechanical state, the major effect of a quantum measurement is to enhance the total displacement fluctuations via quantum backaction noise. This results in a larger effective temperature, which leads to a more mixed state, compared to

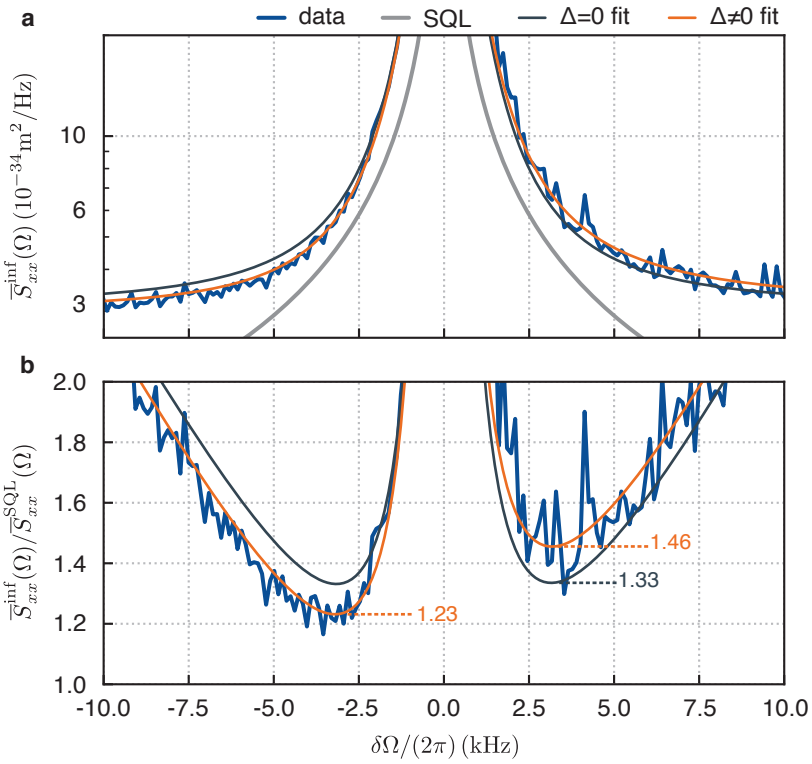


Figure 5.5: Residual spectral correlations arising from a non-zero detuning. a, Inferred displacement spectrum (blue), for $C_q = 7.7$, and the corresponding spectral SQL (gray). The data are fit both to a Lorentzian model (black) and to a full optomechanical model (orange) for general, non-resonant case. b, The data and fit lines, from a, normalized to the spectral SQL. Dashed coloured lines and labels indicates the minimum values of the fit lines, at frequencies both above and below the mechanical resonance. Adapted from [Ros+18].

the case of a classical measurement, where quantum backaction noise is negligible.

Thus, if one aims to precisely estimate the *actual* displacement of the mechanical resonator, with no or minimum disturbance from the measuring system, i. e. the probe optical field, then performing a quantum measurement would seem the worst choice. However, in a quantum measurement, the large displacement fluctuations induced by quantum backaction are always accompanied by a small imprecision noise in the measurement outcome, which allows the observer to keep track, in a clean way, of these total displacement fluctuations, for each measurement realization, which usually takes the form of a recorded photocurrent.

*Unconditional state*

So far, we have only considered statistical moments of an ensemble of such photocurrent records. In particular, we have calculated PSDs, which come from averaging the spectra of each single record together, thus ignoring part of the stochastic information carried by

each of them. The knowledge which only comes from the statistical quantities of an ensemble of measurement records, and not from the single records themselves, forms an *unconditional state* [WM10]. In our case of continuous displacement monitoring, the stationary mechanical unconditional state is Gaussian with the mean displacement and variance $\langle \hat{q} \rangle = 0$ and $\langle \hat{q}^2 \rangle = (\bar{n}_{th} + 1/2)(1 + \mathcal{C}_q)$, respectively. As previously noted, a quantum measurement, for which $\mathcal{C}_q \gg 1$, implies that the displacement variance is larger than the thermal one, i. e. $\langle \hat{q}^2 \rangle > \bar{n}_{th} + 1/2$.

*Conditional state*

Nonetheless, the observers can make use of each single measurement record to update and refine their own state of knowledge, i. e. the best knowledge about the system they possess. The new state obtained in this way is called a *conditional state*, because at any instant of time it is conditioned on the previous recorded measurement outcomes. The conditional state is strongly dependent on the measurement scheme adopted.For linear Gaussian systems, any measurement always generates a more pure conditional state [MK06] which, thereby, provides a more accurate description of the system. This also suggests that a conditional state should be interpreted as a *subjective* piece of knowledge, related to a particular observer which interacts with the system in some way, more than an *objective* property of the system. In fact, multiple observers, interacting with the same system in different ways, in general have different conditional states. In this sense, a state is just a mathematical tool which any observer generates in order to best predict outcomes of measurements done on the system [Wis96; WM10].

The conditional state, based on the stochastic measurement outcomes, evolves following a stochastic dynamics, based on random trajectories in the quantum configuration space, or phase space. As such, the conditional state is also interpreted as a *quantum trajectory*, the quantum analogy to classical phase space trajectories [Car93]. The next section focuses on introducing the concept of quantum trajectory, from the historical and conceptual point of view, and describing how experimentally observe that.

## 5.3 QUANTUM TRAJECTORY OF A MECHANICAL RESONATOR

The concept of a quantum trajectory was first introduced by Carmichael [Car93] in the context of quantum optics, as an alternative description of open quantum systems. Building from the photoelectron counting theory and the associated exclusive and non-exclusive probability densities, Carmichael derived a possible decomposition for the system density operator, which evolves according to a master equation. In such a decomposition, the state density operator results from summing up all the possible paths, from time 0 to t, which include non-unitary evolution, from the master equation, and photon counting events,

from an ideal photon counter. Any combination of these two operations forms a random path for the state, which was called a *quantum trajectory*. Summing over all these trajectories yields the state density operator, in a similar fashion to Feynman path integrals. The photon counting measurement scheme is somewhat arbitrary and provides one unravelling of the master equation, but is not a unique choice. A different unravelling, for example, is provided by photodetection, in which the outcome, a photocurrent, is a diffusive continuous process, instead of the point process arising from photon counting. Despite this arbitrariness, summing up all the trajectories always leads to the same state, which is the solution of the underlying master equation independently of the chosen unravelling.

*Diffusive unravelling from homodyne detection*

Here, we focus on the diffusive unravelling from homodyne photodetection, measuring the quadrature angle $\theta_l$. The quantum trajectory, represented by an operator $\hat{\rho}_c$, evolves according to an SME [Dió88; Bel95; JS06]

$$d\hat{\rho}_c = \frac{1}{i\hbar}\left[\hat{H}, \hat{\rho}_c\right] dt + \mathcal{D}[\hat{c}]\hat{\rho}_c\, dt + \sqrt{\eta}\mathcal{H}[\hat{c}e^{i\theta_l}]\hat{\rho}_c\, dW, \tag{5.3}$$

where $\hat{H}$ is the system's Hamiltonian, $\hat{c}$ one of its observable operators, $\eta$ the total efficiency and $dW$ the infinitesimal increment of a Wiener process.

Equation 5.3 has already been introduced in Section 1.6, in the context of quantum measurement theory. In combination with what is seen there, we can interpret the quantum trajectory, $\hat{\rho}_c$, as the conditional state of the observer who is performing the measurement described by the superoperator $\mathcal{H}$. The recorded photocurrent outcome, $i(t)$, on which the state is conditioned, is linked to the Wiener process in Equation 5.3 by

$$di(t) = \left\langle \frac{\hat{c}e^{i\theta_l} + \hat{c}^\dagger e^{-i\theta_l}}{\sqrt{2}} \right\rangle_c + \frac{dW}{\sqrt{2\eta}}, \tag{5.4}$$

where the quantum average, $\langle\cdot\rangle_c$, is performed over the conditional state, $\hat{\rho}_c$. The unconditional state evolution is recovered upon averaging over all the possible trajectories in Equation 5.3. This ensemble average removes the measurement superoperator and leads back to the Lindblad master equation, as described in Equation 1.43. In this case, the state non-unitary dynamics is affected only by the measurement-induced decoherence, $\mathcal{D}$, resulting in a mixed state. In contrast, the conditional state is also driven by the additional measurement conditioning term, $\mathcal{H}$, which can counteract the decoherence, producing pure states.

Together, Equation 5.4 and Equation 5.3 provide an operational way of constructing the conditional state, from the available measurement outcomes and the deterministic evolution. However, observing pure conditional states remains challenging, as it requires an efficient quantum measurement, for which the dominating decoherence source is

the measurement-induced one. This has been achieved only in microscopic, clean experimental settings, like in cavity [Gue+07] and circuit [Mur+13; Web+14] quantum electrodynamics. The observation for macroscopic systems, as a mechanical resonator [Doh+99; Doh+12], has remained elusive so far, precluded by small achievable measurement efficiency, $\eta_{\mathrm{meas}}$ [Wie+15]. In contrast, our experimental platform features a large measurement efficiency, as shown in Section 5.2.1, enabling the observation of pure quantum trajectories [Ros+19], as we will see in the next sections.

### 5.3.1 *Experimental setup and effective model*

We employ the same setup shown already in Figure 5.2, but the measurements we report here are taken during a subsequent cryogenic cycle. This leads to slightly different parameters, which we measure again each time. The probe laser is locked close to the resonance of a cavity mode at $\lambda = 796.299$ nm, with linewidth $\kappa/(2\pi) = 18.5$ MHz and a detuning of $\Delta \geqslant -0.05\kappa$. The vacuum optomechanical coupling, measured via the coherent response calibration (cf. Section 4.2.4.1), is $g_0/(2\pi) = (129 \pm 2)$ Hz, where the errors are given by the m.a.d.. The phase of the transmitted field is continuously monitored via a BHD, whose total efficiency, comprising total detection efficiency and cavity overcoupling, is $\eta = 74\%$.

The auxiliary laser is locked to the red side of a different cavity mode at $\Delta_a = -5.6$ MHz, and used for stabilization of low-frequency modes, as seen in Section 5.1. The chosen cavity mode is at $\lambda_a = 795.906$ nm and has a linewidth of $\kappa_a/(2\pi) = 13.0$ MHz. The membrane is the same one as used in Section 5.2 and has a resonance frequency of $\Omega_m/(2\pi) = 1.14$ MHz and a quality factor $Q = 1.03 \times 10^9$. We also assume a thermal bath temperature of $T = 11$ K, as obtained in a different cryogenic cycle from quantum noise thermometry (cf. Section 4.2.4.2). The assumption of equal thermalization between these two different thermal cycles is supported by the fact that the optomechanical cavity has always remained in the vacuum environment, and was never detached from the cold finger. In addition, in the large quantum backaction regime, in which the system operates, the thermal noise is negligible and the exact thermal bath temperature does not play an important role.

*Unconditional state*

We characterize the unconditional state from the displacement spectrum of the homodyne photocurrent, shown in Figure 5.6a. We fit it to a Lorentzian function and extract the effective mechanical linewidth, $\Gamma_{\mathrm{eff}}/(2\pi) = 130$ Hz, and the effective average phonon number, $\bar{n}_{\mathrm{eff}} = 18$. Both are affected by dynamical backaction and optical cooling from the red-detuned auxiliary laser, as well as the slightly detuned probe laser. The undetected auxiliary laser contributes to the effective occupation also with its own quantum backaction noise.

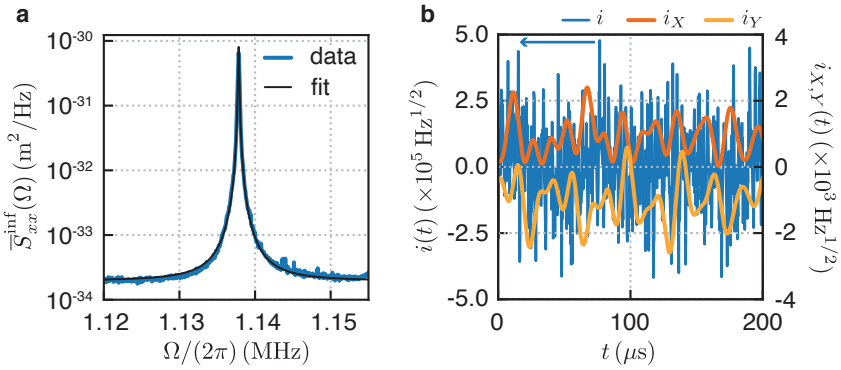


Figure 5.6: Homodyne photocurrent and demodulated quadratures. a, Inferred displacement spectrum (blue) from a phase measurement, averaged over several realizations, with a Lorentzian fit (black). b, Example of calibrated homodyne photocurrent (blue) in shot noise units. Demodulating it at $\Omega_m$ yields the two electronic quadratures, $i_X$ (dark orange) and $i_Y$ (light orange).

From the measured parameters, we estimate a quantum backaction decoherence of $A_+^q/(\Gamma_m \overline{n}_{th}) = 0.16$ (cf. Equation 3.16). From the point of view of the probe laser, such decoherence from the auxiliary quantum backaction cannot be discriminated from the thermal one. Thus, the two of them form an effective thermal bath, characterized by an effective occupation of $\overline{n}'_{th} = 2$ and a total decoherence of $\overline{n}'_{th}\Gamma_{eff} = 2\pi \times 260$ Hz. In the following, with abuse of notation, we will indicate the effective parameters with the same symbols of the thermal bath, that is $\Gamma_m$, $\overline{n}_{th}$ and $\gamma$ will refer to, respectively, the effective thermal bath coupling rate, average phonon occupation and decoherence rate. The probe field is characterized by its quantum backaction decoherence rate, $\Gamma_{qba}/(2\pi) = 2.54$ kHz, and by the measurement rate, $\Gamma_{meas}/(2\pi) = 1.88$ kHz. From them we estimate a measurement efficiency of $\eta_{meas} = \Gamma_{meas}/(\gamma + \Gamma_{qba}) = 67\%$.

We now move to construct a conditional state from this measurement. First, we record and digitize the photocurrent $i(t)$ with a DAQ card (cf. Section 4.1.3.2) and store it permanently on a computer. The next operations are done offline in post-processing on these digital records. Such a recorded time trace contains displacement signals from several mechanical modes, discriminated by their resonance frequency. The signal we are after is only at the frequency components around the mechanical frequency, $\Omega_m$. We extract it by performing a numerical demodulation of the raw time trace, at $\Omega_m$, within a bandwidth $\delta\Omega$, from which we obtain the two electronic quadrature signals

*Demodulated quadratures*

$$i_X = k(t) * [i(t)\cos(\Omega_m t)]\,, \tag{5.5a}$$

$$i_Y = k(t) * [i(t)\sin(\Omega_m t)]\,. \tag{5.5b}$$

The function $k(t)$ represents the kernel of the low-pass filter employed to define the demodulated signal bandwidth. In practice, we use

a Butterworth filter with fourteen poles and a 3 dB bandwidth of $\sim$ 60 kHz. This is chosen to be much larger than the probe field measurement rate while, at the same time, suppressing sufficiently the contributions of other mechanical modes to the total demodulated variance. An example of a raw photocurrent and the demodulated quadratures is shown in Figure 5.6b. These electronic quadratures, $i_X$ and $i_Y$, are a simultaneous measurement of the slowly varying quadratures, $\hat{X}$ and $\hat{Y}$, of the mechanical position, $\hat{q}$, which can be written as $\hat{q} = \hat{X}(t)\cos(\Omega_m t) + \hat{Y}(t)\sin(\Omega_m t)$. For high-Q mechanical resonators, the pair of slow quadratures $\hat{\mathbf{r}} \coloneqq (\hat{X}, \hat{Y})$ also describes the momentum dynamics. If continuously done, such a measurement allows to reconstruct the mechanical complex amplitude. In the ideal limit of no additional noise, this realizes a von Neumann projective measurement on mechanical coherent states [JSo6].

*Quantum trajectory dynamics*

The conditional state, $\hat{\rho}_c$, conditioned on the electronic measurement outcomes, $\mathbf{i} = (i_X, i_Y)$, can be described by the following equation [Doh+12]

$$d\hat{\rho}_c = \left(\mathcal{L}_{th} + \mathcal{L}_{qba}\right)\hat{\rho}_c + \sqrt{\Gamma_{meas}}\left(\mathcal{H}[\hat{X}]\hat{\rho}_c\, dW_X + \mathcal{H}[\hat{Y}]\hat{\rho}_c\, dW_Y\right), \quad (5.6)$$

which is derived from the effective master equation for the mechanical resonator, in a frame rotating at $\Omega_m$, obtained by adiabatically eliminating the cavity mode and performing the RWA for the mechanics [Hof17] (cf. Equation 3.14). The latter is justified by the timescale separation of the problem, in which the resonance frequency is much faster than any other dynamics, i. e. $\Omega_m \gg \Gamma_m, \Gamma_{meas}$. For the effective parameters of our experiment, in fact, we have $\Omega_m/\Gamma_m = 8.8 \times 10^3$ and $\Omega_m/\Gamma_{meas} = 6 \times 10^2$. We also notice that we have now switched to a master equation description, in a Schrödinger picture, in contrast with the unconditional case, in which we employed the Heisenberg picture with the QLE. Although the conditional dynamics could in principle be derived in the Heisenberg picture too, its interpretation is more clear in the master equation approach, which we therefor decide to pursue.

The first two terms on the RHS of Equation 5.6 are the decoherence arising from, respectively, the thermal noise and the quantum backaction noise from the measurements. They are defined as

$$\mathcal{L}_{th}\hat{\rho} = \Gamma_m \bar{n}_{th}\mathcal{D}[\hat{c}^\dagger]\hat{\rho} + \Gamma_m(\bar{n}_{th}+1)\mathcal{D}[\hat{c}]\hat{\rho}, \quad (5.7a)$$

$$\mathcal{L}_{qba}\hat{\rho} = \Gamma_{qba}\mathcal{D}[\hat{X}]\hat{\rho} + \Gamma_{qba}\mathcal{D}[\hat{Y}]\hat{\rho}. \quad (5.7b)$$

where we have introduced the slow mechanical displacement amplitude $\hat{c} = \left(\hat{X} + i\hat{Y}\right)/\sqrt{2}$ and the dissipation superoperator, $\mathcal{D}$, defined in Section 1.3. The last two terms on the RHS of Equation 5.6 describe the conditioning on the measurement records, via the two independent Wiener processes $\mathbf{W} = (W_X, W_Y)$

$$\mathbf{i}(t)dt = \sqrt{4\Gamma_{meas}}\mathbf{r}_c(t)dt + d\mathbf{W}. \quad (5.8)$$

The vector $\mathbf{r}_c$ represents the average displacement over the conditional state, i. e. $\mathbf{r}_c(t) = \mathrm{tr}(\hat{\mathbf{r}}\,\hat{\rho}_c(t))$.

The system is linear and Gaussian and, as such, its state is fully characterized by the average displacement $\mathbf{r}_c(t)$ and its covariance matrix $2(V_c)_{ij} = \langle \hat{r}_i, \hat{r}_j \rangle_c + \langle \hat{r}_j, \hat{r}_i \rangle_c$, with the correlator $\langle \cdot, \cdot \rangle = \langle \cdot\cdot \rangle - \langle \cdot \rangle \langle \cdot \rangle$, which takes a simple diagonal form proportional to the identity in our case, i. e. $(V_c)_{ij}(t) = V_c(t)\delta_{ij}$. These two moments form the *mechanical quantum trajectory* which, from Equation 5.6, evolve according to

*Average displacement and variance of quantum trajectory*

$$d\mathbf{r}_c(t) = -\frac{\Gamma_m}{2}\mathbf{r}_c(t)dt + \sqrt{4\Gamma_{meas}V_c(t)^2}\,d\mathbf{W}, \tag{5.9a}$$

$$\dot{V}_c(t) = -\Gamma_m V_c(t) + \Gamma_m\left(\overline{n}_{th} + \frac{1}{2}\right) + \Gamma_{qba} - 4\Gamma_{meas}V_c(t)^2. \tag{5.9b}$$

The initial conditions are based on the initial state, which we assume to be the unconditional thermal state, where $\mathbf{r}_c(0) = 0$ and $V_c(0) = V_{uc} \coloneqq \overline{n}_{th} + 1/2 + \Gamma_{qba}/\Gamma_m$. In particular, the average displacement $\mathbf{r}_c(t)$ evolves stochastically, conditioned on the measurement outcomes through the Wiener process. In fact, from Equation 5.8 we get $d\mathbf{W} = \mathbf{i}dt - \sqrt{4\Gamma_{meas}}\mathbf{r}_c\,dt$. An operational prescription to compute the first moment of the quantum trajectory is obtained by discretizing Equation 5.9a and inserting the expression of the Wiener increment in terms of the outcomes $\mathbf{i}$, i. e.

*Recursive relation for operational computation*

$$\mathbf{r}_c(t+\Delta t) = \left[1 - \left(\frac{\Gamma_m}{2} + 4\Gamma_{meas}V_c(t)\right)\Delta t\right]\mathbf{r}_c(t) + \sqrt{4\Gamma_{meas}V_c(t)^2}\,\mathbf{i}(t)\Delta t, \tag{5.10}$$

where $\Delta t$ is the time step in the digitized trace and the conditional variance, $V_c(t)$, is calculated from the solution of Equation 5.9b. From the signal processing perspective, Equation 5.10 describes a discrete-time, Lorentzian low-pass filter with a time-dependent bandwidth. At the steady-state, this bandwidth becomes $\Gamma_m/2 + 4\Gamma_{meas}\overline{V}_c \approx 2\Gamma_{meas}$, where the last approximation holds for large measurement efficiency. Formally, in fact, Equation 5.9 are equivalent to the equations for a Kalman filter [Kai82; GLS16], with additional constraints between the process and measurement noises dictated by quantum mechanics.

In order to observe the quantum trajectory, we chop the demodulated photocurrent time traces into 3.2 ms-long segments. We consider each of them as an independent realization of the measurement, and use them to form a statistical ensemble. Then, we calibrate each realization into shot noise units. To do that, we perform a similar measurement and processing, but with the transmitted cavity field blocked. As a result, the measured demodulated photocurrent, $\mathbf{i}_{sn}$, contains only shot noise, represented by the Wiener process in Equation 5.8. In particular, the spectrum of such a photocurrent is flat. We take the square root of the average value of the measured shot noise spectrum, in the range $1.120 \div 1.155$ MHz, as the calibration constant,

c. Then, we calibrate the main photocurrent, $\mathbf{i}$, by dividing through by calibration constant. In this way, the equivalent shot noise level in the spectrum of the calibrated photocurrent will appear at the value of 1 Hz/Hz. Finally, we apply the recursive relation in Equation 5.10 to all the realizations in the ensemble to obtain the average displacement of the quantum trajectories. We show an example in Figure 5.7a. The conditional state variance, shown in Figure 5.7b, is instead obtained by solving the differential Equation 5.9b, with the measured parameters. In particular, the variance evolution clearly shows a collapse, over

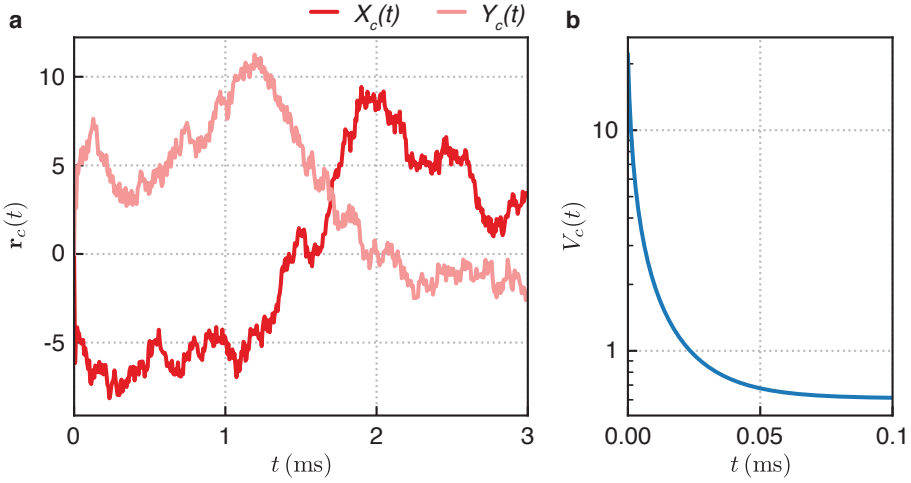


Figure 5.7: Measuring the mechanical quantum trajectory. a, Example of average displacement, $\mathbf{r}_c(t)$, from a quantum trajectory. The two slow quadratures, $X_c(t)$ and $Y_c(t)$, are shown, respectively, in dark and light red. b, Theoretical prediction for the evolution of the conditional variance, $V_c(t)$, during the collapse, from the beginning of the measurement at time $t = 0$ ms. For longer time, not displayed, the conditional variance is stationary at the steady-state value $\overline{V}_c$.

the first $\sim 100\,\mu s$ from the beginning of the measurement. Due to the large measurement efficiency in which the system operates, the predicted steady-state variance is $\overline{V}_c = 0.61$, only 20% larger than the variance of a pure coherent state. The conditional state purity is $\mathcal{P}_c := \mathrm{tr}(\hat{\rho}_c^2) = 1/(2\overline{V}_c) = 82\%$, which constitutes an improvement of more than an order of magnitude compared to the initial thermal state, with purity of $\mathcal{P}_{uc} = 0.02\%$.

*Innovation sequence*

The derivation of the quantum trajectory, shown in Figure 5.7, depends on the modelling used in the SME. In order to gain confidence in its validity, we evaluate the experimental innovation sequence, $\mathbf{v}dt = \mathbf{i}dt - \sqrt{4\Gamma_{meas}V_c(t)}\mathbf{r}dt$. If the model correctly describes the experiment, then such a sequence should be white noise [Wie+15]. We show the innovation spectrum, averaged over all the measured realizations of the quantum trajectory $\mathbf{r}_c$, in Figure 5.8, together with the spectrum of the raw photocurrent, representing the unconditional state. The flat innovation spectrum corroborates the model employed

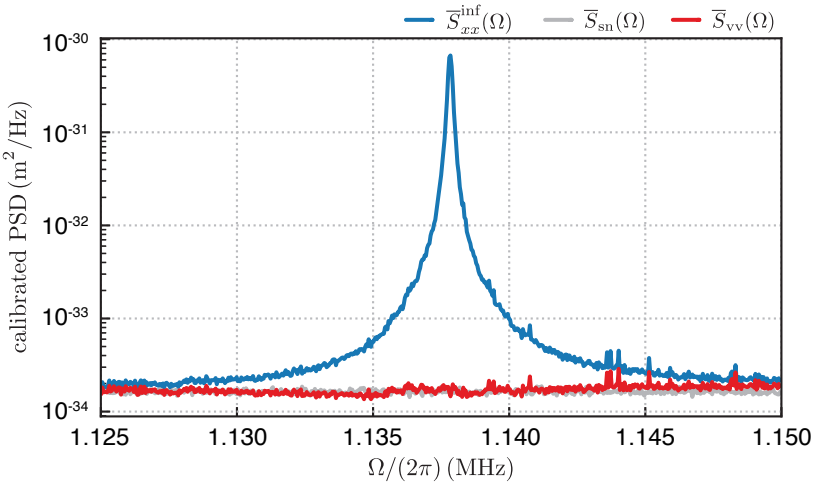


Figure 5.8: Consistency of the innovation sequence. Spectra of the inferred displacement (blue), shot noise (gray) and innovation sequence (red). The innovation spectrum is flat, validating the model assumed in the Equation 5.6. Adapted from [Ros+19].

in deriving the quantum trajectory. A small deviation is also visible, which has an asymmetric lineshape around the resonance, arising from residual optomechanical correlations induced by the small non-zero detuning of the probe laser, not included in Equation 5.6.

#### 5.3.1.1 *Covariance of the conditional mechanical state*

The quantum trajectory cannot be fully observed from the measurement outcomes. In fact, the conditional variance $V_c(t)$ evolves deterministically and is not affected by the actual measurement outcomes, but only by the measurement scheme and efficiency. This is common to all linear Gaussian systems. When deriving the quantum trajectory in Figure 5.7, we resort, for the conditional variance, to the exact solution of the Riccati Equation 5.9b, which is

$$V_c(t) = \overline{V}_c + \frac{2\overline{V}_c + \Gamma_m/(4\Gamma_{\mathrm{meas}})}{e^{(8\overline{V}_c\Gamma_{\mathrm{meas}}+\Gamma_m)t}\left[1+\Gamma_m/(4\Gamma_{\mathrm{meas}}\overline{V}_c)\right]^2-1}. \tag{5.11}$$

The equation describes a collapse from the initial variance, which happens over a finite time, independent of the initial value itself due to the non-linear term arising from the measurement conditioning. The steady-state conditional variance is

*Steady-state*

$$\overline{V}_c = \frac{\sqrt{1+16V_{uc}\Gamma_{\mathrm{meas}}/\Gamma_m}-1}{8\Gamma_{\mathrm{meas}}/\Gamma_m}. \tag{5.12}$$

We can make several interesting observations on $\overline{V}_c$. Firstly, one can show that the steady-state conditional variance is always smaller than the unconditional one, i. e. $\overline{V}_c < V_{uc}$, as expected from linear, Gaussian measurements. In other words, the purity of the conditional state

$\mathcal{P}_c$ always exceeds the one of the corresponding unconditional state. Secondly, the steady-state conditional variance can be used to classify the performed measurement, when compared to the limiting cases of an ideal measurement and no measurement at all. We individuate the following three classes of displacement measurements:

POOR MEASUREMENT Whenever the conditional variance is not reduced below the thermal one, i. e. $\overline{V}_c > V_{th} = \overline{n}_{th} + 1/2$, we have a *poor measurement*. In this case, in fact, not performing the measurement at all by turning off the interaction, $g = 0$, would give rise to an unconditional state which is more pure, i. e. $V_{uc} = V_{th}$. The condition for a poor measurement, in terms of the total efficiency, is

$$\eta \leqslant \frac{1}{4V_{th}^2}. \tag{5.13}$$

QUANTUM MEASUREMENT For more efficient measurements, the conditional variance is reduced below the thermal one. The other limiting case is when the conditional variance corresponds to an average phonon number less than one, i. e. $\overline{V}_c < 3/2$. Despite being arbitrary, this threshold has been used in the scientific community as a gauge for the quantum ground state preparation. When this condition is verified, we talk about a *quantum measurement*. In terms of measurement efficiency, this is equivalent to

$$\eta_{meas} > \frac{1}{9} - \frac{1}{6V_{uc}} \approx \frac{1}{9}. \tag{5.14}$$

In this regime, the steady-state conditional variance is approximately given by

$$\overline{V}_c \approx \frac{1}{\sqrt{4\eta_{meas}}}, \tag{5.15}$$

which depends only on the measurement efficiency $\eta_{meas}$. At the Heisenberg limit of $\eta_{meas} = 1$, we have that $\overline{V}_c = 1/2$, which is the ultimate limit for the steady-state conditional variance of continuous displacement monitoring. In this case, the conditional state is a pure coherent one, with amplitude stochastically evolving in the configuration space. It resembles the classical picture of a phase space, with the main difference being the presence of fundamental, quantum fluctuations, of the order of the zero-point motion. We note that this limit does not hold indefinitely. In fact, achieving exactly $\eta_{meas} = 1$ requires, among other things, to having an infinite measurement strength $\Gamma_{qba}$. As $\Gamma_{qba}$ is increased, at some point it will overcome the mechanical resonance frequency $\Omega_m$, breaking down the RWA on which this quantum trajectory description is based [Doh+12]. Then, in this

*Breaking down of the RWA*

limit Equation 5.12 is not valid anymore and one should consider all the counter-rotating terms in the full master equation. Physically, what is happening is that the measurement is so strong that the conditional variance collapses in a time much shorter than the mechanical period. Then, the mechanical state is essentially frozen over the collapse time and the measurement reduces to a single-quadrature projector. This can lead, then, to a conditional mechanical squeezed state, for which the variance of one quadrature is below the coherent limit of 1/2 [Men+20].

CLASSICAL MEASUREMENT Finally, we can also define an intermediate regime between that of a poor and a quantum measurement. We call it the *classical measurement* regime, obtained whenever the steady-state conditional variance is smaller than the thermal one, but larger than a single phonon, i. e. $V_{th} > \overline{V}_c > 3/2$. In terms of measurement efficiency

$$\frac{1}{4V_{th}^2} > \eta_{meas} > \frac{1}{9} - \frac{1}{6V_{uc}} \approx \frac{1}{9}. \tag{5.16}$$

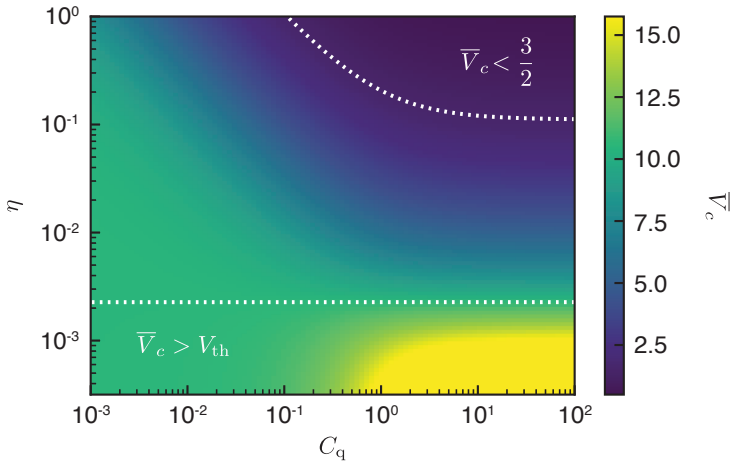


Figure 5.9: Steady-state conditional variance. Conditional variance, $\overline{V}_c$, as a function of quantum cooperativity, $\mathcal{C}_q$, and total efficiency, $\eta$. The dashed white lines define three regions, according to the value of $\overline{V}_c$. Poor measurements are performed whenever $\overline{V}_c > V_{th}$, whereas quantum measurements are defined by $\overline{V}_c < 3/2$. In between, there is the classical measurement regime. The dashed white line defining the boundary of the quantum measurement region corresponds to the contour of constant measurement efficiency, at $\eta_{meas} = 1/9$. The thermal occupation is $\overline{n}_{th} = 10$.

In Figure 5.9 we plot the steady-state conditional variance, divided into the three classes, as a function of two important parameters, the total efficiency $\eta$ and the quantum cooperativity $\mathcal{C}_q$, from which the measurement efficiency is defined.

### 5.3.2 *Retrodiction measurement and past quantum states*

A continuous displacement measurement, carried out up to time $t_0$, prepares a conditional state described by the average displacement $\mathbf{r}_c(t_0)$ and variance $V_c(t_0)$. The previous measurement outcome $\mathbf{i}(t)$, with $t \leqslant t_0$, can be used to verify and obtain the average displacement of the prepared state, $\mathbf{r}_c(t_0)$, as described in the previous section. The conditional state variance, however, evolves deterministically and cannot be verified from the available experimental outcomes. In order to carry out this verification step, the observer could, ideally, perform a projective measurement on coherent states, at time $t_0$, and collect statistics over several experimental realizations. In practice, projective measurements exist as a limit of generalized measurements, which are described in terms of effects and operations. The possible measurement outcomes, and the associated probability, are encoded in an *effect operator*, $\hat{E}_k$, analogous to the projector in ideal measurements. Upon realization of a given outcome $k$, the change in the system state, known as the post-measurement state, is given by an *operation superoperator*, acting on the a-priori state. In our experiment, we implement a generalized measurement, for this verification, in the form of a *retrodiction measurement* [GJM13; Tan+15; ZM17; Lam18]. This is based on the back-propagation of an effect operator from time $t > t_0$ back to $t_0$, based on the outcomes recorded in this future time interval. The back-propagation refines, in a Bayesian sense, the probability distribution for the measurement outcomes, as determined by the *past* state $\hat{\rho}_c$. However, in contrast with standard generalized measurement, the retrodiction has no operation, because the state on which we give information belongs to the past and does not exist anymore at the time of the retrodiction. In this sense, a post-measurement state for retrodiction is unphysical.

*Effects and operations*

*Past quantum state*

Together the quantum trajectory, $\hat{\rho}_c(t_0)$, and the effect, $\hat{E}(t_0)$, form the so-called *past quantum state* [GJM13]. This state can be used to provide more general and accurate expectation values for a system operator $\hat{O}$ according to

$$\left\langle \hat{O} \right\rangle (t_0) = \mathrm{tr}(\hat{O}\hat{\rho}_c(t_0)\hat{E}(t_0))/\mathrm{tr}(\hat{\rho}_c(t_0)\hat{E}(t_0)), \tag{5.17}$$

where one has to keep in mind that $\hat{\rho}_c(t_0)$ and $\hat{E}(t_0)$ only depend, respectively, on the past and future time with respect to $t_0$. Equation 5.17 generalizes the usual expectation value rule in quantum mechanics. If the retrodiction measurement is not performed, one has $\hat{E}(t_0) = \hat{\mathbb{1}}$ and Equation 5.17 only depends on the past through the conditional state, as expected from the standard calculation of expectation values. Vice versa, if the state at time $t_0$ is ignored and only the retrodiction measurement is performed, one has $\hat{\rho}_c \propto \hat{\mathbb{1}}$ and Equation 5.17 exclusively depends on the future through the effect operator. In fact, the effect operator is a dynamical quantity. The evolution of this operator, when

conditioned on future outcomes, is governed by a stochastic backward Itô equation [Lam18]. For our experimental system under the cavity adiabatic elimination and the mechanical RWA, the unnormalized equation for the conditional effect operator, $\hat{E}_c$, is [ZM17; Lam18]

$$
\begin{aligned}
-\mathrm{d}\hat{E}_c(t) &= \hat{E}_c(t-\mathrm{d}t) - \hat{E}_c(t) = \\
&\left(\mathcal{L}^{\dagger}_{\mathrm{th}} + \mathcal{L}^{\dagger}_{\mathrm{qba}}\right)\hat{E}_c\,\mathrm{d}t + \sqrt{\Gamma_{\mathrm{meas}}}\left(\widetilde{\mathcal{H}}^{\dagger}[\hat{X}]\hat{E}_c\,\mathrm{d}W_{E,X} + \widetilde{\mathcal{H}}^{\dagger}[\hat{Y}]\hat{E}_c\,\mathrm{d}W_{E,Y}\right),
\end{aligned}
\tag{5.18}
$$

where the adjoint superoperators, $\mathcal{L}^{\dagger}$, are defined similarly to the superoperators, $\mathcal{L}$, in Equation 5.7, with the replacement $\mathcal{D} \to \mathcal{D}^{\dagger}$ and

*Average displacement and variance of the retrodiction measurement*

$$
\mathcal{D}^{\dagger}[\hat{c}]\hat{E} = \hat{c}^{\dagger}\hat{E}\hat{c} - \frac{\hat{c}^{\dagger}\hat{c}\hat{E} + \hat{E}\hat{c}^{\dagger}\hat{c}}{2}, \tag{5.19a}
$$

$$
\widetilde{\mathcal{H}}^{\dagger}[\hat{c}]\hat{E} = \hat{c}^{\dagger}\hat{E} + \hat{E}\hat{c}. \tag{5.19b}
$$

We note that Equation 5.18 is linear in the conditional state, since the measurement superoperator in Equation 5.19b does not depend on averaged values. This stems from choosing to adopt an unnormalized evolution, according to Equation 5.18.

Based on Equation 5.17 with $\hat{\rho}_c = \hat{\mathbb{1}}$, we use the conditional effect operator obtained from solving Equation 5.18 to calculate the average displacement, $\mathbf{r}_E = \langle \hat{\mathbf{r}} \rangle_E$, and the covariance matrix, $2(V_E)_{ij} = \langle \hat{r}_i, \hat{r}_j \rangle_E + \langle \hat{r}_j, \hat{r}_i \rangle$. The latter is a diagonal matrix, i. e. $(V_E)_{ij} = V_E \delta_{ij}$, similar to the quantum trajectory. The equations of motion for these two moments are

$$
-\mathrm{d}\mathbf{r}_E(t) = \frac{\Gamma_m}{2}\mathbf{r}_E\,\mathrm{d}t + \sqrt{4\Gamma_{\mathrm{meas}}V_E(t)^2}\,\mathrm{d}\mathbf{W}_E. \tag{5.20a}
$$

$$
-\dot{V}_E(t) = \Gamma_m V_E(t) + \Gamma_m\left(\overline{n}_{\mathrm{th}} + \frac{1}{2}\right) + \Gamma_{\mathrm{qba}} - 4\Gamma_{\mathrm{meas}}V_E(t)^2. \tag{5.20b}
$$

Again, the retrodicted average displacement depends on the measurement outcomes via $\mathrm{d}\mathbf{W}_E = \mathbf{i}\mathrm{d}t - \sqrt{4\Gamma_{\mathrm{meas}}}\mathbf{r}_E\,\mathrm{d}t$, whereas the conditional retrodicted variance is deterministic and assumes the value $\overline{V}_E = \overline{V}_c + \Gamma_m/(4\Gamma_{\mathrm{meas}}) \approx \overline{V}_c$ at the steady-state. The approximation holds in the quantum measurement regime, which is the relevant one in our experiment.

The retrodicted average displacement, $\mathbf{r}_E(t_0)$, is operationally obtained from filtering the experimental outcomes at time $t > t_0$ with the recursive relation derived from the discretization of Equation 5.20a, similar to what was done for the quantum trajectory. In Figure 5.10a we show the average displacement, obtained from the recorded realizations, both from the quantum trajectory, evolved up to $t_0$, and from the retrodicted effect operator, evolved backward down to $t_0$.

In particular, we ensure that $t_0$ is away from the initial time evolution of both the quantum trajectory and the effect operator, such

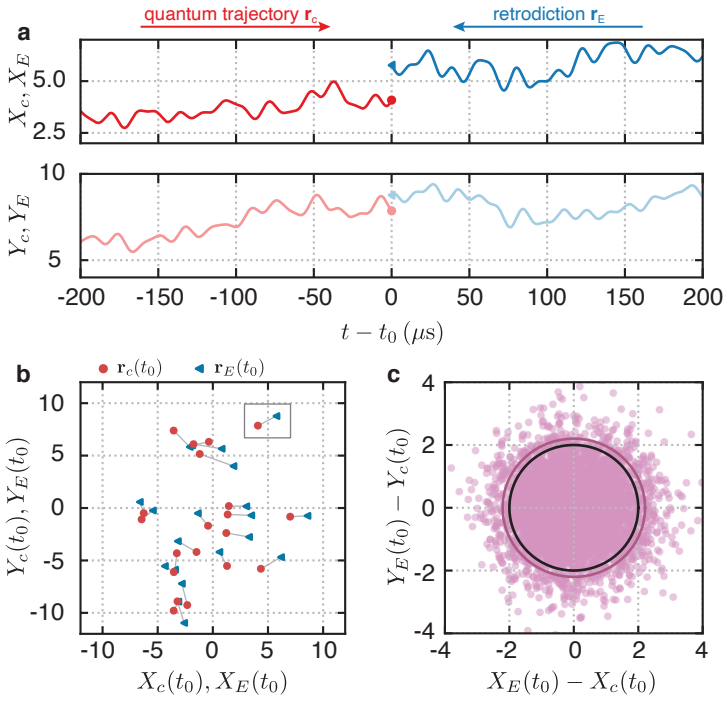


Figure 5.10: Verification of the conditional state. a, Average displacement coming from the quantum trajectory, $\mathbf{r}_c(t)$, (quadratures in dark and light red) and the retrodicted effect, $\mathbf{r}_E(t)$, (quadratures in dark and light blue), calculated up to $t_0$. b, Ensemble of average displacements from quantum trajectories $\mathbf{r}_c(t_0)$ (red circles) and retrodicted effect $\mathbf{r}_E(t_0)$ (blue triangles), at $t_0$, from different experimental realizations. Each pair is connected by a gray line. The example shown in a is highlighted by a gray box. c, Phase space distribution for the distance $\mathbf{d}(t_0)$ (purple circles). The purple (black) line corresponds to two s.d. of the data (pure coherent state), with radius $2\sqrt{V_d}$ ($2\sqrt{1}$). Adapted from [Ros+19].

that the corresponding variance is always at the steady-state. In this case, both $\mathbf{r}_c(t_0)$ and $\mathbf{r}_E(t_0)$ are drawn from Gaussian distributions with variances $\overline{V}_c$ and $\overline{V}_E$. One can expect that the *distance* between these two expectation values, i. e. $\mathbf{d}(t_0) \coloneqq \mathbf{r}_E(t_0) - \mathbf{r}_c(t_0)$, also is a Gaussian variable with a zero mean and a variance equals to the sum of the variances of the quantum trajectory and the retrodiction effect, i. e. $V_d(t_0) = \overline{V}_c + \overline{V}_E \approx 2\overline{V}_c$. Therefore, we are able to verify the variance of the conditional state by comparing the first moments coming from independent sections of the data. In the next section, we prove the latter relation and extend it to the case of a conditional variance not in the steady-state.

*Experimental verification of the conditional state variance*

In Figure 5.10b we collect the average displacements, $\mathbf{r}_c(t_0)$ and $\mathbf{r}_E(t_0)$, from different realizations in a phase space. Each pair is connected by a gray line, which represents the distance outcome, $\mathbf{d}(t_0)$. The ensemble of all distances is shown in Figure 5.10c as a

2D histogram. We calculate the covariance matrix of the distances as $(V_d)_{ij} = \mathbb{E}\left[d_i(t_0)d_j(t_0)\right] - \mathbb{E}\left[d_i(t_0)\right]\mathbb{E}\left[d_j(t_0)\right]$. In practice, we find that $(V_d)_{12} \approx 0$ and $(V_d)_{11} \approx (V_d)_{22}$ within 2%, thereby we only report the average of the diagonal terms, i. e. $V_d = [(V_d)_{11} + (V_d)_{22}]/2$. From the data, we obtain that $V_d = 1.29 \pm 0.02$, which agrees with the predicted value $V_d(t_0) \approx 2\overline{V}_c = 1.24$ to within 4%. The uncertainty in the measured variance reflects statistical uncertainties due to the ensemble finite size, whereas a systematic error of 6% introduced by the demodulation filter has been subtracted (cf. Section 5.3.4). The verified conditional state has, then, a purity of $\mathcal{P}_c = 0.78$ and corresponds to a thermal state, randomly displaced, with an average occupancy of 0.14 phonons, which is much lower than the initial unconditional thermal state. In this sense, this process is sometimes referred to as *cooling-by-measurement* [Van+13].

#### 5.3.2.1 *Derivation of covariance of distance*

Here we prove that

$$V_d(t) = V_c(t) + \overline{V}_E, \tag{5.21}$$

for any time $t$ from the beginning of the measurement, happening at $t = 0$ s, and assuming that the retrodiction measurement has reached the steady-state.

Using the definition of the distance, $\mathbf{d}$, we cast the covariance matrix as

$$\mathbf{V}_d(t) = \mathbb{E}\left[(\mathbf{r}_E(t) - \mathbf{r}_c(t))^2\right] = \mathbb{E}\left[\mathbf{r}_c(t)^2\right] + \mathbb{E}\left[\mathbf{r}_E(t)^2\right] - 2\mathbb{E}\left[\mathbf{r}_c(t)\mathbf{r}_E(t)\right], \tag{5.22}$$

where we took advantage of the fact the $\mathbb{E}[\mathbf{r}_c] = \mathbb{E}[\mathbf{r}_E] = 0$. We use the integral form of Equation 5.9a and Equation 5.20a for calculating the three expectation values in Equation 5.22, i. e.

$$\mathbf{r}_c(t) = \sqrt{4\Gamma_{meas}} \int_0^t V_c(s) e^{-\frac{\Gamma_m}{2}(t-s)} d\mathbf{W}(s), \tag{5.23a}$$

$$\mathbf{r}_E(t) = \sqrt{4\Gamma_{meas}}\overline{V}_E \int_t^\infty e^{-\frac{\Gamma_m}{2}(t-s)} d\mathbf{W}_E(s), \tag{5.23b}$$

where we made use, for $\mathbf{r}_c(t)$, of its initial condition $\mathbf{r}_c(0) = 0$ and $V_c(0) = V_{uc}$, and we assumed that the back-propagation of the effect operator is carried out from an initial time far in the future, at $\infty$, such that at time $t$ the conditional variance has reached the steady-state, $\overline{V}_E$. In addition, we will also make use of the Wiener process properties, i. e. $\mathbb{E}[dW_i] = 0$ and $dW_i dW_j = \delta_{ij} dt$.

$\mathbb{E}\left[\mathbf{r}_c(t)^2\right]$: Firstly, we calculate the two-time correlation function. Exploiting Itô isometry, we obtain

$$\mathbb{E}\left[\mathbf{r}_c(t)\mathbf{r}_c(t')\right] = 4\Gamma_{meas} e^{-\frac{\Gamma_m}{2}(t+t')} \int_0^{\min(t,t')} e^{\Gamma_m s} V_c(s)^2 ds. \tag{5.24}$$

Then, we calculate the variance $\mathbb{E}\left[\mathbf{r}_c(t)^2\right]$ directly from Equation 5.24 imposing $t = t'$, which yields

$$\mathbb{E}\left[\mathbf{r}_c(t)^2\right] = 4\Gamma_{meas} e^{-\Gamma_m t} \int_0^t e^{\Gamma_m s} V_c(s)^2 ds. \tag{5.25}$$

The integral in Equation 5.25 can be solved from a formal integration of Equation 5.9b, from which we get

$$4\Gamma_{meas} e^{-\Gamma_m t} \int_0^t e^{\Gamma_m s} V_c(s)^2 ds = V_{uc} - V_c(t). \tag{5.26}$$

Inserting Equation 5.26 in Equation 5.25 we finally get

$$\mathbb{E}\left[\mathbf{r}_c(t)^2\right] = V_{uc} - V_c(t). \tag{5.27}$$

$\mathbb{E}\left[\mathbf{r}_E(t)^2\right]$: From Equation 5.23b and exploiting $d\mathbf{W}_E(s)d\mathbf{W}_E(s') = \delta(s-s')ds$, we have

$$\mathbb{E}\left[\mathbf{r}_E(t)^2\right] = 4\frac{\Gamma_{meas}}{\Gamma_m}\overline{V}_E^2 = \overline{V}_E + V_{uc}, \tag{5.28}$$

where the last equality can be derived from Equation 5.20b at the steady-state, i. e. putting $\dot{V}_E(t) = 0$.

$\mathbb{E}\left[\mathbf{r}_c(t)\mathbf{r}_E(t)\right]$: In order to correctly asses the cross-correlations between the two average displacements, we need to make use of the relation $d\mathbf{W}_E(t) = \mathbf{i}dt - \sqrt{4\Gamma_{meas}}\mathbf{r}_E dt = \sqrt{4\Gamma_{meas}}(\mathbf{r}_c - \mathbf{r}_E)dt + d\mathbf{W}$, in which the Wiener increment from the retrodiction measurement is linked to the average displacement from the quantum trajectory, $\mathbf{r}_c(t)$. Inserting this relation in Equation 5.23b we get

$$\mathbf{r}_E(t) = 4\Gamma_{meas}\overline{V}_E \int_t^\infty e^{\lambda(t-s)}\mathbf{r}_c(s)ds + \sqrt{4\Gamma_{meas}}\overline{V}_E \int_t^\infty e^{\lambda(t-s)} d\mathbf{W}(s), \tag{5.29}$$

where $\lambda := 4\Gamma_{meas}\overline{V}_E - \Gamma_m/2$. When calculating the cross-correlation, the stochastic terms containing the Wiener increments are defined on time intervals which, apart from a set of measure zero, do not overlap. Therefore, they are uncorrelated according to the Wiener process properties. The only non-zero term in the cross-correlations is

$$\begin{aligned}\mathbb{E}\left[\mathbf{r}_c(t)\mathbf{r}_E(t)\right] &= 4\Gamma_{meas}\overline{V}_E \int_t^\infty e^{\lambda(t-s)}\mathbb{E}\left[\mathbf{r}_c(t)\mathbf{r}_c(s)\right] ds \\ &= 4\Gamma_{meas} e^{-\Gamma_m t} \int_0^t e^{\Gamma_m s} V_c(s)^2 ds = V_{uc} - V_c(t),\end{aligned} \tag{5.30}$$

where the last equality comes from Equation 5.26.

Combining all these together we prove Equation 5.21.

In particular, for a quantum measurement the condition $\eta_{meas} \approx 1$ implies that $\Gamma_{meas} \gg \Gamma_m$, then the following approximation holds

$$\overline{V}_E = \overline{V}_c + \frac{\Gamma_m}{4\Gamma_{meas}} \approx \overline{V}_c. \tag{5.31}$$

Using it in Equation 5.21 yields the simple and intuitive result that $V_d(t) \approx V_c(t) + \overline{V}_c$ and, at the steady-state for the quantum trajectory, $\overline{V}_d \approx 2\overline{V}_c$. This is our main result, which links the experimental variance of an ensemble of data points, obtained from the distance between the average displacements from the quantum trajectory and the retrodiction measurement, to the conditional state variance, $V_c(t)$, otherwise not directly measurable due to its deterministic evolution. This has already been exploited in Figure 5.10.

Equation 5.21 also has a simple interpretation: the retrodiction measurement is an independent tool which is used to verify the conditional state. The experimental statistics, $V_d$, yields the original conditional state variance, $V_c$, plus an additional noise from the measurement, $\overline{V}_E$. For ideal quantum measurements, this additional noise has a variance of $\overline{V}_E = 1/2$ in both quadratures: the retrodiction measurement approximates an ideal, von Neumann projection on coherent states.

### 5.3.3 *Observation of the conditional variance dynamics*

The result proved suggests that this verification method, based on the retrodiction measurement, can be extended to time $t_0$ in which the quantum trajectory is not at the steady-state. This allows to observe the whole dynamics of the state during the measurement. In practice, we perform the same statistical analysis done in Figure 5.10, now at different time $t_0$, within the interval $0\ \text{ms} < t_0 < 3\ \text{ms}$. Given the 3.2 ms-long measurement records, this ensures that the retrodiction measurement variance always is at the steady-state, as assumed in Equation 5.21. We calculate the variance of the distance, $V_d(t_0)$, and the unconditional variance, $V_{uc}$, from the variance of the retrodicted average displacement $\mathbb{E}\left[\mathbf{r}_E(t_0)^2\right]$, at each time $t_0$. The results are shown in Figure 5.11.

The variance of the distance reproduces the conditional state variance, apart from the small offset $\overline{V}_E$. In the first $\sim 100\ \mu\text{s}$ we observe a reduction of this variance, as predicted by the model shown in Figure 5.7b. This reduction stems from the purification of the conditional state that the measurement carries out over time, leading to a localization in the configuration space. For a quantum measurement at the steady-state, the conditional variance is maximally reduced close to the coherent state limit and much lower than the corresponding unconditional variance, in which the quantum backaction noise dominates. In this regard, performing a quantum measurement is the

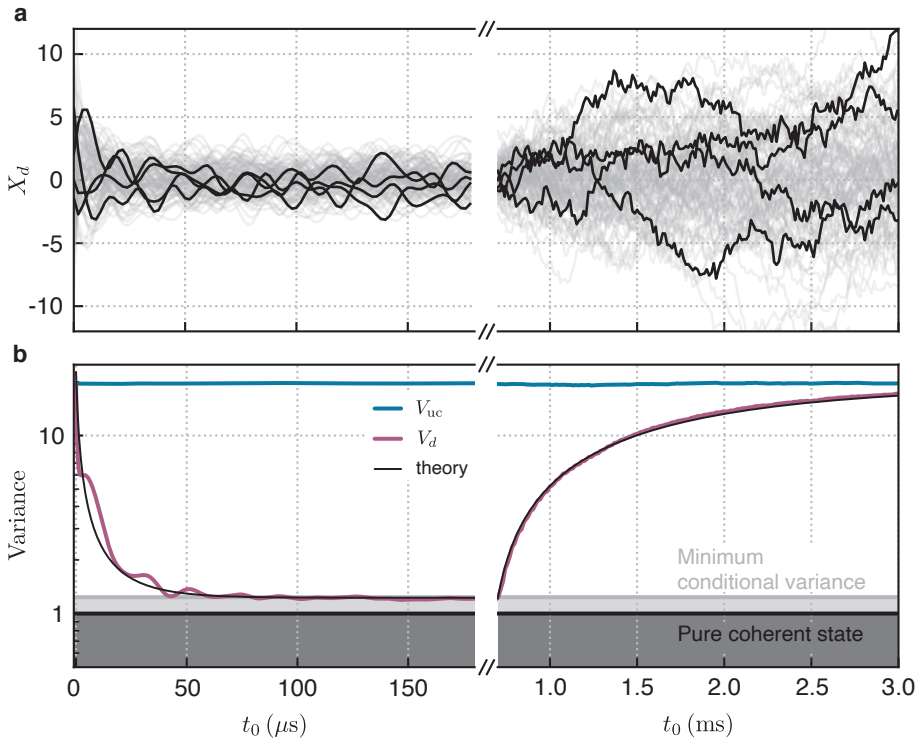


Figure 5.11: Measurement-induced collapse and decoherence. a, Sample of distance $X_d$ quadrature (gray) shown during different time intervals. At time $t_0 = 0.7$ ms the conditioning on the measurement record is interrupted and the conditional state diffuses. Few traces are highlighted in black for illustration purposes. b, Experimental unconditional (blue), from the retrodicted average displacement, and distance (purple) variances. The horizontal black line indicates the lower achievable limit, which is a pure conditional coherent state. The dark gray line represents the minimum variance achieved by our setup. Finally, the thin black light is a theoretical prediction for the distance variance $V_d$. Adapted from [Ros+19].

best choice for estimating and monitoring the mechanical state. The suppression of the thermal and the quantum backaction decoherence is a measurement-based mechanism. In fact, the fluctuating Brownian and radiation pressure forces are still acting on the mechanical system, however the outcome of the quantum measurement provides the observer with a clean and accurate record of fluctuations. This record can thus be used to track the induced random displacement, avoiding any loss of information.

*Decoherence from ignoring the outcomes*

To show that the measurement outcomes counteract the decoherence, we stop to condition the quantum trajectory on the measurement record from time $t_0 = 0.7$ ms, by setting the detection efficiency to zero in Equation 5.10 used to calculate the average displacement. In such a way, we do not have any upcoming information, and our best knowledge is solely based on the unconditional dynamics. The result

is that the conditional variance heats up to the unconditional one via decoherence, as shown in Figure 5.11b.

This concludes the verification of the conditional state, which is a central object in quantum measurements. At this stage, the conditional state still represents a tool that the observers have built to best describe their knowledge about the system. As such, this state may appear useless for further experiments in which the system needs to be prepared in a given configuration, *independently* of the observers. In other words, it would be desirable to convert such conditional state into an unconditional one. This is indeed possible and requires to control the dynamics of the system, based on the state-of-knowledge expressed by the conditional state [DJ99; Doh+12]. For example, the conditional state of a monitored mechanical resonator is almost a pure coherent state with a fluctuating, but known, amplitude, whereas many experiments require to have a fixed amplitude, e. g. at the origin of the phase space. Then, one can envision a strategy in which displacement operations back to the origin are applied, based on the average position from the conditional state. This is, in short, the idea of feedback cooling, which we discuss in details in the next chapter.

### 5.3.4 *Systematic effects of the demodulation filter*

We now quantify the systematic error in the estimation of the variances introduced by the demodulation filter in Equation 5.5. This filter should be compared to the effective one used to compute the average displacement from the quantum trajectory (cf. Equation 5.10). This is a Lorentzian filter, with a bandwidth, at the steady-state, approaching the measurement rate, $\Gamma_{\text{meas}}$. We compare these two filters in Figure 5.12, where we show the spectra of the raw homodyne photocurrent and of the demodulated quadratures $i_X$ and $i_Y$, arranged in the form $i_X \cos(\Omega_m t) + i_Y \sin(\Omega_m t)$, and the magnitude squared of the effective quantum trajectory filter. We can already anticipate that the systematic error is small, since the bandwidth of the latter filter is much smaller than the one from the demodulation filter.

In order to quantify this error, we start by rewriting the steady-state average displacement, from both the quantum trajectory and retrodiction, in terms of a convolution with the proper filter kernels $k_c(t)$ and $k_E(t)$, i. e. $\mathbf{r}_c(t) = k_c(t) * \mathbf{i}(t)$ and $\mathbf{r}_E(t) = k_E(t) * \mathbf{i}(t)$, where $*$ indicates convolution. From Equation 5.9a and Equation 5.20a we find that

$$k_c(t) = \sqrt{4\Gamma_{\text{meas}}}\overline{V}_c H(t) e^{-\alpha t}, \tag{5.32a}$$

$$k_E(t) = \sqrt{4\Gamma_{\text{meas}}}\overline{V}_E H(-t) e^{\alpha t}, \tag{5.32b}$$

where $H(t)$ is the Heaviside step function and $\alpha \coloneqq \Gamma_m/2 + 4\Gamma_{\text{meas}}\overline{V}_c$. We recast the demodulated photocurrent quadratures as convolutions as well, i. e. $\mathbf{i}(t) = \mathbf{k}_{\text{dem}}(t) * i(t)$, where $\mathbf{k}_{\text{dem}}$ is the kernel of the band-

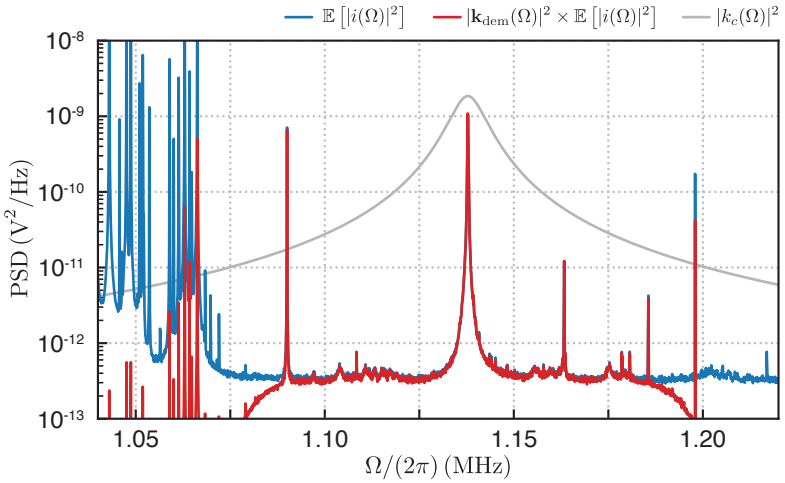


Figure 5.12: Systematic effect of the demodulation filter. The average spectrum of the raw homodyne photocurrent, $i(t)$, is shown in blue. Such photocurrent is demodulated at $\Omega_m$ to obtain the quadratures $i_X$ and $i_Y$. For comparison, we show in red the spectrum of $i_X \cos(\Omega_m t) + i_Y \sin(\Omega_m t)$. The gray line is the squared magnitude of the steady-state filter used for estimating the quantum trajectories. Adapted from [Ros+19].

pass filter and $i(t)$ is the raw homodyne photocurrent. Combining all together we obtain

$$\mathbf{r}_c(t) = k_c(t) * \mathbf{k}_{\rm dem}(t) * i(t) \rightarrow \mathbf{r}_c(\Omega) = k_c(\Omega)\mathbf{k}_{\rm dem}(\Omega)i(\Omega), \tag{5.33a}$$

$$\mathbf{r}_E(t) = k_E(t) * \mathbf{k}_{\rm dem}(t) * i(t) \rightarrow \mathbf{r}_E(\Omega) = k_E(\Omega)\mathbf{k}_{\rm dem}(\Omega)i(\Omega), \tag{5.33b}$$

where the right arrows point to the Fourier transforms. From Equation 5.33 and the convolution theorem we calculate the experimental variances as

$$\mathbb{E}\left[\mathbf{r}_c(t)^2\right] = \int_{-\infty}^{+\infty} \frac{d\Omega}{2\pi} |k_c(\Omega)\mathbf{k}_{\rm dem}(\Omega)|^2 \mathbb{E}\left[|i(\Omega)|^2\right], \tag{5.34a}$$

$$\mathbb{E}\left[\mathbf{r}_E(t)^2\right] = \int_{-\infty}^{+\infty} \frac{d\Omega}{2\pi} |k_E(\Omega)\mathbf{k}_{\rm dem}(\Omega)|^2 \mathbb{E}\left[|i(\Omega)|^2\right], \tag{5.34b}$$

$$\mathbb{E}\left[\mathbf{r}_c(t)\mathbf{r}_E(t)\right] = \int_{-\infty}^{+\infty} \frac{d\Omega}{2\pi} k_c(-\Omega)k_E(\Omega)|\mathbf{D}(\Omega)|^2 \mathbb{E}\left[|i(\Omega)|^2\right]. \tag{5.34c}$$

We can now compare these statistical quantities with and without the presence of the filter $\mathbf{k}_{\rm dem}$, by using the definition of $k_c$, $k_E$ and the Lorentzian fit of the measured PSD of $i(t)$.

We summarize the results in Table 5.1. In particular, we notice that the demodulation filter introduces a systematic underestimation of the variance of the distance, $V_d$. We have corrected for this error in Section 5.3.2, where we have presented the experimental results.

| | WITH $\mathbf{k}_{\text{DEM}}$ | WITHOUT $\mathbf{k}_{\text{DEM}}$ | DIFFERENCE |
|---|---|---|---|
| $\mathbb{E}\left[\mathbf{r}_c(t)^2\right]$ | 21.20 | 21.21 | 0.05% |
| $\mathbb{E}\left[\mathbf{r}_E(t)^2\right]$ | 22.42 | 22.44 | 0.09% |
| $\mathbb{E}\left[\mathbf{r}_c(t)\mathbf{r}_E(t)\right]$ | 21.23 | 21.21 | 0.09% |
| $V_d(t)$ | 1.17 | 1.24 | 5.6% |

Table 5.1: Variance and covariance with and without the demodulation filter.

# 6

# MEASUREMENT-BASED QUANTUM CONTROL OF A MECHANICAL RESONATOR

In the previous chapter we have seen how an observer can use a quantum measurement to generate a pure conditional state. This is done by conditioning the observer state-of-knowledge on the recorded measurement outcomes. However, this refinement has no effect on the unconditional state, which remains a largely mixed state dominated by the quantum backaction noise. As anticipated, converting such conditional state into an unconditional one, and thus independent of the observer, requires to have *control* on the dynamics of the system [WM10; Jac14; Zha+17], e. g. via engineering the Hamiltonian. Every control strategy is based on spending some resources to achieve a specific target. The effectiveness of the strategy is quantified by a *cost function*, which is a functional of the observables of the system and the variables of the control resources, further constrained by limitations often present in realistic applications. For a chosen cost function the control strategy is said to be *optimal* if it minimizes the cost. Finally, when the control is based on the outcome of a measurement performed on the same system, we talk about *feedback control* or *optimal feedback control* if, in addition, the control minimizes the chosen cost function.

The general problem of deriving and experimentally exerting the optimal feedback control strategy on a quantum system is rather complicate. A significant simplification occurs for a specific class of problems, in which the cost function is additive over time. In this case, the *separation principle* holds. It states that the optimal strategy should be only based on the conditional state. This splits the problem in an estimation and a control step, which consists of, respectively, the derivation of the conditional sate and the actuation of the feedback force.

For instance, let's consider the case of a mechanical resonator, the displacement of which is continuously measured. A common control situations is the one in which the cost function minimizes the total energy [MVT98; CHP99]. In this case, the estimation step can be carried out as shown in the previous chapter. The control force, $u_{\mathrm{fb}}(t)$, based on that state, is a viscous force proportional to the average displacement of the conditional state. When exerted on the resonator, by introducing the additional Hamiltonian term $\hat{q}u_{\mathrm{fb}}(t)$, it affects the dynamics and provides the optimal control.

The separation principle makes clear a crucial theoretical aspect of feedback control: the dynamics is controlled by a force based on a conditional state, which itself depends on past measurements of

some observables of the system. That is, the controlled dynamics is, in general, non-Markovian. The consequence of this is that the standard Lindblad master equation cannot be applied anymore, making the Schrödinger picture description hard and less intuitive. While similar problems arise in the Heisenberg picture too, one can still solve the non-Markovian QLE for linear systems, by taking the Fourier transform. Therefore, we prefer this picture over the Schrödinger one. It should also be noted that in the QLE description the explicit measurement outcomes are lost in the operator formalism, which treats the photocurrent as an operator [WM10].

In this chapter we show the experimental implementation of a measurement-based quantum control protocol aiming to prepare the ground state of a mode of a mechanical resonator. We start with a theoretical analysis of the optimal control problem, based on the LQG theory. Despite its simplicity, a practical implementation is often unfeasible. Thus, we derive basic equations in the case of an arbitrary, then sub-optimal, controller. Next, we describe the experimental reality and the specific filter we design to ensure the stability of the experiment. Finally, we move to discuss the main experimental results, which show that the implemented feedback protocol allows to stabilize a mechanical state close to its quantum ground state.

## 6.1 FEEDBACK CONTROL OF A MECHANICAL RESONATOR

Feedback control schemes are ubiquitous in physics and engineering [Bec05] and are of fundamental importance in disparate fields, from biosciences to technological applications. In recent years new quantum technologies emerged [Kur+15], which brought the natural problem of controlling these quantum systems. This led to an intense research effort on achieving measurement-based quantum control of disparate mechanical systems, such as atoms [Kub+09], ions [Bus+06], levitated particles [LKR11], cantilevers [KB06], nanomechanical beams [Wil+15], mirror modes [CHP99] and massive test masses [Vin+08] in gravitational wave detectors. Despite that, however, measurement-based quantum control has remained elusive so far, even in its elementary forms such as the stabilization of the ground state. The closest approach, reported by Wilson et al. [Wil+15], yielded a low-occupancy thermal state, with $\sim 5$ phonons on average, limited by the measurement efficiency of $\eta_{\text{meas}} \approx 0.9\%$.

Building from the quantum measurement and the conditional state generation described in Chapter 5, we have managed to achieve the preparation of the mechanical ground state via feedback cooling [Ros+18], a form of measurement-based quantum control. In this protocol the control strategy aims to minimize the mechanical energy, which forms a quadratic cost function additive in time [DJ99; Doh+00]. Combined with the linear dynamics, the linear displacement measure-

ment and the Gaussian nature of the noise involved, our platform is part of the LQG systems, for which an analytical theory of optimal feedback control exists [NJP09] and has been summarized in Section 1.7. In particular, for these systems the principle of *certainty equivalence* holds, which states that the feedback force should be proportional to the first moments of the estimated conditional state.

Let's now focus on the case of a broad and resonant optomechanical cavity, such that $\Delta = 0$ and $\kappa \gg \Omega_m$, typical of our experiments. We have already seen that, in this case, the cavity can be adiabatically eliminated and the effective unconditional mechanical dynamics, from Equation 3.11, is

$$\dot{\hat{q}} = \Omega_m \hat{p}, \tag{6.1a}$$

$$\dot{\hat{p}} = -\Omega_m \hat{q} - \Gamma_m \hat{p} + \Omega_m \hat{u}_{fb} + \sqrt{4\Gamma_{qba}}\hat{X}_{in} + \sqrt{2\Gamma_m}\hat{\xi} \tag{6.1b}$$

where we have introduced the dimensionless feedback force, $\hat{u}_{fb}$. In addition, we assume that a BHD is used to continuously measure the phase of the transmitted optical field. The calibrated photocurrent, $\hat{\imath} = \sqrt{8\Gamma_{meas}}\hat{q} + \sqrt{2}\hat{Y}_{in}$, represents an effective displacement measurement, with the imprecision noise given by the phase optical quadrature, $\hat{Y}_{in}$. We choose the normalization $\sqrt{2}\hat{Y}_{in}$ such that the measurement noise has a unity variance, consistent with the convention used in Section 1.7. The control problem of reducing the mechanical energy can be mapped into an LQG system by choosing the following matrices [Gar+96]

*Control problem of minimizing the energy*

$$A = \begin{pmatrix} 0 & \Omega_m \\ -\Omega_m & -\Gamma_m \end{pmatrix}, \quad B = \begin{pmatrix} 0 \\ \Omega_m \end{pmatrix}, \quad D = \begin{pmatrix} 0 & 0 \\ 0 & 2\Gamma_m V_{uc} \end{pmatrix},$$
$$C = \begin{pmatrix} \sqrt{8\Gamma_{meas}} & 0 \end{pmatrix}, \quad \Gamma = \begin{pmatrix} 0 & 0 \end{pmatrix}. \tag{6.2}$$

The cost function is expressed by Equation 1.61, with $P = \mathbb{1}/2$ and $Q = e^{-1}$. The former matrix encodes the requirement of minimizing the mechanical energy, $(\hat{q}^2 + \hat{p}^2)/2$, whereas the latter quantifies the effort in exerting a control force. Within the chosen unit, $e = 1$ corresponds to the force magnitude necessary to displace the resonator by an amount equal to its zero-point displacement.

We notice, from Equation 6.2, that the process and measurement noises are uncorrelated, i. e. $\Gamma$ is the null matrix. Physically, this is a consequence of the resonant phase measurement employed, in which the two sources of noise are, respectively, the quantum backaction and imprecision noise, originating in the uncorrelated amplitude and phase optical quadrature. Also, the control matrix in Equation 6.2, B, only allows to affect the momentum, $\hat{p}$, through the force $u_{fb}$. This partial control reflects the lack of experimental tools to directly change the displacement $\hat{q}$. In practice, this does not represent a limitation, because one can control the displacement $\hat{q}$ by exerting

a force, on the momentum, delayed by a quarter of period. During this time, in fact, the harmonic evolution rotates the position into the momentum. For this to work one needs a high-Q mechanical resonator, for which several harmonic cycles happen before the dissipation kicks in [Doh+12].

*Optimal control solution*

Following the methods from Section 1.7 one can find an analytical solution to the optimal control problem and derive both the steady-state mechanical energy once the control loop is closed, from Equation 1.64, and the transfer function of the controller that one needs to experimentally implement to achieve the optimal control, from Equation 1.67. In Figure 6.1 we show the steady-state energy, $\overline{E}$, in units of

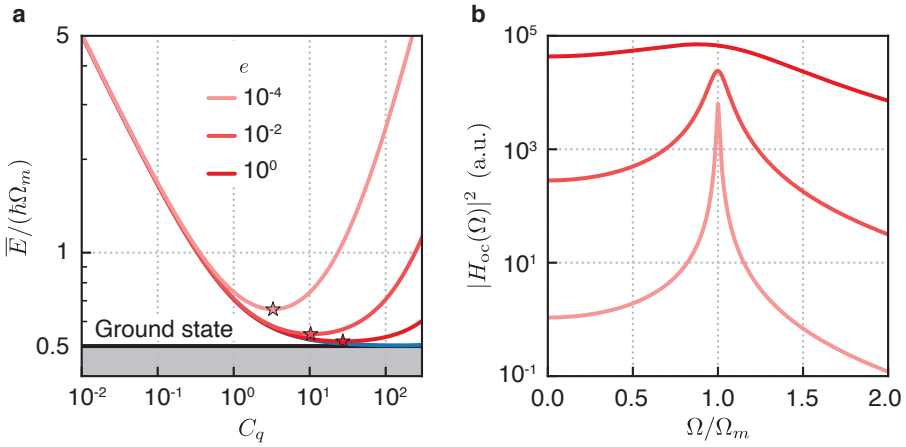


Figure 6.1: LQG closed loop mechanical energy and optimal controller transfer function. a, Closed loop mechanical energy, in units of $\hbar\Omega_m$, as a function of quantum cooperativity, $\mathcal{C}_q$, at different available control effort, increasing from light to dark red. The control limit is represented by the conditional variance, $\overline{V}_c$, in blue. The solid black line corresponds to the mechanical vacuum energy. b, Squared magnitude of the optimal controller transfer function, for different control effort. The coloured line corresponds to the configurations marked with stars in a.

phonon energy, $\hbar\Omega_m$, as a function of the quantum cooperativity, and the corresponding optimal transfer function, for some control efforts, $e$. The lowest achievable energy is determined by the average one from the conditional state, i. e.the conditional variance $\overline{V}_c$. However, reaching this limit, for a fixed quantum cooperativity, requires to have enough control effort at disposal, as shown in Figure 6.1a. There, for a fixed available effort, $e$, there exists an optimal quantum cooperativity which minimized the energy. For higher cooperativities, in fact, the unconditional variance is increased, due to the quantum backaction, and the conditional one is decreased. Therefore, reducing the energy to the conditional level requires to effectively cancel larger fluctuations, which implies a larger feedback force, the strength of which is however limited by the control effort $e$.

The control transfer function, at the optimal $\mathcal{C}_q$ for different control efforts, $e$, is shown in Figure 6.1. This transfer function corresponds to a two-pole band-pass filter centered around $\Omega_m$ [Gar+96], similar to the mechanical susceptibility in Equation 2.20. This transfer function broadens as the quantum cooperativity is increased, and approaches a flat filter in the limit of unlimited control effort, $e \to \infty$, and measurement strength, $\mathcal{C}_q \to \infty$. In this limit, the feedback force only depends on the just-recorded measurement outcome, thus realizing a Markovian feedback [Wis94].

### 6.1.1 *Sub-optimal case*

Despite the simplicity of the transfer function of the optimal controller, its experimental implementation is not always feasible. One major obstacle is represented by the multitude of mechanical modes present in practice, which are not taken into account in the optimal solution derived in the previous section. Using the optimal control strategy stemming from the single-mode model can lead to instabilities of these other mechanical modes, thus precluding its use in real experiments. In fact, we observe this instability when we try to implement the simple two-pole band-pass filter in our membrane-based platform.

The other mechanical modes also behave in a linear fashion, then one can ideally include them in the LQG system description by increasing the dimension of the configuration space. This would require, though, to characterize the parameters of each mode, an experimentally unfeasible task given their large number. Therefor, we decide to implement a different transfer function for the controller, which is then sub-optimal, while being inspired by the optimal case for a single mode.

In the following, we model the implementation of a control force based on a generic linear filter. The resulting equations are useful to understand and interpret the experiments which employ non-optimal control. We start from Equation 6.1 and the measured homodyne photocurrent, $\hat{\imath}$. If the feedback force is not exerted, we obtain the following solutions in the Fourier domain [Wil+15]

$$\hat{q}(\Omega) = \chi_m(\Omega)\hat{f}_{tot}(\Omega), \tag{6.3a}$$

$$\hat{q}_{inf}(\Omega) = \hat{q}(\Omega) + \hat{q}_{imp}(\Omega), \tag{6.3b}$$

where we introduced the photocurrent calibrate in displacement units, i. e. $\hat{q}_{inf} \coloneqq \hat{\imath}/\sqrt{8\Gamma_{meas}}$, and the total force $\hat{f}_{tot}(\Omega) \coloneqq \sqrt{2\Gamma_m}\hat{\xi}(\Omega) + \sqrt{4\Gamma_{qba}}\hat{X}_{in}(\Omega)$, which comprises, respectively the thermal and the quantum backaction force. The effective displacement imprecision noise, in Equation 6.3b, is $\hat{q}_{imp}(\Omega) \coloneqq \hat{Y}_{in}(\Omega)/\sqrt{4\Gamma_{meas}}$.

We now apply a feedback force on the resonator, as done in Equation 6.1b. In this case, however, the feedback force is not derived from the optimal LQG controller, but rather from a generic linear filter

applied to the calibrated photocurrent, i. e. $\hat{u}_{fb}(\Omega) = H_{fb}(\Omega)\hat{q}_{inf}(\Omega)$, where $H_{fb}(\Omega)$ is the transfer function of the filter. For real-time control, we also require that this transfer function is causal. The entire

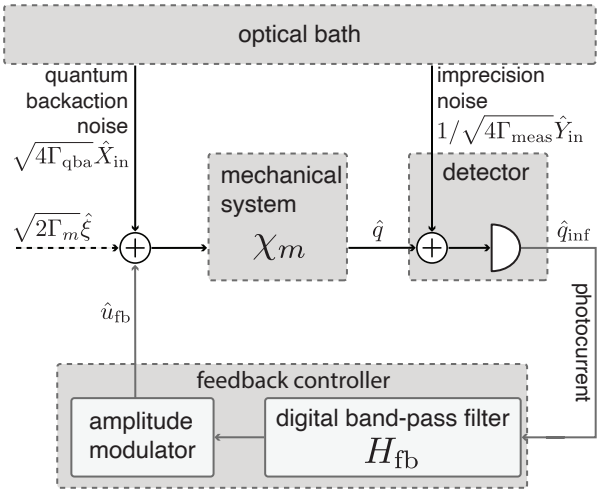


Figure 6.2: Feedback control of a mechanical resonator. An optomechanical system is employed to continuously monitor the displacement of a mechanical resonator. The recorded photocurrent is further processed by an electronic controller, which is used to actuate an additional feedback force on the resonator itself. This represents a LQG system.

control loop is sketched in Figure 6.2. We include the feedback force in the coupled Equation 6.3 and solve for the actual and inferred displacement, under the closed control loop,

*Arbitrary control loop dynamics*

$$\hat{q}(\Omega) = \frac{\chi_m(\Omega)}{1-\chi_m(\Omega)H_{fb}(\Omega)}\left(\hat{f}_{tot}(\Omega) + H_{fb}(\Omega)\hat{q}_{imp}(\Omega)\right), \quad (6.4a)$$

$$\hat{q}_{inf}(\Omega) = \frac{\chi_m(\Omega)}{1-\chi_m(\Omega)H_{fb}(\Omega)}\left(\hat{f}_{tot}(\Omega) + \chi_m(\Omega)^{-1}\hat{q}_{imp}(\Omega)\right). \quad (6.4b)$$

From Equation 6.4a we notice that the feedback loop affects the mechanical susceptibility, giving rise to an effective one

$$\chi_{eff,\,fb}(\Omega) \coloneqq \frac{\chi_m(\Omega)}{1-\chi_m(\Omega)H_{fb}(\Omega)}. \quad (6.5)$$

Also, the displacement $\hat{q}$ is driven by an additional fluctuating force. This force stems from the imprecision noise, $\hat{q}_{imp}$, being fed back by the feedback loop and its strength depends on the controller gain, $|H_{fb}(\Omega)|$. We can already guess that the choice of the transfer function, $H_{fb}(\Omega)$, is crucial for the statistical moments of the mechanical state. In particular, for a properly chosen transfer function the feedback loop effectively cools the mechanical motion, in a similar fashion to optical cooling (cf. Section 3.3).

As usual, the actual displacement is inaccessible to the experimenters, who can infer it from the calibrated photocurrent, $\hat{q}_{\text{inf}}$, expressed in Equation 6.4b. However, one should be careful when interpreting this photocurrent, as it now becomes part of the loop. It is known that such an *in-loop photocurrent* contains additional correlations, not presents in the actual system, arising from different parts of the loop itself [Sha+87]. In our case, the in-loop photocurrent in Equation 6.3b contains the imprecision noise and the mechanical displacement, which is partially driven by the same imprecision noise. This gives rise to correlations in the spectrum of the photocurrent, which can distort the usual mechanical Lorentzian response and, then, should be properly taken into account to make inference on the mechanics. For strong enough in-loop correlations, the measured spectral noise appears to be reduced below the background, which is the shot noise. This effect is known as noise squashing [Buc+99; Wis99], and does not corresponds to squeezing of the quantum noise, in contrast to what happens for free fields out-of-loop.

*In-loop photocurrent*

The symmetrized PSD of the actual displacement and the in-loop photocurrent, from Equation 6.4, are

*Spectra of actual displacement and in-loop photocurrent*

$$\overline{S}_{\hat{q}\,\hat{q}}(\Omega) = |\chi_{\text{eff,fb}}(\Omega)|^2 \left(\overline{S}^{\text{tot}}_{FF}(\Omega) + |H_{\text{fb}}(\Omega)|^2 \overline{S}_{\text{imp}}(\Omega)\right), \tag{6.6a}$$

$$\overline{S}^{\text{inf}}_{\hat{q}\,\hat{q}}(\Omega) = |\chi_{\text{eff,fb}}(\Omega)|^2 \left(\overline{S}^{\text{tot}}_{FF}(\Omega) + |\chi_m(\Omega)|^{-2} \overline{S}_{\text{imp}}(\Omega)\right). \tag{6.6b}$$

From Equation 6.6a we can calculate the effective average phonon number according to Equation 3.23 or, in the case of validity of the equipartition theorem, to Equation 3.24. Experimentally, however, we only have the in-loop photocurrent at our disposal. Then, in order to infer the mechanical average occupation, we fit the measured spectrum to Equation 6.6b. We insert the fitted parameters in Equation 6.6a to calculate the actual spectrum which, subsequently, we numerically integrate to obtain the occupation.

### 6.1.2 *An example: cold damping*

Let's now consider a specific feedback control scheme, in which the transfer function is chosen to be an ideal derivative filter,

$$H_{\text{fb}}(\Omega) = \imath \Gamma_m g_{\text{fb}} \Omega/\Omega_m, \tag{6.7}$$

where $g_{\text{fb}}$ is the dimensionless gain. This filter is the basis of a scheme which is known as *cold damping* [MVT98; CHP01; Gen+08a]. It allows to introduce additional mechanical damping with minimum, "cold" quantum fluctuations. Inserting Equation 6.7 in Equation 6.5 shows that the only effect in the susceptibility is to replace the natural damping, $\Gamma_m$, with the feedback-enhanced damping, $\Gamma_m(1 + g_{\text{fb}})$.

The mechanical occupation, from Equation 3.24, is obtained from the integration of Equation 6.6a, which yields

$$\bar{n}_{\mathrm{eff}} = \int_0^\infty \frac{d\Omega}{\pi} \bar{S}_{\hat{q}\hat{q}}(\Omega) - \frac{1}{2} = \frac{V_{\mathrm{uc}}}{1+g_{\mathrm{fb}}} + \frac{g_{\mathrm{fb}}^2}{1+g_{\mathrm{fb}}} \frac{\Gamma_{\mathrm{m}}}{16\Gamma_{\mathrm{meas}}} - \frac{1}{2}. \quad (6.8)$$

The minimum occupancy, achieved upon optimization of the feedback gain, $g_{\mathrm{fb}}$, is

$$\min_{g_{\mathrm{fb}}} (\bar{n}_{\mathrm{eff}}) = \underbrace{\frac{\sqrt{1+16\Gamma_{\mathrm{meas}}/\Gamma_{\mathrm{m}} V_{\mathrm{uc}}} - 1}{8\Gamma_{\mathrm{meas}}/\Gamma_{\mathrm{m}}}}_{\bar{V}_{\mathrm{c}}} - \frac{1}{2}. \quad (6.9)$$

This exactly corresponds to the occupation of the conditional state, displaced to the origin, with the conditional variance defined in Equation 5.12. The result is rather surprising because, apparently, the cold damping strategy gives rise to the optimal result, despite the transfer function of the controller employed is non optimal.

*Unbounded feedback force PSD*

The resolution of this paradox lies in the large violation of the equipartition theorem in the cold damping approach. In fact, the pure derivative filter does not have a frequency upper bound, which leads to an unbounded force spectrum, driving the mechanical resonator. The momentum spectrum, consequently, is not bounded anymore for large frequencies, $\Omega \gg \Omega_{\mathrm{m}}$, at which

$$\bar{S}_{\hat{p}\hat{p}}(\Omega) = \frac{\Omega^2}{\Omega_{\mathrm{m}}^2} \bar{S}_{\hat{q}\hat{q}}(\Omega) \sim \frac{\Gamma_{\mathrm{m}}}{\Omega_{\mathrm{m}}^2} g_{\mathrm{fb}}^2 \bar{S}_{\mathrm{imp}}(\Omega), \quad (6.10)$$

which is flat and thus generates an infinite momentum variance.

In practice, this divergence is always avoided in the experiments thanks to the presence of a cutoff frequency, above the mechanical resonance, in the actuation [Gen+08a].

## 6.2 EXPERIMENTAL REALITY AND FEEDBACK LOOP DESIGN

Experimentally, we use the same setup described in Chapter 5, also sketched in Figure 6.3, which allows to perform quantum displacement measurements [Ros+18]. The probe laser is locked close to the resonance of a cavity mode, at $\lambda = 796.060$ nm, with a linewidth $\kappa/(2\pi) = 15.9$ MHz and a residual detuning of $\Delta \approx -0.05\kappa$. The phase of the transmitted field is detected by means of a BHD, with a total efficiency of $\eta = 73\%$, which also includes the cavity overcoupling. The only difference with the setup in Figure 5.2 is the overall transfer function, $H_{\mathrm{fb}} \coloneqq H_{\mathrm{main}} + H_{\mathrm{aux}}$, of the FPGA-based feedback controller used to process the recorded homodyne photocurrent. Here, we introduce the main controller filter, $H_{\mathrm{main}}$, which feedback-cools the in-bandgap mode of interest and is designed to minimize its occupation. The chosen transfer function, different from the optimal one based on the single-mode LQG description, is

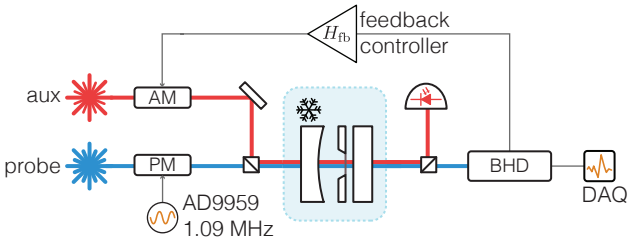


Figure 6.3: Measurement-based control experimental setup. A probe laser, tuned on resonance, performs a displacement quantum measurement, whose outcome is recorded via BHD. The resulting photocurrent is filtered and employed to modulate the amplitude of an auxiliary laser, which exerts a feedback force on the resonator mode to cool it down.

$$H_{main}(\Omega) = g_{fb} e^{i\Omega\tau - i\phi} \left( \frac{\Gamma_{fb}\Omega}{\Omega_{fb}^2 - \Omega^2 - i\Gamma_{fb}\Omega} \right)^2 . \quad (6.11)$$

*Experimental controller transfer function*

The center frequency and the FWHM of the filter are, respectively, $\Omega_{fb}/(2\pi) = 1.195$ MHz and $\Gamma_{fb}/(2\pi) = 77.78$ kHz. Electronic cables and the FPGA unit, which generates this filter, introduce a total time delay of $\tau = 300$ ns. The gain, $g_{fb}$, reflects the electronic gain of the FPGA-based controller, as well as subsequent amplification and transduction. Finally, the overall phase, $\phi$, is digitally controlled and experimentally tuned to yield $\arg(H_{fb}(\Omega_m)) \approx \pi/2$. In such a way, the feedback force, at the mechanical resonance frequency $\Omega_m$, approximates a viscous force, as in the case of cold damping. Any deviation from $\pi/2$ results in an additional elastic force, which has the effect of slightly shifting the resonance frequency.

*Description of the control loop*

We choose to use a high-order frequency in order to suppress the residual gain at frequencies outside the phononic bandgap, where the density of mechanical modes becomes large and it is easy to excite some of them. Nevertheless, there are still few mechanical modes, both at low frequencies and inside the bandgap, for which the filter suppression is not enough to avoid instabilities. In order to stabilize them, we apply additional feedback forces close to the resonance frequencies of these modes. To do that, we electronically split the homodyne photocurrent and process it with independent controllers, one per mode to be stabilized. The employed filters have the same form of $H_{main}$ (cf. Equation 6.11). The electronically processed signals are recombined together, then sent to an amplitude modulator to feed them back as forces on the mechanical resonator. In a similar way, we also feedback-cool few other low-frequency modes which exhibit large displacement excursions, leading to extraneous in-bandgap noise via non-linear transduction, as reported in Section 5.1.

| FREQUENCY | PHASE | BANDWIDTH | GAIN |
|---|---|---|---|
| 159.8 kHz | 150° | 1.216 kHz | 1 |
| 264 kHz | 90° | 4.858 kHz | 3 |
| 428.5 kHz | 100° | 303.6 Hz | 10 |
| 546.4 kHz | 170° | 607.2 Hz | 0.5 |
| 560.3 kHz | 170° | 151.8 Hz | 1 |
| 690.6 kHz | 0° | 151.8 Hz | 1 |
| 1.0183 MHz | 170° | 303.6 Hz | 15 |
| 1.25 MHz | 30° | 9.716 kHz | 20 |
| 1.195 MHz | 178° | 77.78 kHz | $g_{fb}$ |

Table 6.1: Filter settings for feedback-cooling additional mechanical modes. The last row shows the settings for the main filter, $H_{main}$.

All these additional controllers are grouped in an effective, single auxiliary transfer function, $H_{aux}(\Omega)$. The total number of additional controllers varies from different experimental runs. For the one reported here, we employed eight different filters, which are derived from three RedPitaya, each of which can simultaneously output at most three independent filters. In Table 6.1 we report the settings for these filters.

In Figure 6.4 we show the measured overall transfer function of the digital filter, $H_{fb}$, including both the main and the auxiliary ones. As reported in Table 6.1, the closest mode to the in-bandgap one of interest which we need to stabilize is at $\Omega/(2\pi) = 1.25$ MHz. The auxiliary filter for this mode clearly appears in Figure 6.4, however, despite that, it does not add any significant contribution to the total transfer function close to the mechanical mode, $\Omega \approx \Omega_m$.

We use the electronic feedback signal, obtained from applying the total filter shown in Figure 6.4 to the photocurrent, to actuate a force on the mechanical resonator. This is done via classical radiation pressure force, obtained by modulating the amplitude of the auxiliary laser with the feedback signal. This laser is locked to the red side of a different cavity mode at $\lambda_a = 795.057$ nm, with a linewidth and a detuning of, respectively, $\Delta_a/(2\pi) = -4.2$ MHz $\kappa_a/(2\pi) = 12.9$ MHz. The amplitude modulation of the input field is partially transduced, by the cavity, into intracavity amplitude modulation, which yields the wanted radiation pressure force on the resonator.

*Limits of the experimental controller*

We can now use the measured transfer function, shown in Figure 6.4, to numerically study the performance and limits of the employed filter. We show the calculated effective mechanical occupation, under the effect of the experimental controller, in Figure 6.5a, where we optimize the feedback gain, $g_{fb}$, at each $\mathcal{C}_q$. We compare it to the ultimate

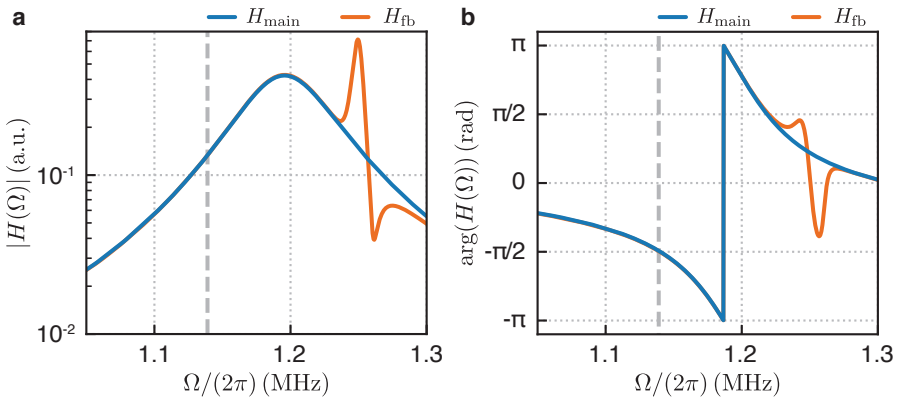


Figure 6.4: Experimental controller transfer function. a, Magnitude and b, phase of the transfer function of the total controller (orange) and the main controller only (blue), used to cool down the mode of interest, located at the frequency marked by the vertical gray dashed line. In the total controller transfer function the only visible auxiliary filter is the one located at 1.25 MHz, used to suppress instabilities induced in one of the other in-bandgap modes. The other auxiliary filters are much more far apart and have a negligible contribution around the mechanical mode of interest. Adapted from [Ros+18].

limit given by the occupation of the conditional state [Doh+12; BM16], achieved by the optimal controller with the same total efficiency of 73%. We predict that our experimental controller, at the optimal $\mathcal{C}_q$, yields the lowest occupation of 0.2 phonons, whereas the optimal controller achieves a lower value of 0.09 phonons. We numerically calculate the variance of both the displacement and the momentum and verify that they differ only by $\leqslant 1\%$, thus justifying the use of the equipartition theorem. We also predict that our experimental controller becomes unstable for sufficiently large gains, as shown in Figure 6.5b. When the instability is approached, the mechanical resonator heats up exponentially. In Figure 6.5c we show few theoretical displacement spectra, at different feedback gains for a fixed $\mathcal{C}_q$. The instability arises due to the excess motion produced by the feedback force through the controller filter, at $\Omega/(2\pi) \approx 1.18$ MHz, close to resonance of the transfer function.

## 6.3 QUANTUM GROUND STATE PREPARATION BY FEEDBACK

We now move to describing the experiments performed with the experimental controller derived in the previous section. We choose the quantum measurement efficiency by tuning the optical power of the probe beam, which changes its $\mathcal{C}_q$ accordingly. For each chosen $\mathcal{C}_q$ we close the feedback loop with the filter previously described, then we collect several inferred displacement spectra, from the in-loop homodyne photocurrent, as we vary the gain of the electronic filter,

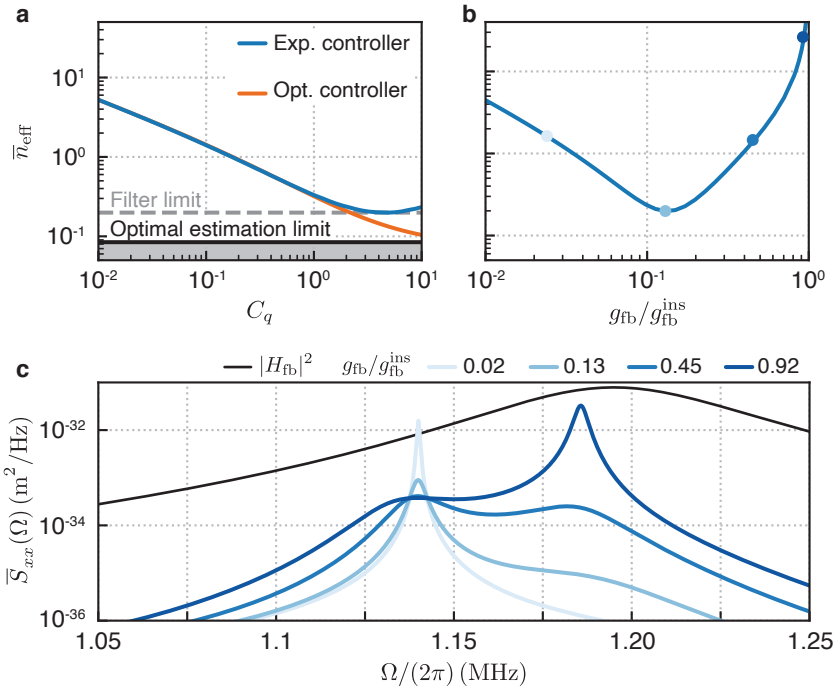


Figure 6.5: Experimental and ideal limits of feedback cooling. a, Mechanical occupation at different quantum cooperativities, $\mathcal{C}_q$, achieved with the experimental (blue) and optimal controller (orange), optimizing the feedback gain at each $\mathcal{C}_q$. The solid black line represents the limit for the optimal control, at $\mathcal{C}_q \to \infty$ and the same experimental total efficiency of 73%. The dashed gray line, instead, is the predicted lowest occupation achievable from the experimental controller. b, Mechanical occupation as a function of the experimental controller gain $g_{\rm fb}$, normalized to the instability gain $g_{\rm fb}^{\rm ins}$, at $\mathcal{C}_q = 5$. c, Actual displacement spectra corresponding to the gain values marked as coloured circles in b. The gray line is the experimental controller transfer function, for reference. The instability is caused by the excess motion induced by the controller at $\Omega/(2\pi) \approx 1.18$ MHz, for large gain. Adapted from [Ros+18].

*Inferring occupations from in-loop spectra*

$g_{\rm fb}$. In Figure 6.6a-c we show some of the measured spectra, $\bar{S}^{\rm inf}_{\hat{q}\hat{q}}(\Omega)$, calibrated in units of phonons $\bar{S}^{\rm 1p}_{\hat{q}\hat{q}}$ (cf. Section 5.2.1), for $\mathcal{C}_q = 2.4$ We fit each spectrum to Equation 6.6b, using the transfer function of the experimental filter, characterized in Figure 6.4, with the electronic gain, $g_{\rm fb}$, the overall phase, $\phi$, the total force noise, $\bar{n}_{\rm tot}$, and imprecision noise, $\bar{n}_{\rm imp}$, occupations kept as free parameters. The results are shown as a function of the digital gain set on the RedPitaya in Figure 6.6d-g. As expected, the fitted gain, $g_{\rm fit}$, is proportional to the digital gain, $g_{\rm fb}$, and all the spectra have a constant overall phase of $\approx \pi/2$. Moreover, all the spectra are consistent with a constant value of $\bar{n}_{\rm tot}$ and $\bar{n}_{\rm imp}$, indicating that there is no additional gain-dependent electronic noise fed back by our feedback loop. We notice that the excess motion at higher frequencies around $1.10 \div 1.20$ MHz, caused by the experimen-

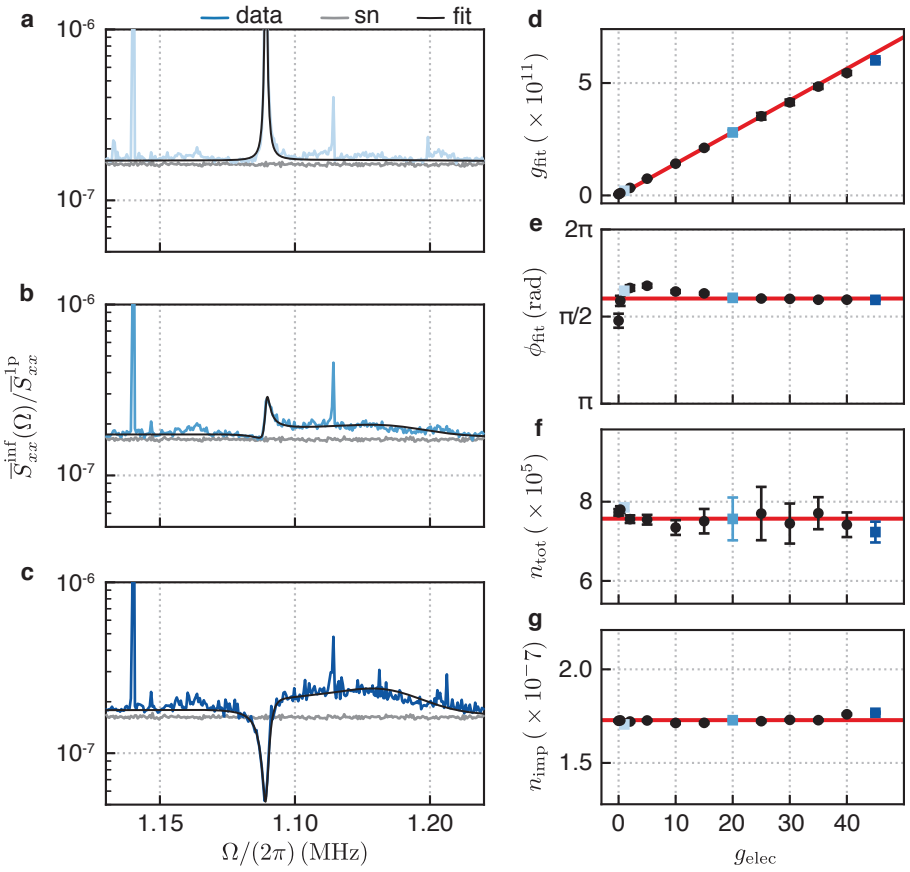


Figure 6.6: Feedback cooling fit results. a, b, c In-loop inferred displacement spectra (blue) and fits (black) for three different gains, at $\mathcal{C}_q = 2.4$. The gray trace is the shot noise. d, Gain, e, phase, f, total force noise and g, imprecision noise occupations resulting from the spectral fits. The red lines are linear/constant fits of these results. Adapted from [Ros+18].

tal controller for high gains, is correctly identified and fitted by the modelled transfer function. In addition, the in-loop spectrum for high gains shows a noise reduction below the shot noise, as observed in Figure 6.6c. This is known as *noise squashing* and corresponds to the appearance of significant correlations in the photocurrent, between the imprecision noise and the mechanical motion. Finally, using the fitted parameters, we can infer, for each spectrum, the corresponding actual out-of-loop displacement spectrum, $\overline{S}_{\hat{q}\hat{q}}(\Omega)$, as shown in Figure 6.7a and b. The mechanical occupation, $\overline{n}_{\mathrm{eff}}$, is shown in Figure 6.7c and is obtained from the integration of the actual displacement spectra, according to Equation 3.23.

We perform similar experiments and data analysis at different probe quantum cooperativity, $\mathcal{C}_q$. In Figure 6.8 we show the overall results for the effective mechanical occupations. We now express the electronic gain in terms of the effective mechanical linewidth, $\Gamma_{\mathrm{eff}}$, obtained from the FWHM of the estimated actual displacement spectrum. We

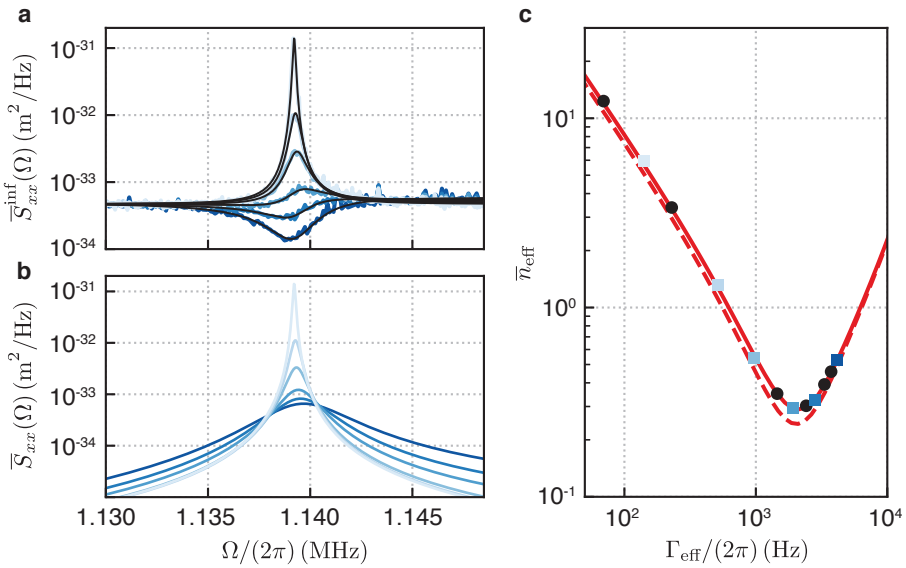


Figure 6.7: Inferring mechanical occupations from measured in-loop spectra. a, Sample of in-loop calibrated spectra (blue) and fits (smooth thin lines), for different electronic gains. b, Out-of-loop actual displacement spectra, estimated from the fit results. c, Effective mechanical occupation, obtained from integration of the displacement spectra in b, as a function of the electronic gain, expressed in terms of effective total mechanical linewidth, $\Gamma_{\mathrm{eff}}$. The solid (dashed) red line is a prediction from the mean values of the fitted (independently estimated) parameters. Adapted from [Ros+18].

observe that for each $\mathcal{C}_q$ there is an optimal electronic gain which yields the lowest occupation. The lowest mechanical occupation we achieve is, at $\mathcal{C}_q = 2.4$, of $\overline{n}_{\mathrm{eff}} = 0.29 \pm 0.03$, where the errors indicate the confidence intervals of the fitted parameters used to calculate the occupation. For higher gains, the occupation heats up due to the uncorrelated imprecision noise which is fed back, by the control loop, as a force on the resonator.

We benchmark our results against the case of the optimal control. There, if unlimited measurement strengths and control efforts are available, the lowest achieved occupation is given by the variance of the conditional state, Equation 5.12. For quantum-limited measurements with a large quantum cooperativity, we have that $\eta_{\mathrm{meas}} \approx \eta$, then the conditional variance is only determined by the total efficiency, $\eta$. For out total efficiency of $\eta = 0.73$ the corresponding occupation is $\overline{n}_{\mathrm{min}} = 1/\sqrt{\eta} - 1/2 = 0.09$. The discrepancy with our experimental results arises from the sub-optimal filter employed. As discussed, this is necessary in order to avoid instabilities of other mechanical modes, which lie outside the phononic bandgap. Improvements of the actual performance can be achieved by designing a mechanical resonator with a larger bandgap and a mode closer to its center, as well as designing optimal filters which take into account the actual multimode nature

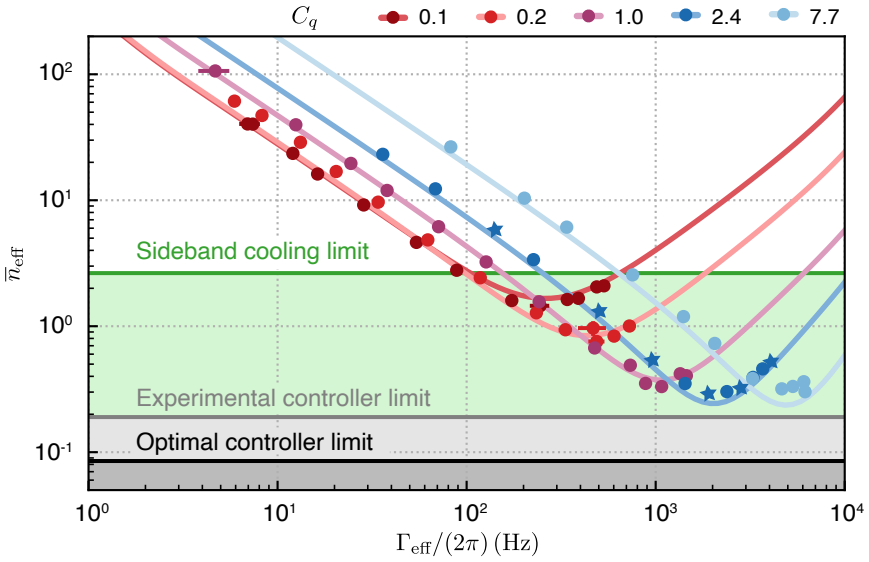


Figure 6.8: Feedback cooling to the quantum ground state. Effective phonon occupations, for different quantum cooperativities, $\mathcal{C}_q$, as a function of the electronic gain, in units of effective mechanical linewidth, $\Gamma_{\rm eff}$. Points are data, error bars indicate the confidence interval from the fit, solid lines are predictions using independently estimated parameters. The black and gray lines indicate the lowest achievable occupation for, respectively, the optimal and experimental controller. The green line indicates instead the sideband cooling limit for this optomechanical system. Adapted from [Ros+18].

of the membrane resonator. Furthermore, one can take advantage of the optomechanical correlations present in the measurement, e. g. by moving from a phase to a rotated quadrature detection, to reduce even more the occupation, for a given choice of the filter [Hab+16].

This experiment shows, for the first time, that measurement-based control can be employed to achieve ground state cooling of a mechanical resonator. In particular, its performance can overcome equivalent cooling techniques, not based on measurements. As an example, we consider a sideband cooling performed with the same cavity mode addressed by the probe laser. In the optimal situation, the lowest limit corresponds to an occupation of 2.6 phonons, which is almost an order of magnitude above what we have obtained. In sideband cooling, in fact, the quantum backaction noise poses limits on the achievable occupation [AKM14]. Measurement-based cooling, instead, can counteract this quantum noise if an efficient measurement is provided. Because of this quantum backaction cancellation [Wis95], feedback cooling to the ground state can be considered as a form of measurement-based quantum control.

### 6.3.1 *Heating rate out of the ground state*

The mechanical state, prepared close to the ground state, is now an unconditional one and will remain so as long as the feedback control is acting on the system. When the control is switched off, the decoherence from the quantum backaction and the thermal bath kicks in and heats the mechanics up to the initial thermal state. To show

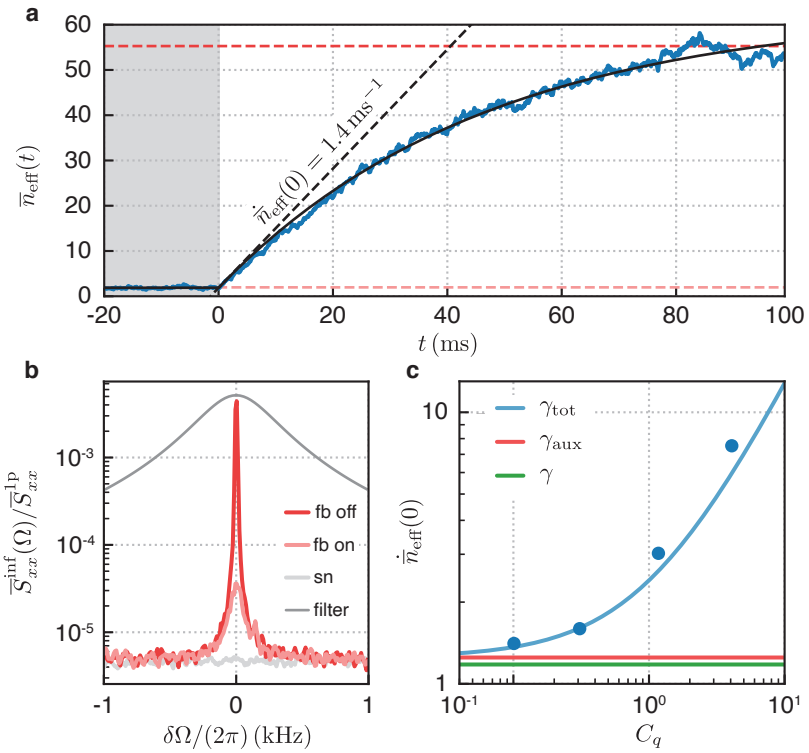


Figure 6.9: Heating rate from a low occupation state. a, Mechanical occupation, $\bar{n}_{\rm eff}(t)$ (blue), during the heating process, caused by switching off the main control loop at $t = 0$ ms. The black line is a fit, the dashed black lines indicate the slope from the initial occupation, $\dot{\bar{n}}_{\rm eff}(0) \approx \gamma_{\rm tot}$. The dashed coloured lines are the initial and final occupations, estimated from the spectra in b. b, Measured displacement spectra, corresponding to the initial (light red) and final (dark red) states. The light gray trace is the shot noise and the dark gray line is the demodulation filter used by the LIA. c, Measured heating rate for different quantum cooperativity (blue circles). The blue line is a prediction from independently estimated parameters, which accounts for thermal (green) and quantum backaction decoherence (red) from the auxiliary laser. Adapted from [Ros+18].

that and to measure the coherence time from the ground state, we start by feedback cooling the mechanical state to a low occupation of $\bar{n}_{\rm eff} \approx 2$. Then, we switch off the main feedback control, $H_{\rm main}$, while monitoring the in-loop homodyne photocurrent. The auxiliary filters, $H_{\rm aux}$, are on all the time, to provide cooling of some low-frequency

modes. We provide more details on the calibration and methods in the next section.

The resulting heating process, averaged over ~ 400 experimental repetitions, is shown in Figure 6.9a. The mechanical state heats up to $\overline{n}_f \approx 60$, which mainly results from the sideband cooling of the auxiliary laser. We fit the heating curve to an exponential law. From the result of the fit we estimate the slope of the initial dynamics, at $t = 0$ ms, corresponding to a total heating rate of 1.4 phonons/ms out of the ground state. This rate corresponds to a total decoherence time of $1/\gamma_{tot} \approx 730$ μs, which contains both the thermal decoherence one, predicted to be 850 μs for a bath at temperature of $T \approx 9$ K for this experiment, as well as the quantum backaction noise decoherence from both the probe and auxiliary laser. We repeat this measurement for different quantum cooperativities, $\mathcal{C}_q$, and show the measured heating rates in Figure 6.9c. The data are well explained by a model which indeed takes into account all the three source of decoherence previously mentioned.

#### 6.3.1.1 *Methods and calibration*

*Variance extraction during the heating process*

We toggle the main control filter on and off by means of an electronic switch, placed after the RedPitaya unit which generates the main filter. The switch is driven by a 200 ms-period square wave. The homodyne photocurrent is electronically split and simultaneously sent to the DAQ card for the spectral analysis and to an LIA, which extracts the total variance, $\sigma^2_{\Omega_m}(t)$, from the frequency components at $\Omega_m$ within a bandwidth of 300 Hz. It is this variance which is averaged over the experiment repetitions. From it, we subtract the shot noise variance, $\sigma^2_{\Omega_m,sn}(t)$, which is measured with the LIA by blocking all the fields but the LO. The resulting variance, proportional to the area of the displacement spectrum, thereby to the mechanical occupation, forms the heating process.

*Calibration of the raw variance into phonons*

We perform a two-step calibration of the raw variance, measured in $V^2$, into an effective mechanical occupation, $\overline{n}_{eff}$. First, we derive in the usual way a voltage-to-displacement conversation factor, from the spectra recorded by the DAQ, the measured coupling rate, $g_0$, and the are of the calibration tone at 1.09 MHz (cf. Section 4.2.4.2). This conversion factor refers to voltages measured by the DAQ, whereas the heating process is measured by the LIA. Since the two instruments might have different systematic errors, e. g. due to electronic imperfection in the photocurrent splitting, we need to assess and correct for this discrepancy. Then, as a second calibration step, we use the optical shot noise as a marker. We filter and integrate the shot noise spectrum, measured by the DAQ, using the same filter employed by the LIA, as shown in Figure 6.9b. The resulting variance is compared to the one outputted by the LIA, and used to correct the voltage from the LIA.

# 7

# ENTROPY PRODUCTION IN A MONITORED MECHANICAL RESONATOR

The experiments reported in the previous chapters focus on a core aspect of any experimental science, that is, the ability of performing measurements on a given system in order to extract information about it. In particular, we have shown that quantum physics has profound implications in the measurement action, as it requires that any extracted information is accompanied by corresponding fluctuations, in order to satisfy an Heisenberg measurement-disturbance relation.

At the same time, information also has deep connections and influences on the thermodynamics of the system, as pointed out already by Maxwell, Szilard and Landauer [PHS15]. In fact, the process of acquiring information from a measurement generally affects the entropic balance of the system being measured [ALR16]. This means that the information should be treated as a real physical thermodynamic quantity, on par with others like heat, energy and work. As a consequence, the second law of thermodynamics should be generalized in order to take into account the eventual entropic contribution of the information gathered from a measurement [SU09].

Here we combine these two approaches and experimentally study the thermodynamics of a mechanical resonator, the displacement of which is monitored by a quantum-limited measurement. We briefly review some of the basics concepts of non-equilibrium and stochastic thermodynamics [Bin+18], then we describe the experiment we performed to observe the informational contribution to the entropy of the measured system. As we will see, the contribution from the quantum measurement dominates the thermodynamics.

## 7.1 NON-EQUILIBRIUM THERMODYNAMICS AND ENTROPY PRODUCTION

Let's review some of the basics thermodynamic concepts, which will be useful later. The canonical setup contains a system comprising few degrees of freedom, which can be monitored and controlled by the observer, interacting with an environment which instead has a large number of degrees of freedom, partially or totally inaccessible to the observer. An important thermodynamic quantity is represented by the total entropy rate, $\dot{S}$. In general, we can split it into two qualitatively different contributions [Bin+18],

$$\dot{S} = \Phi + \Pi. \tag{7.1}$$

The former, $\Phi$, represents the *entropy flux*, which quantifies the entropy exchange between the system and the environment, whereas the latter, $\Pi$, is the *entropy production rate*, which instead expresses the rate at which entropy is produced in the system in an irreversible way. Then, the entropy production rate quantifies the amount of irreversibility present in the dynamics.

*Non-equilibrium steady-state*

For systems in thermal equilibrium at the steady-state, the entropy rate vanishes and both the entropy flux and production rate are zero, i. e. $\Phi = \Pi = 0$. A typical example is given by a mechanical resonator coupled to an environment consisting only of a thermal bath. The situation is different for non-equilibrium systems, like an optomechanical cavity in which the system, comprising an optical and a mechanical mode, couples to an environment, comprising both a thermal and an optical bath. At the steady-state, both modes of the system thermalize to different temperatures from the ones of the respective baths. In these non-equilibrium systems there is a continuous irreversible generation of entropy, which then flows away into the environment. Despite the total entropy rate remains null, as required by a steady-state, both the entropy flux and production rate, individually, are not zero, i. e. $\Phi = -\Pi \neq 0$. This allows to define a second law of thermodynamics, even in the case of non-equilibrium systems, as $\Pi \geqslant 0$, where the equality holds if and only if the thermal equilibrium is achieved.

This picture gets altered in presence of measurements. We have already seen, in Section 5.3, that the outcomes from a measurement lead to a conditional dynamics, understood in terms of stochastic trajectories. Based on this view, one can build a similar perspective for a stochastic thermodynamics, in which the entropic quantities are also affected by the measurement outcomes. As of today, however, a general framework for describing the entropy production rate of a monitored quantum system does not yet exist. Recently, a new theoretical description has been proposed for quantum Gaussian systems subjected to continuous Gaussian measurements [Bel+19]. This class of systems, despite not being universal, is of vast theoretical applicability and embodies a large number of existing experimental platforms, like the optomechanical cavity setup described in this thesis.

*Stochastic thermodynamics*

In stochastic thermodynamics the entropy is defined at the level of a single stochastic trajectory, $\mathbf{r}_c$, realized by the system, thus we talk about conditional entropy, $S_c$. For Gaussian systems this conditional entropy always remains deterministic. Nonetheless, one can recast the conditional entropy increment as $dS_c = \phi_{c,\mathbf{r}} + \pi_{c,\mathbf{r}}$, similar to Equation 7.1. These two terms, $\phi_{c,\mathbf{r}}$ and $\pi_{c,\mathbf{r}}$, are conditioned on a single trajectory, $\mathbf{r}_c$, and thus are stochastic quantities. We call them the stochastic entropy flux and production rate, respectively. They represent the fluctuations of the deterministic conditional counterparts, that is, the conditional entropy flux and production rate, which are

obtained from averaging the stochastic quantities over all the possible trajectories, respectively $\Phi_c \coloneqq \mathbb{E}[\phi_{c,\mathbf{r}}]$ and $\Pi_c \coloneqq \mathbb{E}[\pi_{c,\mathbf{r}}]$.

In order to assess the influence of the measurement, we can compare the conditional entropy flux and production rate to the unconditional counterparts, where the measurement outcomes are ignored. For Gaussian systems, the entropy flux is not affected by the measurement at all, thus one has $\Phi_c = \Phi_{uc}$ [Bel+19]. In contrast, the acquisition of information allows the observer to reduce the irreversibility in the system. As such, the irreversible entropy which is conditionally produced, i. e. the time integral of the conditional entropy production rate, $\Sigma_c = \int \Pi_c \, dt$, is always less than the entropy unconditionally produced, $\Sigma_{uc} = \int \Pi_{uc} \, dt$, such that $\Sigma_c \leqslant \Sigma_{uc}$. Their difference exactly assesses the amount of irreversible entropy cancelled by the acquisition of information through the measurement [Bel+19]. In terms of rates, one has

*Conditional entropy production rate*

$$\Pi_c = \Pi_{uc} + \dot{\mathcal{I}}, \tag{7.2}$$

where $\dot{\mathcal{I}}$ is the rate at which entropy is produced by the acquired information. In particular, its integral, $\mathcal{I}$, can be also expressed as the opposite of the mutual information between the coordinates of the system phase space in the unconditional case, $\langle \hat{\mathbf{r}} \rangle$, and the stochastic ones in the conditional case, $\langle \hat{\mathbf{r}} \rangle_c$. Since the mutual information is always non-negative, the informational theoretic entropy contribution, $\mathcal{I}$, is always non-positive.

In addition, Equation 7.2 suggests that the second law of thermodynamics can be refined to be $\Pi_c \geqslant \dot{\mathcal{I}}$ for monitored systems. This is an important result, as it formally extends the connection between information theory and non-equilibrium thermodynamics [SU09], as pioneered by the Landauer's principle, to an important class of quantum systems.

Despite its importance, an experimental assessment of this informational theoretic contribution is still missing. In the following, we exploit the quantum trajectory description and the retrodiction measurement from Section 5.3 to access the conditional dynamics, from which we infer the thermodynamics of the mechanical resonator.

## 7.2 STOCHASTIC THERMODYNAMICS OF A MONITORED MECHANICAL RESONATOR

The experimental setup is the same shown in Figure 5.6 and the data here reported have been acquired on the same experimental run [Ros+20]. Here, we employ a different power for the probe laser, such that $\Gamma_{qba}/(2\pi) = 0.36$ kHz. The dynamical backaction from both the probe and the auxiliary lasers broadens the mechanical linewidth to $\Gamma_m/(2\pi) = 19$ Hz, with a resonance frequency $\Omega_m/(2\pi) = 1.14$ MHz. In addition, residual laser cooling and the quantum backaction noise

from the auxiliary laser determines an effective thermal bath with occupation $\overline{n}_{th} = 14$. The phase of the transmitted probe laser is monitored via a BHD, with a total efficiency of $\eta = 74\%$.

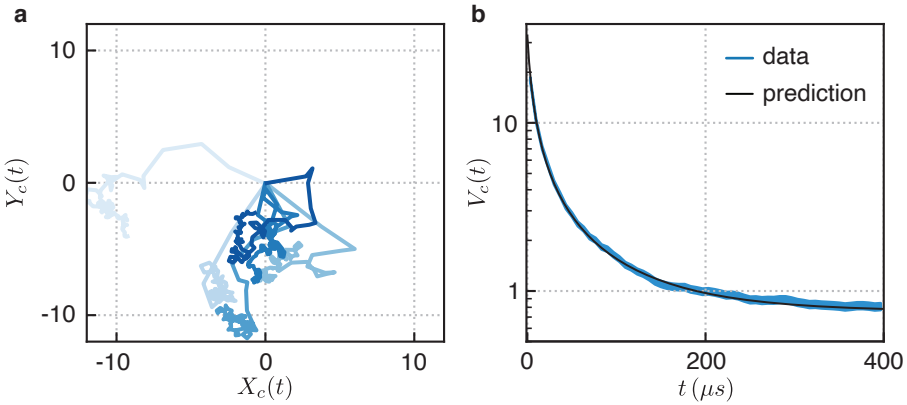


Figure 7.1: Measured conditional state. a, Sample of average displacement over time, $\mathbf{r}_c(t)$, from six different measured quantum trajectories. The conditioning is started at $t = 0$ ms, at which all trajectories agree on the same initial state $\mathbf{r}_c(0) = 0$. b, Measured conditional variance (blue) from comparison with the retrodiction measurement. The black line is a theoretical prediction from independently measured parameters. At the steady-state the conditional variance is $\overline{V}_c = 0.8$.

The recorded photocurrent is used to derive the quantum trajectory and the retrodiction measurement, from which we infer the evolution of the conditional variance based on the experimental distance variance (cf. Section 5.3.3), shown in Figure 7.1. This conditional variance, together with the average displacement $\mathbf{r}_c(t)$, fully characterizes the conditional state [Ros+19]. From it, we can now calculate the stochastic entropy flux and production rate [Bel+19]. However, in order to obtain the correct theoretical expressions, we should be careful with the location of the optical cavity in the system-environment split.

*Thermodynamic consequences of the adiabatic elimination*

In fact, for calculating the quantum trajectory, we performed an adiabatic elimination of the cavity mode from the system dynamics [Hof17]. As already discussed, this approximation is fully justified in the regime of the experiment, $\kappa \gg \Omega_m, g$, and the resulting effective equations of motion for the mechanics are fully consistent with the ones obtained from the full optomechanical model, where the cavity elimination is done afterwards. However, this equivalence does not carry over to the thermodynamic calculations. The reason lies in the artificial division between the system and the environment. In fact, the adiabatic elimination of the cavity moves it from the system to the environment, which now consists of the mechanical thermal bath, the optical cavity mode and its optical bath. Effectively, in the adiabatic elimination regime, the mechanical mode is considered in contact with two baths, which are the usual thermal one and an effective optical

bath with the coupling rate $\Gamma_{opt}$ and the occupation $\overline{n}_{opt}$. In particular, in the resonant case, $\Delta = 0$, this elimination leads to an effective optical bath with infinite temperature, $\overline{n}_{opt} \to \infty$, and zero coupling rate, $\Gamma_{opt} \to 0$, such that their product is still finite, $\Gamma_{opt}\overline{n}_{opt} = A_+$ (cf. Section 3.3). The consequence is that one predicts a null entropy flow between the mechanical resonator and the effective optical bath, despite the presence of an energy flow between them [Ros+20]. This counter-intuitive and unphysical fact arises because the entropy flux is between the cavity mode and the optical bath, both of which are hidden in the environment by the adiabatic elimination. Thus, they are not anymore part of the system and do not contribute to the calculated entropy flux, as sketched in Figure 7.2.

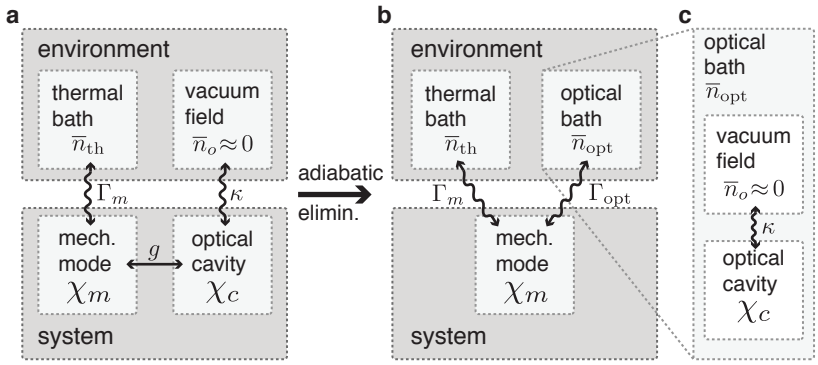


Figure 7.2: Thermodynamic implications of cavity adiabatic elimination. a, An optomechanical system comprises a mechanical mode coupled to an optical cavity, both in thermal contact with their respective baths, which together form the environment. Entropy flows between each mode and its own bath and it is irreversibly produced within the mechanical and optical modes. b, Adiabatically elimination of the cavity mode leads to a system comprising the mechanical mode only, interacting with an environment formed by the thermal bath and an effective optical bath. The entropy flux between the cavity mode and the vacuum field is now embedded in the environment, as shown in c, and thus not part of the system thermodynamics.

To properly assess all the entropic contributions, we should first calculate the thermodynamic quantities from the full optomechanical model, and subsequently perform the adiabatic elimination in the derived expressions. This is performed by taking the limit $\kappa/\Omega_m \to \infty$, and averaging the stochastic entropy flux and production rates only over the cavity mode trajectories.

Following this approach for the unconditional steady-state, we derive the following result

$$\Phi_{uc} = -\Pi_{uc} = -\Gamma_m \mathcal{C}_q - 4V_{uc}\Gamma_{qba}. \tag{7.3}$$

As expected from a non-equilibrium steady-state, the sum of the entropy flux and production rate is zero, while they are not individually zero.

*Stochastic thermodynamics of a monitored resonator*

Moving to the conditional case, we obtain the following stochastic quantities

$$\phi_{c,\mathbf{r}} = \Gamma_m - \left(\frac{\Gamma_m}{\overline{n}_{th}+1/2} + 4\Gamma_{qba}\right)\left(V_c(t) + \mathbf{r}_c(t)^T\mathbf{r}_c(t)\right), \tag{7.4a}$$

$$\begin{aligned}\pi_{c,\mathbf{r}} = &-\Gamma_m + \left(\frac{\Gamma_m}{\overline{n}_{th}+1/2} + 4\Gamma_{qba}\right)\left(V_c(t) + \mathbf{r}_c(t)^T\mathbf{r}_(t)\right) \\ &-\Gamma_m + \Gamma_m V_{uc}/V_c(t) - 4\Gamma_{meas}V_c(t),\end{aligned} \tag{7.4b}$$

where $\mathbf{r}_c(t)$ is the average displacement from the quantum trajectory, as shown in Figure 7.1. Finally, the conditional entropy flux and production rate are obtained from averaging Equation 7.4 over all the quantum trajectories.

We now proceed to experimentally reconstructing this stochastic entropy flux and production rates from the measured average displacement, $\mathbf{r}_c(t)$, and the conditional variance, $V_c(t)$, using Equation 7.4. In Figure 7.3 we show a subset consisting of ten trajectories, as well as the conditional entropic quantities obtained from averaging all the 3600 trajectories together.

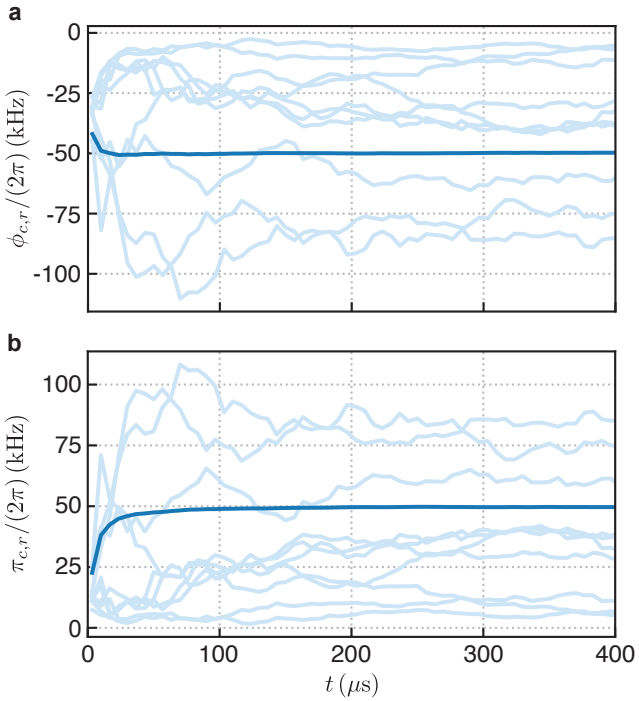


Figure 7.3: Stochastic entropy flux and production rates. a, Stochastic entropy flux and b, production rates (light blue) for a sample of ten trajectories. Averaging all the trajectories yields the conditional entropy flux and production rates (dark blue)

We notice from Figure 7.3 that these entropic quantities fluctuate wildly despite the small thermal bath occupation of 14 phonons,

highlighting the essential role of fluctuations in the thermodynamics of the system. As expected, we find that the conditional entropy flux, $\Phi_c$, equals the unconditional one which is estimated to be $\Phi_{uc}/(2\pi) = -48$ kHz, from Equation 7.3. Instead, the conditional entropy production rate differs from the unconditional one at the beginning of the measurement.

To highlight it, in Figure 7.4 we show their difference, which corresponds to the informational contribution, $\dot{\mathcal{J}}$, from Equation 7.2. For the

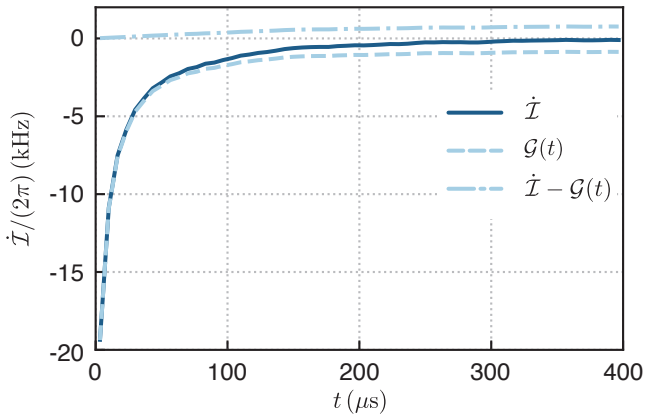


Figure 7.4: Informational contribution to the conditional entropy production rate. We obtain the informational contribution (blue) from the difference between the conditional and unconditional entropy production rates. The dashed (dot-dashed) line is the differential gain (loss) of information due to the measurement (thermal noise).

optomechanical case we find

$$\dot{\mathcal{J}} = \Gamma_m \left( \frac{V_{uc}}{V_c(t)} - 1 \right) - 4\Gamma_{meas} V_c(t). \tag{7.5}$$

At the steady-state, this contribution approaches zero and monitoring does not add any additional information. Nevertheless, monitoring is still necessary in order to maintain the generated conditional state. In fact, the negative entropy production rate, due to the gathered information, is exactly balanced at the steady-state by positive production rate from the noise coming from the thermal bath. The rate of acquired information can be identified, from Equation 7.5, by $\mathcal{G}(t) = -4\Gamma_{meas} V_c(t)$, known as the *differential gain*. We highlight its contribution in Figure 7.4. At the early stage of the measurement, this differential gain dominates, thus reflecting the fact that at the beginning of the measurement there is much to be learnt from monitoring the system. As time goes on, the steady-state is approached and the differential gain drops to the small but non-zero value $\overline{\mathcal{G}} = -4\Gamma_{meas}\overline{V}_c$, which represents the rate at which the detector must acquire information to maintain the achieved conditional state.

This is the first experimental assessment of the informational contribution on the thermodynamics of a quantum monitored system,

demonstrating the key role played by measurement in influencing the thermodynamics of a quantum system.

# 8

# BACKACTION EVASION AND ENTANGLEMENT IN QUANTUM MEASUREMENTS

In this chapter we report some preliminary results of other experiments on quantum measurements. As such, they deserve more studies and represent a natural continuation of the work reported in this thesis.

The first part of the chapter is devoted to describe the implementation of a quantum non-demolition (QND) measurement in our optomechanical system. In such a measurement, the monitored observable is different from the one affected by quantum backaction, which thus does not show up in the outcomes. Therefore, this measurement contributes with an arbitrarily small added noise, not subjected to an SQL. We report the first experimental attempts and their results, which show that the multimode nature of the membrane structure represents a major obstacle for such measurements.

The second part of the chapter focuses on the generation and verification of the entanglement between the mechanics and the optical field. This optomechanical entanglement is predicted by the quantum measurement theory and is peculiar to the act of measuring. We report some first preliminary results on inferring the optomechanical entanglement from the experimentally verifiable entanglement of two properly chosen optical modes.

## 8.1 STROBOSCOPIC QND MEASUREMENT

Quantum mechanics imposes additional fluctuations to a measured system, through the quantum backaction noise. We have amply discussed the case of the measurement of the displacement, $\hat{q}$, of a mechanical resonator, for which the quantum backaction appears on the conjugate momentum observable, $\hat{p}$. Since these two are dynamically linked by the harmonic evolution, the backaction will also appear in the displacement, $\hat{q}$, a quarter of period later. The appearance of the quantum backaction in the measured observable lies in the fact that we are simultaneously measuring two non-commuting observables. In fact, for a high-Q mechanical resonator we can write the displacement in terms of slowly-varying quadrature operators, $\hat{X}$ and $\hat{Y}$, as $\hat{q} = \hat{X}(t)\cos(\Omega_m t) + \hat{Y}(t)\sin(\Omega_m t)$. These quadrature operators do not commute, but they are dynamically coupled. It is this pair of non-commuting observables that we are simultaneously measuring, as pointed out in Section 5.3. As a consequence, the Heisenberg uncertainty relation imposes that, at best, we can measure the displacement

with a noise at the level of vacuum fluctuations, which results in the production of a conditional coherent state. From the perspective of the quantum measurement theory, this displacement measurement forms a POVM which approximates a projective measurement on coherent states [Wis96].

Despite that, one can envision different measurement schemes in which the quantum backaction does not show up in the outcomes. These schemes form a class of quantum measurements known as *backaction-evading (BAE)* or *QND measurements*[1] [BVT80; BK92; WM10]. For instance, measuring a single mechanical displacement quadrature, e. g. $\hat{X}$, would induce the quantum backaction in the orthogonal one, $\hat{Y}$. Opposite to the displacement and momentum, these two quadratures are dynamically uncoupled and the backaction never shows up in the outcomes for $\hat{X}$, which can then show arbitrarily small measurement-induced noise. This would correspond to a POVM which approximates projective measurements on quadrature squeezed states [Wis96].

BAE measurements in optomechanical systems have been proposed and recently experimentally implemented [Suh+14; Lec+15]. Intuitively, one can measure a single mechanical quadrature by toggling the optomechanical interaction, $g$, on and off in correspondence of times at which the orthogonal quadrature is zero, which happens at a rate of $2\Omega_m$. In particular, in the sideband-resolved limit, i. e. $\kappa \ll \Omega_m$, this can be achieved by fully modulating the amplitude of the input field at $2\Omega_m$ [CMJo8]. Spectrally, it corresponds to driving the optomechanical cavity with two optical tones, at detunings $\pm\Omega_m$.

*Stroboscopic measurements*

The situation is different in the opposite limit of non-sideband-resolved cavity, relevant for our experiments. Now, the cavity instantaneously follows the dynamics of the mechanical displacement. Then, a single quadrature measurement can be done by detecting the phase quadrature of the optical field which is flashing for a duration much shorter than the mechanical period, $1/\Omega_m$. During each flash, the mechanical harmonic evolution is frozen and the optical field measures effectively only one mechanical quadrature. Once the light flash is over, the mechanical state continues its rotation at frequency $\Omega_m$ and aligns back along the previously measured quadrature every half a period, $1/(2\Omega_m)$. At this time, another light flash is sent towards the optomechanical cavity to keep measuring the same single quadrature. The protocol is then repeated every half mechanical period. By collecting more and more outcomes, this measurement progressively projects the conditional mechanical state from the initial thermal state onto a quadrature squeezed state. The amount of noise reduction, and eventually squeezing, is determined by the balance between the rate of the measurement-induced collapse and any other decoherence

1 Strictly speaking, QND and BAE measurements are different and the former one implies the latter [WM10]. In practice, however, they are used as synonyms as most, if not all, proposals made so far for BAE measurements are also QND.

rates, like the thermal one. We notice that the quantum backaction has not disappeared, but has been confined in the orthogonal quadrature which is never measured. This *stroboscopic measurement* scheme [BVT80; Bru+20] allows to realize a BAE for a mechanical resonator, but has never been shown experimentally.

### 8.1.1 *Experimental setup and protocol*

Here we describe the implementation of the stroboscopic BAE measurement in our optomechanical setup and discuss some preliminary results. Experimentally, we use the setup sketched in Figure 8.1a. The

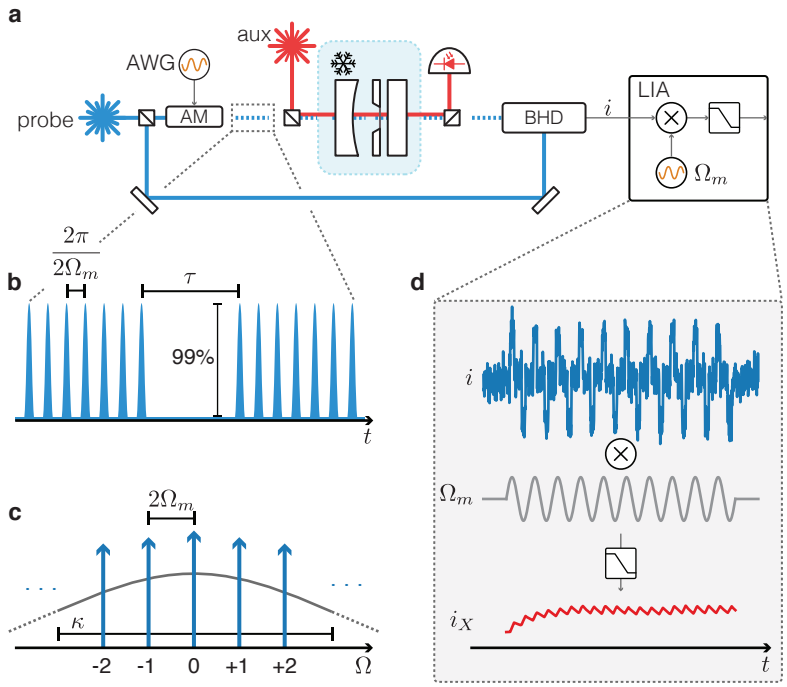


Figure 8.1: Stroboscopic BAE measurement. a, Experimental setup. The probe field is amplitude-modulated to generate a stroboscopic sequence of flashes, which are directed towards an optical cavity. The phase of the transmitted beams is monitored by a BHD, with continuous LO. An auxiliary laser, detuned from a different cavity mode, is also employed. b, Stroboscopic flashes, with repetition rate of $2\Omega_m$. The modulation depth is chosen to be ~ 99% such that a weak locking beam is always present. Two of such stroboscopic packets can be delayed by a time $\tau$. c, Frequency representation of the stroboscopic input probe field. The spacing between tones is constant and equal to $2\Omega_m$. The gray line represents the cavity lineshape. Each tone is labelled with an integer, where 0 corresponds to the laser carrier. d, Sketch of the electronic processing. The mechanical quadrature is retrieved by demodulating the homodyne photocurrent, $i(t)$, at frequency $\Omega_m$ at the right phase.

stroboscopic measurement is performed by a probe laser, the amplitude of which is modulated by means of a fiber-based modulator. The

modulation depth is chosen to be ~ 99% such that a weak continuous field is always present even in the "off" configuration. This weak field allows to lock the laser carrier to the cavity mode. The modulator is driven by a train of smooth pulses, from an arbitrary waveform generator, at a repetition rate of $2\Omega_m$ with a small duty cycle, such that each flash lasts much less than the mechanical period (cf. Figure 8.1b). In addition, we also use a weak auxiliary laser, locked to the red side of a different cavity mode. This laser provides a broad sideband cooling of the membrane modes, which is necessary to reduce some of the observed in-bandgap noise (cf. Section 5.1). We set the power of the auxiliary laser to the minimum value necessary for stabilization, in order to keep the additional quantum backaction small. We notice that here we do not feedback-cool any low-frequency modes.

Spectrally, the stroboscopic input probe field contains several tones, evenly spaced at $2\Omega_m$. Their relative phase and amplitude are determined by the exact shape of the pulses. We label these tones with positive (negative) integers, for frequencies above (below) the carrier, which is the reference tone marked with 0, as shown in Figure 8.1c. Each tone can be considered as a CW field at a fixed detuning from the cavity resonance, consequently each of them is part of the standard optomechanical interaction as outlined in Chapter 3. In particular, each tone acquires symmetric mechanical sidebands due to the displacement of the membrane modes.

Finally, the phase of the transmitted stroboscopic field is detected by means of a BHD operated with a continuous LO, which enables to extract the proper mode by electronic processing. This is done with an LIA, as sketched in Figure 8.1d. The continuously measured photocurrent carries the mechanical (shot noise) information when the flashes are on (off). The mechanical information is retrieved by demodulating the photocurrent at $\Omega_m$ with a phase such that the flashes occur at the extrema of the reference sine wave. In this way, one demodulated quadrature maximally weights the photocurrent during the flashes, with alternating sign, and minimally when the flashes are off, during which only the shot noise is present. Once filtered, this demodulated quadrature provides a measurement outcome for a single mechanical quadrature.

*Experiment protocol*

The experiment we conceived comprises a preparation, an evolution and a verification step and aims to measure the *natural* mechanical heating rate out of a low-occupation state, due to the thermal bath only. In Section 6.3.1 we measured this heating rate exploiting continuous displacement measurements. However, that inevitably resulted in an additional contribution to the heating rate from the quantum backaction decoherence. Here instead, we want to take advantage of the stroboscopic BAE measurement to confine this backaction in the unmonitored mechanical quadrature. At first, we perform a stroboscopic measurement with a first packet of flashes, as described

in Figure 8.1, which allows to generate a conditional state with the variance along one quadrature reduced down to the level of zero point fluctuations. Subsequently, the optical field is switched off, such that the mechanical conditional state only diffuses under effect of the thermal noise [Bru+20]. Finally, another packet of stroboscopic flashes is sent towards the cavity after some time delay, $\tau$, from the first one, to perform another single-quadrature measurement to verify how much the state has diffused in the meanwhile. The protocol is then repeated several time at different delays to collect a statistics from which one can estimate the variance of the heating process, thus the heating rate from the initial slope.

### 8.1.2 *Preliminary results*

We implement the above protocol and collect preliminary results, which however show the presence of excess noise at frequencies around the mechanical resonance. This noise heats the prepared conditional state up, making its variance higher than expected. In addition, the measured variance at different delays does not show any clear evidence of a heating process. After excluding an electronic origin for this excess noise, e. g. through the modulator or in the detection, we come up with a plausible explanation which individuates the source of this noise in an *optical aliasing effect*, sketched in Figure 8.2, similar to the aliasing occurring in data periodically sampled [PM07]. In fact, *Optical aliasing*

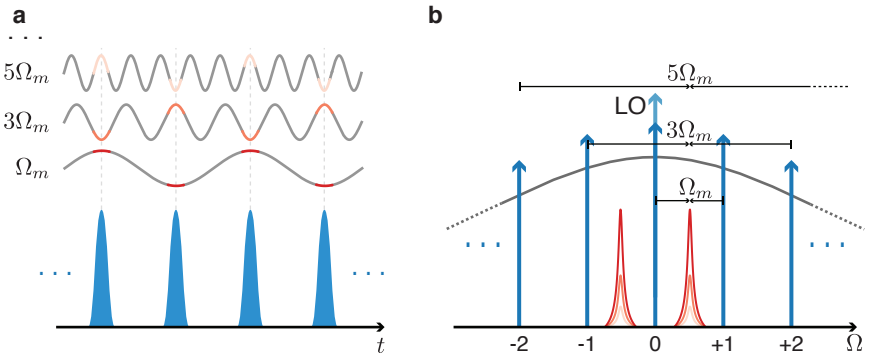


Figure 8.2: Optical aliasing in stroboscopic measurements. a, A stroboscopic measurement at $2\Omega_m$, represented by the blue flashes, cannot discriminate between the mechanical motion from a mode at $\Omega_m$ or its odd harmonics. b, In frequency domain, each optical tone acquires symmetric mechanical sidebands at the frequency of the mechanical modes. The demodulated BHD photocurrent contains all the sidebands, at around $\pm\Omega_m$, from each tone. Here we only sketch the pair of sidebands around the carrier tone. At these sideband frequencies, however, both the in-bandgap mode of interest, which appears as a $\pm\Omega_m$ sideband around order 0 and $+1$, and its odd harmonics, e. g. modes at $3\Omega_m$ which appears as sidebands around order $-1$ and $+2$, contribute.

a stroboscopic measurement at $2\Omega_m$ would not only measure the mechanical quadrature from the mode at $\Omega_m$, but also the ones from the odd harmonics. Spectrally, on top of any pair of sidebands at $\pm\Omega_m$ around a given tone, let's say 0, there will also be mechanical sidebands at $+(2n+1)\Omega_m$ from tone $-n$ and at $-(2n+1)\Omega_m$ from tone $n+1$, for $n$ integer, as sketched in Figure 8.2b. The total number of tones contributing is given by how many of them are not suppressed by the cavity response, which is quantified by the ratio $\kappa/(2\Omega_m)$, much larger than unity for a broad cavity necessary to achieve a stroboscopic BAE measurement. In addition, the membrane structure is highly multimode, especially at the location of these higher harmonics which are outside the phononic bandgap.

To corroborate this hypothesis, we stroboscopically flash the probe laser and measure the spectrum of the transmitted phase quadrature, continuously acquired. The result is shown in Figure 8.3a. We observe,

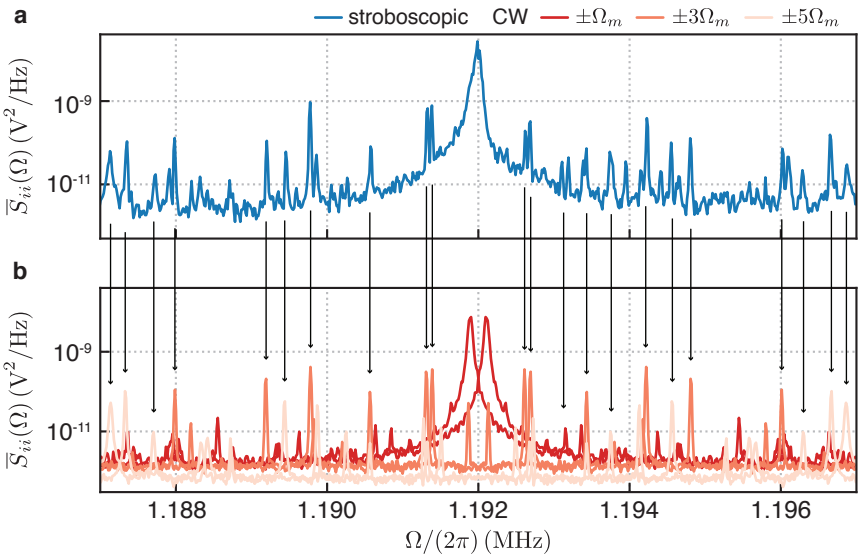


Figure 8.3: Verifying the presence of optical aliasing. a, Spectrum of the homodyne photocurrent, while flashing the probe laser. The in-bandgap mode is at $\Omega_m/(2\pi) = 1.192$ MHz, the other visible peaks are the excess noise from optical aliasing. b, The spectrum of the homodyne photocurrent spectrum is also recorded with a CW probe laser. In order to understand what is happening in a, at around $+\Omega_m$, we plot this continuous spectrum several times, flipped and shifted accordingly to the order to which it refers to. In particular, we simulate the presence of tones 0, $\pm1$, $\pm2$ and $+3$. The black arrows indicate the correspondence between the additional peaks in the stroboscopic spectrum from a, and the peaks from the continuous spectrum.

apart from the in-bandgap mode at $\Omega_m/(2\pi) = 1.192$ MHz, additional peaks all around. Subsequently, we stop flashing the probe laser and continuously operate it, reducing the optical power in order to match the averaged one while flashing. We then acquire a phase spectrum

which does not show the additional peaks in the bandgap. The measured stroboscopic spectrum would actually contain the sidebands from the other tones, according to the optical aliasing hypothesis. We mimic this effect by shifting and flipping the measured continuous spectrum to match the corresponding tone from which it refers to. In Figure 8.3b we do that for the tones 0, $\pm 1$, $\pm 2$, $+3$, and show the resulting spectrum in the frequency range around $\Omega_m$. We notice, with high-accuracy, the correspondence between these peaks and the ones stroboscopically measured in Figure 8.3a, corroborating our hypothesis of optical aliasing.

In particular, this folding of higher order modes in the detection window happens optically and cannot be filtered out at the detection stage or electronically. A possible solution to mitigate this problem is to design a membrane resonator with a different phononic crystal geometry, which will open up additional bandgaps at odd harmonics of the mode of interest at $\Omega_m$. This will reduce the mode density at those frequencies, but would not avoid the defect itself to have harmonics there. Avoiding that would additional require to break the harmonicity of the defect. It turns out that engineering such a design is a cumbersome task and the efforts made so far still are only partially successful, requiring yet more work to be done.

## 8.2 STATIONARY OPTOMECHANICAL ENTANGLEMENT

One of the big challenges of quantum physics, which puzzled generations of scientists, is to understand the transition between the quantum and the classical world. The need for this transition becomes evident when considering the quantum measurement problem, where a measuring apparatus, brought into contact with a system in a given quantum state, produces random outcomes [Zur03b]. The Copenhagen interpretation of quantum mechanics settled this controversy by introducing an arbitrary cut between the *observed* quantum world, i. e. the system, and the *observing* classical world, i. e. the apparatus comprising a meter and a conscious, e. g. a human, or even unconscious, e. g. a computer, observer [Hei50]. This division works well for the understanding of many experiments, where the meter is represented by a complex system with many degrees of freedom, making its quantum description, effectively, intractable. While operationally justified, this approach keeps the interpretation problem still open. The exact location of this cut is somewhat arbitrary and can be moved away to include, in the quantum description, part of the apparatus. In fact, a generic measurement can be thought as a unitary interaction between the system and meter, ultimately representing an entangling operation. Describing and observing this entanglement would then allow to embody the meter into the quantum world and shift the cut between the meter and the observer.

Cavity optomechanics represents a promising platform for studying this problem. The mechanical resonator is the *system* under measurement, the displacement of which is coupled to the phase quadrature of an optical cavity field, which forms the *meter*. The output field is subsequently measured by a detector, i. e. the *observer*, to infer the mechanical displacement. In the previous chapters we detailed several experiments in which this system has been employed as a quantum-limited apparatus. The simplicity of this meter allows to embody it in the quantum description of the measurement problem, making an experimental demonstration of the system-meter entanglement feasible. This entanglement now appears in the form of a stationary opto-mechanical entanglement, as already theoretically predicted more than a decade ago [Gen+08b]. The main challenge for a direct experimental demonstration lies in the fact that the state of the mechanical resonator is not directly accessible and can only be inferred from output optical modes. Despite this, the existence of entanglement between time-ordered optical modes, initially uncorrelated, is sufficient to prove the entanglement of one of these optical modes with the mechanical resonator. Inferring the optomechanical entanglement in this way has been explored theoretically [Hof+11] and experimentally [Pal+13] in a pulsed electromechanical system. More recently, Gut et al. [Gut+19] generalized this idea, showing how one can in fact measure the stationary optomechanical entanglement in a system continuously operated.

### 8.2.1 *Experimental setup and single-mode predictions*

Let's consider the case of an optomechanical cavity continuously driven by a coherent optical field. As a result of the interaction, this field acquires a pair of symmetric sidebands around its carrier, at the mechanical resonance frequency. The red (blue) sideband stems from a Stokes (anti-Stokes) scattering process. The Stokes process down-converts an input photon into a red-detuned photon, which is entangled with a phonon as in a two-mode-squeezing interaction. Conversely, the anti-Stokes process removes a phonon in order to up-convert an input photon into a blue-detuned one, as in a beam-splitter interaction. Based on these two processes, we can now define proper time-ordered modes which are in an entangled state. Intuitively, the former-occurring mode should contain frequency components close to the Stokes sidebands, as these are in an entangled state with the mechanics. As such, we label this optical mode the *entangler*. The latter-occurring mode, labelled *readout*, contains spectral components around the anti-Stokes sidebands, which result from a state-swap with the mechanics, thus are entangled with the entangler mode. These

optical modes can be obtained by filtering the output field, $\hat{a}_{out}(t)$, as described in Section 1.5. Formally, this corresponds to

$$\hat{s}_j = \int_{-\infty}^{\infty} f_j(t)\hat{a}_{out}(t)dt, \tag{8.1}$$

where $j = E, R$ indicates which mode we are considering, i. e. the entangler or readout, and $f_j(t)$ is the appropriate normalizable mode function. The operators $\hat{s}_j$ are mode operators, satisfying the commutation relation $[\hat{s}_j, \hat{s}_k^\dagger] = \delta_{jk}$. For the case of a single mechanical mode, the entanglement is retrieved in the optical modes defined according to [Gut+19]

*Time-ordered optical modes*

$$f_E(t) = \sqrt{2\Gamma_s}e^{(\Gamma_s - i\Omega_s)t}H(-t), \tag{8.2a}$$

$$f_R(t) = \sqrt{2\Gamma_s}e^{-(\Gamma_s - i\Omega_s)t}H(t), \tag{8.2b}$$

which are Lorentzian filters, with bandwidth $\Gamma_s$, around the optical sidebands centered at frequency $\mp\Omega_s$, respectively. The Heaviside function, $H(t)$, ensures that the two modes are time-ordered, that is, they are non-zero in disjoint, subsequent time intervals. A sketch of these modes, both in time and frequency domain, is shown in Figure 8.4a. In order to verify the entanglement between these two

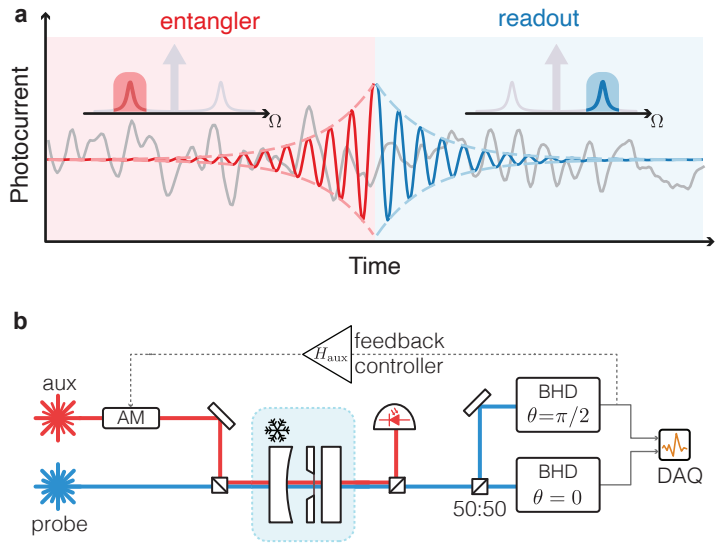


Figure 8.4: Experimental setup for generating and verifying the optomechanical entanglement. a, Sketch of the measurement protocol. From the recorded complex field amplitude (gray trace) we filter out, in post-processing, two time-ordered modes, which are the entangler (red) and the readout (blue). In time domain, their mode functions correspond to oscillations at $\mp\Omega_m$ with a decaying amplitude. In frequency domain, they are Lorentzian band-pass filters centered at $\mp\Omega_m$ (insets). b, Experimental setup for verifying the entanglement of these modes.

modes one can measure the complex output field, $\hat{a}_{out}$, and use it in

Equation 8.2 to obtain outcomes for the complex amplitude of the modes $\hat{s}_j$.

In practice, the experimental setup employed is shown in Figure 8.4b. The mechanical mode of the soft-clamped membrane has a resonance frequency of $\Omega_m/(2\pi) = 1.13$ MHz, a quality factor of $Q = 0.78 \times 10^9$ and stands in a cryogenic environment at $T = 8$ K. Its displacement is measured by a meter, represented by a probe laser locked almost resonantly to a cavity mode, at $\lambda = 799.638$ nm with linewidth $\kappa/(2\pi) = 9$ MHz and $\Delta/(2\pi) \approx -1.44$ MHz. We measure a vacuum optomechanical coupling rate of $g_0/(2\pi) = 150$ Hz via quantum noise thermometry (cf. Section 4.2.4.2). In addition, we also employ an auxiliary laser, locked to the red side of a different cavity mode, at $\lambda_a = 798.052$ nm with $\kappa_a/(2\pi) = 8.6$ MHz and $\Delta_a/(2\pi) = -2.9$ MHz. This laser is used to stabilize, via sideband and feedback cooling, some of the low-frequency modes of the membrane structure.

*Measurement of the field amplitude*

To verify the entanglement of two time-ordered optical modes we need to reconstruct the complex amplitude of the output field. We do that by means of an eight-port homodyne detector [Wal87]. We split the transmitted probe field into two equal beams, which we send towards two independent BHDs, arranged to measure the amplitude, $\hat{X}_{out}$, and phase, $\hat{Y}_{out}$, quadrature. The simultaneous measurement of these non-commuting observables imposes an additional noise on the measurement. This noise is introduced by the uncorrelated vacuum field entering from the unused port of the 50 : 50 BS used to split the transmitted field. Each BHD hence has a maximum achievable total efficiency of 50%. Including this, we estimate for the two detectors a total efficiency of $\eta_X \approx 25\%$ and $\eta_Y \approx 35\%$. The photocurrents from the detectors, $i_X$ and $i_Y$, are continuously acquired and digitized by DAQ. The recorded traces are further chopped into shorter segments, of $\sim 9$ ms duration. Each of these represents a *realization*, that is, an independent experimental repetition which is used to form statistical ensembles of the modes' outcomes. We first use these realizations to compute the PSDs of the amplitude and phase quadrature measurements, as well as their cross-PSD, as shown in Figure 8.5. We fit these data to a standard optomechanical model (cf. Section 3.4), from which we extract the optomechanical coupling rate, $g/(2\pi) = 101$ kHz, and the probe laser detuning, $\Delta/(2\pi) = -1.44$ MHz.

In order to filter out some optical modes we need to estimate, for each realization, the complex amplitude of the transmitted field. To do that we combine the photocurrents from the two BHDs according to $s_{out,j}(t) = (i_{X,j}(t) + i i_{Y,j}(t))/\sqrt{2}$, where $i_{X,j}(t)$ and $i_{Y,j}(t)$ are the $j$th realizations from the BHD measuring the amplitude and phase quadrature, respectively. We also notice that the estimator, $s_{out,j}(t)$, contains both the wanted outcome from the field amplitude, $\hat{a}_{out}$, and an unwanted additional noise contribution, due to inefficiencies, which affects the estimator statistics [Hoe17]. Nevertheless, for stationary

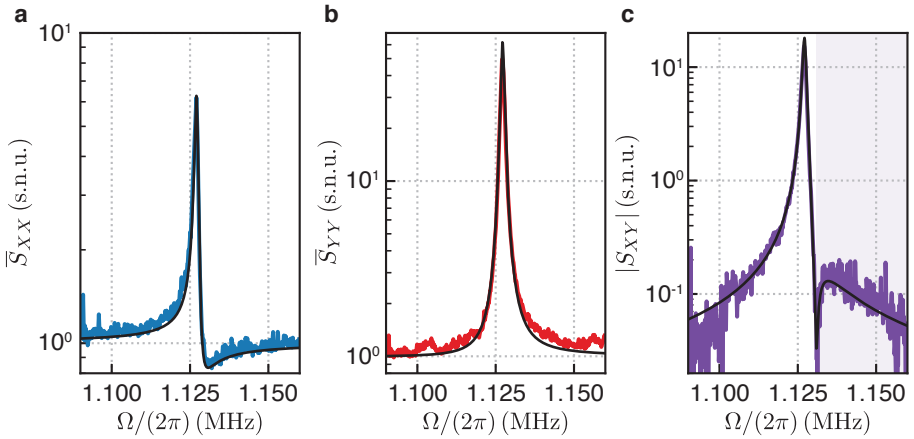


Figure 8.5: Measured amplitude and phase spectra. a, b, Spectra of the amplitude and phase quadrature of the transmitted field, respectively, as measured simultaneously by an eight-port homodyne detector. c, Absolute value of the amplitude-phase quadrature cross-spectrum. The shaded area indicates actual spectral negative values. All the three spectra are simultaneously fitted to a model, the result of which is shown as black lines.

processes as the ones we are dealing with, this noise contribution to the statistics can be calibrated out directly on the final covariance matrix. Then, we apply Equation 8.1 on $s_{out,j}(t)$ to estimate the filtered modes. To ensure the crucial time-ordering, we apply a mode function only on the first (second) half of each realization for estimating the entangler (readout) mode. The resulting numbers, $s_{E,j}$ and $s_{R,j}$, are complex and their real and imaginary parts, $\{X_{E,j}, Y_{E,j}, X_{R,j}, Y_{R,j}\}$, are estimations of the modes' quadratures. This ensemble is used to calculate the covariance matrix, $\widetilde{\sigma}^2_{ER}$. To normalize and calibrate this matrix we repeat the same protocol on a different realization set, coming from a measurement of the shot noise only. That is, all the beams from the optomechanical cavity are blocked and only the LOs are directed to the BHDs. Using the same mode functions, we get a diagonal covariance matrix for the shot noise, $\widetilde{\sigma}^2_{sn}$. In practice, there are non-zero elements outside of the diagonal. However, we find that they are three orders of magnitude smaller than the diagonal elements and within the statistical uncertainty, thus can be safely neglected. The diagonal elements carries the information about the gain of the detectors and the transduction factors, thus can be used to normalize the entangler-readout matrix, $\widetilde{\sigma}^2_{ER}$, according to

*Covariance matrix estimation*

$$\left(\sigma^2_{ER}\right)_{jk} \coloneqq \frac{\left(\widetilde{\sigma}^2_{ER}\right)_{jk}}{\sqrt{\left(\widetilde{\sigma}^2_{sn}\right)_{jj}\left(\widetilde{\sigma}^2_{sn}\right)_{kk}}}, \tag{8.3a}$$

$$\left(\sigma^2_{sn}\right)_{jk} \coloneqq \frac{\left(\widetilde{\sigma}^2_{sn}\right)_{jk}}{\sqrt{\left(\widetilde{\sigma}^2_{sn}\right)_{jj}\left(\widetilde{\sigma}^2_{sn}\right)_{kk}}}. \tag{8.3b}$$

Finally, the normalized shot noise matrix, Equation 8.3b, can be further used to calibrate out the additional noise from the eight-port homodyne detector according to

$$(V_{ER})_{jk} \coloneqq (\sigma^2_{ER})_{jk} - \delta_{jk}\frac{(\sigma^2_{sn})_{jj}}{2}, \tag{8.4a}$$

$$(V_{sn})_{jk} \coloneqq \frac{(\sigma^2_{sn})_{jk}}{2}. \tag{8.4b}$$

The final covariance matrix, $V_{ER}$, estimates the state covariance matrix and can be used to verify the entanglement between the two optical modes. A simple entanglement witness, linear in the covariance elements, is represented by the sum of EPR variances [Dua+00; Gio+03] and can be calculated according to

$$w_{EPR} = \mathrm{tr}\,(Z_{EPR}V_{ER}), \quad Z_{EPR} = \frac{1}{2}\begin{pmatrix} 1 & 0 & 1 & 0 \\ 0 & 1 & 0 & -1 \\ 1 & 0 & 1 & 0 \\ 0 & -1 & 0 & 1 \end{pmatrix}, \tag{8.5}$$

where the state is entangled if $w_{EPR} < 1$. This witness might not be always the best choice for detecting the largest number of entangled states. An optimal witness matrix, $Z_{opt}$, can be numerically obtained as shown in [HE06] We calculate, from the estimated covariance matrix, both the EPR and optimal witness, and compare them to the unity threshold.

### 8.2.2 *Preliminary results*

As a first attempt, we employ the mode functions defined in Equation 8.2 to filter the optical modes out of the measurements and verify their entanglement. Using the measured and fitted parameters, we predict an optimal witness of $w_{opt} = 0.7$ for the modes defined by $\Omega_s = \Omega_m$ and $\Gamma_s \approx 2\Gamma_{qba}$ [Gut+19]. In practice, however, we do not observe this witness less than unity, that is, entanglement, when applying these mode functions to our data. We suspect that one of the reasons lies in the multimode nature of the mechanical structure. As already seen in fact, the membrane supports several modes at high density, in particular outside the bandgap. For the measurement set we are discussing here, these modes spectrally appear as peaks which are three orders of magnitude taller than the background floor. The functions in Equation 8.2 are single-pole Lorentzian filters with linewidth $\Gamma_s \approx 2\Gamma_{qba}$, not enough to suppress some of these other modes. Then, they contribute to the total covariance matrix, $V_{ER}$, and lead to additional uncorrelated noise, which spoils the quantum state coherence.

The possible definitions for the entangler and readout modes are not limited to Equation 8.2. In fact, the inference of the optomechanical entanglement only relies on the time-ordering properties of the optical modes, not on their specific functional form. Then, we decide to introduce in the mode functions of Equation 8.2 proper notch filters to largely suppress the additional mechanical modes. To do that optimally, we resort to the Wiener filtering theory [Kai82]. This filter

*Wiener filters*

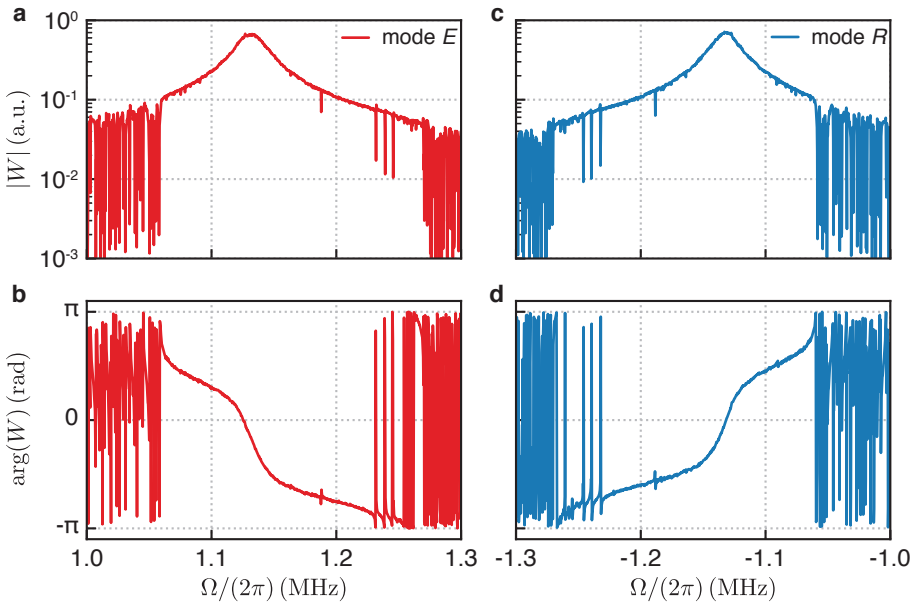


Figure 8.6: Wiener filter for entangler and readout modes. a, (c,) Magnitude and b, (d,) phase of the transfer function of the Wiener filter for the entangler (readout) mode. The transfer function contains a main Lorentzian filter, at $|\Omega_s|/(2\pi) = 1.132$ MHz, with linewidth $\Gamma_s/(2\pi) = 11$ kHz. These two parameters can be scanned to search for the lowest entanglement witness. Also, the transfer function contains several notch filters at the location of the other mechanical modes, in order to maximally suppress them once applied to the measured photocurrents.

is calculated from: (i) the experimental auto-correlation of the measured complex amplitude of the field, which includes contributions from both the mode of interest and other mechanical modes to be filtered away; (ii) the theoretical cross-correlation between the quantity to estimate, i. e. the amplitude of the filtered mode, and the measured quantity, i. e. the field complex amplitude. The auto-correlation is estimated from the inverse Fourier transform of the PSD of the complex realizations, $s_{out}$. The cross-correlations comes from a theoretical model, with parameters based on the fits from Figure 8.5 and the quantities to estimate are defined by Equation 8.1 and Equation 8.2. In Figure 8.6 we show the Fourier transform of the Wiener filters for $\Gamma_s/(2\pi) = 11$ kHz and $\Omega_s/(2\pi) = 1.132$ MHz. We notice that these transfer functions are Lorentzian filters, similar to Equation 8.2, with notch filters at the location of the other mechanical modes, mainly

outside the bandgap. These notch filters are optimized such that the mean square error between the expected theoretical observable and the outcome from applying the Wiener filter to the measured complex realization $s_{out}$ is minimized.

We use these Wiener filters to define the entangler and readout modes, from which we then calculate the associated covariance matrix, $V_{ER}$, and the entanglement witnesses. In Figure 8.7 we show a collections of the results, as we scan the center frequency, $\Omega_s$, and linewidth, $\Gamma_s$, of the Wiener filters. The optimal entanglement witness now reaches smaller values, the lowest of which is $w_{opt} = 1.1$ for $\Omega_s/(2\pi) = 1.132$ MHz and $\Gamma_s/(2\pi) = 11$ kHz. This is close to the unity threshold, but not below it, precluding the observation of the optomechanical entanglement.

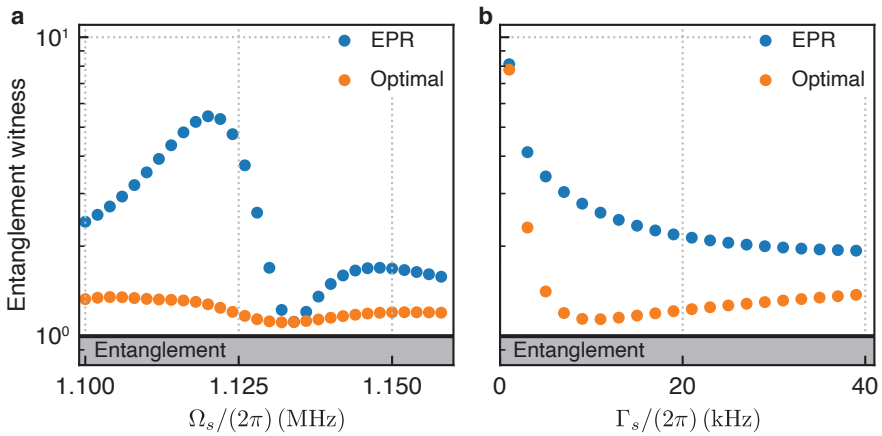


Figure 8.7: Entanglement witness for entangler and readout modes. a, b, EPR (blue circles) and optimal (orange circles) witness as a function of the Lorentzian center frequency, $\Omega_s$, and linewidth, $\Gamma_s$, respectively. A witness less than unity indicates an entangled state. In a, the bandwidth of the mode is fixed at $\Gamma_s/(2\pi) = 11$ kHz, whereas in b, the center frequency of the mode is fixed at $\Omega_s/(2\pi) = 1.132$ MHz.

Further studies are necessary to investigate the causes of the discrepancy between the experimental results and the predictions. We suspect that the presence of other mechanical modes also redistributes the correlations between several modes, not only the one of interest [Hoe17]. This would require to find the right modes which share the quantum correlations. A possible practical solution might be to implement a numerical optimization program for finding the best mode functions which minimize some entanglement witness. In fact, for this problem, which takes a quadratic form, there exist linear programming methods which can solve it efficiently. This implementation needs yet to be done, and will be a future research directions for newcomers.

# 9 QUANTUM CORRELATIONS FOR SENSING AND ENTANGLEMENT GENERATION

The generation of the optomechanical entanglement, predicted by the quantum measurement theory, highlights the important role of correlations in both the mechanical and optical systems, as we have also briefly reviewed in Chapter 3.

This chapter is devoted to discuss in detail some of these correlations and how to experimentally take advantage of them. In the first part, we report an experiment which uses the ponderomotive correlations to enhance the displacement sensitivity of an optomechanical cavity. We show that, when properly arranged, such an experiment enables sensitivities below the SQL. In the second part, instead, we use these correlations to experimentally generate optical entangled states, which are the building blocks of many quantum information processing applications. In particular, this shows that the mechanical interface is capable of generating the entanglement between two different quantum systems, like microwave and optical fields, a key step towards quantum networks.

## 9.1 MEASUREMENTS BELOW THE SQL

In the context of displacement sensing, we have derived in Section 3.4.1.1 a very important limit for a standard phase measurement, the SQL. This limit, despite being an important technological one and a benchmark, does not represent the ultimate limit for the achievable sensitivity. In fact, we have assumed in its derivation that the imprecision and the quantum backaction noises, forming the measurement added noise, are uncorrelated. These two sources of noise derive from the different quadrature fluctuations of the optical field driving the optomechanical experiment. Thereby, nothing fundamental imposes them to be uncorrelated and this assumption can be relaxed. Based on this, several theoretical proposals have been made to overcome the SQL exploiting correlations in the measuring optical field[Kim+01; CM04], either at the input or, equivalently, at the output in front of the detector. Despite the vast theoretical research over the last decades, an experimental realization has remained elusive so far[Gio04]. We can envision several situations in which these correlations are present. For example, one can use a squeezed optical field[Cav81], instead of a coherent one, to drive the optomechanical experiment. However, this requires to have at disposal a squeezed source, usually obtained from a properly pumped non-linear optical medium, then increasing the

overall experimental complexity. On the other end, the optomechanical interaction itself can generate squeezing in the output field, as theoretically shown in Section 3.5. Then, one can properly arrange the detection stage in order to exploit maximally these correlations, for improving the sensitivity limit. This proposal, usually referred to as a *variational measurement*, has been theoretically pioneered by Vyatchanin and Zubova [VZ95].

As we have shown in Section 5.2, our experimental platform enables displacement measurements at the SQL to within 33%. Thus, it offers a promising route towards measurement with sensitivity below the SQL. In the following, we start by describing the theory of the variational approach, then we move to report the experimental results achieved.

### 9.1.1 *Use of quantum correlations at the detection*

In Section 3.4.2 we have seen that ponderomotive correlations are present for a general quadrature homodyne measurement. They disappear in the special case of a resonant phase measurement, in which $\Delta = 0$ and $\theta = \pi/2$ in Equation 3.41. This is also the regime in which the experiments so far discussed have been performed.

Now, we relax the assumption of a phase measurement, and let the quadrature angle, $\theta$, be arbitrary. In the limit of a broad cavity, $\kappa \gg \Omega_m$, we have, from Equation 3.41, that the inferred displacement spectrum is

*Spectrum for an arbitrary quadrature*

$$\begin{aligned}\overline{S}^{\text{inf}}_{\hat{q}\,\hat{q}}(\Omega) &= \overline{S}_{\text{add}}(\Omega) + |\chi_m(\Omega)|^2 \overline{S}_{\text{th}}(\Omega) \\ &= \overline{S}^{\theta}_{\text{imp}}(\Omega) + |\chi_m(\Omega)|^2 \left(\overline{S}_{\text{th}}(\Omega) + \overline{S}_{\text{qba}}(\Omega)\right) + 2\Re\left[\chi_m(\Omega)\right] \overline{S}^{\theta}_{\text{corr}}(\Omega),\end{aligned} \tag{9.1}$$

where

$$\overline{S}^{\theta}_{\text{imp}}(\Omega) = \frac{1}{8\Gamma_{\text{meas}} \sin(\theta)^2}, \tag{9.2a}$$

$$\overline{S}_{\text{th}}(\Omega) = 2\Gamma_m \left(\overline{n}_{\text{th}} + \frac{1}{2}\right), \tag{9.2b}$$

$$\overline{S}_{\text{qba}}(\Omega) = 2\Gamma_{\text{qba}}, \tag{9.2c}$$

$$\overline{S}^{\theta}_{\text{corr}}(\Omega) = \frac{1}{2\tan(\theta)}. \tag{9.2d}$$

We show an example of this spectrum in Figure 9.1b, and compare it to the SQL and a standard phase measurement. In Figure 9.1a instead, we highlight the appearance of sub-SQL regions, as a function of the frequency and the quadrature angle.

Now, the added noise, $\overline{S}_{\text{add}}$, also contains the correlations term, $\overline{S}_{\text{corr}}$, which has an asymmetric lineshape around the mechanical resonance, and assumes negative values on one of the two sides of the resonance. As a consequence, the total added noise can become lower than the

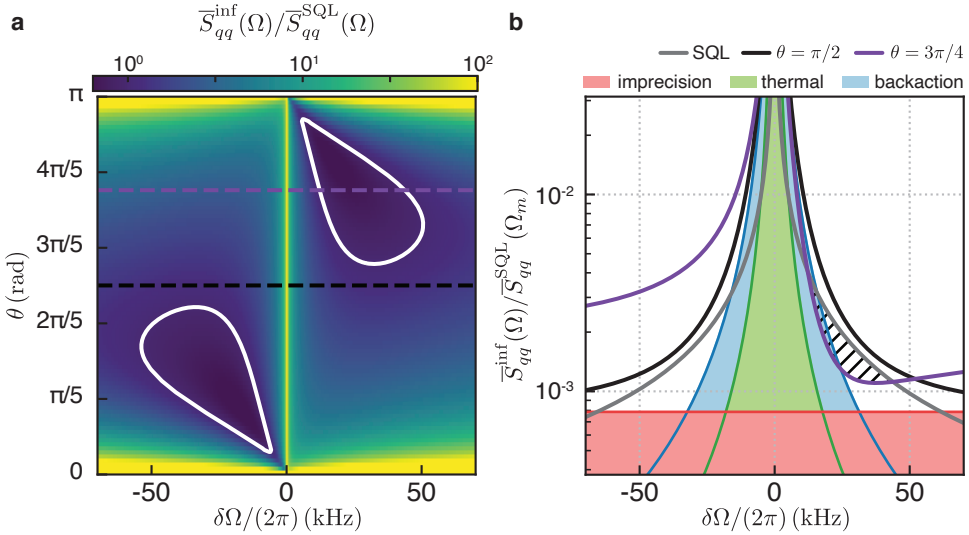


Figure 9.1: Displacement noise below the SQL. a, Inferred displacement spectra, normalized to the spectral SQL, as a function of relative frequency from the mechanical resonance, $\delta\Omega = \Omega - \Omega_m$, and the detection angle, $\theta$. The white contours delimit the regions of sub-SQL. b, Spectra corresponding to the horizontal cut marked in a, at $\theta = \pi/2$ (black) and $\theta = 3\pi/4$ (purple). Both contain the imprecision (red), intrinsic (green) and quantum backaction noise (blue). The spectrum at $\theta = 3\pi/4$ also contains the arising correlations between the quantum backaction and the imprecision noise. These correlation lead to sub-SQL spectral values (hatched region) for some frequencies off the mechanical resonance. The spectral SQL is shown in gray. The parameters used are $\Omega_m/(2\pi) = 1$ MHz, $\Gamma_m/(2\pi) = 100$ Hz, $\overline{n}_{th} = 50$, $\kappa/(2\pi) = 10$ MHz, $\Delta/\kappa = 0$, $\Gamma_{qba} = 3\Gamma_m\overline{n}_{th}$, $\eta = 1$.

spectral SQL. In particular in the ideal case of unity efficiency, the added noise can reach the *ultimate quantum limit* [Cleo4; Cle13], at each frequency, upon optimization of the measurement strength, $\Gamma_{qba}$, and the angle, $\theta$, i. e.

*Ultimate quantum limit*

$$\min_{\Gamma_{qba},\theta} \overline{S}_{add}(\Omega) = |\chi_m(\Omega)|^2\Gamma_m. \tag{9.3}$$

This represents the ultimate limit for the noise added by the measurement and corresponds to the same spectral noise associated to the zero point motion. To understand it, we recall that an ideal optomechanical system is a quantum amplifier for the mechanical displacement [Cle13]. In addition, this amplifier is also phase-insensitive, as it simultaneously measures both mechanical quadratures (cf. Section 5.3). Thus, the Heisenberg uncertainty relation imposes an added noise to the amplifier at least equal to half a quanta [Cle+10]. It is exactly this noise that Equation 9.3 represents.

We further notice that, at the mechanical resonance $\Omega_m$, the quantum limit in Equation 9.3 exactly matches the spectral SQL, i. e. $|\chi_m(\Omega_m)|$, which is usually precluded by the non-zero thermal occupation, $\overline{n}_{th}$.

However away from the mechanical resonance, the spectral thermal noise contributes negligibly compared to the added noise, which can then be reduced below the SQL. As usual, this requires to have a significant quantum backaction and no excess imprecision noise due to inefficiencies. In other words, the measurement efficiency, $\eta_{\text{meas}}$, should be close to unity. This is exactly the regime in which our platform operates.

*Lower bound on the added noise*

In the limiting case of far-off resonance frequencies, i. e. $|\delta\Omega| = |\Omega - \Omega_m| \gg \Gamma_m$, the mechanical susceptibility can be approximated by $\chi_m(\Omega) \approx -(2\delta\Omega)^{-1}$, and the added noise, compared to the SQL, achieves the value

$$\frac{\overline{S}_{\text{add}}(\Omega)}{\overline{S}^{\text{SQL}}_{\hat{q}\hat{q}}(\Omega)} \sim \sqrt{\frac{1}{\eta_{\text{meas}}} - 1} \tag{9.4}$$

at the optimal quadrature angle $\theta \to -\tan^{-1}(1/(4\Gamma_{\text{meas}}))$ and frequency $\delta\Omega \to 2\Gamma_{\text{meas}}\sqrt{\eta_{\text{meas}}^{-1} - 1}$.

### 9.1.2 *Displacement sensitivity below the SQL*

To perform this displacement measurement below the SQL we employ the experimental setup sketched in Figure 9.2 [Mas+19]. A probe laser

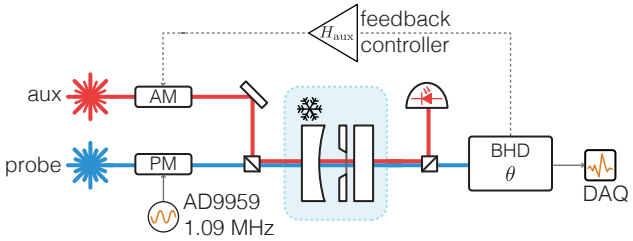


Figure 9.2: Experimental setup for displacement measurements below the SQL. A resonant probe laser is use to measure the displacement of a mechanical resonator, inside an optical cavity. An arbitrary quadrature of the transmitted field is monitored via a BHD. A weak auxiliary laser is also used for stabilization purposes.

is locked close to the resonance of a cavity mode, at $\lambda = 796.068$ nm with a linewidth $\kappa/(2\pi) = 16.2$ MHz and a residual detuning of $\Delta/(2\pi) \approx -1.6$ MHz. This laser performs a displacement measurement of the mechanical resonator, which lies inside the optical cavity, via the optomechanical interaction at the vacuum coupling rate of $g_0/(2\pi) = 121$ Hz. The mechanical mode of interest features a resonance frequency of $\Omega_m/(2\pi) = 1.14$ MHz and a quality factor $Q = 1.03 \times 10^9$, and it is coupled to a cryogenic thermal bath at $T = 10$ K. Both the coupling rate, $g_0$, and the bath temperature, T, have been measured via a quantum noise thermometry experiment, similar to the one reported in Section 4.2.4.2. We also perform an independent calibration of the coupling rate, $g_0$, from the measurement of

the optomechanical coherent response (cf. Section 4.2.4.1). This independent measurement yields a coupling rate $g_0/(2\pi) = 125$ Hz, which differs by only 3% from the previously measured rate. In the following, we use the coupling rate, $g_0$, to calibrate the measured spectra into displacement units, necessary for comparisons to the SQL. For this calibration, we employ the $g_0$ value coming from the quantum noise thermometry, as it turns out to be robust against systematic errors in the calibration of the phase modulator, provided that it operates under the same condition, as discussed in Section 4.2.5. The transmitted probe field is directed towards a BHD, which can measure any arbitrary quadrature angle in the range $\theta \in [0.1\pi, 0.9\pi]$. This is achieved by using a slope lock technique, as explained in Section 4.1.3.2. The achieved total efficiency, comprising the total detection efficiency and the cavity overcoupling, is $\eta = 73\%$.

We also use an auxiliary laser to stabilize, via both sideband and feedback cooling, low-frequency modes of the membrane structure, which otherwise generate extraneous in-bandgap noise. We lock this laser to the red side of a different cavity mode, at $\lambda_a = 797.057$ nm with linewidth $\kappa_a/(2\pi) = 10.8$ MHz and detuning $\Delta_a/(2\pi) = -3.5$ MHz. This field contributes to the total mechanical decoherence with the quantum backaction. For the chosen power and in terms of the natural thermal decoherence, the contribution of the quantum backaction is $A_{+,a}/\gamma = 0.4$. This auxiliary laser also affects the mechanics via dynamical backaction. In order to account for all these effects we introduce effective mechanical parameters. For instance, for the best result we have an effective resonance frequency of $\Omega_m/(2\pi) = 1.135$ MHz, a linewidth of $\Gamma_m/(2\pi) = 32$ Hz and a bath occupation of $\bar{n}_{th} = 8$ phonons.

*Best sub-SQL displacement measurement*

We set the power of the probe laser such that its quantum cooperativity assumes the value of $\mathcal{C}_q = 20.7$, then we record and calibrate into displacement units the homodyne photocurrent spectra, at different quadrature angles. We show some of them in Figure 9.3. For a standard phase measurement at $\theta = \pi/2$, the measured spectrum approaches the SQL off resonance. We fit this spectrum to a Lorentzian model to extract the effective mechanical parameters, which we use to draw the spectral SQL, $\bar{S}^{SQL}_{\hat{q}\hat{q}}(\Omega) = |\chi_{eff}(\Omega)|$, using the effective mechanical susceptibility as discussed in Section 5.2.2. As we rotate the detected quadrature, correlations start to arise leading to a total sensitivity below the SQL, as clearly shown in the insets of Figure 9.3. At the quadrature angle $\theta = 4\pi/5$, optimal for our experiment, we observe a total displacement sensitivity, comprising both the added noise and the intrinsic noise, which is 1.5 dB below the SQL.

In Figure 9.4 we show the full set of measured spectra, normalized to the SQL, and predictions based on independently measured parameters. We observe that the performance is generally degraded on the lower-than-resonance frequency side of the spectra, compared to both

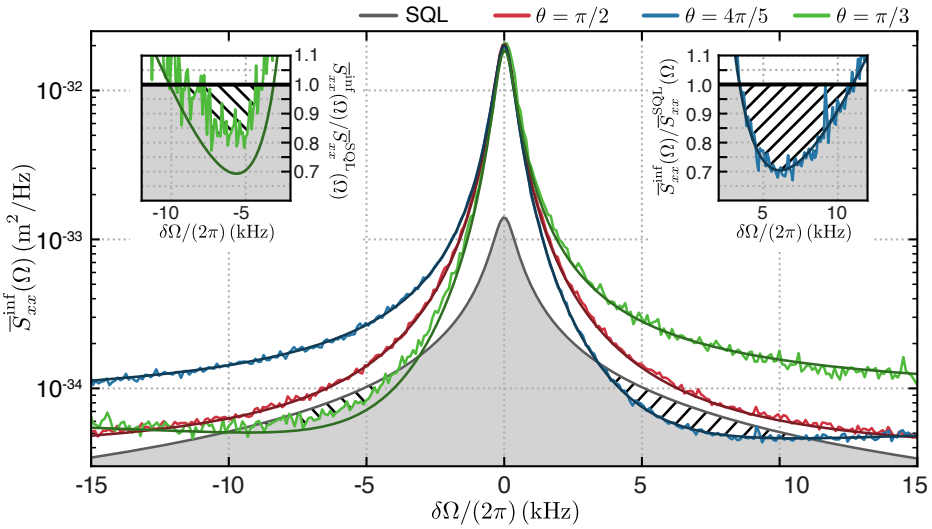


Figure 9.3: Measured displacement spectra below the SQL. Measured spectra for the inferred displacement, as a function of the relative frequency from the effective mechanical resonance, $\delta\Omega = \Omega - \Omega_{\rm eff}$. The red curve is a standard phase measurement, at $\theta = \pi/2$, whereas the blue (green) trace corresponds to a rotated quadrature, at $\theta = 4\pi/5(\pi/3)$. Black solid lines are fit. The spectral SQL is shown in gray. In the insets we show an enlarged view of the frequency regions with sub-SQL displacement sensitivity. Adapted from [Mas+19].

the expectations and the measurements on the higher-than-resonance frequency side. We attribute this degradation to the presence of an uncorrelated extraneous cavity noise on that side, possibly arising from the cavity mirrors' noise.

This is the first experimental realization of a displacement sensor operating below the SQL, as dictated by quantum mechanics. This enhanced sensitivity could be directly applicable in sensing applications [PD10], opening a new regime of precision measurement. More recently, Yu et al. [Yu+20] have performed a similar experiment with test masses of a gravitational wave detector. They have shown that the experiment operates in a similar sub-SQL regime, upon subtraction of classical imprecision noise.

#### 9.1.2.1 *Data analysis and fit*

*Fitting the imprecision noise*

We now describe the analysis and fitting procedures applied to the data. At first, we calibrate the spectra in displacement units by means of the measured coupling rate, $g_0$. and a known phase modulation tone (cf. Section 4.2.4.2). Then, we readout the background values of the spectra, which form the imprecision noise $\overline{S}_{\rm imp}$ at different quadrature angles. We fit them to the model in Equation 3.39, where the optomechanical coupling, $g$, is fixed from the measured $g_0$ and the measured transmitted power, see e. g. Equation 4.5. The only free

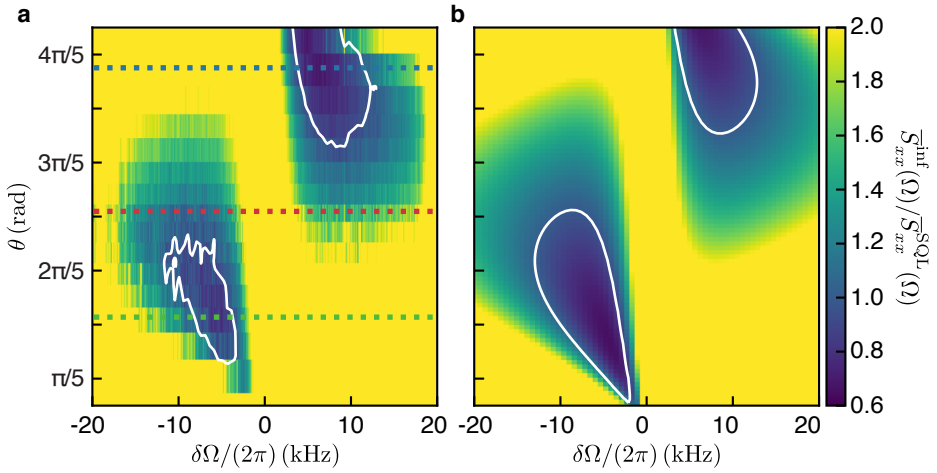


Figure 9.4: Measured displacement spectra below the SQL at multiple quadratures. a, Measured spectra for the inferred displacement and b, theoretical predictions, as a function of the relative frequency, $\delta\Omega$, and the quadrature angle, $\theta$. White contours indicate a total noise at the SQL, i. e. $\bar{S}_{xx}^{\mathrm{inf}} = \bar{S}_{xx}^{\mathrm{SQL}}$. The dashed coloured lines correspond the to spectra in Figure 9.3. Adapted from [Mas+19].

parameters are the total detection efficiency, $\eta_d$, and the laser detuning, $\Delta$. From the fit shown in Figure 9.5, we extract $\eta_d = 77\%$ and $\Delta/\kappa = -0.13$, consistent with independent predictions.

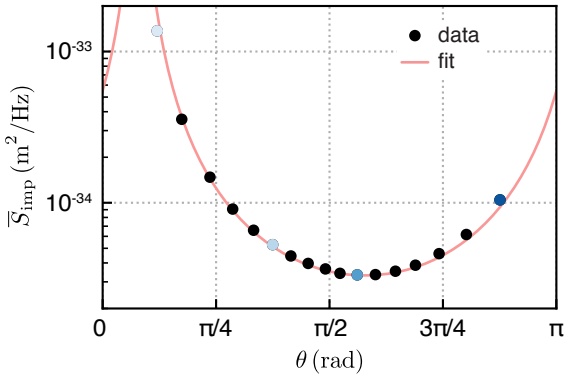


Figure 9.5: Fit of the imprecision noise. Imprecision spectral noise (circles) from the calibrated measured spectra, as a function of the detected quadrature angle, $\theta$. The light red line is a fit to the optomechanical model. Coloured circles mark the data points coming from the spectra shown in Figure 9.6a. Adapted from [Mas+19].

*Fitting the displacement spectra*

Next, we fit the measured spectra shown in Figure 9.4 to the full optomechanical model, using Equation 3.41 with $\theta = \phi$. The results are shown in Figure 9.6. For each fit, we choose as free parameters the homodyne angle, $\theta$, the optomechanical coupling, $g$, and the probe laser detuning, $\Delta$, whereas we fix all the remaining parameters by independent measurements and predictions. The free parameters are chosen to reflect the uncertainty in the measured quadrature angles,

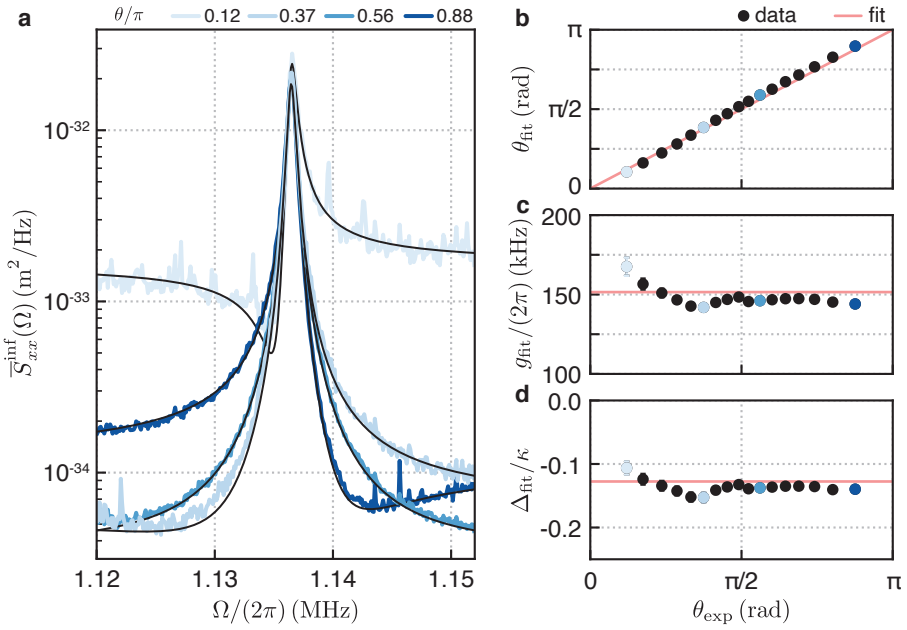


Figure 9.6: Fit of displacement spectra. a, Some measured displacement spectra (blue traces), at different quadrature angles, with the resulting fits (black lines). b, Quadrature angle, c, optomechanical coupling and d, detuning (circles) resulting from fitting all the spectra. The coloured circles mark the data points corresponding to the spectra shown in a. The light red lines are linear/constant fit of the resulting parameters from the fit. Adapted from [Mas+19].

especially when they are close to the amplitude quadrature, and eventual slow drifts of the optical input power during the duration of the experiment, of roughly an hour.

In Figure 9.6a we show some calibrated spectra with the corresponding fits, while in Figure 9.6b-d we collect all the fitted parameters as a function of the measured quadrature angles. We notice that the fitted homodyne angles closely follow the measured ones. The fitted coupling rates and detunings show correlated fluctuations around their mean values. These correlations can be explained by a drift of the optical input power. On one side, in fact, this power directly affects the intracavity average occupation, $\overline{n}_{cav}$, thus the coupling rate g. On the other side, a power drift also results in a different amplitude of the PDH stabilization error signal. If an electronic offset is present, as usual in the experimental reality, the change of the error signal amplitude leads to a change of the set-point which the feedback loop stabilizes to, yielding a different detuning.

## 9.2 PONDEROMOTIVE ENTANGLEMENT OF PROPAGATING OPTICAL MODES

So far, we have been using the ponderomotive correlations present in the optical field to improve the sensitivity of a displacement measurement. Thus, the optical field has been merely considered as a measuring system. Now, we switch perspective and consider the mechanical resonator no more as the main measured system but as an interface [Kur+15; Che+20], capable of generating correlations in the state of light leading to the emergence of quantum optical states.

We have seen, in Section 3.5, how the mechanical motion generates squeezed states of the output optical field. These correlations are actually shared between two modes co-propagating in the same field, which form a bipartite entangled state. These states are at the heart of quantum information processing applications [Hor+09]. In many cases, however, these two entangled modes need to be spatially separated into two different independent fields to be of any use. In this way in fact, the entangled parties can be distributed among two different locations, which can then share quantum information [Kim08].

The entangled modes in a ponderomotive squeezed field are not spatially separated, therefore requiring additional filtering and processing. Alternatively, one can use the same mechanical motion to generate and share ponderomotive correlations between two independent fields. In this way, two modes belonging to the two output fields can become quantum correlated, leading to a *ponderomotive entanglement*, as proposed theoretically several decades ago [GMT01; GMT03]. In the following, we describe a theoretical model for the ponderomotive entanglement. From this model, we derive a toy version which is useful for building a physical intuition. Then, we report the experimental results we achieved in our platform.

### 9.2.1 *Ponderomotive entanglement*

We assume to have two lasers driving two independent cavity modes, which are optomechanically interacting with a single mechanical mode. The linearized QLE for the fluctuation operators can be derived following the same steps done in Section 3.2.2, thus obtaining

$$\dot{\hat{X}}_j = -\frac{\kappa_j}{2}\hat{X}_j - \Delta\hat{Y}_j + \sqrt{\kappa_{j,1}}\hat{X}^{\theta_{in}}_{j,in,1} + \sqrt{\kappa_{j,2}}\hat{X}_{j,in,2}, \tag{9.5a}$$

$$\dot{\hat{Y}}_j = -\frac{\kappa_j}{2}\hat{Y}_j + \Delta\hat{X}_j + 2g_j\hat{q} + \sqrt{\kappa_{j,1}}\hat{Y}^{\theta_{in}}_{j,in,1} + \sqrt{\kappa_{j,2}}\hat{X}_{j,in,2}, \tag{9.5b}$$

$$\dot{\hat{q}} = \Omega_m\hat{p}, \tag{9.5c}$$

$$\dot{\hat{p}} = -\Omega_m\hat{q} - \Gamma_m\hat{p} + \sum_j 2g_j\hat{X}_j + \sqrt{2\Gamma_m}\hat{\xi},, \tag{9.5d}$$

where $j = A, B$ labels the two cavity modes and the corresponding input fields and $g_j$ is the optomechanical coupling rate of mode $j$,

which is a real number since we have taken each intracavity field as a phase reference. The mechanical motion is now driven by two sources of quantum backaction, from the independent amplitude quadratures of the input fields to the cavity modes. The induced displacement and the thermal motion are imprinted in the phase quadratures of both cavity modes. Thus, the phase quadrature of one mode and the amplitude quadrature of the other mode become correlated: this is the basic mechanism for generating correlations between the two lasers, which becomes entangled when the thermal noise is negligible.

Using Equation 9.5 and the input-output relation Equation 1.13, we can calculate a general expression for the cross-PSD between the output quadrature $\hat{X}_j^{\theta_j}$ of laser j at angle $\theta_j$ and $\hat{X}_k^{\theta_j}$ of laser k at angle $\theta_k$, i. e.

$$\bar{S}^{\text{out}}_{\hat{X}_j^{\theta_j}\hat{X}_k^{\theta_k}}(\Omega) = \frac{1}{2}\delta_{jk} + \frac{\bar{S}_{\text{imp}}(\Omega)^{-1}}{2}\bar{S}_{\hat{q}\,\hat{q}}(\Omega) + \bar{S}_{\text{corr}}(\Omega), \tag{9.6}$$

where

$$\bar{S}_{\hat{q}\,\hat{q}}(\Omega) = |\chi_{\text{eff}}(\Omega)|^2 \left(\bar{S}_{\text{th}}(\Omega) + \sum_j \bar{S}^j_{\text{qba}}(\Omega)\right), \tag{9.7a}$$

$$\bar{S}_{\text{imp}}(\Omega)^{-1} = \frac{\sqrt{\Gamma^j_{\text{meas}}\Gamma^k_{\text{meas}}}}{2}\Re\left[e^{-\imath(\theta_j-\theta_k)}c_{jk}(\Omega) - e^{-\imath(\theta_j+\theta_k)}\alpha_{jk}(\Omega)\right], \tag{9.7b}$$

$$\bar{S}_{\text{corr}}(\Omega) = -\frac{\sqrt{\Gamma^j_{\text{meas}}\Gamma^k_{\text{meas}}}}{4}\Big\{\Re\left[\chi_{\text{eff}}(\Omega)\right]\Im\left[e^{-\imath(\theta_j+\theta_k)}\alpha_{jk}(\Omega)\right] + \Im\left[\chi_{\text{eff}}(\Omega)\right]\Re\left[e^{-\imath(\theta_j-\theta_k)}\beta_{jk}(\Omega)\right]\Big\}. \tag{9.7c}$$

We have also introduced the following definitions

$$\alpha_{jk}(\Omega) \coloneqq \sqrt{\kappa_j\kappa_k}\left[\chi_{c,j}(\Omega)\chi_{c,k}(-\Omega) + \chi_{c,k}(\Omega)\chi_{c,j}(-\Omega)\right] = \alpha_{kj}(\Omega), \tag{9.8a}$$

$$\beta_{jk}(\Omega) \coloneqq \sqrt{\kappa_j\kappa_k}\left[\chi_{c,j}(\Omega)\chi_{c,k}(\Omega)^* - \chi_{c,j}(-\Omega)\chi_{c,k}(-\Omega)^*\right] = \beta_{kj}(\Omega)^*, \tag{9.8b}$$

$$c_{jk}(\Omega) \coloneqq \sqrt{\kappa_j\kappa_k}\left[\chi_{c,j}(\Omega)\chi_{c,k}(\Omega)^* + \chi_{c,j}(-\Omega)\chi_{c,k}(-\Omega)^*\right] = c_{kj}(\Omega)^* \tag{9.8c}$$

and, as usual, the measurement rate $\Gamma^j_{\text{meas}} = \eta_j 4g_j^2/\kappa_j$, with the total efficiency $\eta_j \coloneqq \eta^j_d\eta^c_c$.

The output fields are continuous propagating fields, and as such contain a multitude of modes. In order to define and verify the presence of entangled states in these fields, we need to properly define two modes out of them. This can be done by filtering, as introduced in Section 1.5.

We remind the reader that, for a ponderomotive squeezed field, the entangled modes are represented by two symmetric spectral components, roughly Fourier modes, at $\pm\Omega \approx \pm\Omega_m$ around the laser carrier. Now instead, we have two lasers interacting with the same mechanical mode. We can then expect that the entanglement will involve four spectral components, which are the symmetric Fourier modes, $\hat{a}^A_{\pm\Omega}$ and $\hat{a}^B_{\pm\Omega}$, of the two lasers, similar to a four-mode squeezing process [Sch+87]. A full characterisation of this quadripartite state is cumbersome, as it requires to have four simultaneous homodyne detectors with LOs at the frequency of each Fourier modes in the state. Electronically, this corresponds to measuring a signal at baseband, hindered by the electronic flicker noise. Nevertheless, this quadripartite state can be reduced to a bipartite one by considering a quadrature mode for each field, as introduced in Section 1.5.1. These modes are a combination of symmetric spectral components around each carrier and conveniently represent the modes measured by a homodyne detector [Lvo15]. Therefor, a full characterization of this bipartite state only requires two independent detectors with LOs at the laser carriers.

*Four-mode process*

We now consider exact Fourier quadrature modes, $(\hat{X}^{\theta_A}_A(\Omega), \hat{Y}^{\theta_A}_A(\Omega))$ and $(\hat{X}^{\theta_B}_B(\Omega), \hat{Y}^{\theta_B}_B(\Omega))$, parameterized by the frequency, $\Omega$, and quadrature angles, $\theta_A$ and $\theta_B$. These modes can be obtained from averaging the homodyne photocurrents for an infinitely long time. Despite being unphysical, they represent an easy theoretical tool and well approximate the experimental modes obtained from averaging for a time much longer than any other dynamical timescale. In fact, their variance is just the spectral value of the PSD in Equation 9.6 of the underlying quadratures, at frequency $\Omega$. To verify the entanglement of these two modes we use a common entanglement witness, $w(\Omega)$, based on summing the variance of the EPR quadrature modes, defined as $\hat{X}_\pm(\Omega) = (\hat{X}^{\theta_A}_A(\Omega) \pm \hat{X}^{\theta_B}_B(\Omega))/\sqrt{2}$ and $\hat{Y}_\pm(\Omega) = Y^{\theta_A}_A(\Omega) \pm \hat{Y}^{\theta_B}_B(\Omega))/\sqrt{2}$ [Dua+00; Gio+03]. Whenever the entanglement witness satisfies $w(\Omega) < 1$ the two-mode state is entangled. Explicitly, this witness takes the form

*EPR witness for ponderomotive entanglement*

$$w(\Omega) \coloneqq \langle \hat{X}_+(\Omega)^2 \rangle + \langle \hat{Y}_-(\Omega)^2 \rangle = \overline{S}_{\hat{X}_+\hat{X}_+}(\Omega) + \overline{S}_{\hat{Y}_-\hat{Y}_-}(\Omega) = 1 + f_{qw}(\Omega)\overline{S}_{\hat{q}\hat{q}}(\Omega) + w_{corr}(\Omega), \quad (9.9)$$

with

$$f_{qw}(\Omega) = \Re\left[\sum_j \frac{\Gamma^j_{meas}}{4} c_{jj}(\Omega) + \frac{\sqrt{\Gamma^A_{meas}\Gamma^B_{meas}}}{2}\alpha_{AB}(\Omega)e^{-i2\Theta}\right] \quad (9.10)$$

and

$$w_{\mathrm{corr}}(\Omega) = -\Im\left[\chi_{\mathrm{eff}}(\Omega)\right]\Re\left[\sum_j \frac{\Gamma^j_{\mathrm{meas}}}{4}\beta_{jj}(\Omega)\right] + \Re\left[\chi_{\mathrm{eff}}(\Omega)\right]\Im\left[\frac{\sqrt{\Gamma^A_{\mathrm{meas}}\Gamma^B_{\mathrm{meas}}}}{2}\alpha_{AB}(\Omega)e^{-\imath 2\Theta}\right], \quad (9.11)$$

where $\Theta = (\theta_A + \theta_B)/2$.

#### 9.2.1.1 *Toy model*

In order to gain a physical intuition about the ponderomotive entanglement, we now consider the case of a resonant detection, $\Delta_j = 0$, with broad cavities, $\kappa_j \gg \Omega_m$, and equal measurement strengths, $\Gamma^A_{qba} = \Gamma^B_{qba} = \Gamma_{qba}$. This is also the relevant case for the experiments. We start by taking these limits in Equation 9.5. Here, we can also introduce a new joint basis for the cavity fields, defined by $\hat{X}_\pm = (\hat{X}_A \pm \hat{X}_B)/\sqrt{2}$ and $\hat{Y}_\pm = (\hat{Y}_A \pm \hat{Y}_B)/\sqrt{2}$. In this new basis, the output fields take the following simple form

$$\hat{X}_{+,\mathrm{out}}(\Omega) = \hat{X}_{+,\mathrm{in}}(\Omega), \quad (9.12a)$$

$$\hat{Y}_{+,\mathrm{out}}(\Omega) = \hat{Y}_{+,\mathrm{in}}(\Omega) + \sqrt{8\Gamma_{qba}}\chi_m(\Omega)\left(\sqrt{2\Gamma_m}\hat{\xi}(\Omega) + \sqrt{2\Gamma_{qba}}\hat{X}_{+,\mathrm{in}}(\Omega)\right), \quad (9.12b)$$

$$\hat{X}_{-,\mathrm{out}}(\Omega) = \hat{X}_{-,\mathrm{in}}(\Omega), \quad (9.12c)$$

$$\hat{Y}_{-,\mathrm{out}}(\Omega) = \hat{Y}_{-,\mathrm{in}}(\Omega). \quad (9.12d)$$

*Dark and bright modes*

The two new fields are now decoupled from each other and their dynamics can be promptly understood, as sketched in Figure 9.7. In

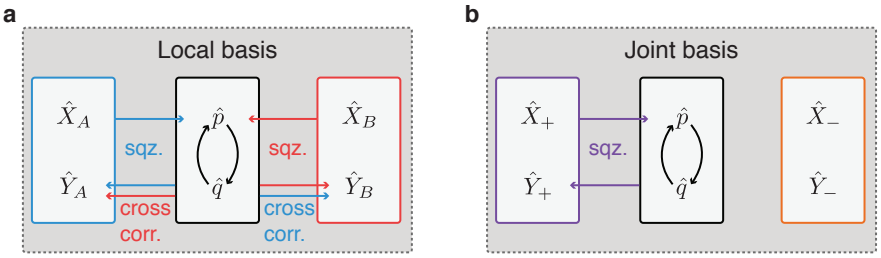


Figure 9.7: Ponderomotive entanglement in the local and joint basis. a, Sketch of the system dynamics in the local basis. Each laser field is squeezed and contains cross-correlations with the other. b, After moving to the joint basis, the two fields decouple from each other into a dark mode, which remains coherent and dark to the mechanical motion, and a bright mode, which instead undergoes the standard optomechanical interaction, thus becomes squeezed. Adapted from [Che+20].

fact, the "−" field is also decoupled from the mechanics and remains

dark to its motion. Given the initial optical coherent state, it remains coherent throughout all the evolution and the spectrum of any of its quadrature at angle $\Theta$ is at the shot noise level, i. e. $\overline{S}_{\hat{Y}^{\Theta}_{-}\hat{Y}^{\Theta}_{-}}(\Omega) = 1/2$. Conversely, the "+" field is optomechanically coupled to the resonator, undergoing the usual dynamics discussed in Chapter 3. In particular, this "+" field becomes ponderomotive squeezed. The spectrum of one of its quadrature at angle $\Theta$ can be calculated from Section 3.5, yielding

$$\overline{S}_{\hat{X}^{\Theta}_{+}\hat{X}^{\Theta}_{+}}(\Omega) = \frac{1}{2} + 8\Gamma_{\text{meas}}\sin(\theta)^2\overline{S}_{\hat{q}\,\hat{q}}(\Omega) + 4\Gamma_{\text{meas}}\Re\left[\chi_m(\Omega)\right]\sin(2\theta). \tag{9.13}$$

This new joint basis also corresponds to the EPR basis for the quadrature modes. Then, one can easily calculate the inseparability witness, defined in Equation 9.9, from Equation 9.13 and the spectrum for the "−" mode. In particular, the spectrum of the ponderomotive squeezed field, Equation 9.13, can be lower bounded as in Equation 3.46, where the measurement efficiency, $\eta_{\text{meas}}$, now refers to the "+" field and is defined as

$$\eta_{\text{meas}} \equiv \frac{\sum_j \Gamma^j_{\text{meas}}}{\gamma + \sum_j \Gamma^j_{\text{qba}}} = \frac{2\Gamma_{\text{meas}}}{\Gamma_m(\overline{n}_{\text{th}} + 1/2) + \Gamma_{\text{qba}}}. \tag{9.14}$$

Then, the entanglement witness takes the simple asymptotic value of

$$w(\Omega) = 1 - \frac{\eta_{\text{meas}}}{2}, \tag{9.15}$$

showing that entangled states are generated whenever the optical fields carry out an efficiency quantum measurement, $\eta_{\text{meas}} \approx 1$. This toy model, based on Equation 9.12, also makes clear the central role of ponderomotive correlations in the entanglement generation.

### 9.2.2 *Experimental verification of the bipartite entanglement*

We now move to the experimental verification of this entanglement [Che+20]. The setup used is sketched in Figure 9.8. The mechanical mode of the membrane resonator has a resonance frequency of $\Omega_m/(2\pi) = 1.139$ MHz, a quality factor $Q = 1.04 \times 10^9$ and is in a thermal bath at $T = 10$ K. The two fields, A and B, are obtained from two independent lasers, referred to as probe and auxiliary in previous experiments. They are locked via PDH close to the resonance of two different cavity modes, at $\lambda_A = 796.154$ nm with linewidth $\kappa_A/(2\pi) = 13.3$ MHz and detuning $\Delta_A/(2\pi) \approx -2.7$ MHz and at $\lambda_B = 796.750$ nm with linewidth $\kappa_B/(2\pi) = 12.6$ MHz and detuning $\Delta_B/(2\pi) \approx -2.5$ MHz, respectively. We choose the powers of the input lasers such that their measurement strengths are $\Gamma^A_{\text{qba}}/(2\pi) = 1.35$ kHz

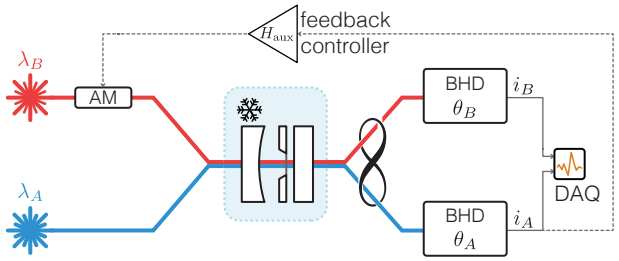


Figure 9.8: Experimental setup for the ponderomotive entanglement. Two independent lasers interact with a common mechanical resonator. As a results, correlations between them build up and their state become entangled. A feedback loop, from the BHD of laser A to an amplitude modulator in laser B, is used to stabilized some low-frequency modes of the membrane.

and $\Gamma^{B}_{qba}/(2\pi) = 0.89$ kHz, exceeding the thermal decoherence rate of $\gamma/(2\pi) = 0.2$ kHz. The two lasers are also linearly polarized in orthogonal directions, which allows to spatially split the transmitted fields with a PBS. Once split, they are sent towards two independent BHDs, which can measure arbitrary quadratures in the full range $[0, 2\pi)$ by combing both slope and dither lock techniques. The total efficiencies are $\eta_{d,A} = 60\%$ and $\eta_{d,B} = 77\%$. Combining these parameters together, we estimate a total measurement efficiency of $\eta_{meas} = 58\%$ from Equation 9.14. Finally, the homodyne photocurrent of laser A is used to feedback-cool some of the low-frequency mechanical modes, via a modulation of the amplitude of laser B. The feedback settings are adjusted according to the quadrature angle measured by the homodyne detector [Che20].

*Experimental quadrature modes*

The Fourier quadrature modes used in the theory are ideal and require having access to infinitely long photocurrents. In practice, we only have at our disposal a finite duration, the inverse of which determines the smallest mode bandwidth we can define. We digitize and acquire simultaneously the photocurrents, $i_j(t)$, from both BHDs at some quadrature angles $\theta_A$ and $\theta_B$. Then in post-processing, we chop the recorded measurements in shorter *realizations*, but still longer than the mechanical correlation time, $1/\Gamma_{eff}$. We define the experimental quadrature modes by demodulating the time traces at a specific frequency, $\Omega$, and applying a low-pass filter. The two demodulated electronic quadratures are combined together in a single complex number, $i_{j,\Omega}$, which is formally expressed as

$$i_{j,\Omega} = \int_{-\infty}^{+\infty} e^{\imath\Omega t} h(t) i_j(t) dt, \tag{9.16}$$

where the demodulation is taken into account by the complex exponential, and the function $h(t)$ is the causal kernel of the low-pass filter, which goes to zero at $\pm\infty$. The electronic quadratures form the real and imaginary part of $i_{j,\Omega}$, and correspond to different combinations

of the symmetric spectral components measured by the homodyne detectors, as expressed in Equation 1.37. In particular for stationary processes as the ones we are dealing with, the two electronic quadratures are uncorrelated and their statistics is the same [Bar+13]. In the following, we make use of this result and only consider the real part of Equation 9.16 for inferring the statistics of the underlying quantum state.

*Measurement protocol*

We apply this definition for the experimental quadrature modes to all the realizations and build a statistical ensemble formed by the outcomes of the quadrature pair $\{X_A^{\theta_A}, X_B^{\theta_B}\}$. Then, from this ensemble we can form an histogram and use it to estimate the covariance matrix. Subsequently, we advance both measured quadrature angles by $\pi/2$, corresponding to measuring the quadrature pair $\{Y_A^{\theta_A}, Y_B^{\theta_B}\}$, and repeat the measurement to collect a new ensemble and form an histogram. Finally, we repeat it once more, this time blocking the fields from the optomechanical cavity and recording only the shot noise. The resulting ensemble contains outcomes of the quadrature pair $\{X_A^{sn}, X_B^{sn}\}$, and is used to calibrate the other two ensembles into units of shot noise variance. This calibration is done by imposing the raw variances $\mathrm{Var}[X_A^{sn}]$ and $\mathrm{Var}[X_B^{sn}]$, in units of $V^2$, to be equal to $1/2$.

At first, we choose specific modes by setting $\theta_A \approx \theta_B \approx 0$, demodulating at $\Omega/(2\pi) = 1.1416$ MHz and low-pass filtering with a bandwidth of 200 Hz. The calibrated histograms from the above outlined measurement protocol are shown in Figure 9.9. From the

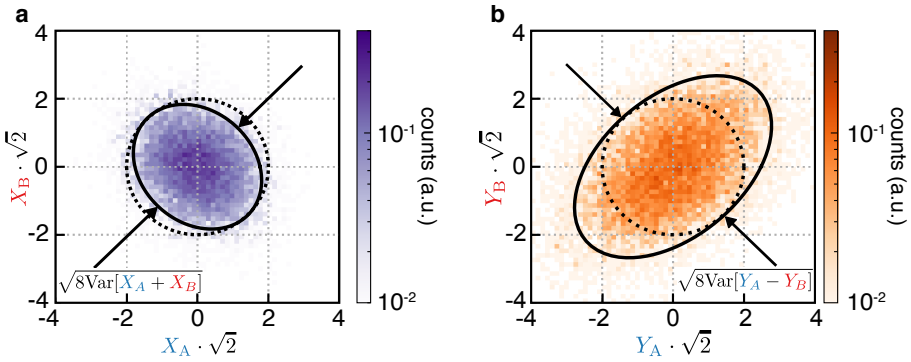


Figure 9.9: EPR quadrature statistics. a, Histogram of X and b, Y quadrature data, respectively, for $\Theta = 0$. The dashed black circles indicate the shot noise distribution (with s.d. of $1/\sqrt{2}$), with a radius of two times the shot noise s.d.. The solid black ellipses are the covariance ellipses of the measured data, multiplied by 2. The arrows indicate the diagonal/anti-diagonal cuts, the variances of which are relevant for the entanglement verification. Adapted from [Che+20].

diagonal (anti-diagonal) cut of the histogram in Figure 9.9a (b) we can promptly extract the variance of the EPR sum (difference) quadrature, i. e. $\mathrm{Var}[X_A + X_B]$ ($\mathrm{Var}[Y_A - Y_B]$), which results to be below (at) the shot noise level. These two variances can be summed together in order

to estimate the entanglement witness as in Equation 9.9. From the measured values we obtain that $w = 0.83 \pm 2\%(\text{stat.}) \pm 0.3\%(\text{syst.})$ for these specific modes, well below 1 within the experimental errors. This proves that the chosen modes are in a bipartite entangled state. The reported statistical error comes from the ensemble size of $\approx 10^4$ samples, used to estimate the variances, whereas the systematic error is due to imperfections in the BHDs [Che+20; Che20]. We further measure the EPR variances and the entanglement witness at different homodyne angles, $\Theta \approx \theta_A \approx \theta_B$, and we show the results in Figure 9.10a, as well as theoretical predictions from independently measured parameters. From the data, we observe that the largest two-mode squeezing occurs for the sum quadrature, $\hat{X}_+$, and it amounts to 1.8 dB below the shot noise.

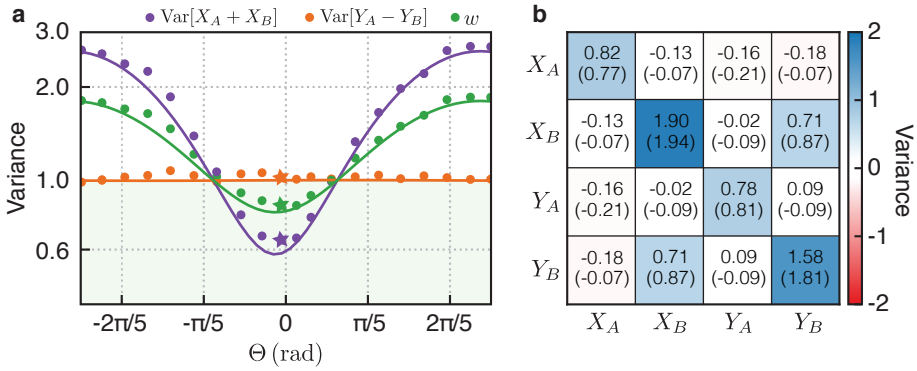


Figure 9.10: Homodyne tomography and covariance matrix. a, Relevant EPR variances (+, purple and −, orange) and entanglement witness (green) measured at different joint homodyne angles, Θ. The star symbols correspond to the 2D histograms shown in Figure 9.9. The solid lines are theoretical predictions. b, Reconstructed covariance matrix from homodyne tomography. The values reported are experimental results, whereas the ones in parentheses are theoretical predictions. The color representation highlights the significant non-zero entries. Each variance is obtained from an ensemble containing $\approx 10^4$ samples, thus the statistical error of the variance estimators is $\approx 2\%$ of the reported values. Adapted from [Che+20].

*State tomography*

We also perform a Gaussian homodyne tomography [DMS07] in order to reconstruct the state covariance matrix, which would allow to fully characterize the entanglement. For stationary processes, this tomography consists in measuring five linearly independent combinations of the two quadrature modes at different angles, one after the other. Then, the resulting measured variances and covariances can be inverted to yield the state covariance matrix. We choose to measure the following pairs of angles, $\{\theta_A, \theta_B\} = \{0,0\}$, $\{\pi/2, \pi/2\}$, $\{0, \pi/2\}$, $\{\pi/2, 0\}$, $\{\pi/4, \pi/4\}$. From them, we reconstruct the covariance matrix shown in Figure 9.10b, which compares well with the predicted values in parentheses. We further process the measured covariance matrix to

extract the minimum symplectic eigenvalue of its partial transpose [ASI04], which is $2\nu_- = 0.79$. For Gaussian system, this can be used to evaluate the logarithmic negativity, which forms an entanglement measure. We obtain a value of $E_N := \max\left(0, -\log_2(2\nu_-)\right) = 0.35$.

*Entanglement of modes at different frequencies*

So far, we have been focusing on specific quadrature modes, centered at the somewhat arbitrary frequency $\Omega/(2\pi) = 1.1416$ MHz. Now, we decide to sweep this frequency and characterize the state and the entanglement of all these modes. We notice that this would correspond to repeat the analysis done previously, in post-processing, on the same raw data. To do that, however, we do not apply the same numerical demodulation, but we use an fast Fourier transform (FFT) algorithm for the sake of computational advantage. In fact, these two approaches are formally equivalent, that is, one can describe the FFT with the same Equation 9.16, but in practice the FFT gives rise to a much faster computation. Now, the duration of the realizations chopped from the longer photocurrent time traces is chosen to be of $\sim 9$ ms. Formally, this corresponds to having a boxcar window of that length as a low-pass kernel, $h(t)$, in Equation 9.16. The bandwidth of the corresponding spectral mode becomes then 110 Hz. We compute the FFT of the sum and difference of these realizations from both BHDs, and average their squared magnitude to estimate the PSD, as shown in Figure 9.11a. The spectral value at each frequency bin should be interpreted as the variance of an EPR quadrature of modes with a center frequency and a bandwidth equal to the center and the width of that frequency bin. The spectral resolution is much narrower than any other feature, then the approximation of Fourier quadrature modes is valid and one can use Equation 9.6 to understand and fit the measurements. In particular, we notice that the spectrum for the difference quadrature is mostly at the shot noise level, while the spectrum of the sum quadrature shows a ponderomotive squeezing feature. This highlights once more the connection between ponderomotive squeezing and entanglement. From these two spectra, we can construct the inseparability witness, $w(\Omega)$, as a function of the mode frequency $\Omega$, as shown in Figure 9.11b. This witness violates the separability threshold of 1 for several modes in a bandwidth of $\sim 20$ kHz Furthermore, by performing the Gaussian homodyne tomography, we can reconstruct the covariance matrices for all these modes and calculate from these matrices the minimum symplectic eigenvalue of their partial transpose, $2\nu_-$. When its value is below unity the state is entangled, and this happens for modes over a bandwidth of $\sim 30$ kHz. In addition, the logarithm of $2\nu_-$ is the logarithmic negativity, and quantifies the amount of entanglement. Given the additivity of this measure, we can integrate the logarithmic negativity over frequencies to obtain a total extractable entanglement rate [TR17] of 753 ebit/s.

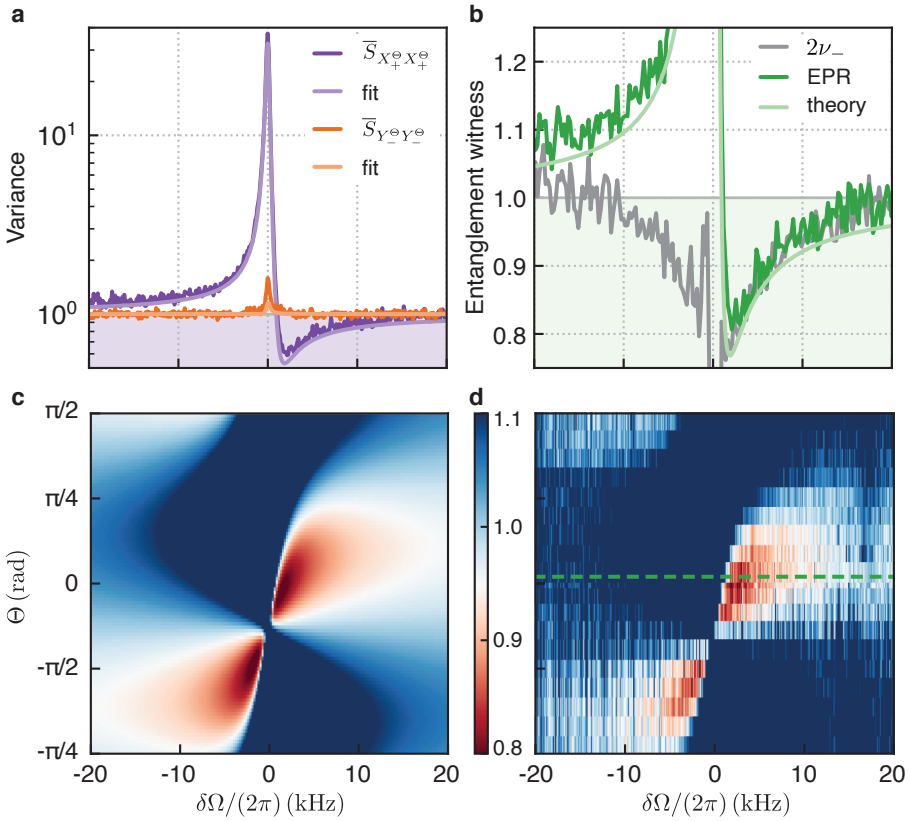


Figure 9.11: Ponderomotive entanglement at different frequencies. a, EPR variances, at angle $\Theta = 0$, as a function of the mode center frequency, $\Omega$. The smooth light-coloured lines are fits. b, The inseparability witness (green), from the EPR variance, and the minimum symplectic eigenvalue of the covariance matrix partial transpose (gray) from homodyne tomography, at different mode frequencies $\Omega$. c, Theoretical predictions and d, measured witness spectra, $w(\Theta, \Omega)$. The dashed green line indicates the measurement shown in b. The horizontal axes are referenced to the effective mechanical resonance frequency, $\delta\Omega = \Omega - \Omega_{\text{eff}}$. Adapted from [Che+20].

#### 9.2.2.1 *Calibration and fit*

The shown experimental results only depend on the calibration into shot noise units as already explained, and not on a correct modelling of the optomechanical interaction. Nevertheless, we fit the data to a model in order to extract the main parameters and corroborate the underlying physical phenomena.

*Fitting the imprecision noise*

At first, we calculate the PSD of the measured realizations and calibrate them into displacement units, as usual. Then, we readout their background values, which are the spectral imprecision noises, $\overline{S}_{\text{imp}}$, as a function of the quadrature angle, measured from the DC homodyne photocurrent (cf. Section 4.2.2). We fit these data to a model in order to extract the total efficiencies, which result in $\eta_A = 60\%$ and $\eta_B = 77\%$.

*Fitting the displacement spectra*

Next, we calibrate the measured spectra to shot noise units. This is done by measuring the shot noise spectrum and assigning to each frequency bin the spectral value of 1/2. The calibrated PSD and cross-PSD for the best result, at $\Theta = 0$, are shown in Figure 9.12. Each

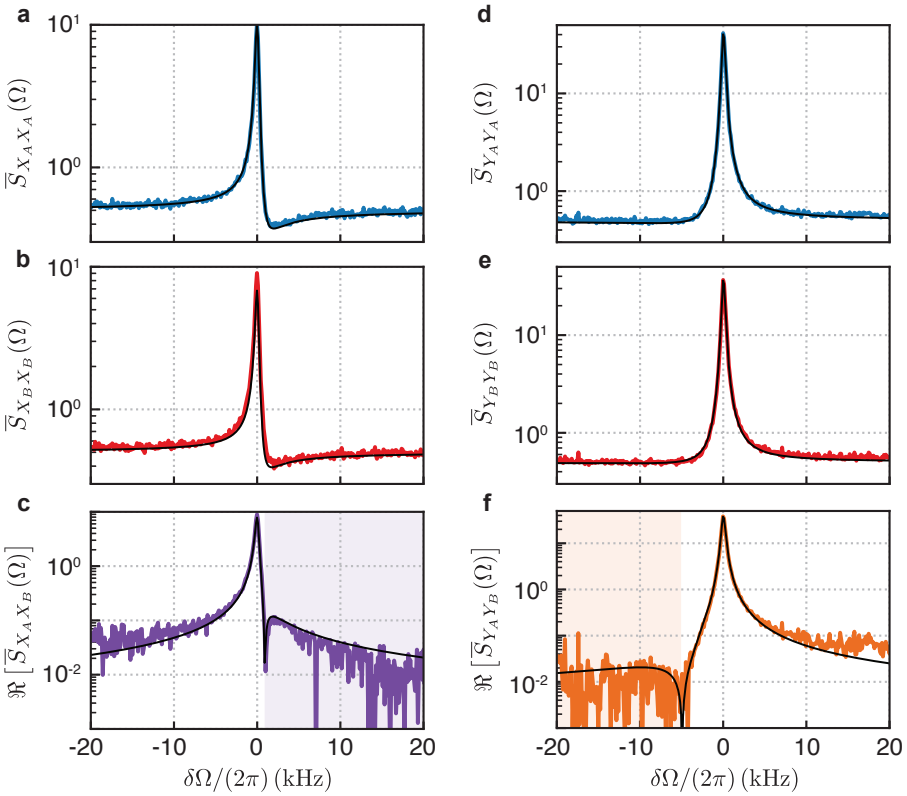


Figure 9.12: Simultaneous fit of measured spectra. a, b, c, Spectra and cross-spectra for the simultaneously measured $\hat{X}$ quadratures of the two lasers, at $\Theta = 0$. In c, we show the absolute value of the cross-spectrum for the sake of visualization. The shaded area corresponds to actual negative values d, e, f, Spectra and cross-spectra for the simultaneously measured $\hat{Y}$ quadratures of the two lasers. The black lines are fits which are all performed simultaneously. Adapted from [Che+20].

measurement is composed of three steps: first, we measure the combination of quadratures at $\theta_A, \theta_B$, from which we calculate their PSD and cross-PSD, e. g. Figure 9.12a-c; second, we advance the homodyne angle by $\pi/2$ and measure the new orthogonal combination and calculate again the spectra, e. g. Figure 9.12d-f; third, we measure the shot noise which we use for the calibration. Each measurement then results in six independent spectra, four of which come from self-correlations and the remaining two from cross-correlations during the same step. We simultaneously fit all these six spectra to the model in Equation 9.6, with the appropriate choice of j, k, $\theta_A$ and $\theta_B$. The only free parameters are the optomechanical couplings, $g_j$, and detunings, $\Delta_j$, in order to account for drifts over the duration of the experiment. The overall

results from the fits are shown in Figure 9.13, as well as their mean values.

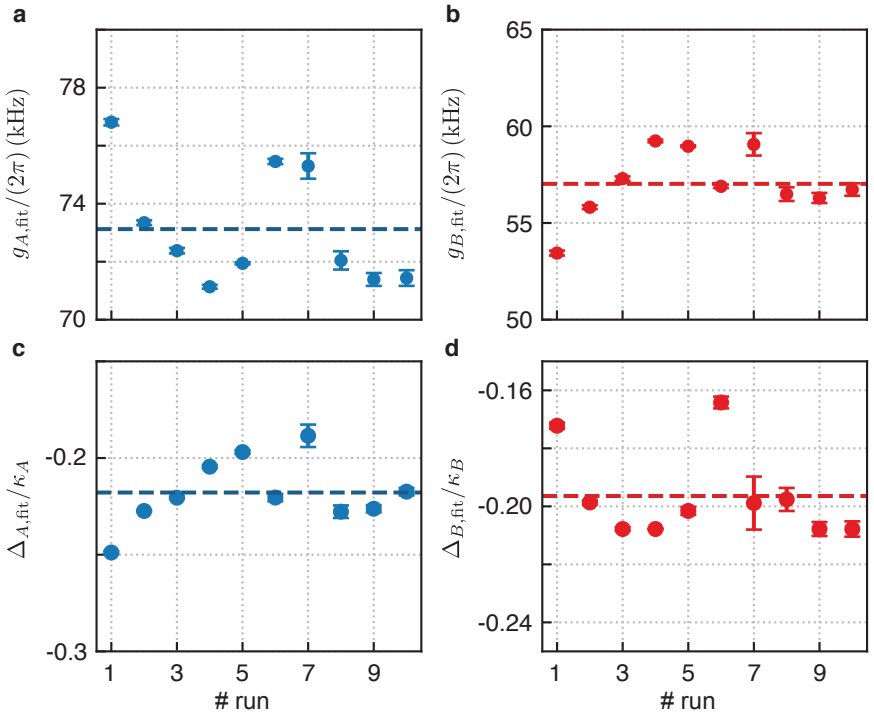


Figure 9.13: Resulting parameters from fits. The optomechanical couplings, $g_j$, and detunings, $\Delta_j$, are taken as free parameters in the fit. The results for laser A and B are shown, respectively, in a, c and b, d. The dashed lines are the average values of the fitted parameters over all the runs. The error bars reflect the confidence interval from the fits. Adapted from [Che+20].

# CONCLUSION AND OUTLOOK

Quantum measurement is an ancient yet fascinating topic of modern physics, which carries profound implications in our understating of Nature. Concurrently, it represents an essential tool for technological applications, as shown by the vast development during the last forty years. In particular, the interest on quantum measurement and control of mechanical systems is growing rapidly, due to its potentiality in applications and fundamental researches. We hope that this thesis has provided a flavour of the topic.

In conclusion, let's summarize the main results presented. We have realized an optomechanical cavity based on a dielectric membrane resonator. Owing to the unprecedented low mechanical dissipation and the high detection efficiency, we performed an efficient quantum measurement of the displacement of this mechanical resonator. This measurement operates at the Heisenberg measurement-disturbance limit to within 33%, making the system the closest mechanical realization to the Heisenberg microscope thought experiment. This quantum measurement enables the production of a state-of-knowledge, or conditional state, which is almost a pure coherent state. We experimentally implemented a protocol, based on mechanical quantum trajectories and a retrodiction measurement, which allows to fully verify this conditional state. Also, this allows to observe the measurement-induced dynamics, from the reduction of the state variance to the decoherence stemming from quantum backaction. Based on the measurement outcomes, we implemented a control feedback loop to stabilize a mechanical mode in its ground state, with a residual thermal occupation of 0.29 phonons. This realized a long-standing goal in the field and concluded a twenty-year-long series of experimental efforts in achieving a measurement-based quantum control of mechanical degrees of freedom. This capability of our system allowed us to further explore several routes. On one side, we have shown the thermodynamic implications of a quantum measurement. In particular, we have experimentally assessed the dramatic contribution to the entropy production generated by the measurement. On the other side, we made use of the correlations present in the quantum measurement. First, we have exploited them at the detection stage to perform displacement measurements with a total noise sensitivity below the SQL. Then, we have shared these correlations among two optical probe lasers, which were measuring the same mechanical motion. We experimentally verified that the bipartite optical state, after the interaction with the mechanics, becomes entangled.

This optomechanical platform is also appealing for realizable applications and further studies on quantum measurements, including:

ELECTRO-OPTO-MECHANICAL COUPLING Mechanical resonators can be employed to couple optical and microwave fields together, which represents a crucial step towards quantum networks based on, e. g., superconducting qubits. This electro-opto-mechanical coupling has been shown in several experiments, using either piezoelectric materials [Boc+13; For+20] or mechanical resonators capacitively coupled to electrical circuits [Bag+14; Hig+18]. We are realizing a system similar to the latter. In particular, we designed a soft-clamped membrane with two defects embedded in the phononic crystal [CTS20]. One of them is coupled to an optical cavity, as detailed in this thesis. The other, instead, is coated with a thin layer of superconducting metal and forms one of the plates of a capacitor in a superconducting circuit. Once the electrical coupling is optimized, the microwave mode would also perform a quantum measurement of the mechanical displacement. In a similar manner to what has been shown in Section 9.2, this would enable the generation of an entangled state between an optical and a microwave mode, a milestone for future quantum information processing applications.

IMPROVING GRAVITATIONAL WAVE DETECTORS To further enhance the sensitivity of gravitational wave detectors, the injection of vacuum squeezed light has been recently implemented [Tse+19]. This improves the sensitivity in a limited spectral window, while degrading it elsewhere. A better performance could be achieved if the angle of squeezing is rotated in a frequency-dependent matter [McC+20]. Among the several proposals to do that, one exploits the OMIT effect [Ma+14]. The advantage lies in the compactness of the required optical cavity, of only few centimeters, compared to the tens of meter scale of other proposals. The sideband-resolved optomechanical cavity is driven by a red detuned control laser, which opens a transparency window around the cavity resonance. The linewidth of the dispersive response within such a window is dictated by the optical damping rate, proportional to the power of the control laser. This forms a tunable narrow filter which can be used to process the squeezed vacuum, before delivering it to the main interferometer.

Another possible improvement is about the detection bandwidth. In fact, important astronomical events, like neutron stars coalescence, take place at high frequencies, up to $\sim 5$ kHz. Current detectors use signal recycling techniques to improve their sensitivity. These are a form of resonance enhancement, thus subjected to the usual gain-bandwidth trade-off, limiting the useful de-

tection bandwidth to, at most, 1 kHz. One way to overcome this limitation is offered by the method of white light signal recycling. It turns out that a possible implementation is given by a resolved-sideband optomechanical cavity [Mia+15]. In particular, under continuous driving with a blue-detuned laser, the cavity response mimics a negative dispersive filter. Tuning the power and the detuning of the control laser allows to exactly match the phase delay experienced by the optical sidebands in the interferometer, due to signal recycling, and thus cancel it. To counteract the instability resulting from driving on the blue side, one also need to implement a feedback loop to cool and stabilize the mechanical motion. Then, the optomechanical cavity can be used to filter the outcoming field from the interferometer, before the detection.

The success of both proposals rely, however, on a strong requirement: that the mechanical thermal noise contributes negligibly either to the vacuum squeezed field or to the optical sidebands encoding the astronomical information. For a 150 Hz-wide optomechanical filter, this corresponds to requiring, for the mechanical element, that $Q/T \geqslant 10^9\ K^{-1}$, unrealistic to achieve only few years ago. The optomechanical cavity based on a soft-clamped membrane that we have introduced approaches this requirement closer than ever. In fact, from the experiments reported in this thesis we have shown that a $Q/T \approx 10^8\ K^{-1}$ is possible, in a moderate cryogenic environment at liquid Helium temperature and for circulating optical powers of the order of $\mathcal{O}(10\,\mathrm{mW})$. We expect to improve that ratio and match the needed requirement once the optomechanical cavity is operated in a dilution refrigerator at mK temperature [Pag+20]. Here, the main limitation would be posed by heating of the membrane due to absorption of the optical radiation. We have started to investigate that by characterizing the dissipation of a 60-nm-thick membrane resonator, as a function of the optical power and the fridge temperature. The results are shown in Figure O.1 and more details can be found in Appendix C. By assuming perfect thermalization between the membrane structure and the fridge, we can use the measured quality factor as a proxy to infer the heating effect of the optical absorption. For 1 μW of impinging power we measure $Q \approx 0.3 \times 10^9$ and infer $T_{inf} \approx 150\,\mathrm{mK}$, from which follows that $Q/T_{inf} \approx 2 \times 10^9 K^{-1}$, an encouraging results for these applications. We also expect that using thinner membranes would give higher quality factors, without affecting significantly the absorption heating. In fact, the lower bulk absorption of optical radiation is compensated by the higher thermal resistance.

EXPLORING DIFFERENT QUANTUM MEASUREMENTS Displacement quantum measurements effectively realize projections in the co-

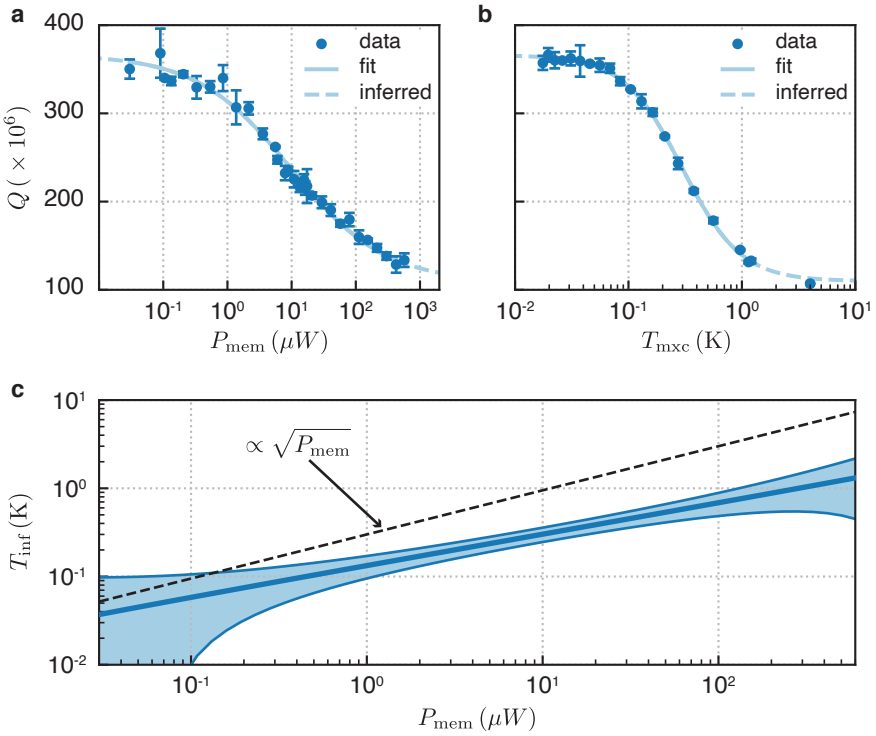


Figure O.1: Effect of absorption heating at mK temperature. Quality factors (blue circles) extracted from ringdown measurements for a, different probe optical powers impinging on the resonator at fridge temperature $\approx$ 20 mK and b, different fridge temperatures at a fixed optical power of 100 nW. The data are fit to a generic polynomial model, the result of which is shown as solid light blue lines. The dashed lines are extrapolations based on the fit results. c, Inferred membrane temperature as a function of optical power (solid blue). The shaded area reflects the error in doing such an inversion. The dashed black line represents a square root law and is meant just as a guide for the eye.

herent states basis. As such, their precision is always limited, at most, by the mechanical zero point motion. In terms of conditional state, this corresponds to at most a coherent state, with equal variances in both quadratures. This limit arises from the detection arrangement, in which the homodyne LO is chosen to be on resonance with the laser carrier, thus detecting both red and blue mechanical sidebands. As proposed by Lammers [Lam18], one can overcome this limit by performing quantum measurements where the LO is resonant with either one of the two sidebands. Depending on the chosen sideband, one can observe a quantum trajectory with a squeezed quadrature variance and a retrodiction measurement on coherent states, or vice versa. This is an appealing route to explore, given that our system already satisfies all the requirements. In particular, it represents a powerful tool, which is capable of (i) generating conditional me-

chanical squeezed states, which can be turned into unconditional ones by means of a feedback and (ii) performing retrodiction measurements with precision below the zero point fluctuations, useful for mechanical state tomography, even of non-Gaussian states.

Looking forward, continuous displacement measurements in our optomechanical system can be tailored to implement crucial protocols in quantum information processing applications, as state teleportation and entanglement swapping [Hof+13; HH15]. If equipped with nonlinear measurements, generation of mechanical non-classical states is also possible [Rin+18].

# A

# SYMBOLS

## A.1 OPTICS

| SYMBOL | NAME |
|---|---|
| $\Omega_c$ | Cavity resonance frequency |
| $\mathcal{F}$ | Cavity finesse |
| $\kappa$ | Cavity energy decay rate |
| $\eta_{c,j} = \kappa_j/\kappa$ | Cavity overcoupling |
| $\chi_c(\Omega) = \frac{\sqrt{\kappa}}{\kappa/2 - \imath(\Delta+\Omega)}$ | Cavity susceptibility |
| $\Omega_L$ | Laser frequency |
| $\Delta$ | Laser-cavity detuning |
| $\hat{a}$ | Cavity field amplitude |
| $\hat{a}_{in}$ | Input field amplitude |
| $\overline{a}$ | Mean cavity field amplitude |
| $\overline{a}_{in}$ | Mean input field amplitude |
| $\hat{i}$ | Photocurrent operator |
| $\eta_\imath$ | Optical loss efficiency |
| $\eta_{qe}$ | Photodiode quantum efficiency |
| $\nu$ | Interference visibility |
| $\eta_d \coloneqq \eta_\imath \eta_{qe} \nu^2$ | Total detection efficiency |
| $\eta \coloneqq \eta_d \eta_c$ | Total efficiency |

Table A.1: Symbols related to the optical and the detection systems.

## A.2 MECHANICS

| SYMBOL | NAME |
|---|---|
| $e_{ij}$ | Strain tensor |
| $\sigma_{ij}$ | Stress tensor |
| $\nu$ | Poisson's ratio |
| $E$ | Young's modulus |
| $h$ | Membrane thickness |
| $D = Eh^3/\left(12(1-\nu^2)\right)$ | Flexural rigidity |
| $Q$ | Mechanical quality factor |
| $\Omega_m$ | Mechanical resonance frequency |
| $\Gamma_m$ | Mechanical damping rate |
| $m$ | Effective mass |
| $\chi_m(\Omega) = \frac{\Omega_m}{\Omega_m^2 - \Omega^2 - \imath\Gamma_m\Omega}$ | Mechanical susceptibility |
| $\hat{q}$ | Dimensionless displacement operator |
| $\hat{p}$ | Dimensionless momentum operator |
| $x_{zp} = \sqrt{\frac{\hbar}{2m\Omega_m}}$ | Zero-point displacement |
| $p_{zp} = \sqrt{\frac{\hbar m\Omega_m}{2}}$ | Zero-point momentum |
| $\hat{\xi}$ | Brownian thermal force operator |
| $\overline{n}_{th}$ | Thermal bath average phonon number |

Table A.2: Symbols related to the mechanical system.

## A.3 OPTOMECHANICS

| SYMBOL | NAME |
|---|---|
| $r_m, t_m$ | Membrane reflection and transmission coefficients |
| $z_m$ | Membrane-mirror distance |
| $G$ | Optomechanical coupling constant |
| $g_0$ | Vacuum optomechanical coupling rate |
| $g$ | Field-enhanced optomechanical coupling rate |
| $\overline{n}_{cav}$ | Cavity average photon number |
| $P_{in}$ | Input optical power |
| $P_{tr}$ | Transmitted optical power |
| $A_{\pm}$ | Stokes/anti-Stokes scattering rates |
| $\Gamma_{opt}$ | Optical damping rate |
| $\overline{n}_{opt}$ | Effective optical bath occupation |
| $\gamma = \Gamma_m \left(\overline{n}_{th} + 1/2\right)$ | Thermal decoherence rate |
| $\Gamma_{qba} = \Gamma_{opt}\left(\overline{n}_{opt} + 1/2\right)$ | Quantum backaction decoherence rate |
| $\gamma_{tot} = \gamma + \Gamma_{qba} + \ldots$ | Total decoherence rate |
| $\Gamma_{meas} = \eta\Gamma_{qba}$ | Measurement rate |
| $\mathcal{C}_q = \Gamma_{qba}/\gamma$ | Quantum cooperativity |
| $\eta_{meas} = \Gamma_{meas}/\gamma_{tot}$ | Measurement efficiency |
| $\overline{S}_{imp}$ | Spectral imprecision noise |
| $\overline{S}^{inf}_{\hat{q}\hat{q}}(\Omega)$ | Inferred displacement spectrum |
| $\overline{S}^{SQL}_{\hat{q}\hat{q}}(\Omega) = \lvert\chi_m(\Omega)\rvert$ | Spectral SQL |
| $\overline{S}^{zp}_{\hat{q}\hat{q}} = 1/\Gamma_m$ | Resonant zero-point displacement spectrum |

Table A.3: Symbols related to the optomechanical system.

# B

# EXCESS LASER NOISE

Hereby, we describe the methods for characterizing the excess noise in the amplitude and the phase of a laser, and report the measurement results for one of our TiS lasers [Ros+18]. Characterizing this excess noise and achieving a quantum-noise-limited laser is important in optomechanical experiments in order to avoid introducing excess imprecision and backaction noise.

Let's start by the fluctuations in the propagating input field, $\hat{a}_{in}(t) = (\hat{X}_{in}(t) + \imath\hat{Y}_{in}(t))/\sqrt{2}$. In presence of excess classical noise, the correlations become [Jay+12]

$$\left\langle \hat{X}_{in}(t)\hat{X}_{in}(t')\right\rangle = \delta(t-t')\frac{1}{2}\left(1 + C_{XX}\right), \tag{B.1a}$$

$$\left\langle \hat{Y}_{in}(t)\hat{Y}_{in}(t')\right\rangle = \delta(t-t')\frac{1}{2}\left(1 + C_{YY}\right), \tag{B.1b}$$

$$\left\langle \hat{X}_{in}(t)\hat{Y}_{in}(t')\right\rangle = \delta(t-t')\frac{\imath}{2}. \tag{B.1c}$$

The excess noise is described by the quantities $C_{XX}$ and $C_{YY}$, which are implicitly dependent on the average optical power. In addition, we have assumed for simplicity that there are no cross-correlations between the amplitude and the phase quadratures noises, i. e. $C_{XY} = 0$. If any, in fact, these cross-correlations will be limited by the Cauchy-Schwarz inequality.

The excess noise is also usually not a white noise, but has a dependence on the frequency, $\Omega$. We now provide some methods which are useful to characterize the spectral dependence of such noises.

## B.1 AMPLITUDE QUADRATURE

To measure the amplitude quadrature noise, we directly detect the laser field on a photodiode and record the PSD of the corresponding photocurrent, at several impinging optical powers, P. From the spectra, we obtain the amplitude noise variance, at each power, by integrating the spectra at a given Fourier frequency, $\Omega$, within a bandwidth of 20 kHz. We plot the resulting variances in Figure B.1b as a function of optical power, for $\Omega/(2\pi) = 1.14$ MHz. For comparison, we also plot the noise variances at $\Omega/(2\pi) = 4.5$ MHz, where the dominating noise is the shot noise. We fit these variances to a second-order polynomial, where the linear (quadratic) term is due to shot (classical) noise. From the fit we extract the ratio between the quadratic and linear coefficients, which is the classical noise contribution to the total noise variance, in units of shot noise, per optical power. For the chosen frequency, we

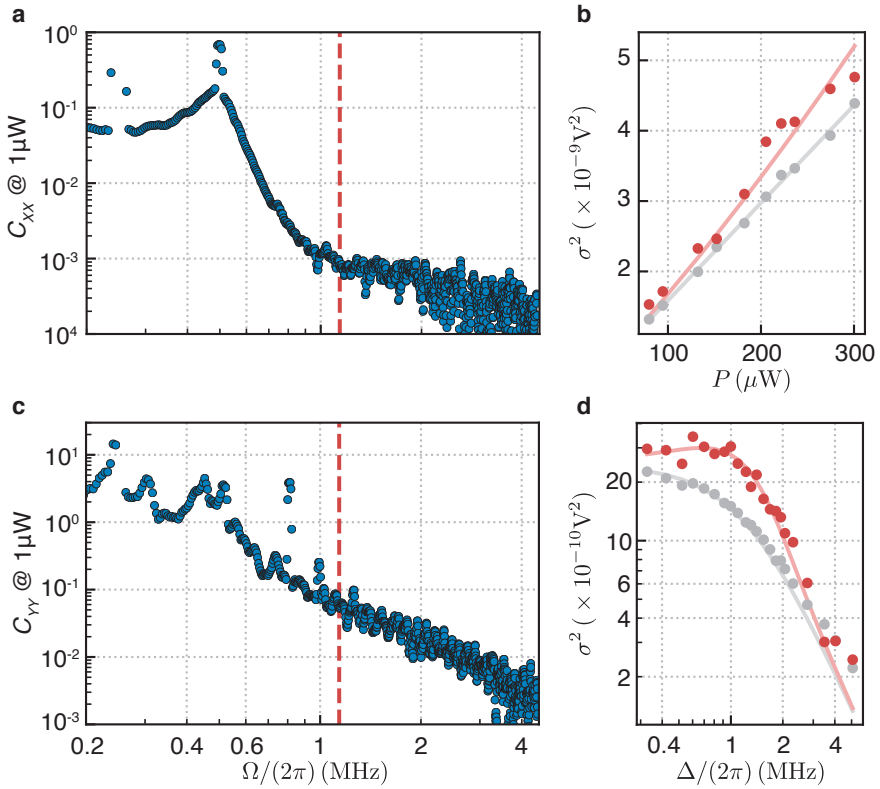


Figure B.1: Laser excess noise. a, c, Amplitude and phase noise, respectively, at different frequencies. The dashed red line marks the resonance frequency $\Omega_m/(2\pi) = 1.14$ MHz of the mechanical mode studied. b, d, Integrated detected variance (red circles) at $\Omega_m$ at different optical powers and detunings, respectively. The solid red line is a quadratic fit, for the amplitude noise, and a fit from the cavity rotation model, for the phase noise. The gray circles are variances at 4.5 MHz, where the dominating source of noise is the shot noise. The solid gray line is a fit. Adapted from [Ros+18].

obtain that the classical noise has a contribution of $8 \times 10^{-4}$ to the total noise variance, for 1 μW of optical power. By repeating the analysis at different Fourier frequencies, we estimate the spectral dependence of the amplitude quadrature noise, $C_{XX}$. In Figure B.1a we show the results, referenced to a 1 μW of optical power.

The broad resonance observed in the spectrum of $C_{XX}$, at ~ 500 kHz, is due to the relaxation oscillations of the laser medium. The center frequency and the linewidth are also determined by the optical power of the pump laser. We choose to use ≈ 2.5 W of pump power, which guarantees a stable lasing operation and reduces the amplitude quadrature noise around the mechanical resonance frequency at ~ 1 MHz, which is the important region for the optomechanical experiments.

## B.2 PHASE QUADRATURE

Direct photodetection is not sensitive to the phase quadrature. To measure its noise, then, we need to use an optical system which performs a phase-to-amplitude conversion, for instance an empty optical cavity. In fact, the quadratures of a transmitted field from a cavity are rotated compared to the input ones, according to the detuning, $\Delta$, from the resonance of the cavity mode addressed. That is, the input phase quadrature partially appears in the output amplitude quadrature, which can be simply measured by means of a direct photodetection, as done in the previous section. The maximum rotation is expected to be at frequencies $\Omega \sim \kappa/2$. In particular, if one knows the cavity linewidth, $\kappa$, the detuning, $\Delta$, and the input amplitude noise, $C_{XX}$, measured before, then from the measured amplitude noise of the output field one can extract the contribution stemming only from the input phase noise.

In practice, we use a 27-mm long cavity, formed by a plane and a spherical mirrors, with radius of curvature of 50 mm. At the chosen working wavelength of 850 nm, the cavity has the narrowest linewidth of $\kappa/(2\pi) = 2.44$ MHz, which corresponds to a finesse of 2300. The two employed mirrors have identical coatings, so we assume that the cavity is symmetric, that is,the overcoupling is $\eta_c = 0.5$. Once assembled, this cavity is put in a vacuum environment and evacuated to high-vacuum.

We drive a cavity mode with the laser, at a fixed optical power, from one port and we directly detect the transmitted field through the other port. The laser is locked to the side of the cavity resonance via a slope lock. We record the PSD of the photocurrent at different detunings, $\Delta$. We integrate the spectra, at fixed $\Omega$ and bandwidth 20 kHz, to estimate the output amplitude noise variance, as done previously, as a function of the detuning, $\Delta$. In Figure B.1d we show these measurements for $\Omega/(2\pi) = 1.14$ MHz and, for comparison, at $\Omega/(2\pi) = 4.5$ MHz, where we expect to have contributions only from the shot noise. We fit these data to a model for the transmitted field [Gal+91; Zha+95], which takes into account the cavity dynamics (cf. Section 1.1) and the correlations in Equation B.1. For the output amplitude spectrum, normalized to the average output power, we obtain

$$\overline{S}^{\text{out}}_{XX}(\Omega) = 1 + \frac{4(1-\eta_c)\eta_c\kappa^2}{\Delta^2 + (\kappa/2)^2} \times \\ \times \frac{\left((\kappa/2)^2\Omega^2 + (\Delta^2 + (\kappa/2)^2)^2\right) C_{XX}(\Omega) + \Delta^2\Omega^2 C_{YY}(\Omega)}{\Delta^4 + 2\Delta^2\left((\kappa/2)^2 - \Omega^2\right) + \left((\kappa/2) + \Omega^2\right)^2}. \tag{B.2}$$

In practice, we normalize the integrated variance to the one calculated at 4.5 MHz, which we expect to be shot-noise-limited. Then, at each

frequency $\Omega$ we fit the data to Equation B.2, where the only free parameter is the phase noise, $C_{YY}$. In fact, we fix the amplitude noise value, $C_{XX}$, from the findings of the previous section. Once repeated for all frequencies, we find the spectral dependence of the excess phase noise, as shown in Figure B.1c. At $\Omega/(2\pi) = 1.14$ MHz we find that it has a contribution of $5 \times 10^{-2}$ to the total noise variance, for an optical power of 1 $\mu$W.

The laser phase noise is upper bounded by the measured phase noise, which also contains any other source of noise from the cavity, e. g. the one arising from the mirrors' substrate thermal noise. In order to reduce the effect of the cavity noise, we choose to use a low finesse cavity, such that the optomechanical coupling to the mirrors' motion is small, for the optical power used. Also, we operate the cavity in a vacuum environment. Firstly, this removes the thermorefractive noise due to the fluctuating refractive index of the air along the optical path. Secondly, we have observed that the spectrum of the transmitted amplitude contains excess noise in the form of a frequency comb, when the cavity is operated in air. The peaks of this comb are evenly spaced by $\sim$ 20 kHz, from baseband up to few MHz, at the cavity cutoff. We have observed that this comb disappears once the cavity is in vacuum.

# C

# MECHANICAL DISSIPATION AT ULTRA-LOW TEMPERATURES

The next generation of experiments will involve the coupling of an optomechanical cavity to a microwave mode. For best performances and a quantum-limited operation, it requires to be operated in an ultra-cold environment at mK temperature. It is important, then, to characterize the mechanical properties of the membrane resonator at such low temperatures. In particular, the mechanical dissipation for silicon nitride membranes has been observed to depend on the temperature at which the material is kept [Zwi+08; YCS15].

## C.1 EXPERIMENTAL SETUP

*Dilution refrigerator*

We have also observed roughly a threefold reduction in the mechanical dissipation rate in the experiments reported so far, going from room temperature to $T \approx 10$ K. To reach even lower temperature, we make use of a commercial dry dilution refrigerator, a Bluefors LD-250[1]. This cryogenic system is based on a mixture of the isotopes Helium-3 and Helium-4, hosted in a mixing chamber (MXC). When this mixture is cooled below 0.86 K, a spontaneous separation of a concentrated and a dilute phase, respectively rich and poor of Helium-3, happens. Extracting the evaporating Helium-3 from the dilute phase allows to exploit the enthalpy of mixing of this mixture to cool the MXC environment, in principle to an arbitrary low temperature. In practice, the finite size of the tubes and the thermal radiation from the surroundings limit the base temperature to around 20 mK. The extracted Helium-3 is recycled and used to repopulate the concentrated phase, thus closing the cryogenic cycle. The necessary pre-cooling of the hot Helium-3 gas inserted during the circulation is provided by a closed-cycle pulse tube cooler, which provides enough continuous cooling power at 4 K. We depict a sketch of this refrigerator in Figure C.1a. The MXC is attached to a copper plate which also thermalizes to base temperature. This plate is used as the working area for the experiments, for which the lowest achievable temperature is needed.

*Sample holder*

To characterize the mechanical dissipation of a membrane resonator, we interferometrically measure the motion of its mode as it rings down upon excitation. The resonator is assembled in a sample holder, shown in Figure C.1b. The base block, made of oxygen-free high conductivity copper, is tightly screwed on the MXC plate. At its center, we drill a through hole for the propagation of the light, on top of

1 bluefors.com

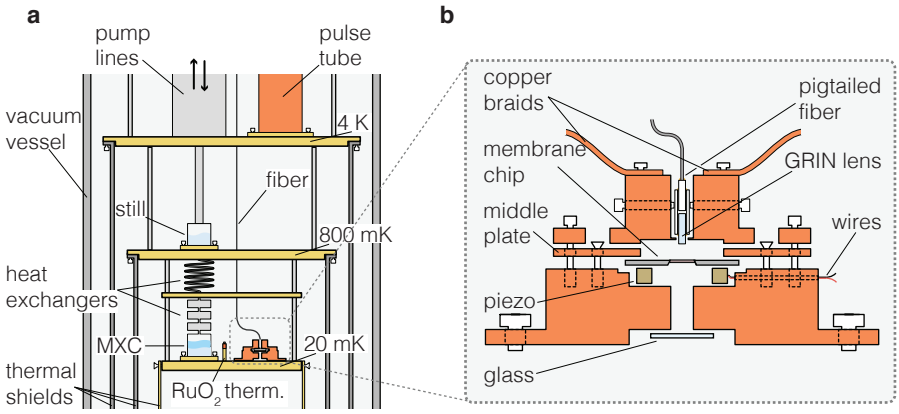


Figure C.1: Setup for the characterization of membranes at mK temperature. a, Section view of a dry dilution refrigerator. The sample is placed on the coldest plate, at 20 mK. The temperature is measured by a resistive $RuO_2$ thermometer, next to the MXC. b, Section view of the sample holder which hosts the membrane resonator chip. An optical fiber delivers the laser light and collects the reflection from the membrane, the phase of which encodes the displacement and is interferometrically detected.

which we put a piezo ring with a membrane chip lying down. The piezo-membrane stack is clamped down by a middle thin copper plate. Then, a top copper cap, which hosts an optical fiber, covers the piezo-membrane stack. Two copper braids provide a thermal link between this cap and the cold MXC plate. Moreover, we cover the lower end of the through hole with a thin glass layer, in order to enclose the membrane resonator in a small volume region. This stems from the phenomenological observation that the quality factor degrades when the resonator chip is cooled down with no encapsulation around. We suspect this arises from the condensation of surrounding gas molecules on the membrane surface. When an enclosure is present instead, the gas molecules condense into its walls as well, reducing the risk of contamination of the membrane surface. The laser light is delivered into the cryostat by means of an optical pigtailed fiber and focused onto the sample by a GRIN lens. This allows to achieve a very small waist size, necessary to avoid scattering of light at the apertures of the soft-clamped membrane. We insert the fiber-lens assembly into the top cap, which we translate horizontally in order to align the optical axis with the membrane defect. The small working distance of $\approx 1$ mm between the membrane and the lens end facet reduces the effect of tilting between them.

*Optical detection scheme*

The optical setup comprises a Mach-Zehnder interferometer with a heterodyne detection scheme, as sketched in Figure C.2. A TiS laser, at $\lambda = 830$ nm, is used to generate a LO and a probe beam. The former is frequency shifted by means of an acousto-optic modulator (AOM), driven by a coherent tone at 60 MHz. The probe beam is fiber-coupled

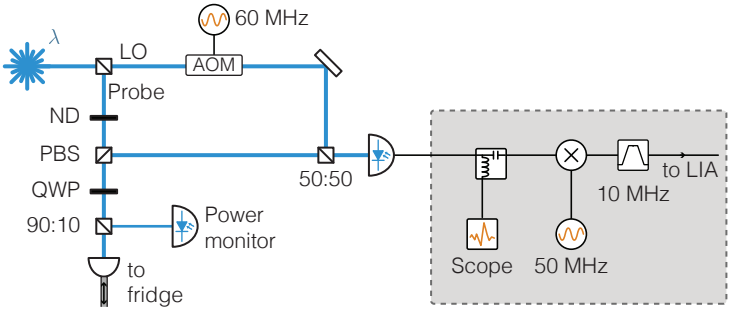


Figure C.2: Optical interferometer setup and electronic detection.

and delivered to the mechanical sample inside the fridge. Its optical power can be controlled by a continuously variable neutral density filter wheel, mounted on a servo motor. After the attenuator, a 10% of the light is tapped into a photodetector in order to monitor the optical power entering the fridge. The light reflected from the mechanics is coupled back into the fiber, then is spatially isolated from the incoming beam and overlapped with the LO on a 50 : 50 BS. We directly detect one output of the BS with a commercial amplified photodetector. The resulting photocurrent contains an interference beat note, at 60 MHz, with phase modulation sidebands around it due to the mechanical motion. We down-convert this electric signal to 10 MHz and detect both the carrier and the upper mechanical sidebands, at $10 + \Omega_m/(2\pi)$ MHz, by means of an LIA.

## C.2 FIRST RESULTS

In practice, we drive the in-bandgap mechanical mode via a piezo excitation and continuously monitor the decaying energy of the upper mechanical sideband. We fit these data to an exponential model and extract the mechanical energy decay rate, $\Gamma_m$, from which we infer the mechanical quality factor, Q. In Figure C.3a we show the data for an 100-nm-thick membrane, as we vary the probe optical power impinging on the membrane, $P_{mem}$, at a fixed fridge temperature of $\approx 20$ mK. The mechanical mode quality factor, at room temperature, is measured to be $Q = 19 \times 10^6$. We fit the data to the following phenomenological model

*Dependence on the optical power*

$$Q(x) = \frac{1}{k_0 + k x^a} + Q_0, \tag{C.1}$$

with $k_0$, $k$, $a$ and $Q_0$ free parameters. The measurement roughly shows a fourfold increase in the quality factor as we reduce the power from a mW to few μW. We hypothesize that this dependence is caused by heating of the membrane generated by the absorption of the optical radiation. In fact, the refractive index of silicon nitride membranes has a small yet non-zero imaginary component, which has been estimated to be $\mathrm{Im}(n) \approx 5 \times 10^{-6}$ at $\lambda \approx 840$nm [Nie16]. Consequently, the spot of

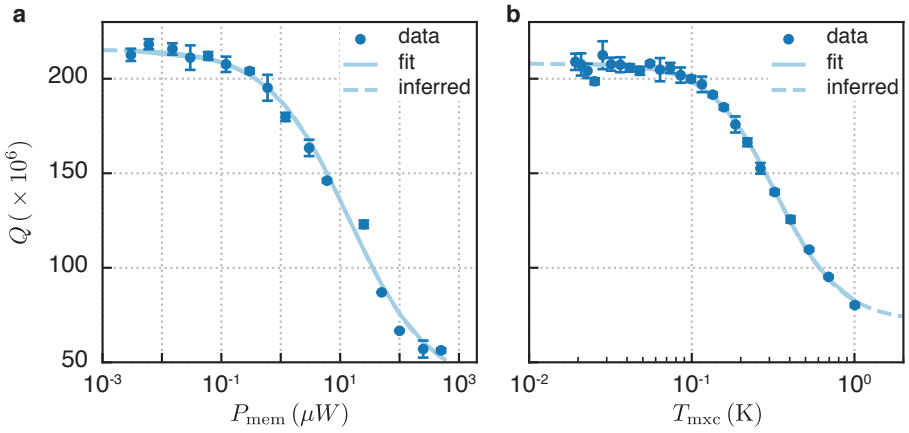


Figure C.3: Mechanical quality factor as a function of the optical power and the fridge temperature. a, Quality factors (blue circles) extracted from ringdown measurements, at different probe optical powers impinging on the resonator. The fridge temperature is ~ 20 mK. b, Measured quality factors (blue circles) at different fridge temperatures, for a fixed optical power of ~ 60 nW. The data are fit to a generic polynomial model, the result of which is shown as solid light blue lines. The dashed lines are extrapolations based on the fit results.

the probe laser deposits some amounts of heat on the membrane defect. For amorphous glassy solids, the thermal conductivity is known to reduce drastically with temperature [ZP71] and silicon nitride makes no exception [LP98; Fto+15]. Combined with the finite cooling power of the fridge, the generated heat from the optical absorption raises the equilibrium temperature of the membrane structure.

*Dependence on the temperature*

In Figure C.3b we show the measured quality factors, with a fixed optical power of $P_{\mathrm{mem}} \approx 60$ nW, as we ramp up the mixing chamber temperature, which is measured by a resistive thermometer located on the same plate. We fit these data to the same model in Equation C.1. The measurements show an increase of the quality factor as the temperature is reduced below 1 K, similar to other independent experiments [Zwi+08; YCS15; Fis+16]. In particular, Fischer et al. characterized a SiN membrane in a Si phononic shield, with an optical detection scheme and at dilution refrigerator temperatures as well. The physical origin of the intrinsic mechanical dissipation is yet not fully understood for SiN resonators. Recently, more evidences have pointed to surface losses as the cause [VS14]. For amorphous materials as silicon nitride, such losses are due to the interaction between two-level system defects present on the surface and the strain field of the structure[Phi87]. The number of interacting defects and their strength cause the mechanical energy dissipation, which indeed depends on the temperature. The data presented here indicate the presence of a temperature-dependent dissipation, but further studies need to be done to ascertain the origin.

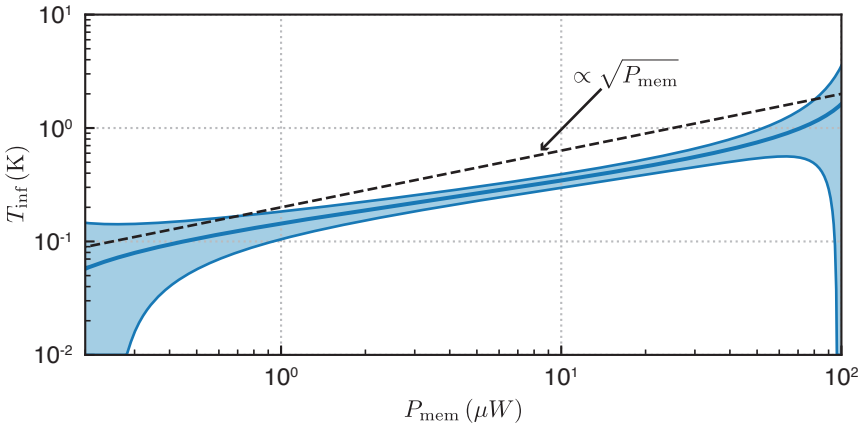


Figure C.4: Effect of the absorption heating under optical illumination. The measured quality factors are used as a proxy to infer the membrane temperature. To this end, the polynomial fit function in Figure C.3b is inverted and applied to the other fit function in a. The shaded area reflects the error in doing this inversion. The dashed black line represents a square root law and is meant just as a guide for the eye.

*Heating due to optical absorption*

To further investigate the effect of the absorption heating, we use the quality factors, measured as a function of fridge temperature, as a proxy for the membrane temperature. To this end, we invert the fit function in Figure C.3b and apply it to the fitted quality factors as a function of optical power, shown in Figure C.3a. The resulting curve is shown in Figure C.4, where the shaded area represents the uncertainty in this inversion procedure. This error is larger where the quality factor flattens, because it becomes harder to discriminate its change due to a given temperature variation. Formally, we can invert Equation C.1 where the independent variable, $x$, is now assumed to be the temperature, $T$. Then, a given uncertainty in the quality factor, $\Delta Q$, propagates to the temperature as $\Delta T = |dT(Q)/dQ|\Delta Q$. The shaded area corresponds to this uncertainty, where we assume a constant $\Delta Q = 10 \times 10^6$.

This result should however be taken *cum grano salis*, because it relies on the strong assumption that the membrane mode temperature exactly thermalizes to the fridge temperature, as read from the resistive thermometer. In general, there might be other processes, as radiative heating or mechanical vibrations at the mode frequency, which can displace the mode temperature away from the thermal equilibrium with the fridge environment. More reliable and quantitative results can be obtained by performing a mechanical noise thermometry experiment within an optomechanical cavity, as discussed in Section 4.2.5. This is indeed the direction of further experiments.

# BIBLIOGRAPHY


[Abb+09] Abbott, B. et al. "Observation of a Kilogram-Scale Oscillator near Its Quantum Ground State." *New J. Phys.* 11, 7 (2009), p. 073032. DOI: 10.1088/1367-2630/11/7/073032.

[ASI04] Adesso, G., Serafini, A., and Illuminati, F. "Extremal Entanglement and Mixedness in Continuous Variable Systems." *Phys. Rev. A* 70, 2 (2004), p. 022318. DOI: 10.1103/PhysRevA.70.022318.

[ALR16] Alonso, J. J., Lutz, E., and Romito, A. "Thermodynamics of Weakly Measured Quantum Systems." *Phys. Rev. Lett.* 116, 8 (2016), p. 080403. DOI: 10.1103/PhysRevLett.116.080403.

[Ash70] Ashkin, A. "Acceleration and Trapping of Particles by Radiation Pressure." *Phys. Rev. Lett.* 24, 4 (1970), pp. 156–159. DOI: 10.1103/PhysRevLett.24.156.

[Ash78] Ashkin, A. "Trapping of Atoms by Resonance Radiation Pressure." *Phys. Rev. Lett.* 40, 12 (1978), pp. 729–732. DOI: 10.1103/PhysRevLett.40.729.

[AKM14] Aspelmeyer, M., Kippenberg, T. J., and Marquardt, F. "Cavity Optomechanics." *Rev. Mod. Phys.* 86, 4 (2014), pp. 1391–1452. DOI: 10.1103/RevModPhys.86.1391.

[Bag+14] Bagci, T. et al. "Optical Detection of Radio Waves through a Nanomechanical Transducer." *Nature* 507, 7490 (2014), pp. 81–85. DOI: 10.1038/nature13029.

[Bar+13] Barbosa, F. A. S., Coelho, A. S., Cassemiro, K. N., Nussenzveig, P., Fabre, C., Villar, A. S., and Martinelli, M. "Quantum State Reconstruction of Spectral Field Modes: Homodyne and Resonator Detection Schemes." *Phys. Rev. A* 88, 5 (2013), p. 052113. DOI: 10.1103/PhysRevA.88.052113.

[Bar+19] Barzanjeh, S., Redchenko, E. S., Peruzzo, M., Wulf, M., Lewis, D. P., Arnold, G., and Fink, J. M. "Stationary Entangled Radiation from Micromechanical Motion." *Nature* 570, 7762 (2019), pp. 480–483. DOI: 10.1038/s41586-019-1320-2.

[Bec05] Bechhoefer, J. "Feedback for Physicists: A Tutorial Essay on Control." *Rev. Mod. Phys.* 77, 3 (2005), pp. 783–836. DOI: 10.1103/RevModPhys.77.783.

[Bel95] Belavkin, V. P. "Quantum Filtering of Markov Signals with White Quantum Noise." In: *Quantum Communications and Measurement*. Ed. by Belavkin, V. P., Hirota, O., and Hudson, R. L. Boston, MA: Springer US, 1995, pp. 381–391. DOI: 10.1007/978-1-4899-1391-3_37.

[Bel+19] Belenchia, A., Mancino, L., Landi, G. T., and Paternostro, M. "Entropy Production in Continuously Measured Quantum Systems." *arXiv:1908.09382 [quant-ph]* (2019). arXiv: 1908.09382 [quant-ph].

[Ber+86] Bergquist, J. C., Hulet, R. G., Itano, W. M., and Wineland, D. J. "Observation of Quantum Jumps in a Single Atom." *Phys. Rev. Lett.* 57, 14 (1986), pp. 1699–1702. DOI: 10.1103/PhysRevLett.57.1699.

[Bia+11] Biancofiore, C., Karuza, M., Galassi, M., Natali, R., Tombesi, P., Di Giuseppe, G., and Vitali, D. "Quantum Dynamics of an Optical Cavity Coupled to a Thin Semitransparent Membrane: Effect of Membrane Absorption." *Phys. Rev. A* 84, 3 (2011), p. 033814. DOI: 10.1103/PhysRevA.84.033814.

[Bin+18] Binder, F., Correa, L. A., Gogolin, C., Anders, J., and Adesso, G., eds. *Thermodynamics in the Quantum Regime: Fundamental Aspects and New Directions*. Vol. 195. Fundamental Theories of Physics. Cham: Springer International Publishing, 2018. DOI: 10.1007/978-3-319-99046-0.

[Bla01] Black, E. D. "An Introduction to Pound–Drever–Hall Laser Frequency Stabilization." *Am. J. Phys.* 69, 1 (2001), pp. 79–87. DOI: 10.1119/1.1286663.

[Boc+13] Bochmann, J., Vainsencher, A., Awschalom, D. D., and Cleland, A. N. "Nanomechanical Coupling between Microwave and Optical Photons." *Nat. Phys.* 9, 11 (2013), pp. 712–716. DOI: 10.1038/nphys2748.

[BM16] Bowen, W. P. and Milburn, G. J. *Quantum Optomechanics*. Boca Raton: CRC Press, 2016.

[Bra68] Braginsky, V. B. "Classical and Quantum Restrictions on the Detection of Weak Disturbances of a Macroscopic Oscillator." *J. Exp. Theor. Phys.* 26, 4 (1968), pp. 831–834.

[BK92] Braginsky, V. B. and Khalili, F. Y. *Quantum Measurement*. Cambridge: Cambridge University Press, 1992.

[BM67] Braginsky, V. B. and Manukin, A. B. "Ponderomotive Effects of Electromagnetic Radiation." *J. Exp. Theor. Phys.* 25, 4 (1967), pp. 653–655.

[BMT70] Braginsky, V. B., Manukin, A. B., and Tikhonov, M. Y. "Investigation of Dissipative Ponderomotive Effects of Electromagnetic Radiation." *J. Exp. Theor. Phys.* 31, 5 (1970), pp. 829–830.

[BVT80] Braginsky, V. B., Vorontsov, Y. I., and Thorne, K. S. "Quantum Nondemolition Measurements." *Science* 209, 4456 (1980), pp. 547–557. DOI: 10.1126/science.209.4456.547.

[Bro+12] Brooks, D. W. C., Botter, T., Schreppler, S., Purdy, T. P., Brahms, N., and Stamper-Kurn, D. M. "Non-Classical Light Generated by Quantum-Noise-Driven Cavity Optomechanics." *Nature* 488, 7412 (2012), pp. 476–480. DOI: 10.1038/nature11325.

[Bru+20] Brunelli, M., Malz, D., Schliesser, A., and Nunnenkamp, A. "Stroboscopic Quantum Optomechanics." *Phys. Rev. Research* 2, 2 (2020), p. 023241. DOI: 10.1103/PhysRevResearch.2.023241.

[Buc+99] Buchler, B. C., Gray, M. B., Shaddock, D. A., Ralph, T. C., and McClelland, D. E. "Suppression of Classic and Quantum Radiation Pressure Noise by Electro-Optic Feedback." *Opt. Lett.* 24, 4 (1999), p. 259. DOI: 10.1364/OL.24.000259.

[Bus+06] Bushev, P., Rotter, D., Wilson, A., Dubin, F., Becher, C., Eschner, J., Blatt, R., Steixner, V., Rabl, P., and Zoller, P. "Feedback Cooling of a Single Trapped Ion." *Phys. Rev. Lett.* 96, 4 (2006), p. 043003. DOI: 10.1103/PhysRevLett.96.043003.

[Car87] Carmichael, H. J. "Spectrum of Squeezing and Photocurrent Shot Noise: A Normally Ordered Treatment." *J. Opt. Soc. Am. B* 4, 10 (1987), p. 1588. DOI: 10.1364/JOSAB.4.001588.

[Car93] Carmichael, H. *An Open Systems Approach to Quantum Optics: Lectures Presented at the Université Libre de Bruxelles October 28 to November 4, 1991*. Berlin, Heidelberg: Springer Berlin Heidelberg, 1993.

[CTS20] Catalini, L., Tsaturyan, Y., and Schliesser, A. "Soft-Clamped Phononic Dimers for Mechanical Sensing and Transduction." *Phys. Rev. Applied* 14, 1 (2020), p. 014041. DOI: 10.1103/PhysRevApplied.14.014041.

[Cav81] Caves, C. M. "Quantum-Mechanical Noise in an Interferometer." *Phys. Rev. D* 23, 8 (1981), pp. 1693–1708. DOI: 10.1103/PhysRevD.23.1693.

[Cha+11] Chan, J., Alegre, T. P. M., Safavi-Naeini, A. H., Hill, J. T., Krause, A., Gröblacher, S., Aspelmeyer, M., and Painter, O. "Laser Cooling of a Nanomechanical Oscillator into Its Quantum Ground State." *Nature* 478, 7367 (2011), pp. 89–92. DOI: 10.1038/nature10461.

[Cha+10] Chang, D. E., Regal, C. A., Papp, S. B., Wilson, D. J., Ye, J., Painter, O., Kimble, H. J., and Zoller, P. "Cavity Opto-Mechanics Using an Optically Levitated Nanosphere." *Proc. Natl. Acad. Sci. U.S.A.* 107, 3 (2010), pp. 1005–1010. DOI: 10.1073/pnas.0912969107.

[Che20] Chen, J. "Quantum Correlations Generated by a Soft-Clamped Membrane-in-the-Middle System." PhD thesis. Copenhagen: University of Copenhagen, 2020.

[Che+20] Chen, J., Rossi, M., Mason, D., and Schliesser, A. "Entanglement of Propagating Optical Modes via a Mechanical Interface." *Nat. Commun.* 11, 1 (2020), p. 943. DOI: 10.1038/s41467-020-14768-1.

[CL11] Cheung, H. K. and Law, C. K. "Nonadiabatic Optomechanical Hamiltonian of a Moving Dielectric Membrane in a Cavity." *Phys. Rev. A* 84, 2 (2011), p. 023812. DOI: 10.1103/PhysRevA.84.023812.

[Chu+18] Chu, Y., Kharel, P., Yoon, T., Frunzio, L., Rakich, P. T., and Schoelkopf, R. J. "Creation and Control of Multi-Phonon Fock States in a Bulk Acoustic-Wave Resonator." *Nature* 563, 7733 (2018), pp. 666–670. DOI: 10.1038/s41586-018-0717-7.

[Cia90] Ciarlet, P. G. *Plates and Junctions in Elastic Multi-Structures. An Asymptotic Analysis*. Recherches En Mathématiques Appliquées 14. Masson, Springer-Verlag, 1990.

[Cia80] Ciarlet, P. G. "A Justification of the von Kármán Equations." *Arch. Rational Mech. Anal.* 73, 4 (1980), pp. 349–389. DOI: 10.1007/BF00247674.

[Cle04] Clerk, A. A. "Quantum-Limited Position Detection and Amplification: A Linear Response Perspective." *Phys. Rev. B* 70, 24 (2004), p. 245306. DOI: 10.1103/PhysRevB.70.245306.

[CMJ08] Clerk, A. A., Marquardt, F, and Jacobs, K. "Back-Action Evasion and Squeezing of a Mechanical Resonator Using a Cavity Detector." *New J. Phys.* 10, 9 (2008), p. 095010. DOI: 10.1088/1367-2630/10/9/095010.

[Cle+10] Clerk, A. A., Devoret, M. H., Girvin, S. M., Marquardt, F., and Schoelkopf, R. J. "Introduction to Quantum Noise, Measurement, and Amplification." *Rev. Mod. Phys.* 82, 2 (2010), pp. 1155–1208. DOI: 10.1103/RevModPhys.82.1155.

[Cle13] Clerk, A. A. "Quantum Noise and Quantum Measurement (Les Houches Lecture Notes)." In: *Quantum Machines: Measurement and Control of Engineered Quantum Systems*. Ed. by Devoret, M. H., Huard, B., Schoelkopf, R. J., and Cugliandolo, L. F. Oxford University Press, 2013.

[CHP99] Cohadon, P. F., Heidmann, A., and Pinard, M. "Cooling of a Mirror by Radiation Pressure." *Phys. Rev. Lett.* 83, 16 (1999), pp. 3174–3177. DOI: 10.1103/PhysRevLett.83.3174.

[CM04] Corbitt, T. and Mavalvala, N. "Review: Quantum Noise in Gravitational-Wave Interferometers." *J. Opt. B: Quantum Semiclass. Opt.* 6, 8 (2004), S675–S683. DOI: 10.1088/1464-4266/6/8/008.

[CHP01] Courty, J.-M., Heidmann, A., and Pinard, M. "Quantum Limits of Cold Damping with Optomechanical Coupling." *Eur. Phys. J. D* 17, 3 (2001), pp. 399–408. DOI: 10.1007/s100530170014.

[DMS07] D'Ariano, G. M., Maccone, L., and Sacchi, M. F. "Homodyne Tomography and the Reconstruction of Quantum States of Light." In: *Quantum Information with Continous Variables of Atoms and Light*. Ed. by Cerf, N. J., Leuchs, G., and Polzik, E. S. Imperial College Press, 2007.

[Dió88] Diósi, L. "Continuous Quantum Measurement and Itô Formalism." *Phys. Lett. A* 129, 8-9 (1988), pp. 419–423. DOI: 10.1016/0375-9601(88)90309-X.

[DJ99] Doherty, A. C. and Jacobs, K. "Feedback Control of Quantum Systems Using Continuous State Estimation." *Phys. Rev. A* 60, 4 (1999), pp. 2700–2711. DOI: 10.1103/PhysRevA.60.2700.

[Doh+99] Doherty, A. C., Tan, S. M., Parkins, A. S., and Walls, D. F. "State Determination in Continuous Measurement." *Phys. Rev. A* 60, 3 (1999), pp. 2380–2392. DOI: 10.1103/PhysRevA.60.2380.

[Doh+12] Doherty, A. C., Szorkovszky, A., Harris, G. I., and Bowen, W. P. "The Quantum Trajectory Approach to Quantum Feedback Control of an Oscillator Revisited." *Philos. Trans. Royal Soc. A* 370, 1979 (2012), pp. 5338–5353. DOI: 10.1098/rsta.2011.0531.

[Doh+00] Doherty, A. C., Habib, S., Jacobs, K., Mabuchi, H., and Tan, S. M. "Quantum Feedback Control and Classical Control Theory." *Phys. Rev. A* 62, 1 (2000), p. 012105. DOI: 10.1103/PhysRevA.62.012105.

[Dua+00] Duan, L.-M., Giedke, G, Cirac, J. I., and Zoller, P. "Inseparability Criterion for Continuous Variable Systems." *Phys. Rev. Lett.* 84, 12 (2000), pp. 2722–2725.

[Dum+19] Dumont, V., Bernard, S., Reinhardt, C., Kato, A., Ruf, M., and Sankey, J. C. "Flexure-Tuned Membrane-at-the-Edge Optomechanical System." *Opt. Express* 27, 18 (2019), p. 25731. DOI: 10.1364/OE.27.025731.

[Eic+09] Eichenfield, M., Camacho, R., Chan, J., Vahala, K. J., and Painter, O. "A Picogram- and Nanometre-Scale Photonic-Crystal Optomechanical Cavity." *Nature* 459, 7246 (2009), pp. 550–555. DOI: 10.1038/nature08061.

[Fab+94] Fabre, C., Pinard, M., Bourzeix, S., Heidmann, A., Giacobino, E., and Reynaud, S. "Quantum-Noise Reduction Using a Cavity with a Movable Mirror." *Phys. Rev. A* 49, 2 (1994), pp. 1337–1343. DOI: 10.1103/PhysRevA.49.1337.

[Fed+20] Fedorov, S. A., Beccari, A., Arabmoheghi, A., Wilson, D. J., Engelsen, N. J., and Kippenberg, T. J. "Thermal Intermodulation Noise in Cavity-Based Measurements." *arXiv:2004.05700 [physics, physics:quant-ph]* (2020). arXiv: 2004.05700 [physics, physics:quant-ph].

[Fis+16] Fischer, R., Kampel, N. S., Assumpção, G. G. T., Yu, P.-L., Cicak, K., Peterson, R. W., Simmonds, R. W., and Regal, C. A. "Optical Probing of Mechanical Loss of a Si_{3}N_{4} Membrane below 100 mK." *arXiv:1611.00878 [cond-mat, physics:physics]* (2016). arXiv: 1611.00878 [cond-mat, physics:physics].

[For+20] Forsch, M., Stockill, R., Wallucks, A., Marinković, I., Gärtner, C., Norte, R. A., van Otten, F., Fiore, A., Srinivasan, K., and Gröblacher, S. "Microwave-to-Optics Conversion Using a Mechanical Oscillator in Its Quantum Ground State." *Nat. Phys.* 16, 1 (2020), pp. 69–74. DOI: 10.1038/s41567-019-0673-7.

[Fow89] Fowles, G. R. *Introduction to Modern Optics*. 2nd ed., Dover ed. New York: Dover Publications, 1989.

[Fto+15] Ftouni, H., Blanc, C., Tainoff, D., Fefferman, A. D., Defoort, M., Lulla, K. J., Richard, J., Collin, E., and Bourgeois, O. "Thermal Conductivity of Silicon Nitride Membranes Is Not Sensitive to Stress." *Phys. Rev. B* 92, 12 (2015), p. 125439. DOI: 10.1103/PhysRevB.92.125439.

[Gal+91] Galatola, P., Lugiato, L., Porreca, M., Tombesi, P., and Leuchs, G. "System Control by Variation of the Squeezing Phase." *Opt. Commun.* 85, 1 (1991), pp. 95–103. DOI: 10.1016/0030-4018(91)90056-J.

[GJM13] Gammelmark, S., Julsgaard, B., and Mølmer, K. "Past Quantum States of a Monitored System." *Phys. Rev. Lett.* 111, 16 (2013), p. 160401. DOI: 10.1103/PhysRevLett.111.160401.

[Gar+96] Garbini, J. L., Bruland, K. J., Dougherty, W. M., and Sidles, J. A. "Optimal Control of Force Microscope Cantilevers. I. Controller Design." *J. Appl. Phys.* 80, 4 (1996), pp. 1951–1958. DOI: 10.1063/1.363085.

[GZ04] Gardiner, C. W. and Zoller, P. *Quantum Noise: A Handbook of Markovian and Non-Markovian Quantum Stochastic Methods with Applications to Quantum Optics*. 3rd ed. Springer Series in Synergetics. Berlin ; New York: Springer, 2004.

[GVK12] Gavartin, E., Verlot, P., and Kippenberg, T. J. "A Hybrid On-Chip Optomechanical Transducer for Ultrasensitive Force Measurements." *Nat. Nanotechnol.* 7, 8 (2012), pp. 509–514. DOI: 10.1038/nnano.2012.97.

[Gen+08a] Genes, C., Vitali, D., Tombesi, P., Gigan, S., and Aspelmeyer, M. "Ground-State Cooling of a Micromechanical Oscillator: Comparing Cold Damping and Cavity-Assisted Cooling Schemes." *Phys. Rev. A* 77, 3 (2008), p. 033804. DOI: 10.1103/PhysRevA.77.033804.

[Gen+08b] Genes, C., Mari, A., Tombesi, P., and Vitali, D. "Robust Entanglement of a Micromechanical Resonator with Output Optical Fields." *Phys. Rev. A* 78, 3 (2008), p. 032316. DOI: 10.1103/PhysRevA.78.032316.

[GLS16] Genoni, M. G., Lami, L., and Serafini, A. "Conditional and Unconditional Gaussian Quantum Dynamics." *Contemp. Phys.* 57, 3 (2016), pp. 331–349. DOI: 10.1080/00107514.2015.1125624.

[Gha+18] Ghadimi, A. H., Fedorov, S. A., Engelsen, N. J., Bereyhi, M. J., Schilling, R., Wilson, D. J., and Kippenberg, T. J. "Elastic Strain Engineering for Ultralow Mechanical Dissipation." *Science* 360, 6390 (2018), pp. 764–768. DOI: 10.1126/science.aar6939.

[GMT03] Giannini, S., Mancini, S., and Tombesi, P. "Information Theoretic Aspects in Ponderomotive Systems." *Quantum Inf. Comput.* 3 (2003), pp. 265–279.

[Gio04] Giovannetti, V. "Quantum-Enhanced Measurements: Beating the Standard Quantum Limit." *Science* 306, 5700 (2004), pp. 1330–1336. DOI: 10.1126/science.1104149.

[GMT01] Giovannetti, V, Mancini, S, and Tombesi, P. "Radiation Pressure Induced Einstein-Podolsky-Rosen Paradox." *Europhys. Lett.* 54, 5 (2001), pp. 559–565. DOI: 10.1209/epl/i2001-00284-x.

[GV01] Giovannetti, V. and Vitali, D. "Phase-Noise Measurement in a Cavity with a Movable Mirror Undergoing Quantum Brownian Motion." *Phys. Rev. A* 63, 2 (2001), p. 023812. DOI: 10.1103/PhysRevA.63.023812.

[Gio+03] Giovannetti, V., Mancini, S., Vitali, D., and Tombesi, P. "Characterizing the Entanglement of Bipartite Quantum Systems." *Phys. Rev. A* 67, 2 (2003), p. 022320. DOI: 10.1103/PhysRevA.67.022320.

[Gla63] Glauber, R. J. "The Quantum Theory of Optical Coherence." *Phys. Rev.* 130, 6 (1963), pp. 2529–2539. DOI: 10.1103/PhysRev.130.2529.

[Gor+10] Gorodetsky, M. L., Schliesser, A., Anetsberger, G., Deleglise, S., and Kippenberg, T. J. "Determination of the Vacuum Optomechanical Coupling Rate Using Frequency Noise Calibration." *Opt. Express* 18, 22 (2010), p. 23236. DOI: 10.1364/OE.18.023236.

[Gue+07] Guerlin, C., Bernu, J., Deléglise, S., Sayrin, C., Gleyzes, S., Kuhr, S., Brune, M., Raimond, J.-M., and Haroche, S. "Progressive Field-State Collapse and Quantum Non-Demolition Photon Counting." *Nature* 448, 7156 (2007), pp. 889–893. DOI: 10.1038/nature06057.

[Gut+19] Gut, C. et al. "Stationary Optomechanical Entanglement between a Mechanical Oscillator and Its Measurement Apparatus." *arXiv:1912.01635 [cond-mat, physics:quant-ph]* (2019). arXiv: 1912.01635 [cond-mat, physics:quant-ph].

[Hab+16] Habibi, H., Zeuthen, E., Ghanaatshoar, M., and Hammerer, K. "Quantum Feedback Cooling of a Mechanical Oscillator Using Variational Measurements: Tweaking Heisenberg's Microscope." *J. Opt.* 18, 8 (2016), p. 084004. DOI: 10.1088/2040-8978/18/8/084004.

[Hei27] Heisenberg, W. "Über den anschaulichen Inhalt der quantentheoretischen Kinematik und Mechanik." *Z. Physik* 43, 3-4 (1927), pp. 172–198. DOI: 10.1007/BF01397280.

[Hei50] Heisenberg, W. *The Physical Principles of the Quantum Theory*. New York: Dover Publications, 1950.

[Hig+18] Higginbotham, A. P., Burns, P. S., Urmey, M. D., Peterson, R. W., Kampel, N. S., Brubaker, B. M., Smith, G., Lehnert, K. W., and Regal, C. A. "Harnessing Electro-Optic Correlations in an Efficient Mechanical Converter." *Nat.*

*Phys.* 14, 10 (2018), pp. 1038–1042. DOI: 10.1038/s41567-018-0210-0.

[Hoe17] Hoelscher-Obermaier, J. "Generation and Detection of Quantum Entanglement in Optomechanical Systems." PhD thesis. Vienna: University of Vienna, 2017.

[Hof17] Hofer, S. G. "Quantum Control of Optomechanical Systems." PhD thesis. Elsevier, 2017. DOI: 10.1016/bs.aamop.2017.03.003.

[HH15] Hofer, S. G. and Hammerer, K. "Entanglement-Enhanced Time-Continuous Quantum Control in Optomechanics." *Phys. Rev. A* 91, 3 (2015), p. 033822. DOI: 10.1103/PhysRevA.91.033822.

[Hof+11] Hofer, S. G., Wieczorek, W., Aspelmeyer, M., and Hammerer, K. "Quantum Entanglement and Teleportation in Pulsed Cavity Optomechanics." *Phys. Rev. A* 84, 5 (2011), p. 052327. DOI: 10.1103/PhysRevA.84.052327.

[Hof+13] Hofer, S. G., Vasilyev, D. V., Aspelmeyer, M., and Hammerer, K. "Time-Continuous Bell Measurements." *Phys. Rev. Lett.* 111, 17 (2013), p. 170404. DOI: 10.1103/PhysRevLett.111.170404.

[Hor+09] Horodecki, R., Horodecki, P., Horodecki, M., and Horodecki, K. "Quantum Entanglement." *Rev. Mod. Phys.* 81, 2 (2009), pp. 865–942. DOI: 10.1103/RevModPhys.81.865.

[HS98] Huang, Y. L. and Saulson, P. R. "Dissipation Mechanisms in Pendulums and Their Implications for Gravitational Wave Interferometers." *Rev. Sci. Intrum.* 69, 2 (1998), pp. 544–553. DOI: 10.1063/1.1148692.

[HE06] Hyllus, P. and Eisert, J. "Optimal Entanglement Witnesses for Continuous-Variable Systems." *New J. Phys.* 8, 4 (2006), pp. 51–51. DOI: 10.1088/1367-2630/8/4/051.

[Jac14] Jacobs, K. *Quantum Measurement Theory and Its Applications*. Cambridge ; New York: Cambridge University Press, 2014.

[JS06] Jacobs, K. and Steck, D. A. "A Straightforward Introduction to Continuous Quantum Measurement." *Contemp. Phys.* 47, 5 (2006), pp. 279–303. DOI: 10.1080/00107510601101934.

[Jay+08] Jayich, A. M., Sankey, J. C., Zwickl, B. M., Yang, C, Thompson, J. D., Girvin, S. M., Clerk, A. A., Marquardt, F, and Harris, J. G. E. "Dispersive Optomechanics: A Membrane inside a Cavity." *New J. Phys.* 10, 9 (2008), p. 095008. DOI: 10.1088/1367-2630/10/9/095008.

[Jay+12] Jayich, A. M., Sankey, J. C., Børkje, K, Lee, D, Yang, C, Underwood, M, Childress, L, Petrenko, A, Girvin, S. M., and Harris, J. G. E. "Cryogenic Optomechanics with a Si $_3$ N $_4$ Membrane and Classical Laser Noise." *New J. Phys.* 14, 11 (2012), p. 115018. DOI: 10.1088/1367-2630/14/11/115018.

[Kai82] Kailath, T. *Lectures on Wiener and Kalman Filtering*. (International Centre for Mechanical Sciences. Courses and Lectures 140). Wien: Springer, 1982.

[Kam+17] Kampel, N. S., Peterson, R. W., Fischer, R., Yu, P.-L., Cicak, K., Simmonds, R. W., Lehnert, K. W., and Regal, C. A. "Improving Broadband Displacement Detection with Quantum Correlations." *Phys. Rev. X* 7, 2 (2017), p. 021008. DOI: 10.1103/PhysRevX.7.021008.

[KK64] Kelley, P. L. and Kleiner, W. H. "Theory of Electromagnetic Field Measurement and Photoelectron Counting." *Phys. Rev.* 136, 2A (1964), A316–A334. DOI: 10.1103/PhysRev.136.A316.

[Kim08] Kimble, H. J. "The Quantum Internet." *Nature* 453, 7198 (2008), pp. 1023–1030. DOI: 10.1038/nature07127.

[Kim+01] Kimble, H. J., Levin, Y., Matsko, A. B., Thorne, K. S., and Vyatchanin, S. P. "Conversion of Conventional Gravitational-Wave Interferometers into Quantum Nondemolition Interferometers by Modifying Their Input and/or Output Optics." *Phys. Rev. D* 65, 2 (2001), p. 022002. DOI: 10.1103/PhysRevD.65.022002.

[KB06] Kleckner, D. and Bouwmeester, D. "Sub-Kelvin Optical Cooling of a Micromechanical Resonator." *Nature* 444, 7115 (2006), pp. 75–78. DOI: 10.1038/nature05231.

[Kub+09] Kubanek, A., Koch, M., Sames, C., Ourjoumtsev, A., Pinkse, P. W. H., Murr, K., and Rempe, G. "Photon-by-Photon Feedback Control of a Single-Atom Trajectory." *Nature* 462, 7275 (2009), pp. 898–901. DOI: 10.1038/nature08563.

[Kur+15] Kurizki, G., Bertet, P., Kubo, Y., Mølmer, K., Petrosyan, D., Rabl, P., and Schmiedmayer, J. "Quantum Technologies with Hybrid Systems." *Proc. Natl. Acad. Sci. U.S.A.* 112, 13 (2015), pp. 3866–3873. DOI: 10.1073/pnas.1419326112.

[LaH+04] LaHaye, M. D., Buu, O., Camarota, B., and Schwab, K. C. "Approaching the Quantum Limit of a Nanomechanical Resonator." *Science* 304, 5667 (2004), pp. 74–77. DOI: 10.1126/science.1094419.

[Lam18] Lammers, J. "State Preparation and Verification in Continuously Measured Quantum Systems." PhD thesis. Hannover: Leibniz Universität, 2018.

[LL08] Landau, L. D. and Lifšic, E. M. *Theory of Elasticity*. ed. 3. Course of Theoretical Physics Vol. 7. Amsterdam: Elsevier, 2008.

[LLP08] Landau, L. D., Lifšic, E. M., and Pitaevskij, L. P. *Statistical Physics, Part 1*. ed. 3. Course of Theoretical Physics Vol. 5. Amsterdam: Elsevier, 2008.

[Law95] Law, C. K. "Interaction between a Moving Mirror and Radiation Pressure: A Hamiltonian Formulation." *Phys. Rev. A* 51, 3 (1995), pp. 2537–2541. DOI: 10.1103/PhysRevA.51.2537.

[Lec+15] Lecocq, F., Clark, J. B., Simmonds, R. W., Aumentado, J., and Teufel, J. D. "Quantum Nondemolition Measurement of a Nonclassical State of a Massive Object." *Phys. Rev. X* 5, 4 (2015), p. 041037. DOI: 10.1103/PhysRevX.5.041037.

[Lee+11] Lee, K. C. et al. "Entangling Macroscopic Diamonds at Room Temperature." *Science* 334, 6060 (2011), pp. 1253–1256. DOI: 10.1126/science.1211914.

[Lee+10] Lee, K. H., McRae, T. G., Harris, G. I., Knittel, J., and Bowen, W. P. "Cooling and Control of a Cavity Optoelectromechanical System." *Phys. Rev. Lett.* 104, 12 (2010), p. 123604. DOI: 10.1103/PhysRevLett.104.123604.

[LP98] Leivo, M. M. and Pekola, J. P. "Thermal Characteristics of Silicon Nitride Membranes at Sub-Kelvin Temperatures." *Appl. Phys. Lett.* 72, 11 (1998), pp. 1305–1307. DOI: 10.1063/1.120979.

[LKR11] Li, T., Kheifets, S., and Raizen, M. G. "Millikelvin Cooling of an Optically Trapped Microsphere in Vacuum." *Nat. Phys.* 7, 7 (2011), pp. 527–530. DOI: 10.1038/nphys1952.

[LR00] Lifshitz, R. and Roukes, M. L. "Thermoelastic Damping in Micro- and Nanomechanical Systems." *Phys. Rev. B* 61, 8 (2000), pp. 5600–5609. DOI: 10.1103/PhysRevB.61.5600.

[Lvo15] Lvovsky, A. I. "Squeezed Light." In: *Photonics, Volume 1: Fundamentals of Photonics and Physics*. Ed. by Andrews, D. Vol. 1. West Sussex, UK: Wiley, 2015, pp. 121–164.

[Ma+14] Ma, Y., Danilishin, S. L., Zhao, C., Miao, H., Korth, W. Z., Chen, Y., Ward, R. L., and Blair, D. G. "Narrowing the Filter-Cavity Bandwidth in Gravitational-Wave Detectors via Optomechanical Interaction." *Phys. Rev. Lett.* 113, 15 (2014), p. 151102. DOI: 10.1103/PhysRevLett.113.151102.

[MK06] Maassen, H. and Kümmerer, B. "Purification of Quantum Trajectories." In: *Institute of Mathematical Statistics Lecture Notes - Monograph Series*. Beachwood, Ohio, USA: Institute of Mathematical Statistics, 2006, pp. 252–261. DOI: 10.1214/lnms/1196285826.

[Mal13] Maldovan, M. "Sound and Heat Revolutions in Phononics." *Nature* 503, 7475 (2013), pp. 209–217. DOI: 10.1038/nature12608.

[MT94] Mancini, S. and Tombesi, P. "Quantum Noise Reduction by Radiation Pressure." *Phys. Rev. A* 49, 5 (1994), pp. 4055–4065. DOI: 10.1103/PhysRevA.49.4055.

[MVT98] Mancini, S., Vitali, D., and Tombesi, P. "Optomechanical Cooling of a Macroscopic Oscillator by Homodyne Feedback." *Phys. Rev. Lett.* 80, 4 (1998), pp. 688–691. DOI: 10.1103/PhysRevLett.80.688.

[Mar+07] Marquardt, F., Chen, J. P., Clerk, A. A., and Girvin, S. M. "Quantum Theory of Cavity-Assisted Sideband Cooling of Mechanical Motion." *Phys. Rev. Lett.* 99, 9 (2007), p. 093902. DOI: 10.1103/PhysRevLett.99.093902.

[Mar+16] Martynov, D. V. et al. "Sensitivity of the Advanced LIGO Detectors at the Beginning of Gravitational Wave Astronomy." *Phys. Rev. D* 93, 11 (2016), p. 112004. DOI: 10.1103/PhysRevD.93.112004.

[Mas+19] Mason, D., Chen, J., Rossi, M., Tsaturyan, Y., and Schliesser, A. "Continuous Force and Displacement Measurement below the Standard Quantum Limit." *Nat. Phys.* 15, 8 (2019), pp. 745–749. DOI: 10.1038/s41567-019-0533-5.

[Mat19] Mathiassen, J. B. "Characterising and Modelling Thermal Substrate Noise for a Membrane in the Middle Optomechanical Cavity." PhD thesis. Copenhagen: University of Copenhagen, 2019.

[McC+20] McCuller, L. et al. "Frequency-Dependent Squeezing for Advanced LIGO." *Phys. Rev. Lett.* 124, 17 (2020), p. 171102. DOI: 10.1103/PhysRevLett.124.171102.

[Men+20] Meng, C., Brawley, G. A., Bennett, J. S., Vanner, M. R., and Bowen, W. P. "Mechanical Squeezing via Fast Continuous Measurement." *arXiv:1911.06412 [cond-mat, physics:physics, physics:quant-ph]* (2020). arXiv: 1911.06412 [cond-mat, physics:physics, physics:quant-ph].

[Mia+15] Miao, H., Ma, Y., Zhao, C., and Chen, Y. "Enhancing the Bandwidth of Gravitational-Wave Detectors with Unstable Optomechanical Filters." *Phys. Rev. Lett.* 115, 21 (2015), p. 211104. DOI: 10.1103/PhysRevLett.115.211104.

[Mur+13] Murch, K. W., Weber, S. J., Macklin, C., and Siddiqi, I. "Observing Single Quantum Trajectories of a Superconducting Quantum Bit." *Nature* 502, 7470 (2013), pp. 211–214. DOI: 10.1038/nature12539.

[NSD86] Nagourney, W., Sandberg, J., and Dehmelt, H. "Shelved Optical Electron Amplifier: Observation of Quantum Jumps." *Phys. Rev. Lett.* 56, 26 (1986), pp. 2797–2799. DOI: 10.1103/PhysRevLett.56.2797.

[Neu+17] Neuhaus, L., Metzdorff, R., Chua, S., Jacqmin, T., Briant, T., Heidmann, A., Cohadon, P.-F., and Deleglise, S. "PyRPL (Python Red Pitaya Lockbox) — An Open-Source Software Package for FPGA-Controlled Quantum Optics Experiments." In: *2017 Conference on Lasers and Electro-Optics Europe & European Quantum Electronics Conference (CLEO/Europe-EQEC)*. Munich, Germany: IEEE, 2017, pp. 1–1. DOI: 10.1109/CLEOE-EQEC.2017.8087380.

[NW18] Neumann, J. von and Wheeler, N. A. *Mathematical Foundations of Quantum Mechanics*. 2018.

[Nie16] Nielsen, W. H. P. "Quantum Cavity Optomechanics with Phononic Bandgap Shielded Silicon Nitride Membranes." PhD thesis. 2016.

[Nie+17] Nielsen, W. H. P., Tsaturyan, Y., Møller, C. B., Polzik, E. S., and Schliesser, A. "Multimode Optomechanical System in the Quantum Regime." *Proc. Natl. Acad. Sci. U.S.A.* 114, 1 (2017), pp. 62–66. DOI: 10.1073/pnas.1608412114.

[NJP09] Nurdin, H. I., James, M. R., and Petersen, I. R. "Coherent Quantum LQG Control." *Automatica* 45, 8 (2009), pp. 1837–1846. DOI: 10.1016/j.automatica.2009.04.018.

[O'C+10] O'Connell, A. D. et al. "Quantum Ground State and Single-Phonon Control of a Mechanical Resonator." *Nature* 464, 7289 (2010), pp. 697–703. DOI: 10.1038/nature08967.

[Ock+18] Ockeloen-Korppi, C. F., Damskägg, E., Pirkkalainen, J.-M., Asjad, M., Clerk, A. A., Massel, F., Woolley, M. J., and Sillanpää, M. A. "Stabilized Entanglement of Massive Mechanical Oscillators." *Nature* 556, 7702 (2018), pp. 478–482. DOI: 10.1038/s41586-018-0038-x.

[Pag+20] Page, M. A. et al. "Gravitational Wave Detectors with Broadband High Frequency Sensitivity." *arXiv:2007.08766 [astro-ph, physics:physics]* (2020). arXiv: 2007.08766 [astro-ph, physics:physics].

[Pal+13] Palomaki, T. A., Teufel, J. D., Simmonds, R. W., and Lehnert, K. W. "Entangling Mechanical Motion with Microwave Fields." *Science* 342, 6159 (2013), pp. 710–713. DOI: 10.1126/science.1244563.

[PHS15] Parrondo, J. M. R., Horowitz, J. M., and Sagawa, T. "Thermodynamics of Information." *Nat. Phys.* 11, 2 (2015), pp. 131–139. DOI: 10.1038/nphys3230.

[Pet+16] Peterson, R. W., Purdy, T. P., Kampel, N. S., Andrews, R. W., Yu, P.-L., Lehnert, K. W., and Regal, C. A. "Laser Cooling of a Micromechanical Membrane to the Quantum Backaction Limit." *Phys. Rev. Lett.* 116, 6 (2016), p. 063601. DOI: 10.1103/PhysRevLett.116.063601.

[Phi87] Phillips, W. A. "Two-Level States in Glasses." *Rep. Prog. Phys.* 50, 12 (1987), pp. 1657–1708. DOI: 10.1088/0034-4885/50/12/003.

[PD10] Poggio, M. and Degen, C. L. "Force-Detected Nuclear Magnetic Resonance: Recent Advances and Future Challenges." *Nanotechnology* 21, 34 (2010), p. 342001. DOI: 10.1088/0957-4484/21/34/342001.

[Pog+07] Poggio, M., Degen, C. L., Mamin, H. J., and Rugar, D. "Feedback Cooling of a Cantilever's Fundamental Mode below 5 mK." *Phys. Rev. Lett.* 99, 1 (2007), p. 017201. DOI: 10.1103/PhysRevLett.99.017201.

[PM07] Proakis, J. G. and Manolakis, D. G. *Digital Signal Processing*. 4th ed. Upper Saddle River, N.J: Pearson Prentice Hall, 2007.

[PPR13] Purdy, T. P., Peterson, R. W., and Regal, C. A. "Observation of Radiation Pressure Shot Noise on a Macroscopic Object." *Science* 339, 6121 (2013), pp. 801–804. DOI: 10.1126/science.1231282.

[Pur+13] Purdy, T. P., Yu, P.-L., Peterson, R. W., Kampel, N. S., and Regal, C. A. "Strong Optomechanical Squeezing of Light." *Phys. Rev. X* 3, 3 (2013), p. 031012. DOI: 10.1103/PhysRevX.3.031012.

[Pur+17] Purdy, T. P., Grutter, K. E., Srinivasan, K., and Taylor, J. M. "Quantum Correlations from a Room-Temperature Optomechanical Cavity." *Science* 356, 6344 (2017), pp. 1265–1268. DOI: 10.1126/science.aag1407.

[Rie+18] Riedinger, R., Wallucks, A., Marinković, I., Löschnauer, C., Aspelmeyer, M., Hong, S., and Gröblacher, S. "Remote Quantum Entanglement between Two Micromechanical Oscillators." *Nature* 556, 7702 (2018), pp. 473–477. DOI: 10.1038/s41586-018-0036-z.

[Rin+18] Ringbauer, M, Weinhold, T. J., Howard, L. A., White, A. G., and Vanner, M. R. "Generation of Mechanical Interference Fringes by Multi-Photon Counting." *New J. Phys.* 20, 5 (2018), p. 053042. DOI: 10.1088/1367-2630/aabb8d.

[RB04] Rogalski, A and Bielecki, Z. "Detection of Optical Radiation." *Bull. Pol. Ac.: Tech.* 52, 1 (2004), pp. 43–66.

[Ros+18] Rossi, M., Mason, D., Chen, J., Tsaturyan, Y., and Schliesser, A. "Measurement-Based Quantum Control of Mechanical Motion." *Nature* 563, 7729 (2018), pp. 53–58. DOI: 10.1038/s41586-018-0643-8.

[Ros+19] Rossi, M., Mason, D., Chen, J., and Schliesser, A. "Observing and Verifying the Quantum Trajectory of a Mechanical Resonator." *Phys. Rev. Lett.* 123, 16 (2019), p. 163601. DOI: 10.1103/PhysRevLett.123.163601.

[Ros+20] Rossi, M., Mancino, L., Landi, G. T., Paternostro, M., Schliesser, A., and Belenchia, A. "Experimental Assessment of Entropy Production in a Continuously Measured Mechanical Resonator." *arXiv:2005.03429 [cond-mat, physics:quant-ph]* (2020). arXiv: 2005.03429 [cond-mat, physics:quant-ph].

[Saf+13] Safavi-Naeini, A. H., Gröblacher, S., Hill, J. T., Chan, J., Aspelmeyer, M., and Painter, O. "Squeezed Light from a Silicon Micromechanical Resonator." *Nature* 500, 7461 (2013), pp. 185–189. DOI: 10.1038/nature12307.

[SU09] Sagawa, T. and Ueda, M. "Minimal Energy Cost for Thermodynamic Information Processing: Measurement and Information Erasure." *Phys. Rev. Lett.* 102, 25 (2009), p. 250602. DOI: 10.1103/PhysRevLett.102.250602.

[Say+11] Sayrin, C. et al. "Real-Time Quantum Feedback Prepares and Stabilizes Photon Number States." *Nature* 477, 7362 (2011), pp. 73–77. DOI: 10.1038/nature10376.

[SVR16] Schmid, S., Villanueva, L. G., and Roukes, M. L. *Fundamentals of Nanomechanical Resonators*. Cham: Springer International Publishing, 2016. DOI: 10.1007/978-3-319-28691-4.

[Sch+14] Schreppler, S., Spethmann, N., Brahms, N., Botter, T., Barrios, M., and Stamper-Kurn, D. M. "Optically Measuring Force near the Standard Quantum Limit." *Science* 344, 6191 (2014), pp. 1486–1489. DOI: 10.1126/science.1249850.

[Sch+87] Schumaker, B. L., Perlmutter, S. H., Shelby, R. M., and Levenson, M. D. "Four-Mode Squeezing." *Phys. Rev. Lett.* 58, 4 (1987), pp. 357–360. DOI: 10.1103/PhysRevLett.58.357.

[Sha+87] Shapiro, J. H., Kumar, P., Saleh, B. E. A., Teich, M. C., Saplakoglu, G., and Ho, S.-T. "Theory of Light Detection in the Presence of Feedback." *J. Opt. Soc. Am. B* 4, 10 (1987), p. 1604. DOI: 10.1364/JOSAB.4.001604.

[Sud+17] Sudhir, V., Schilling, R., Fedorov, S. A., Schütz, H., Wilson, D. J., and Kippenberg, T. J. "Quantum Correlations of Light from a Room-Temperature Mechanical Oscillator." *Phys. Rev. X* 7, 3 (2017), p. 031055. DOI: 10.1103/PhysRevX.7.031055.

[Suh+14] Suh, J., Weinstein, A. J., Lei, C. U., Wollman, E. E., Steinke, S. K., Meystre, P., Clerk, A. A., and Schwab, K. C. "Mechanically Detecting and Avoiding the Quantum Fluctuations of a Microwave Field." *Science* 344, 6189 (2014), pp. 1262–1265. DOI: 10.1126/science.1253258.

[Tan+15] Tan, D., Weber, S. J., Siddiqi, I., Mølmer, K., and Murch, K. W. "Prediction and Retrodiction for a Continuously Monitored Superconducting Qubit." *Phys. Rev. Lett.* 114, 9 (2015), p. 090403. DOI: 10.1103/PhysRevLett.114.090403.

[Teb+20] Tebbenjohanns, F., Frimmer, M., Jain, V., Windey, D., and Novotny, L. "Motional Sideband Asymmetry of a Nanoparticle Optically Levitated in Free Space." *Phys. Rev. Lett.* 124, 1 (2020), p. 013603. DOI: 10.1103/PhysRevLett.124.013603.

[Teu+11] Teufel, J. D., Donner, T., Li, D., Harlow, J. W., Allman, M. S., Cicak, K., Sirois, A. J., Whittaker, J. D., Lehnert, K. W., and Simmonds, R. W. "Sideband Cooling of Micromechanical Motion to the Quantum Ground State." *Nature* 475, 7356 (2011), pp. 359–363. DOI: 10.1038/nature10261.

[Tho+08] Thompson, J. D., Zwickl, B. M., Jayich, A. M., Marquardt, F., Girvin, S. M., and Harris, J. G. E. "Strong Dispersive Coupling of a High-Finesse Cavity to a Micromechanical Membrane." *Nature* 452, 7183 (2008), pp. 72–75. DOI: 10.1038/nature06715.

[Tsa19] Tsaturyan, Y. "Ultracoherent Soft-Clamped Mechanical Resonators for Quantum Cavity Optomechanics." PhD thesis. Copenhagen: University of Copenhagen, 2019.

[Tsa+17] Tsaturyan, Y., Barg, A., Polzik, E. S., and Schliesser, A. "Ultracoherent Nanomechanical Resonators via Soft Clamping and Dissipation Dilution." *Nat. Nanotechnol.* 12, 8 (2017), pp. 776–783. DOI: 10.1038/nnano.2017.101.

[Tse+19] Tse, M. et al. "Quantum-Enhanced Advanced LIGO Detectors in the Era of Gravitational-Wave Astronomy." *Phys. Rev. Lett.* 123, 23 (2019), p. 231107. DOI: 10.1103/PhysRevLett.123.231107.

[TR17] Tserkis, S. and Ralph, T. C. "Quantifying Entanglement in Two-Mode Gaussian States." *Phys. Rev. A* 96, 6 (2017), p. 062338. DOI: 10.1103/PhysRevA.96.062338.

[Van+13] Vanner, M. R., Hofer, J., Cole, G. D., and Aspelmeyer, M. "Cooling-by-Measurement and Mechanical State Tomography via Pulsed Optomechanics." *Nat. Commun.* 4, 1 (2013), p. 2295. DOI: 10.1038/ncomms3295.

[Vij+12] Vijay, R., Macklin, C., Slichter, D. H., Weber, S. J., Murch, K. W., Naik, R., Korotkov, A. N., and Siddiqi, I. "Stabilizing Rabi Oscillations in a Superconducting Qubit Using Quantum Feedback." *Nature* 490, 7418 (2012), pp. 77–80. DOI: 10.1038/nature11505.

[VS14] Villanueva, L. G. and Schmid, S. "Evidence of Surface Loss as Ubiquitous Limiting Damping Mechanism in SiN Micro- and Nanomechanical Resonators." *Phys. Rev. Lett.* 113, 22 (2014), p. 227201. DOI: 10.1103/PhysRevLett.113.227201.

[Vin+08] Vinante, A. et al. "Feedback Cooling of the Normal Modes of a Massive Electromechanical System to Submillikelvin Temperature." *Phys. Rev. Lett.* 101, 3 (2008), p. 033601. DOI: 10.1103/PhysRevLett.101.033601.

[VZ95] Vyatchanin, S. and Zubova, E. "Quantum Variation Measurement of a Force." *Phys. Lett. A* 201, 4 (1995), pp. 269–274. DOI: 10.1016/0375-9601(95)00280-G.

[Wal87] Walker, N. "Quantum Theory of Multiport Optical Homodyning." *J. Mod. Opt.* 34, 1 (1987), pp. 15–60. DOI: 10.1080/09500348714550131.

[WM08] Walls, D. F. and Milburn, G. J. *Quantum Optics*. 2nd ed. Berlin: Springer, 2008.

[Web+14] Weber, S. J., Chantasri, A., Dressel, J., Jordan, A. N., Murch, K. W., and Siddiqi, I. "Mapping the Optimal Route between Two Quantum States." *Nature* 511, 7511 (2014), pp. 570–573. DOI: 10.1038/nature13559.

[Wei+10] Weis, S., Rivière, R., Deléglise, S., Gavartin, E., Arcizet, O., Schliesser, A., and Kippenberg, T. J. "Optomechanically Induced Transparency." *Science* 330, 6010 (2010), pp. 1520–1523. DOI: 10.1126/science.1195596.

[Wie+15] Wieczorek, W., Hofer, S. G., Hoelscher-Obermaier, J., Riedinger, R., Hammerer, K., and Aspelmeyer, M. "Optimal State Estimation for Cavity Optomechanical Systems." *Phys. Rev. Lett.* 114, 22 (2015), p. 223601. DOI: 10.1103/PhysRevLett.114.223601.

[Wil+07] Wilson-Rae, I., Nooshi, N., Zwerger, W., and Kippenberg, T. J. "Theory of Ground State Cooling of a Mechanical Oscillator Using Dynamical Backaction." *Phys. Rev. Lett.* 99, 9 (2007), p. 093901. DOI: 10.1103/PhysRevLett.99.093901.

[Wil+15] Wilson, D. J., Sudhir, V., Piro, N., Schilling, R., Ghadimi, A., and Kippenberg, T. J. "Measurement-Based Control of a Mechanical Oscillator at Its Thermal Decoherence Rate." *Nature* 524, 7565 (2015), pp. 325–329. DOI: 10.1038/nature14672.

[Wis94] Wiseman, H. M. "Quantum Theory of Continuous Feedback." *Phys. Rev. A* 49, 3 (1994), pp. 2133–2150. DOI: 10.1103/PhysRevA.49.2133.

[Wis95] Wiseman, H. M. "Using Feedback to Eliminate Back-Action in Quantum Measurements." *Phys. Rev. A* 51, 3 (1995), pp. 2459–2468. DOI: 10.1103/PhysRevA.51.2459.

[Wis96] Wiseman, H. M. "Quantum Trajectories and Quantum Measurement Theory." *Quantum Semiclass. Opt.* 8, 1 (1996), pp. 205–222. DOI: 10.1088/1355-5111/8/1/015.

[Wis99] Wiseman, H. M. "Squashed States of Light: Theory and Applications to Quantum Spectroscopy." *J. Opt. B: Quantum Semiclass. Opt.* 1, 4 (1999), pp. 459–463. DOI: 10.1088/1464-4266/1/4/317.

[WM10] Wiseman, H. M. and Milburn, G. J. *Quantum Measurement and Control*. Cambridge University Press, 2010.

[Wol+15] Wollman, E. E., Lei, C. U., Weinstein, A. J., Suh, J., Kronwald, A., Marquardt, F., Clerk, A. A., and Schwab, K. C. "Quantum Squeezing of Motion in a Mechanical Resonator." *Science* 349, 6251 (2015), pp. 952–955. DOI: 10.1126/science.aac5138.

[Yar89] Yariv, A. *Quantum Electronics*. ed. 3. New York: John Wiley & Sons, 1989.

[Yu+20] Yu, H., McCuller, L., Tse, M., Kijbunchoo, N., Barsotti, L., and Mavalvala, N. "Quantum Correlations between Light and the Kilogram-Mass Mirrors of LIGO." *Nature* 583, 7814 (2020), pp. 43–47. DOI: 10.1038/s41586-020-2420-8.

[YCS15] Yuan, M., Cohen, M. A., and Steele, G. A. "Silicon Nitride Membrane Resonators at Millikelvin Temperatures with Quality Factors Exceeding $10^8$." *Appl. Phys. Lett.* 107, 26 (2015), p. 263501. DOI: 10.1063/1.4938747.

[YS80] Yuen, H. and Shapiro, J. "Optical Communication with Two-Photon Coherent States–Part III: Quantum Measurements Realizable with Photoemissive Detectors." *IEEE Trans. Inform. Theory* 26, 1 (1980), pp. 78–92. DOI: 10.1109/TIT.1980.1056132.

[ZP71] Zeller, R. C. and Pohl, R. O. "Thermal Conductivity and Specific Heat of Noncrystalline Solids." *Phys. Rev. B* 4, 6 (1971), pp. 2029–2041. DOI: 10.1103/PhysRevB.4.2029.

[Zha+17] Zhang, J., Liu, Y.-x., Wu, R.-B., Jacobs, K., and Nori, F. "Quantum Feedback: Theory, Experiments, and Applications." *Phys. Rep.* 679 (2017), pp. 1–60. DOI: 10.1016/j.physrep.2017.02.003.

[ZM17] Zhang, J. and Mølmer, K. "Prediction and Retrodiction with Continuously Monitored Gaussian States." *Phys. Rev. A* 96, 6 (2017), p. 062131. DOI: 10.1103/PhysRevA.96.062131.

[Zha+95] Zhang, T. C., Poizat, J. P., Grelu, P, Roch, J. F., Grangier, P, Marin, F, Bramati, A, Jost, V, Levenson, M. D., and Giacobino, E. "Quantum Noise of Free-Running and Externally-Stabilized Laser Diodes." *Quantum Semiclass. Opt.* 7, 4 (1995), pp. 601–613. DOI: 10.1088/1355-5111/7/4/015.

[ZDGV15] Zippilli, S., Di Giuseppe, G., and Vitali, D. "Entanglement and Squeezing of Continuous-Wave Stationary Light." *New J. Phys.* 17, 4 (2015), p. 043025. DOI: 10.1088/1367-2630/17/4/043025.

[Zur03a] Zurek, W. H. "Decoherence and the Transition from Quantum to Classical – REVISITED." *arXiv:quant-ph/0306072* (2003). arXiv: quant-ph/0306072.

[Zur03b] Zurek, W. H. "Decoherence, Einselection, and the Quantum Origins of the Classical." *Rev. Mod. Phys.* 75, 3 (2003), pp. 715–775. DOI: 10.1103/RevModPhys.75.715.

[Zwi+08] Zwickl, B. M., Shanks, W. E., Jayich, A. M., Yang, C., Bleszynski Jayich, A. C., Thompson, J. D., and Harris, J. G. E. "High Quality Mechanical and Optical Properties of Commercial Silicon Nitride Membranes." *Appl. Phys. Lett.* 92, 10 (2008), p. 103125. DOI: 10.1063/1.2884191.

## COLOPHON

This thesis was typeset using the typographical look-and-feel `classicthesis` developed by André Miede and Ivo Pletikosić. The style was inspired by Robert Bringhurst's seminal book on typography "*The Elements of Typographic Style*". `classicthesis` is available for both LaTeX and LyX:

https://bitbucket.org/amiede/classicthesis/